Production of resonant particles in pion-deuteron interactions at 4 GeV/c

Bell, Ian George

How to cite:

Bell, Ian George (1975) *Production of resonant particles in pion-deuteron interactions at 4 GeV/c*, Durham theses, Durham University. Available at Durham E-Theses Online: http://etheses.dur.ac.uk/8197/

Production of Resonant Particles in Pion-Deuteron Interactions at 4 GeV/c

A thesis presented

by

Ian George Bell B.Sc.

for the

Degree of Doctor of Philosophy

at the

University of Durham

January 1975

TO MY PARENTS

ABSTRACT

From a 400K picture sample of an exposure of 4 GeV/c π^+ mesons in deuterium, the two channels

$$\pi^+ d \to p_s p \pi^+ \pi^-$$

and $$\pi^+ d \to d \pi^+ \pi^+ \pi^-$$

are examined both by mass cut techniques and by a statistical cluster searching technique in the full 3n-5 dimensional kinematic space defined by the number of final state particles (n).

The clustering technique is shown to reproduce the distributions found by mass cut methods with some sharpening of the angular distributions and an increase in the statistics of the resonance signals available for analysis.

The method is tested by applying it to a Monte Carlo simulated experiment and the results are shown to give a high degree of separation of the various sub-channels.

The reaction $\pi^+ d \to p_s p \pi^+ \pi^-$, with a cross-section of 2.10 ± 0.17 mb, is seen to be dominated by the production of the ρ^0 and f^0 mesons. The regions of the ρ^0 and f^0 mesons are examined, and their spin structures determined by density matrix element analyses. These show that at low t values there are substantial S and S+P wave components under the ρ^0 and f^0 respectively. The ρ^0 meson data are shown to be compatible with >90% pure pion exchange at low values of t.

For the coherent reaction $\pi^+ d \to d \pi^+ \pi^+ \pi^-$, which is dominated by ρ^0 production and the d^* effect, the cross section is seen to be 0.316 ± 0.025 mb. The d^* effect is shown to be compatible with the production of an intermediate Δ state, the subsequent decay of which leaves an intact deuteron in the final state.

But it is also a world of great mystery and beauty, reflected in those fantastic photographs of events in the bubble-chamber, which show the trajectories of unimaginably small particles, moving at unimaginable speeds in curves and spirals, colliding, recoiling or exploding and giving birth to other particles or wavicles. The actors in this pageant are invisible, but they leave trails, rows of tiny bubbles in a liquid, loosely comparable to the condensation trails of high-flying jet planes - except that these tracks are sharp, thin lines whose length, angles and curvatures can be measured with sufficient exactitude to determine a particle's energy, speed, electric charge, and so on. This technique enables the physicist to observe the unthinkable - the transformation of mass into energy and of energy into mass. When a photon, a concentrated "package of light", without rest-mass, flies past an atomic nucleus, the photon is converted into an electron and a positron, both of which have mass, or even into two pairs of them. Vice versa, when an electron and a positron meet they destroy each other, converting their joint masses into high-energy gamma rays. To have penetrated to this depth below the world of appearances is one of the greatest triumphs of human ingenuity. Though the physicists themselves keep warning us that the ghosts we find down there elude the grasp of our understanding, at least we can measure their footprints in the bubble-chamber.

Extract from "The Roots of Coincidence" by Arthur Koestler

CONTENTS

Chapter 3 Analysis Techniques and Cluster Searching

List of Figures

Follows Page

Chapter 1

Chapter 2

Chapter 3

Chapter 4

Chapter 5

Chapter 6

Appendices

List of Tables

Page

Chapter 1

Chapter 2

Chapter 3

Chapter 4

Chapter 5

Chapter 6

Chapter 7

Introduction

This thesis is an account of the work carried out by the author whilst at Durham University and contains a description of the investigations made into, and the analysis of, the interactions of pi-mesons with deuterons. The experiment from which the data come, an exposure of 4 GeV/c π^+ mesons in deuterium, was undertaken by the High Energy Nuclear Physics Group at Durham in collaboration with similar groups from the University of Birmingham and the Rutherford High Energy Laboratory.

During the last decade or so, the construction of high energy beams of pions, kaons and protons has enabled the strong interactions of matter to be investigated, and the bubble chamber has proved to be a particularly useful instrument in this line of research. These investigations have resulted in the discovery of many short-lived resonance states which subsequently decay into two or more relatively stable particles. It is the determination of the methods of production and the properties of these resonances which in more recent times has been a topic of considerable interest. Many means of analysis have been devised to determine the properties of the short-lived resonances, in order to formulate a theory of the strong interaction, but to date there appears to be no theory which satisfactorily explains all of the features.

Since, in any given reaction channel, a resonant particle is not produced in every event, one of the goals of any analysis is to separate the resonance from the background which is present in the data. Some techniques have been recently examined which attempt as far as possible to do this. It is one of the points of this thesis to compare and contrast a method of event separation developed at Durham, based upon n-dimensional statistical searching techniques, with the standard methods used in bubble chamber film analysis.

In Chapter 1 the problems associated with the use of deuterium as a target are discussed, together with the general problems inherent in the bubble chamber technique. This is followed in Chapter 2 with a description of the 4 GeV/c π^+d experiment and the analysis system associated with it. Chapter 3, after a review of graphical display methods, introduces the statistical searching technique and the results of the use of the method to separate 3 sub-channels from a set of Monte-Carlo simulated events are presented. The channel $\pi^+d \rightarrow p_s p\pi^+\pi^-$ is discussed in Chapters 4 and 5 where the resonant particles ρ^0 and f^0 are examined in detail. This channel is basically the 3-body final state $p\pi^+\pi^-$, and the statistical searching, or clustering, technique takes place in a 4-dimensional space. As an example of the use of the clustering technique in a higher number of dimensions, the 4-body final state of the coherent channel $\pi^+d \rightarrow d\pi^+\pi^+\pi^-$ is examined in Chapter 6 where a 7-dimensional space is required. Again in this chapter, as in general in Chapter 4, the channel is examined firstly by standard methods and then by the clustering technique.

Chapter 1 General Comments on Deuterium Interactions and Bubble Chambers

1.1 Introduction

The main parts of this thesis are concerned with the interactions of 4 GeV/c π^+mesons with neutrons. Because it is not possible to produce targets of free neutrons, these have to be provided by complex nuclei and in bubble chamber experiments the neutron targets are supplied by the deuterons in deuterium. The deuteron is a very loosely bound system of a proton and a neutron within a potential well of depth $\sim$25 MeV with a binding energy of 2.2 MeV. To a good approximation, therefore, the neutron is free.

The interactions of π^+mesons in deuterium basically divide into two kinds: those where the incident pion interacts with either the proton or the neutron within the deuteron and those, the so-called coherent processes, where the π^+meson does not resolve the deuteron as two separate nucleons and the interaction is one with the deuteron as a whole. At the incident momentum of 4 GeV/c the occurrence of coherent interactions is small, accounting for only some 5-6% of the total number of events. For those events where the π^+meson interacts with the neutron in the deuteron, the reaction is treated in the impulse approximation (see Appendix B) as if the proton had taken no part in the interaction and remained throughout the process as a spectator nucleon.

Despite this simplification there are a number of problems associated with the use of deuterium because the neutron is not a truly free target. In this chapter, problems associated with the use of deuterium as a source of neutrons will be discussed and methods of overcoming these difficulties will be described. This will be followed by a summary of the technical problems associated with the bubble chamber technique insofar as they affect the accuracy of the experiment.

1.2 Problems Associated with Deuterium Targets

Because the neutron target is confined to the dimensions of the deuteron both it and the accompanying proton will have Fermi momenta of the order of 100 MeV/c. As far as the interaction on the neutron is concerned the initial momentum of the neutron will lead to variations in the centre of mass energy and the flux of neutron targets, which will depend upon whether the struck nucleon was moving towards or away from the primary particle. The accompanying, spectator, proton emerges from the interaction with its Fermi momentum and it therefore also contributes to the overall energetics of the interaction.

Also, since the neutron and proton are fairly close together in the deuteron each may shadow the other from the primary particle. Finally, when an interaction of the kind that is being considered does occur, where the target neutron charge exchanges to a proton, Pauli exclusion effects involving the recoil proton and the spectator proton are expected. These problems are now discussed in some detail.

1.2.1 The Spectator Proton

In the inelastic charge exchange process:

$$\pi^+ n \rightarrow p \pi^+ \pi^-$$

the final state proton, or recoil proton, may take on a variety of final state momenta and, if the interaction were one involving a truly free neutron, would in general be easily recognised. In deuterium interactions however, the equivalent reaction is written as

$$\pi^+ d \rightarrow p_s p \pi^+ \pi^-$$

or

$$\pi^+ \binom{n}{p_s} \rightarrow \begin{matrix} p \\ p_s \end{matrix} \ \pi^+ \pi^-$$

where p_s represents the spectator proton. According to the Hulthen distribution of nucleon momenta within the deuteron (see Appendix B), in $\sim 2/3$ of the cases the spectator proton will have a momentum less than 90 MeV/c, which in the bubble chamber will produce a track too short to be seen. Moreover, in 99% of the cases the spectator proton will have a momentum of less than 300 MeV/c. Experimentally, this leads to a situation where in some 20% of the events both of the final state protons have a momentum less than 300 MeV/c and hence there is an ambiguity in identifying the spectator proton. Throughout the analysis this ambiguity is handled by arbitrarily assigning that proton with the lower momentum, in the laboratory reference frame, to be the spectator proton. This method is supported by FAKE calculations which show that this assignment will be incorrect only in 3% of the total number of interactions. It is also supported by the experimental spectator momentum distribution in the interaction $\pi^+ d \rightarrow p_s p \pi^+ \pi^-$, which agrees very well with that predicted from the Hulthen distribution, a fact that will be returned to in Chapter 4. From this agreement it is also concluded that the impulse approximation is an adequate description of the pion-neutron interaction within the deuteron.

1.2.2 Centre of Mass Energy Variation

If the pion interaction takes place upon a stationary neutron target then small variations of centre of mass energy from one interaction to another would arise from the, usually very small, momentum bite of the beam. However, since the neutron is not stationary within the deuteron there is a much larger variation in the πn centre of mass energy. For 4 GeV/c π^+d interactions the mean value of the π^+n centre of mass energy is 2.9 GeV and, for the possible momentum variation of up to 300 MeV/c for the neutron, a variation of 10% in the mean centre of mass energy will result. One consequence of this is that there will be no single Dalitz plot boundary or Van Hove plot boundary to contain the data.

1.2.3 Flux Factor

Since, according to the Hulthen momentum distribution, the target nucleon has a non-zero momentum, an asymmetry exists in the flux of target nucleons depending upon whether the nucleons are moving towards or away from the beam particle. If the interaction cross-section were independent of centre of mass energy then this asymmetry in the flux would result in a higher number of events where the target neutron moves towards the beam than where the target neutron moves away from the beam particle.

The flux F is defined by:

$$F = |\vec{\beta}_1 - \vec{\beta}_2| \qquad (1.1)$$

where β_1 and β_2 are the velocities ($^V/C$) of the beam and target particles respectively. The experimental distribution of F for the reaction $\pi^+d \rightarrow p_s p\pi^+\pi^-$ is shown in Fig. 1.1.

Fig. 1.1

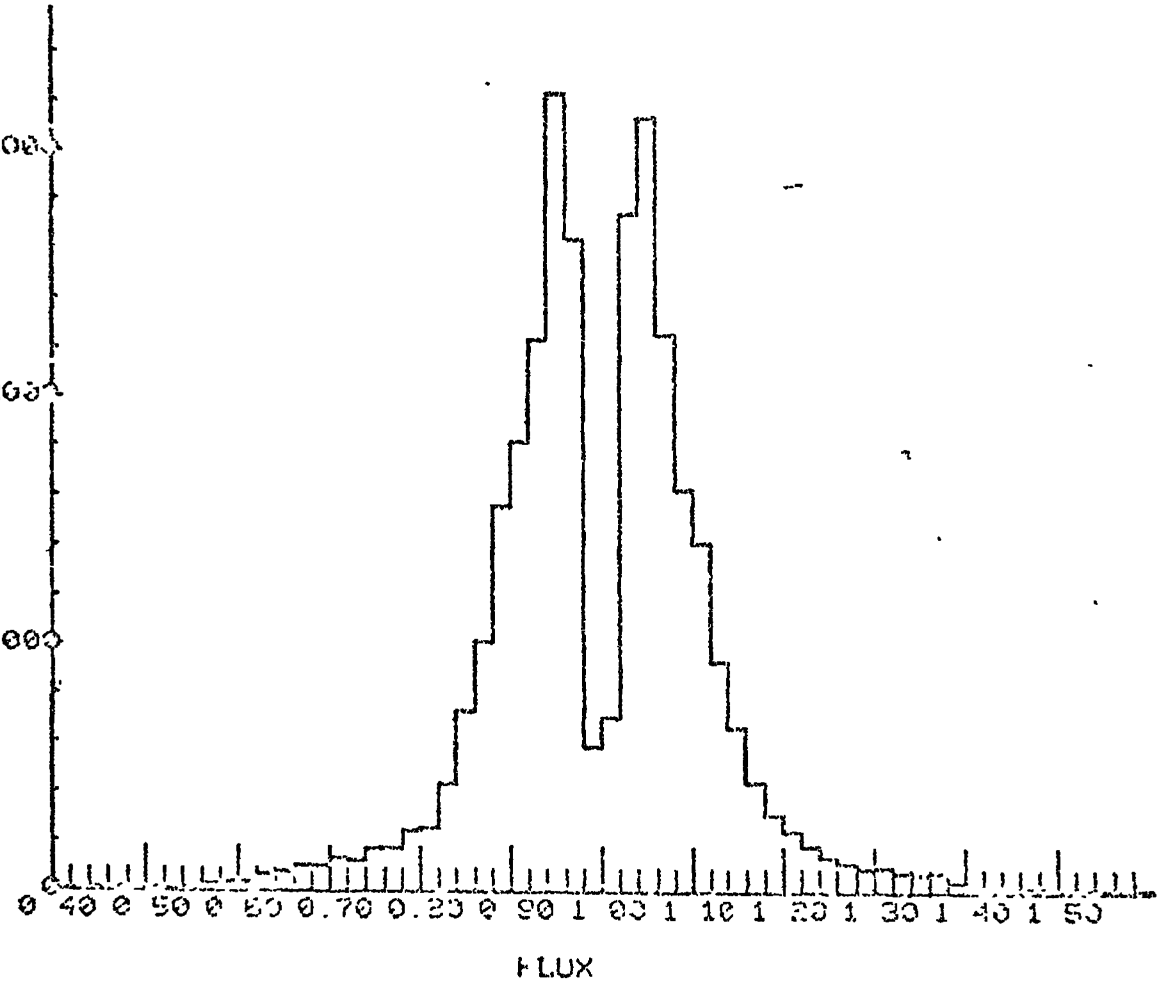

Frequency distribution of the Flux for the reaction $\overset{+}{\pi}d \rightarrow p_s p\pi^{+}\pi^{-}$ at 4 GeV/c incident momentum.

It has been assumed there that the target neutron in this reaction has a velocity equal and opposite to that of the spectator proton. In this figure the values of F below 1.0 result from those events where the target neutrons were travelling along the beam direction (and hence the spectator nucleon travelling towards the beam) and the values of F above 1.0 arise from the reverse case. Defining the number of events in which the flux F is greater than 1.0 as f and the number with F<1.0 as b, the experimental ratio $^f/b$ is found to be

$$\left(\frac{f}{b}\right)_e = 0.977 \pm 0.009$$

For the case of a cross-section constant with energy, this ratio is calculated to be

$$\left(\frac{f}{b}\right)_c = 1.05$$

where it has been assumed that the Hulthen distribution may be parameterised by the function $H \sim p^2 \exp\left(-\frac{p^2}{\alpha^2}\right) dp$, and the effective turn-over point (α) in the momentum distribution is 45 MeV/c. It is clear that the experimental distribution is not in agreement with that expected for the case of constant cross-section with energy. This therefore implies that the interaction cross-section decreases with increasing centre of mass energy, since b>f, which is found to be the case experimentally where resonance production cross-sections are found to vary with beam momentum p as p^{-n}.

1.2.4 Shadowing Effect

At 4 GeV/c the π^+p and π^+n total cross-sections are 27.5 and 34.1 mb respectively, whereas the total π^+d cross-section of ~57 mb is smaller than the sum of these two individual cross-sections. The difference of approximately 5 mb is due to each of the two nucleons shadowing the other from the beam particle, preventing an interaction in some cases. The effective pion-deuteron total cross-section can be written in terms of the individual nucleon cross-section as

$$\sigma(\pi d) = \sigma(\pi n) + \sigma(\pi p) - \frac{\sigma(\pi n)\ \sigma(\pi p)}{4\pi\ \langle r^2 \rangle} \qquad 1.2$$

where $\langle r^2 \rangle$ denotes the mean square separation of the individual nucleons. Inserting the cross-section values quoted above into Eq. 1.3 yields a value of 15 (Fermi)^2 for $\langle r^2 \rangle$, which is consistent with the observed size of the deuteron.

1.2.5 Pauli Exclusion Principle

The deuteron is a spin 1 nucleus, the two nucleons of which are largely in the $^3S_1$ state (96%) and to a lesser extent in the $^3D_1$ state (4%), where the triplet fermion system has an overall symmetric wave function. Take for example a strong interaction where inelastic charge exchange is involved, such as in the interaction $\pi^+ d \rightarrow p_s p \pi^+ \pi^-$, and assume that the spin of the initial neutron is not flipped. As the four-momentum transfer squared, t, to the nucleon tends to zero, then the final p-p state tends to a system of identical fermions in the same symmetric configuration as the initial state. The Pauli exclusion principle, which states that a symmetric wave function for a system of two identical fermions is not allowed, will therefore lead to a depletion of the number of events at low t for interactions which do not involve spin flip. When there is spin flip the

the interactions may also be affected by the Pauli exclusion principle, for reasons explained below.

The triplet spin wave functions for the deuteron may be written

$$\psi\,(1,1) = \psi_p(\tfrac{1}{2},\tfrac{1}{2})\;\psi_n(\tfrac{1}{2},\tfrac{1}{2}) \qquad 1.3$$

$$\psi\,(1,0) = \frac{1}{\sqrt{2}}\left\{\psi_p(\tfrac{1}{2},\tfrac{1}{2})\;\psi_n(\tfrac{1}{2},-\tfrac{1}{2}) + \psi_p(\tfrac{1}{2},-\tfrac{1}{2})\;\psi_n(\tfrac{1}{2},\tfrac{1}{2})\right\} \qquad 1.4$$

$$\psi\,(1,-1) = \psi_p(\tfrac{1}{2},-\tfrac{1}{2})\;\psi_n(\tfrac{1}{2},-\tfrac{1}{2}) \qquad 1.5$$

where the subscripts indicate the two different nucleons and where the notation (S,S_z) is used. It is noted that the spin configurations indicated by Eqs. 1.3, 1.4 and 1.5 are symmetric. For the final state di-proton system, which by the Pauli exclusion principle must be in an overall antisymmetric state, the above triplet spin state can only occur in conjunction with an antisymmetric orbital angular momentum state for the two protons, that is with an odd L orbital angular momentum system. For a symmetric (even L) orbital angular momentum system then by the Pauli exclusion principle, the spin wave function of the di-proton must be in the antisymmetric singlet state:

$$\psi(0,0) = \frac{1}{\sqrt{2}}\;\{\psi_1(\tfrac{1}{2},\tfrac{1}{2})\;\psi_2(\tfrac{1}{2},-\tfrac{1}{2}) - \psi_1(\tfrac{1}{2},-\tfrac{1}{2})\;\psi_2(\tfrac{1}{2},\tfrac{1}{2})\} \qquad 1.6$$

Considering, firstly, interactions which do not involve spin flip of the neutron then the final state p-p system remains in the triplet spin state of Eqs. 1.3, 1.4 and 1.5 (but with the ψ_n replaced by $\psi_{p'}$). The Pauli exclusion principle will then forbid those states with even L. Secondly, for interactions which involve spin flip, then the transition of the state $\psi\,(_{1,0})$ into either of the states $\psi(1,1)$ or $\psi(1,-1)$ is forbidden unless it is accompanied by a change of orbital angular momentum into an odd L value. The states $\psi(1,1)$ and $\psi(1,-1)$ may proceed via spin flip into either of the states $\psi(1,0)$ or $\psi(0,0)$ only if the transition into $\psi(1,0)$ is accompanied by a change into an odd L system and the transition into the state $\psi(0,0)$ leaves the p-p state in an even L orbital angular momentum state.

The deuteron differential cross section may be expressed in terms of the partial flip and non-flip cross-sections by

$$\frac{d\sigma}{dt}_{\text{TOT}} = \left[1-\frac{H(q)}{3}\right]\frac{d\sigma}{dt}_{\text{flip}} + \left[1-H(q)\right]\frac{d\sigma}{dt}_{\substack{\text{non}\\\text{flip}}} \qquad 1.7$$

where $H(q)$ is the deuteron form factor expressed in terms of the three momentum transfer q ($q=\sqrt{t}$) as

$$H(q) = 4\pi\int \phi^2(r)\ \frac{\sin qr}{qr}\ r^2\, dr \qquad 1.8$$

and $\phi(r)$ is the deuteron spatial wave function. (See Appendix B). By evaluating the deuteron form factor from Eq. 1.8, and substituting into Eq. 1.7, the correction terms necessary to apply to the observed differential cross-section at varying values of q, because of the effect of the Pauli exclusion principle, may be obtained. Shown in Fig. 1.2 is a plot of $H(q)$, the deuteron form factor, against t, the four momentum transfer squared.

Table 1.1 below lists the variation of the cross-section correction factors obtained from Eq. 1.7 for both pure spin-flip and pure spin non-flip reactions. As can be seen from this table, the effects of the Pauli exclusion principle are small except at very small values of momentum transfer, t, to the nucleon

Fig. 1.2

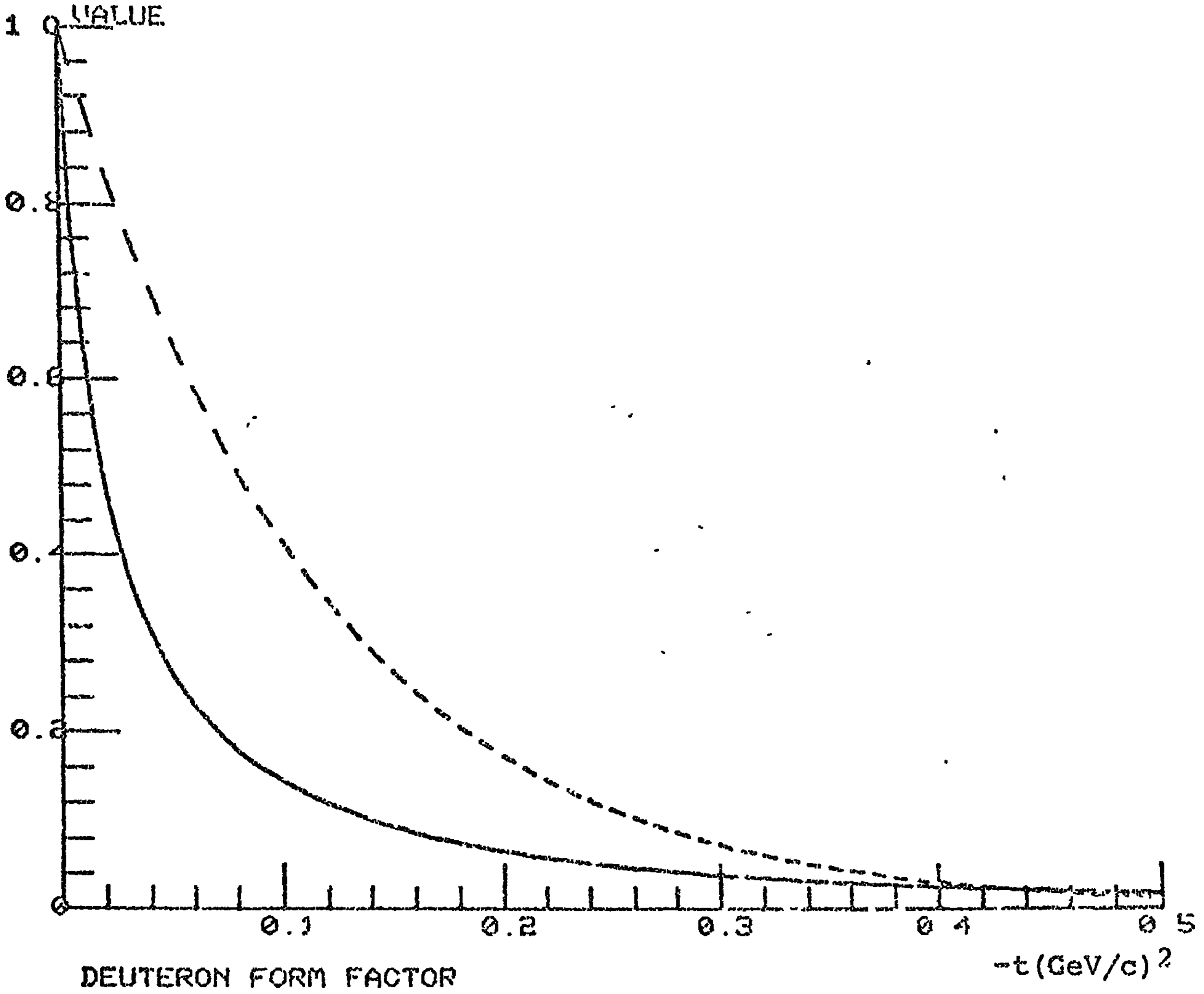

Solid curve is the Deuteron Form Factor evaluated from the Hulthen Potential for the Deuteron. Dashed curve is for a Gaussian Deuteron spacial wave function giving a Form Factor of exp(-17t).

Table 1.1 Effect of the Pauli Exclusion Principle

Momentum Transfer $-t$ $(GeV/c)^2$	$q = \sqrt{t}$ GeV/c	Correction Factors Pure Flip	 Pure non-flip
0.02	0.141	1.18	1.82
0.04	0.200	1.11	1.40
0.06	0.245	1.07	1.25
0.08	0.283	1.05	1.18
0.10	0.316	1.04	1.14
0.12	0.346	1.03	1.11
0.14	0.374	1.03	1.09
0.16	0.400	1.02	1.08
0.18	0.424	1.02	1.06
0.20	0.447	1.01	1.05

1.2.6 Event Loss due to Interaction Topology

Another loss of events occurs at small values of momentum transfer when neither of the final state nucleons, say in the reaction $\pi^+ d \rightarrow p_s p \pi^+ \pi^-$, is visible in the chamber. The event then appears as a two-pronged interaction with no protons in the final state and, because of the acceptance criteria that two-pronged events must have two identifiable protons, is thus rejected at the scanning table. FAKE calculations have shown that this loss of events is small, accounting for less than 2% of the events with $t<0.1(GeV/c)^2$. Here it is assumed that a uniform depopulation of events in this t region results from the Pauli exclusion principle. The loss of events due to interaction topology is therefore considered negligible with respect to the accumulated effects of statistical errors and the Pauli exclusion principle.

1.3 Problems associated with the Bubble Chamber Technique

The bubble chamber is an isotropic detector efficient over 4π steradians, which permits the trajectories of charged tracks within an event, and the ionization of their paths, to be determined. The deuterium bubble chamber is also a detector with spacial resolution of the order of a millimetre or less. This is important with respect to the following points:

(a) For the study of complex events in which short-lived hyperons or kaons are produced. Hyperons or kaons decaying within a few millimetres of their production point can be identified and analysed. This is particularly important at low energies where the time dilation factors for the particles in question are small.

(b) For the study of peripheral interactions in which the recoiling nucleon is of short range. This is important at all energies since it is the momentum transfer which governs the momentum of the recoil particle, not the beam momentum.

(c) For the study of interactions upon the neutrons of deuterium it is necessary to see and identify the spectator proton or, if it is not seen in the chamber, to know that its momentum is small. This, also, is important at all energies.

The bubble chamber is essentially a simple device whose configuration and data retrieval arrangements do not change, no matter how complicated are the events being analysed. The momenta of the charged particles can be determined to an accuracy of a few percent in existing chambers and measurements of angles can be made to within 2-3 milliradians. This yields a resolution in effective mass calculations between groups of final state particles of 10-20 MeV/c^2.

1.3.1 Limitations of the Technique

The limitations of the bubble chambers which are in use at the present can be broken down into 3 groups; statistical limitations, limitations on precision and the lack of effective γ-ray conversion. These will be set out in the sections which follow.

(a) Statistical Limitations

For a rare reaction channel the low cycling rate of present day chambers, a maximum of ∿1 picture per second, leads to a small final sample of events. For example, an experimental run of 3 million pictures with 10 metres of track per picture would be required to produce 1000 events at the 10μb cross-section level. Experiments based on 500K pictures often yield only ∿100 events in a resonance peak which is sufficient only to note the existence of the resonance but insufficient to allow its quantum numbers to be determined.

(b) Limited Precision

Errors on the determination of momenta of charged particles from their curvature in the magnetic field of the chamber lead to two possible fundamental limitations of the analysis.

(i) Limitations on the effective mass resolution of 10-20 MeV/c^2 lead to an experimental situation in which the natural width of many of the seen resonant states is smaller than the resolution of the experiment. Specifically, the examination of possible fine structure in resonance peaks is handicapped by the resolution. Even for a resonance broad in comparison with the experimental resolution, large statistics may not give accurate mass values unless a check is made that there are no systematic shifts - a check which is itself hampered by the experimental resolution.

(ii) Poor event identification in an experiment leads to a situation where it is not possible to obtain unbiased samples of events from a reaction without a background of incorrectly assigned events from other channels. For example, a particularly well known ambiguity is that between the Λ^0 and Σ^0 hyperons which exists at all energies, rising from ~10% at 1.5 GeV/c to ~80% at 3 GeV/c.

(c) γ-conversion

The large radiation length in a deuterium bubble chamber of 8.2 metres leads to a lack of effective gamma ray conversion in these chambers. This prevents the presence of a π^0 in an interaction to be directly recognised and thus events with more than one missing neutral particle cannot be analysed except by quite complicated techniques (Ref. 1.1).

1.4 Experimental Errors on Track Measurement

There are many different sources of error which contribute to the overall error of determination of particle trajectories, but broadly they can be divided into two groups.

Firstly, there are those errors which are intrinsic in the chamber, for example thermal convection, turbulence and multiple coulomb scattering. Secondly, there are those errors due to optical distortion, inaccuracies in the knowledge of the magnetic field, and errors of measurement. Of these two categories of errors, the dominant contributions are those of coulomb scattering and measurement error.

1.4.1 Coulomb Scattering Error

Multiple coulomb scattering gives rise to a spurious curvature of the track, which is interpreted as an error in the momentum of the track. The effective error Δp on the momentum p of a track from coulomb scattering is proportional to $1/\sqrt{L}$ where L is the track length, and is given by (Ref. 1.2)

$$\left(\frac{\Delta p}{p}\right)_c = \frac{1.8\text{x}10^4}{\sqrt{\psi L}\;\;H\beta} \qquad 1.9$$

where β is the velocity $(\frac{V}{C})$ of the particle, H is the magnetic field in gauss, and ψ is the radiation length of the liquid. For a track of length 50 cm at a velocity $\beta = 1$ in a magnetic field of 17.5 K gauss, this error is $(\frac{\Delta p}{p})_c = 0.5\%$.

1.4.2 Thermal Effects

Temperature differences within the bubble chamber liquid give rise to convection currents of velocity approximately 3 cm/sec. For a growth time of 1 millisecond for the bubbles before photography, the bubble will have moved 30μm from its original position. This produces an uncertainty in the true bubble position in the chamber which, although smaller than the apparent size of the bubble in chamber space (the size of the Airey disc is ~250μm), contributes to the overall error.

Another uncertainty of some 30 microns arises from the "twinkling" effect in which the bubble appears to move because of the variations of refractive index in the liquid due to thermal turbulence.

1.4.3 Measurement Error

The measurement error on a track of length L cm is proportional to L^{-2} and can be written in terms of the magnetic field H gauss and momentum p MeV/c as

$$\left(\frac{\Delta p}{p}\right)_m = \frac{F_o\,p}{3.75\times10^{-5}L^2H} \qquad 1.10$$

where F_o is the typical measurement error in chamber space on any one point, and is approximately 50μm for a track measured on an automatic measuring machine such as the Hough Powell Device (HPD). For a track of momentum 1 GeV/c and of length 50 cm in a magnetic field of 17.5 K gauss, the error calculated from Eq. 1.10 is

$$\left(\frac{\Delta p}{p}\right)_m = 0.25\%$$

In the 4 GeV/c π^+d experiment therefore, where typical values for p and L are those used to evaluate Eqs. 1.9 and 1.10, the measurement errors on the tracks are limited by the coulomb error term of Eq. 1.9.

1.5 The Aims of the Experiment

The experiment was designed primarily to study, with high statistics and accuracy, the neutral meson systems in the reaction

$$\underset{(p_s)}{\pi^+ n} = \underset{(p_s)}{p} \quad X^0 \qquad 1$$

with an incident pion momentum of 4 GeV/c giving a centre of mass energy of 2.9 GeV. This yields for X^0 a variation of invariant masses up to a maximum of approximately 2 GeV/c^2, a mass high enough to encompass all of the well known meson resonances. In the above reaction X^0 represents any neutral meson system which, in order that a successful kinematic fit may be obtained, must not contain more than one neutral particle.

(a) X^0 = a dipion system (Specifically $\pi^+\pi^-$)

For a $\pi^+\pi^-$ system reaction 1 renders a fully constrained kinematic fit and, despite the fact that the use of a deuterium nucleus to provide the target neutron imposes some slight uncertainty in the centre of mass energy, this is preferable to the case of the partially constrained kinematic fit offered by the charge conjugate reaction $\pi^-p\rightarrow n\pi^+\pi^-$. Therefore the study of the ρ^0 and f^0 mesons with the highest statistics then available in a bubble chamber experiment was of interest. The examination of the spin structures of these well established resonances was to become an important part of the experiment.

(b) X^0 = a tripion system (specifically $\pi^+\pi^-\pi^0$)

In a bubble chamber the study of a $\pi^+\pi^-\pi^0$ system produced by π^+ interactions can only be performed with a neutron target, being inaccessible in the charge symmetric reaction $\pi^-p\rightarrow nX^0$ since this contains two neutral particles in the final state (see section 2.7.4). At the time of the proposal of the experiment there were many problems associated with a $\pi^+\pi^-\pi^0$ state and only certain examples are given here.

(i) A_2 splitting

Suggestions of a possible double structure in the A_2 mass region ($\sim$1300 MeV/c^2) had been made for the charged modes of the A_2 meson, but no A_2^0 splitting had been seen and it was thought desirable to confirm (or not) the A_2 splitting in the non-charged mode.

(ii) $\omega - \rho$ interference

Although the exchanges are in principle the same in $\pi N \rightarrow N(\omega,\rho)$ as in $\pi N \rightarrow \Delta(\omega,\rho)$ it was thought interesting to ensure that the nature of $\omega - \rho$ interference is the same in the two cases. In order to study this interference the normal 3π ω^0 decay must also be studied, and this is not possible in πp collisions for reasons explained above.

(iii) $\pi^+ n \rightarrow p\omega$

The production properties of the ω meson in this reaction were to be studied in order to compare with previous results which indicated that more than simple ρ exchange was involved.

(c) Coherent interactions

It was also proposed to study the so-called coherent deuteron reaction $\pi^+ d \rightarrow dX^+$ since much interest was then being shown in this reaction, possible d^* and A_1 production being the points of interest.

Of the above effects, those considered in this thesis are the ρ^0 and f^0 spin structures and the coherent deuteron interactions.

All of these effects require very high statistics to study and thus the experiment was proposed as a 700K picture exposure.

The film was digitized using H.P.D. automatic measuring machines for speed, accuracy and because of the ionization information thus available.

Chapter 2 General Experimental and Analysis Considerations

Introduction

Every bubble chamber experiment must pass from its inception through various stages, not the least of which are those of exposure and measurement, before any data analysis can occur and in this chapter a description of these important parts of the 4 GeV/c π^+d experiment will be given. The beam line and chamber operation will be discussed and the processing of the film from the scanning of an event to its insertion onto a data summary tape (DST) will be traced. Finally an examination of the precision of mass determinations of combinations of final state particles for both charged and charged/neutral configurations will be made, followed by a discussion of cross-sections as a prelude to the calculation of partial cross-sections in later chapters of this thesis.

2.1 The Exposure

The exposure was conducted at CERN and took place in two parts: the first was during late August and early September 1970 and the second in December 1972. These two exposures were of approximately equal size, being 450K and 400K pictures respectively. Analysis of the film from the first run has almost been completed by the three collaborating laboratories: Birmingham University, the Rutherford High Energy Laboratory (RHEL) and Durham University. The second batch of film is now in the process of being analysed, and is nearing completion.

The experiment was performed using 4 GeV/c π^+ mesons which were produced when the extracted proton beam from the CERN proton synchrotron was allowed to impinge on a copper target in the U5 beam line. From the numerous particles thus produced the π^+ mesons were momentum analysed, separated, and directed into the 2-metre deuterium bubble chamber (2-m DBC). In order that a reasonable number of beam tracks were present on each frame, so as to give definite vertical separation, the flux of pions was reduced to (12 ± 3) per pulse before entering the 2-m DBC.

2.2 The Beam Line and Bubble Chamber

Shown schematically in Fig. 2.1 is the CERN U5 beam line (Ref. 2.1) which is an up-dated version of the earlier U3 beam. The optics of the system are basically divided into 3 parts:

a) Formation and Momentum Analysis Stage

b) Separation Stage

c) Final cleaning and preparation stage for the 2 metre Deuterium Bubble Chamber

A list of the essential elements of the system, and key to Fig. 2.1 is given in Table 2.1. For the required beam of 4 GeV/c pions the beam line was run with only 2 of the possible 3 R.F. cavities in operation, since it is generally found that pion beams of this momentum are easily separated by rejecting the protons whence the kaons, muons etc. are also automatically rejected.

2.2.1 2-particle R.F. separation

The momentum analysed beam passes successively through

Fig. 2.1

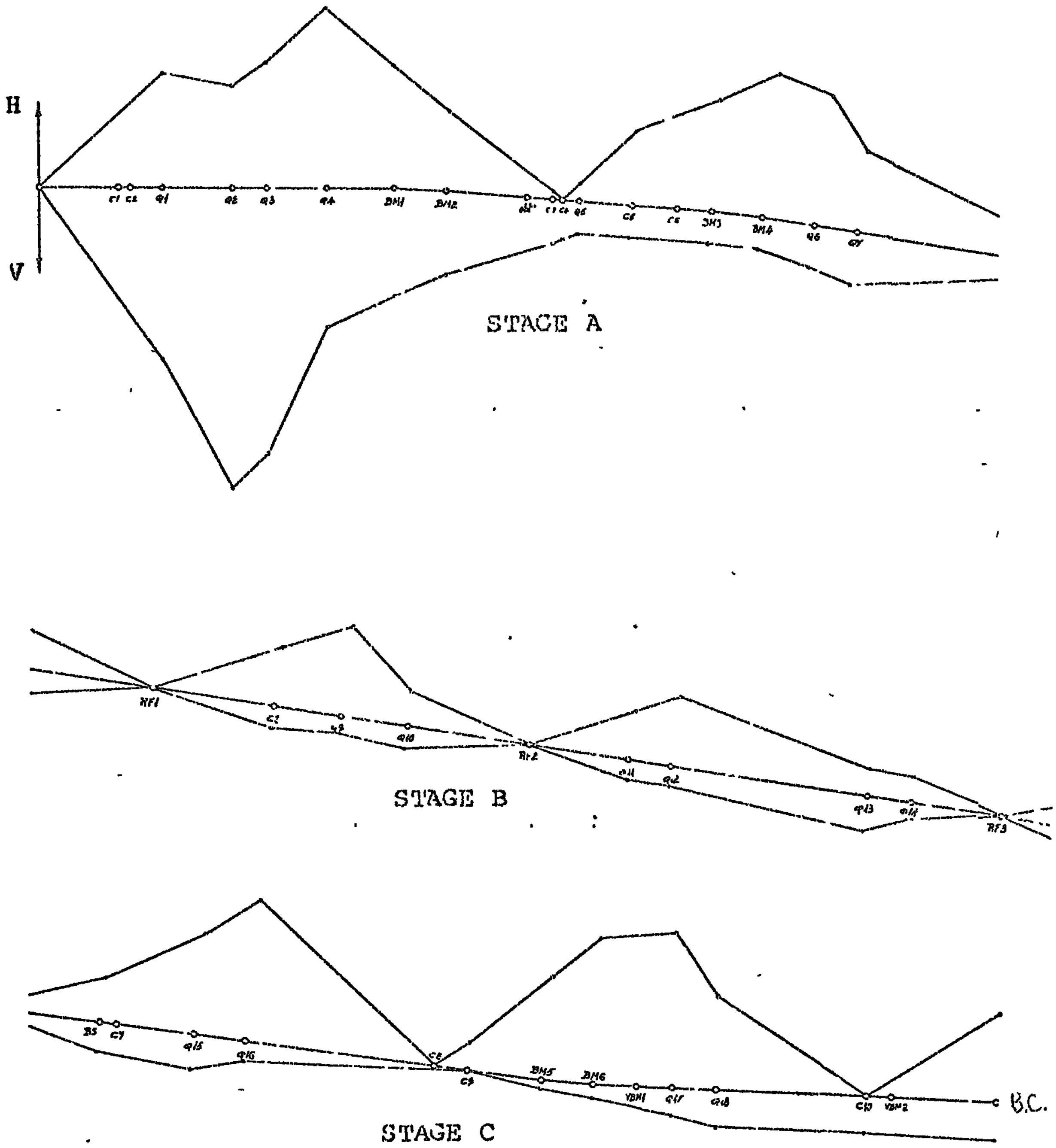

Diagrammatic representation of the U5 beam line showing horizontal (H) and vertical (V) focussing. For kev to Fig. see Table 2.1 .

Table 2.1

List of U5 Beam Line Elements

No.	Element Description	Symbol in Fig. 2.1	Distance from Preceding Element (m)	
1	Target - copper	T	0	
2	Horizontal Collimator	C1	4.5	
3	Vertical Collimator	C2	0.65	
4	2m Quadrupole	Q1	1.85	
5	2m Quadrupole	Q2	4.00	
6	1m Quadrupole	Q3	2.50	
7	2m Quadrupole	Q4	3.50	
8	Bending magnet	BM1	3.87	
9	Bending magnet	BM2	3.00	Stage A
10	Vertical collimator	C3	5.92	62m
11	Horizontal collimator	C4	0.58	
12	0.75m Quadrupole	Q5	1.00	
13	Horizontal collimator	C5	2.25	
14	Vertical collimator	C6	2.25	
15	Bending magnet	BM3	2.00	
16	Bending magnet	BM4	3.00	
17	2m Quadrupole	Q6	3.05	
18	2m Quadrupole	Q7	2.50	
19	Separator	RF1	15.50	
20	2m Quadrupole	Q8	7.09	
21	2m Quadrupole	Q9	3.91	
22	2m Quadrupole	Q10	3.91	
23	Separator	RF2	7.09	Stage B
24	2m Quadrupole	Q11	5.75	50m
25	2m Quadrupole	Q12	2.50	
26	2m Quadrupole	Q13	11.50	
27	2m Quadrupole	Q14	2.50	
28	Separator	RF3	5.75	
29	Beam stopper	BS	7.55	
30	Vertical collimator	C7	1.50	Stage C
31	2m Quadrupole	Q15	3.50	53m
32	2m Quadrupole	Q16	3.00	
33	Horizontal collimator	C8	11.00	

Table 2.1 (cont'd)

No.	Element Description	Symbol in Fig. 2.1	Distance from Preceding Element	
34	Vertical Collimator	C9	1.90	Stage C 53m
35	Bending magnet	BM5	4.26	
36	Bending magnet	BM6	3.00	
37	Vertical bending magnet	VBM1	2.18	
38	2m Quadrupole	Q17	2.22	
39	2m Quadrupole	Q18	2.50	
40	Horizontal collimator	C10	9.00	
41	Vertical bending magnet	M8	2.00	
42	Bubble chamber	BC	5.00	

two radio frequency fields RF1, RF2 as shown in fig. 2.2(a). These fields exert in one plane a sinusoidally time varying deflection force on the particles, and adjustment of the phasing ϕ_{12} of RF1 with respect to RF2 can be made, and is then kept constant. Between the two RF cavities there lies a beam optical system which refocusses, with unit magnification, the image from the centre of RF1 into the centre of RF2. The relative phase ϕ_{12} is adjusted so as to make the overall deflection of the wanted particles a maximum, with the unwanted particles being brought back to the original beam axis and this independently of their entry phase provided that the amplitudes of RF1 and RF2 are equal. These unwanted particles are then allowed to pass into the beam stopper, whose width is adjusted so as to give maximum shielding against them. The deflection amplitude of wanted particles is given by

$$D = 2A \sin \frac{\tau}{2} \qquad 2.1$$

where A = amplitude of the RF fields

and τ = the phase difference between the wanted and unwanted particles

τ can be calculated for two particles of momentum p by

$$\tau = \frac{2\pi L}{\lambda} \left(\sqrt{1 + 1/\beta_1^2} - \sqrt{1 + 1/\beta_2^2} \right) \qquad 2.2$$

where subscript 1 = unwanted particle

2 = wanted particle

L = length between RF1 and RF2

λ = wavelength of RF fields

ϕ_{12} is then adjusted to the value and the amplitude A is made large enough to allow the wanted particles to pass outside the stopper. The condition chosen is D>A, that is

$$2\left|\sin \tau/_2\right| \geq 1$$

2.2.2 Experimental Operation

All of the elements numbered 2 to 40 in table 2.1 were controlled, after initial adjustment by the resident CERN staff, by members of the three collaborating laboratories; the author being one of the Durham representatives at each of the two exposures. Careful monitoring of the bending magnet and quadrupole magnet currents enabled both the momentum and focussing of the beam (respectively) to be held stationary. The various collimators were also controlled in order to keep the final flux of particles into the chamber at ~12 pions/pulse, digital readouts from in-line spark chambers facilitating this flux monitoring. As determined from beam line characteristics, and later verified by measurements, the final particle momentum in the first exposure was 4.02 GeV/c with a momentum bite of 0.25%, and in the second exposure 3.94 ± 0.02 GeV/c. A plot of the beam momentum is shown in Fig. 2.2(b) containing the distributions for both first and second exposures.

2.2.3 The Bubble Chamber

Three monochromatic electronic flash tubes were used for the illumination of the 2m DBC, each tube illuminating approximately the same size of internal volume of the chamber.

Fig. 2.2

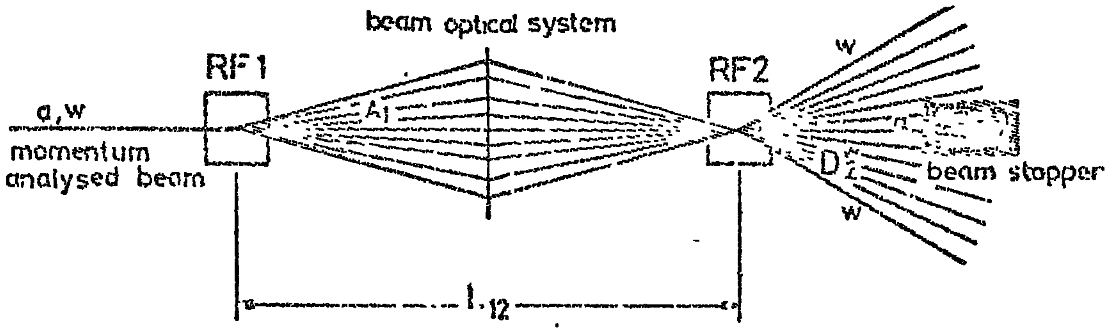

(a) Two-particle R-F separation.

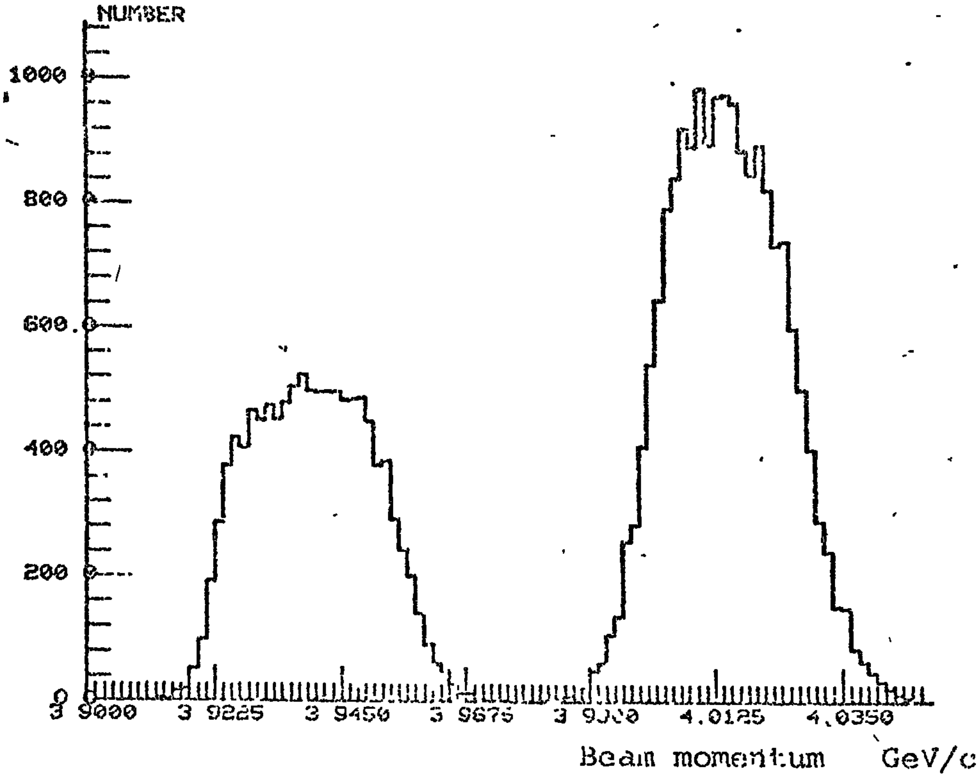

(b) Beam momentum distribution for first (right) and second (left) exposures.

Fiducial marks, which were used for reference in the geometrical reconstruction which followed later in the analysis, were present on three different window faces of the chamber. These three planes were (Ref. 2.2):

1) the outer face of the camera window (front glass; plane 1)

2) the inner face of the camera window (front glass; plane 2)

and 3) the inner face of the flash window (back glass; plane 3)

planes number 2 and 3 being in contact with the liquid. Fig. 2.3(a) shows a diagram of the fiducial crosses as seen from camera number 2. There are 6 fiducials in plane 1, 15 in plane 2 and 9 in plane 3; alignment crosses and data box fiducial marks are not shown in this figure.

Three cameras were used for the photography, set with co-ordinates relative to the centre of the chamber as shown in table 2.2 below and subtending a stereo angle of ∿10° at the front glass of the chamber. The distance from the camera plane to the chamber front glass was ∿200 cm.

Table 2.2 Camera Co-ordinates

Camera	X(cm)	Y(cm)	Z(cm)
1	13.2	29.0	∿ 200 cm
2	-31.8	0.0	
3	13.2	-29.0	

These three views, in conjunction with the known fiducial positions, enabled a geometrical reconstruction in 3-dimensions with a point accuracy of ∿50μ to be achieved.

The chamber was operated in its double pulsed mode, with ∿1/10 second elapsed time between pictures in each of the pulses

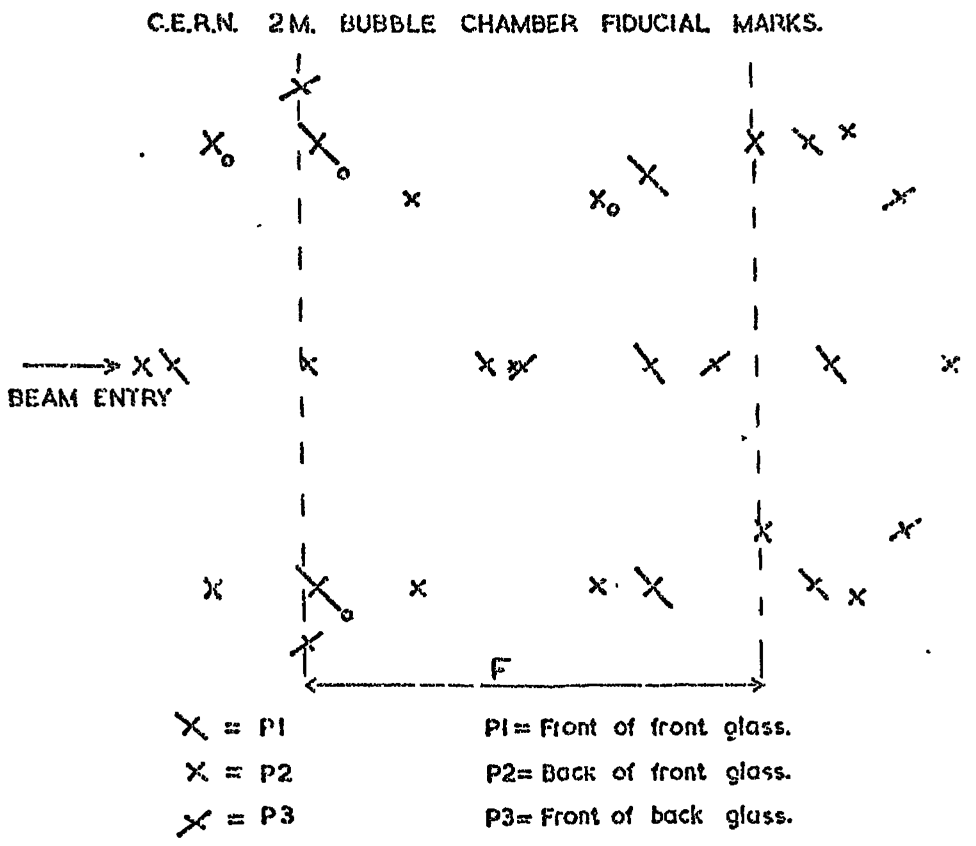

Fig. 2.3(a) Fiducial marks and fiducial volume F .

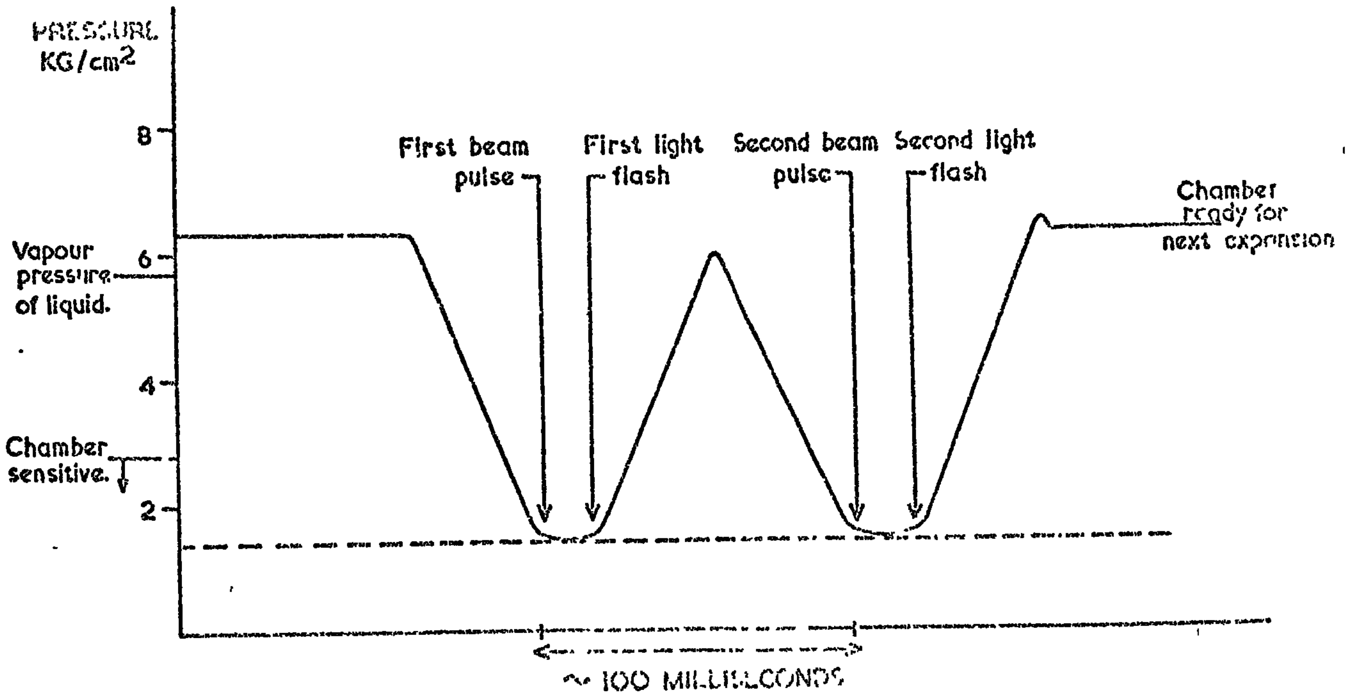

FIG. (2-3(b)) TYPICAL CURVE OF DOUBLE PULSE OF BUBBLE CHAMBER.

and ~ 2 seconds delay between each double pulse. Shown in Fig. 2.3 (b) is the sequence of operation of the bubble chamber.

Applied throughout the chamber volume, a magnetic field of central value 17.5 Kgauss was used in order that momentum determinations could be made of all charged tracks in an event. Variations of the magnetic field throughout the chamber volume were well known, and a complete map of the magnetic field was available such that particle path variations, due to these deviations from uniformity, could be corrected.

Test strips of film, consisting of some 30 frames from the end of each roll, were scanned during chamber operation. A constant monitoring was thus carried out of such quantities as track density (bubbles/cm), bubble size, and track count; general good quality of the pictures thereby being maintained. The distance between Brenner marks, which are used by the automatic measuring machines for alignment and frame counting, was also carefully checked so as to avoid variations. The track density was maintained at ~ 14 bubbles/cm in space, with an Airey disc diameter of ~ 300 μm. Fig. 2.4 shows a frame of film taken during the first exposure.

2.3 Contamination of the π^+ beam

Any beam contamination must be due to the four charged particles p, K^+, μ^+, d. Of these, the deuteron contamination is highly improbable at this energy using two RF separation cavities, so the three contaminations which have been investi-

Fig. 2.4 Frame of film from first exposure.

gated are those of p, K^+, μ^+. Although it would seem possible to estimate these contaminations from δ-ray counts, this method has been found to be unsatisfactory, giving no effective resolution between pions and either of p, K^+, μ^+.

a) μ^+- contamination

This has been calculated assuming that μ-contamination results from pion decay ($\pi \to \mu + \nu$) between the last collimator (C10) and the bubble chamber, a distance of 7 metres. Using a pion lifetime of 2.6×10^{-8} seconds, and a Lorentz factor γ of 29.1, the percentage of pion decays is 3%. Assuming, then, that a difference in displacement of ≥ 1 cm over 200 cm is sufficient for the muon to be seen to be 'off-beam' (equivalent to a μ momentum in the lab of ≤ 3.8 GeV/c), then the μ-contamination is estimated to be $(0.4 \pm 0.1)\%$.

b) K^+- contamination

This contamination has been estimated from the number of Tau decays of the K-meson which can be fitted to a sample of some 3000 3-pronged events. An upper limit of 1 event was found as a Tau candidate. Using the expression

$$L = \frac{N_\tau \beta c \tau}{F}$$

N_τ = No of τ decays

β = P/E

F = branching ratio of K as Tau

τ = lifetime

for kaon path length, an estimate of the number of kaons was found as $\leq (0.5 \pm 0.1)\%$.

c) Proton contamination

This has been estimated, using a method described by

Gordon (Ref. 2.3) which uses pure proton beam film as a normalisation.

The method relies upon two assumptions

$$\text{(i)} \quad \frac{\sigma(\pi d\to pp\pi^+\pi^-)}{\sigma(\pi d\ \text{total})} = \frac{\sigma(pd\to ppp\pi^-)}{\sigma(pd\ \text{total})}$$

and

(ii) That the ratio of probabilities

$$\frac{\text{P(lucky proton fit to a true pion beam)}}{\text{P(lucky pion fit to a true proton beam)}} = \frac{2}{1}$$

which can be shown to be true from Monte-Carlo simulations. This method leads to an estimate of proton contamination of (4±3)%.

Of the three assumed contaminants, it is apparent that the proton contamination is the most dominant. Whereas all contaminations were taken into account where cross-sections were concerned, the proton beam was considered serious enough to warrant a fitting hypothesis at least to the more frequently occuring channels, for example $\pi^+d\to pp\pi^+\pi^-$ was supplemented with $pd\to ppp\pi^-$. This practice was, however, not completely satisfactory since FAKE simulations have shown that in some 20% of the cases a spurious proton fit occurs to the real pion beam event (as implied in Gordon's method).

2.4 Scanning of the Film

The fiducial volume used in the scanning of the film is shown in Fig. 2.3. Apart from strange particle production, the general reaction to be studied was of the type:

$$\pi^+d\to pp_sX^0 \quad (\text{or } \pi^+n\to p X^0)$$

where p_s implies a "spectator" proton (see Appendix B) and X^0 represents any neutral meson system.

The initial scanning rules at Durham were to scan for every event occuring on the film within the defined fiducial volume, the recorded scanning information being sufficient for the compilation of computer produced measuring lists. The recorded scan data for each event were: the roll, frame, event (within the frame) and zone number followed by an associated proton bank (short <3cm, long >3 and < 25 cm, grey protons), an associated pion bank (short and long pions), a V^0 marker and a kink marker. Beam track count statistics were also recorded, for both first and second pulses, at intervals of every 50 frames. The class of topologies then extracted from the total scan data were:

a) All events with a V^0

b) All odd pronged events

c) All even (> 2) prongs, only if they were accompanied by at least one stopping proton (either short or long)

d) Two pronged events only if they were accompanied

  i) by a stopping proton

  ii) by a grey or stopping proton (where a grey proton was defined as a fast positive track of near-minimum ionization whose trajectory lay between two lines on a template).

The practice of recording every event did, however, result in a large volume of stored information. About half-way through the Durham film, therefore, the scanning rules were changed to those previously defined for the computer produced measuring lists. This practice solved the data storage problem and a master list was set up for every event in order that all its essential statistics and its progress through the measuring system could be monitored. This scanning produced between 300 and 350 events per segment of film (∿775 frames), a number consistent with that obtained before the scanning criteria were applied.

2.5 Measuring of Events

The measurement of the film was performed on the RHEL HPD1 automatic measuring machine. Firstly however, each event had to be pre-measured (pre-digitized) in order that the HPD would know where, approximately, the tracks of an event were to be found on any particular frame being considered.

2.5.1 Pre-digitization

The film was pre-measured at Durham using 3 image plane digitizers, each of which was capable of a point accuracy on the table of ∿25 μm. The sequence of measurements for an event were (per view):

a) Primary Vertex
b) Beam Track
c) 2 Fiducial crosses
d) Secondary vertex
e) Tracks associated with secondary vertex (2 pts per track)
f) Tracks associated with primary vertex (2 pts per track)
g) 2 more Fiducial crosses
h) Primary vertex

A fiducial check was incorporated into the on-line controlling computer program (an IBM 1130 being used), by using the known separation of the four fiducial crosses measured on each view. The primary vertex was also used for checking purposes, being measured at the beginning and end of the event. Any fringe counting system errors which were not detected by the fiducial check were thus detected at the vertex check. Distortions of the projection system were removed by the use of a statistical regression method. Twenty fiducial crosses were measured firstly on a film plane digitizer, and the same fiducial crosses were then measured on each of the image plane digitizers. The co-efficients obtained from the regression were then used to transform the measured film points into an ideal film plane (defined by the film plane digitizer) by formulae of the form:

$$X = a + bx + cy + dx^2 + ey^2 + fx^2y + gy^2x + hxy \qquad 2.3$$

$$Y = a' + b'x + c'y + d'x^2 + d'y^2 + F'x^2y + g'y^2x + h'xy \qquad 2.4$$

where X and Y are the corrected co-ordinates

x and y are the measured co-ordinates

a, b, a', b' etc are the regression co-efficients.

The final Durham output record was then translated into the HPD input format, the basic point of the operation being that two points per track plus the associated vertex point are sufficient information to define a road on the film. A road is a circular path on the film, 512 μm wide, which contains the track and from which the HPD extracts the digitizings. Two of the measured four fiducial crosses at Durham were used by the HPD for translation and rotation from the Durham film plane into the HPD co-ordinate system.

2.5.2 The HPD

The HPD (Hough-Powell Device) is an automatic measuring machine which works on the flying spot technique. A light spot of diameter ~10 μm (or a laser beam in later versions) scans across the film, perpendicularly to the films edge, whilst the film is moved mechanically along its length. As can be appreciated this produces a slightly skew scan the effect of which is mathematically removed. The light spot, whilst scanning, is held in simultaneous focus on the film and on a digitizing grating. The film position gives the x co-ordinate and the grating reading the y co-ordinate of any digitizing in the road area defined on the film. Ten fiducial crosses are also measured, the approximate positions of which are passed as constants to the HPD controlling program. There are two types of scan possible on such a machine, known as normal and abnormal scans. Whereas in the normal scan described above the light spot scans perpendicularly to the films edge, in the abnormal scan it travels parallel to the edge. It is necessary that two scan types are available on such a machine because some tracks lie at such an angle that only difuse digitizings are obtained on a normal scan. The spacing of the scan lines on the film is ~90 μm and a typical RMS error for a track measured on an HPD is ~2-3 μm on the film. Apart from the obvious advantages of accuracy and speed of measurement (the HPD scans a complete frame in ~3-5 secs) in using an automatic measuring machine, there is another advantage and that is: the machine measures the relative bubble density of all the tracks in an event. This is indeed a great advantage since, as will be explained later, many ambiguities in final fits to interactions can be resolved automatically without having to return to the scanning table to judge ionization by eye.

2.6 Bubble Density and Particle Velocity

It has been shown in various experiments (Refs. 2.4 and 2.5) that the bubble density produced by a particle travelling with velocity β is given by the expression

$$D \alpha \, {}^{1}/_{\beta}{}^{2}$$

that is, the number of bubbles/cm n is related to some minimum ionization n_0 by

$$n = n_0/\beta^2$$

$$\text{or} \quad n = n_0\left(1 + \frac{m^2}{p_2}\right) \qquad 2.5$$

Figure 2.5 shows a diagram of the behaviour of bubble density with momentum for pion, kaon and proton. Normally by eye it is possible to distinguish relative bubble densities of 1.4 to 1 and upwards. For example, the bubble density can be distinguished from minimum ionizing for momenta up to:

1.48 GeV/c for a proton
0.78 GeV/c for a kaon
0.22 GeV/c for a pion

However, HPD systems are capable of distinguishing relative bubble densities of 1.15 to 1, given sufficient track length. This gives corresponding momentum identification limits of:

$p \sim 2.5$ GeV/c
$K \sim 1.28$ GeV/c
$\pi \sim 0.36$ GeV/c

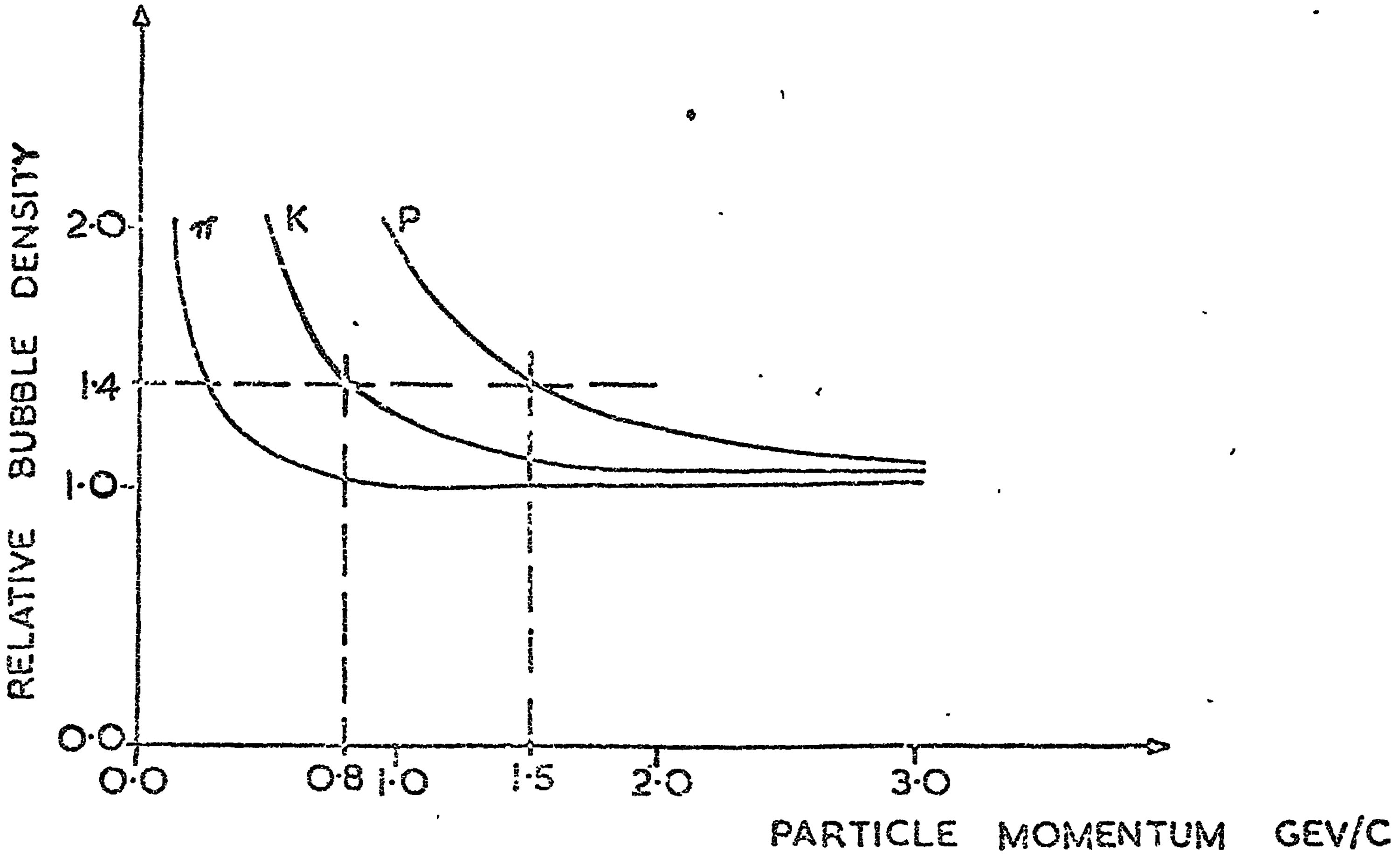

FIG. (2-5) THE RELATIVE BUBBLE DENSITY AS A FUNCTION OF THE PARTICLE MOMENTUM (PION, KAON AND PROTON)

The advantage is now clear, as may be seen for example in a 1.0 GeV/c track which is π/K ambiguous. By eye, it is impossible to resolve the ambiguity since both pion and kaon would appear as minimum ionizing tracks. Automatic measurement, on the other hand, could resolve the ambiguity since a kaon would appear as not minimum ionizing.

2.7 Processing of Events

A flow diagram of the system of event processing is shown in Fig. 2.6. The various steps necessary to arrive at the HPD stage have already been described and in the next five sections the steps from the HPD to a data summary tape will be dealt with.

2.7.1 Haze

After the HPD had digitized the contents of the roads defined by the pre-measurement of an event, they (the digitizings) were then passed to the programme HAZE. In this step the contents of the roads are examined and the digitizings grouped into master points for the various tracks. A master point is equivalent to a normal measured point, say, on a film plane digitizer, but they are a much more accurate measure of the track because of the many pieces of digitizing information used to derive them. On average, one master point is produced for every ~2.5 cm of track in real space. From such measurements the error on a reconstructed point in space is typically 30 μ in the (X,Y) plane and ~300 μ in the Z direction.

2.7.2 Geometrical Reconstruction

The programme Geometry is the RHEL 3-dimensional recon-

Fig. 2.6

SCHEMATIC FLOW DIAGRAM FOR EVENTS

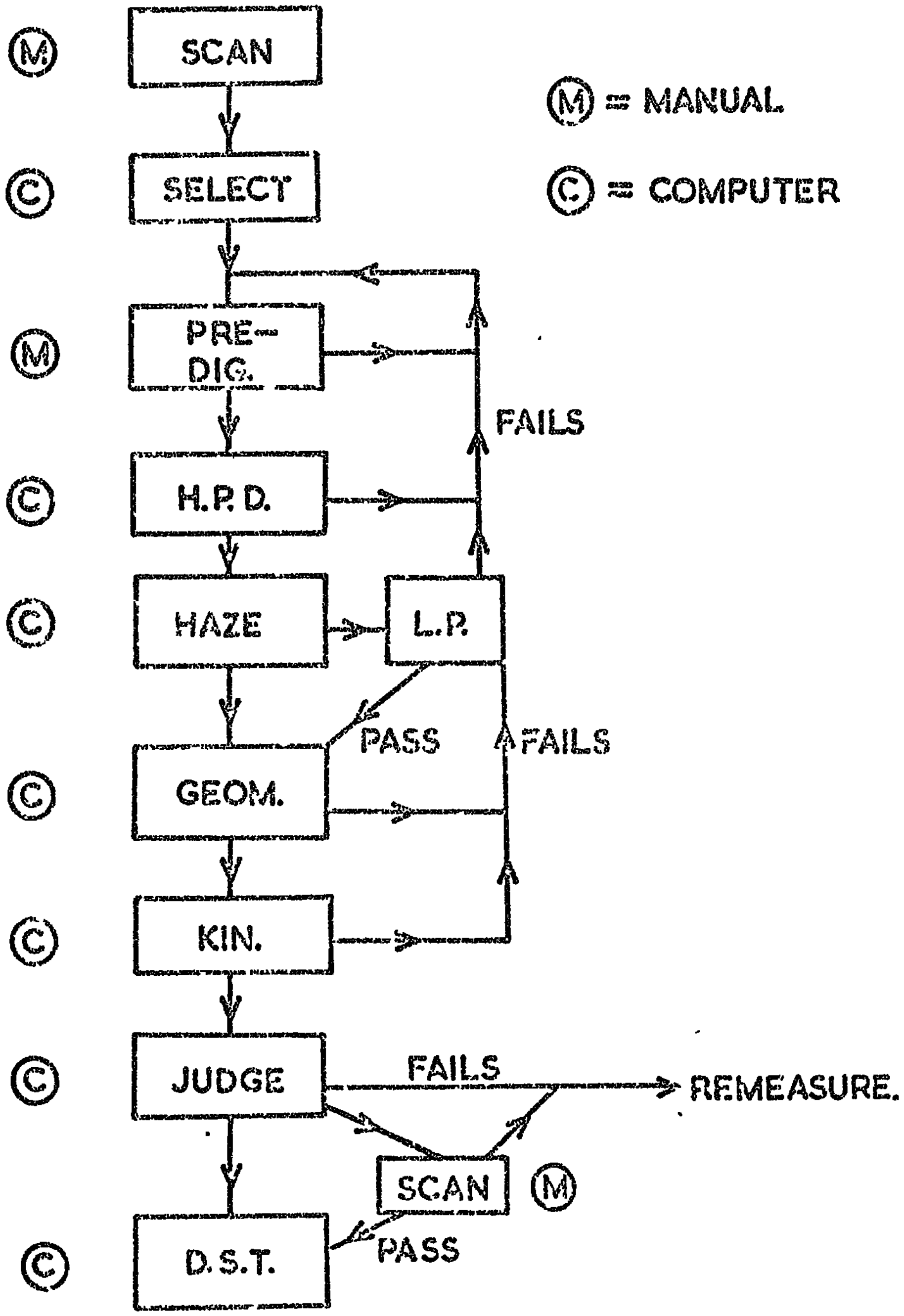

struction routine for bubble chamber events (Ref. 2.6). The principal task of this routine is the calculation of the momentum $\vec{p}$ at the centre of each track and an error matrix on this momentum. Also the routine evaluates the spatial co-ordinates of all vertices together with their errors. Firstly the programme constructs a film plane reference system, containing the event, in which all film stretches have been removed by a fiducial fitting procedure. After this has been achieved the film co-ordinates are transformed into ray co-ordinates, where a ray is defined by a co-ordinate pair, of the point at which the ray intersects the front grass of the chamber, and the direction ratios of the ray. Most of the calculation is carried out in terms of these rays and the final fit to obtain the momentum is made by fitting a helix to the rays of the three views. In cases where the curvature of the track is significantly changed by slowing down in the chamber liquid, a mass dependent correction to the helix fit is made. This correction is made assuming for the track the masses of the pion, kaon and proton. In this way, even at this stage, a probable mass assignment may be given to a track.

2.7.3 Light Pen

This is a patch-up system used for the recovery of events which fail in the geometrical reconstruction because of HAZE errors. There are cases when the master points obtained by HAZE for a view are incorrect, these occur for example when HAZE interprets a crossing track, in the same road as the true track, as being the correct one. At the light pen the three views of the failing track in an event are displayed on a visual display unit. A haze on-line programme is then redirected by an operator to the correct track, or is instructed to use only part of the available track length when a scatter occurs on a track. Two examples of these HAZE errors are shown in Figs. 2.7 and 2.8, where the master points reconstructed are indicated by 'X''S, and the pre-digitized points are indicated by 'M''S; in both of these figures only the HPD roads are displayed. In Fig. 2.7 an event is shown where a fault number 56 has occured in Geometry indicating a large helix fit error which has been produced by the incorrect identification of the beam track on view 3. (RHS in Fig. 2.7). A vertex reconstruction error is indicated in Fig. 2.8 where the wrong beam track has been chosen by HAZE on views 1 and 3. Both of these errors are easily recoverable at the light pen, indeed most of the HAZE errors are corrected at this stage.

2.7.4 Kinematic Fitting

The programme KINEMATICS is that part of the RHEL system for bubble chamber analysis which takes the event reconstructed by geometry, and identifies the reaction by the process of fitting various hypotheses to it. The final kinematic fit must satisfy the conservation of energy and momentum described by the 4 constraint equations:

$$\begin{aligned}
\Sigma p_x &= \Sigma(p_i \cos\lambda_i \cos\phi_i) - p\cos\lambda\cos\phi \to 0 \\
\Sigma p_y &= \Sigma(p_i \cos\lambda_i \sin\phi_j) - p\cos\lambda\sin\phi \to 0 \\
\Sigma p_z &= \Sigma p_i \sin\lambda_i - p\sin\lambda \to 0 \\
\Sigma E &= \Sigma\left(\sqrt{p_i^2 + m_i^2}\right) - \left(\sqrt{p^2+m^2} + M_D\right) \to 0
\end{aligned}$$

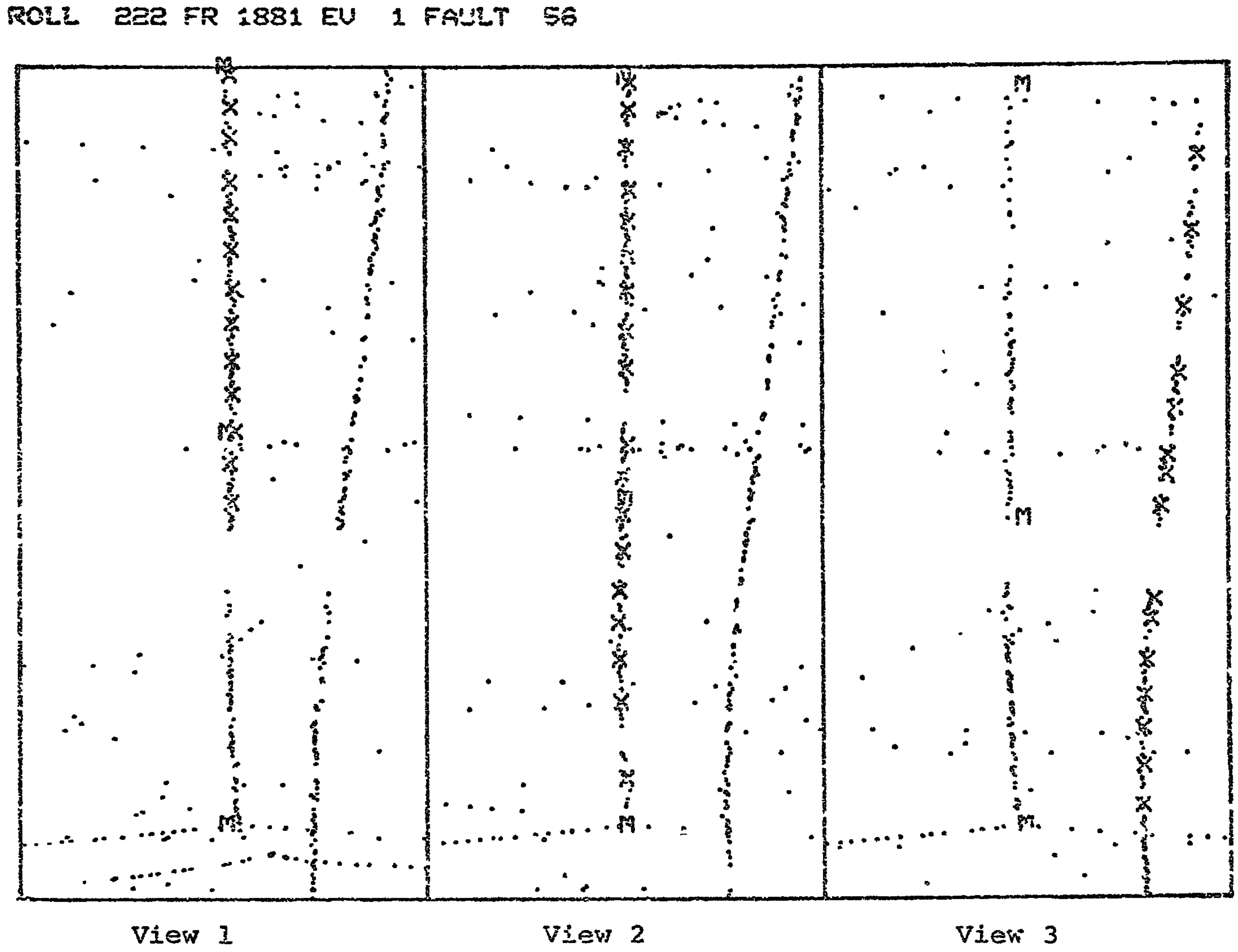

Fig. 2.7 Example of Haze error recoverable at the Light Pen.

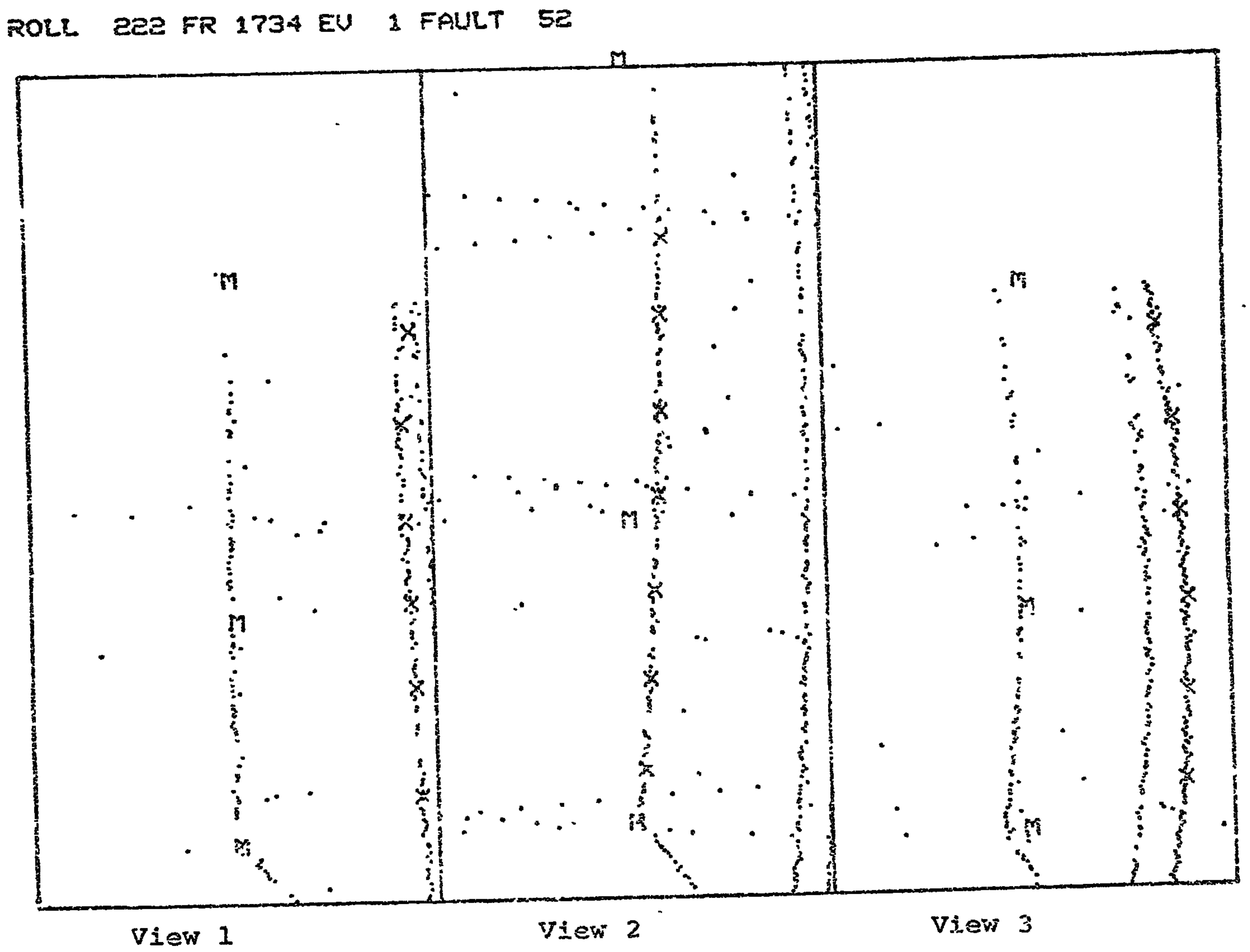

Fig. 2.8 Example of Haze error recoverable at the Light Pen.

where the limits can be set as constants in the programme, the maximum constraint imbalance being set to 1 MeV. With no neutral particles in the final state all the variables are constrained, there are 4 degrees of freedom, and the fit is called a 4-C fit. If, however, there is a neutral, known mass, particle missing in the final state then the momentum equations are used to solve for p, λ and ϕ, leaving the energy equation as the only constraint. In this case there is only 1 degree of freedom and the fit is called a 1-C fit. Obviously, for more than one missing neutral particle there are insufficient equations to solve for the number of particles and the event becomes a no-fit (or missing mass fit).

2.7.5 Judge

The programme JUDGE is basically an ionization testing routine which compares the ionization measured with that calculated for a particle of given momentum. If the calculated ionization differs by a pre-determined amount from that measured then that particular hypothesis is rejected. Other criteria may also be imposed to reject fits, such as a maximum allowed helix fit residual or a comparison of probabilities between two 1-C fits, although the latter is more usually used in final event separation into channels. Events on which no ionization decision could be made, perhaps because a track had been through the light pen where ionization information is sometimes lost, were returned to the scanning table for visual examination. At this stage if no decision could be made then the even was tagged as ambiguous and all fits were written to DST, together with events which had passed all tests. The final pass rate through the system from HPD to DST was ~95%, and furthermore the number of events returned to the scanning table for examination was ~15 events/segment.

2.8 Precision

The accuracy expected for the mass of a multi-particle system can be estimated using a calculation based on a missing mass technique. With film measuring accuracy of ~2-3 μm and space point reconstruction accuracy of ~50 μm, multiparticle mass resolution for fully-constrained fits is approximately ± 7 MeV/c^2 for a multiparticle mass in the region of 1 GeV/c^2.

For 1-C fits the resolution is slightly worse than this, being about ± 15 MeV/c^2 at the mass of the ω^0-meson (795 MeV/c^2). This error has been calculated by two methods, the first of which uses the formula (Ref. 2.7)

$$\Delta = \frac{W_G{}^2}{W_{obs}} \qquad \begin{array}{l} \Delta = W_{obs} - \Gamma \\ W_G = 2.355\,\sigma_g = \text{Full width} \\ \text{half maximum of a gaussian,} \end{array}$$

which relates the observed width of the resonance with the true width and the gaussian error. The second method entailed a Breit-Wigner fit to the $(\pi^+\pi^-\pi^0)$ mass spectrum from events in the channel $\pi^+ n \to p\pi^+\pi^-\pi^0$, at the ω^0 mass. The Breit-Wigner formula was convoluted with gaussian error distribution as the resolution function. The analytic expression for the convoluted fit was obtained from a Breit-Wigner of the form

$$P(X) = \frac{\Gamma/2\pi}{X^2+\Gamma^2/4} \qquad X = E - E_0$$

and a Gaussian error distribution of

$$P(\xi) = \frac{1}{\sqrt{2\pi}\,\sigma} \quad e^{-{}^2/2\sigma_g^{\,2}}$$

The result of a measurement is $x = X + \xi$, of the form

$$P(x) = \frac{\Gamma}{(2\pi)^{3/2}\,\sigma_g} \int_{-\infty}^{\infty} \frac{e^{-\xi^2/2\ {}^2}}{(X-\xi)^2 + \Gamma^2/4}\, d\xi \qquad 2.6$$

The result of this fit is shown in Fig. 2.9, the fitted mass and width being

M_0 = 787.8 MeV/c^2

Γ = 11.0 MeV/c^2

and with an error of

σ_g = 16 MeV/c^2

2.9 Cross Section Evaluation

The total cross sections are calculated using the mean free path (λ) between interactions where λ is given by

$\lambda = \frac{L}{n\sigma}$ .... 2.7 where n = no of interaction centres/cc

σ = cross section

Expanding this expression in terms of total track length for all interactions, it becomes

$\sigma = \frac{NA}{L\,N_0\,d}$ 2.8

where N = total no. of interactions

A = deuterium atomic weight

L = total beam track length

N_0 = Avagadro's Number (6.022×10^{23})

d = density of liquid deuterium

The total beam track length is determined from the average number of beam tracks per frame (=10.3) and the length of the fiducial volume (L), making use of the fact that the distribution of interaction points is linear throughout the fiducial

Fig. 2.9

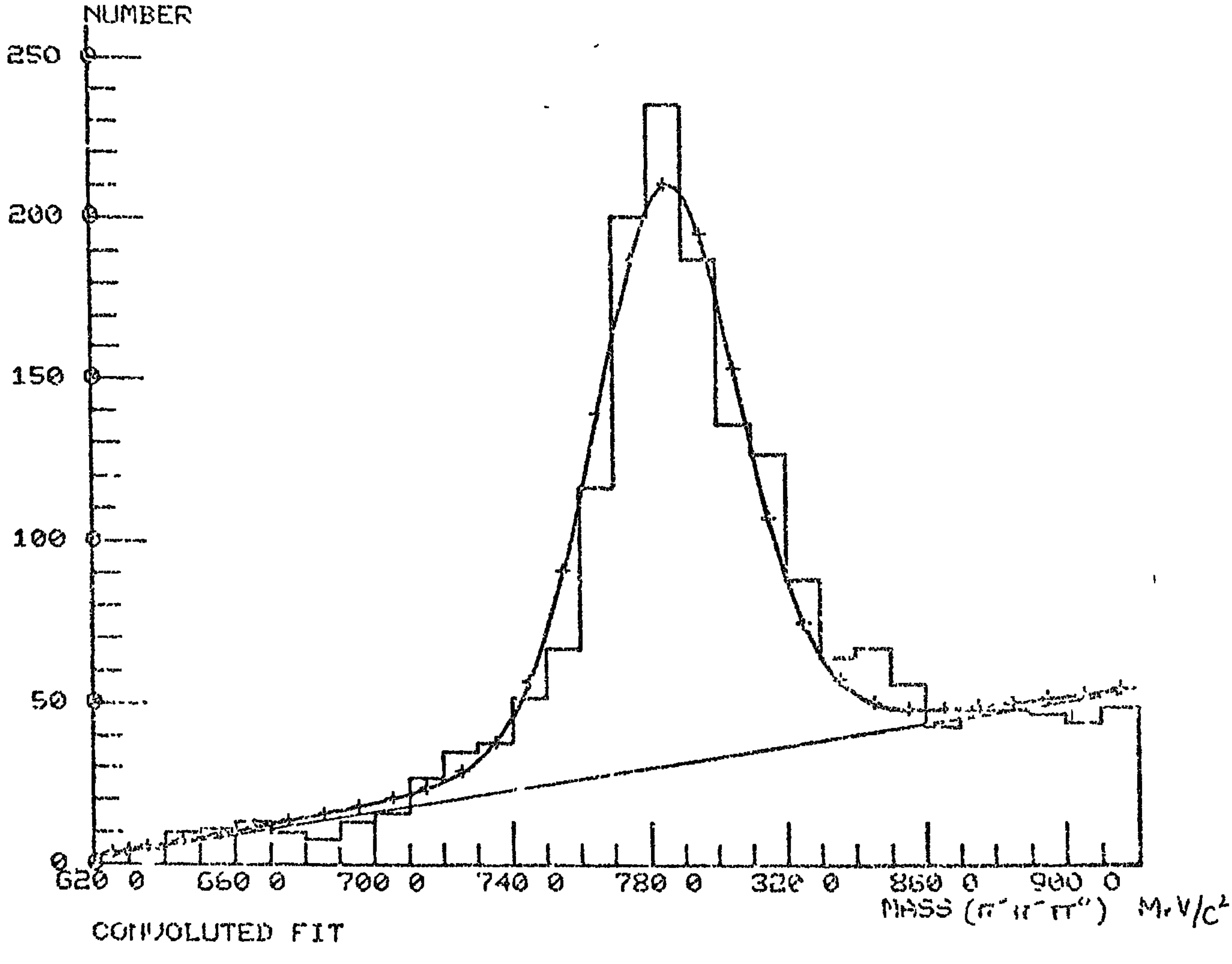

Breit-Wigner fit, convoluted with a Gaussian resolution function, to the ω^0 mass region for the reaction $\pi^+ d \rightarrow p_s p \pi^+ \pi^- \pi^0$ at 4 GeV/c.

volume. The total length of beam track, L, is given by

$$L = \left[10.3 \cdot L \cdot N - L \cdot N/_2 \right]$$

N = Number of frames containing N events
L = 107 cm.

On a sample of 38750 frames, the number of events (all topologies) found was 84846. A break-down of the events into prong sizes if shown in table 2.3 below. These figures give a cross section, calculated from Eq. 2.8 above, allowing for 5% beam contamination

$$\sigma = 50.4 \pm 8.6 \text{ mb}$$

the large error originating from the determination of the number of beam tracks per frame. This figure agrees quite well with that obtained from counter experiments of 56±1 mb (Ref. 2.8).

Calculation of partial cross-sections was done by assuming the counter value of 56 mb, and then calculating the microbarn equivalent from Eq. 2.8 by setting N=1.

Table 2.3 Scan Data from 50 Segments

Prong Size	Number	σ mb
1	8776	5.77
2	30834	20.23
3	14574	9.58
4	24197	15.91
5	3109	2.05
6	3143	2.07
7	118	0.08
8	93	0.06
9	2	0.001
ALL	84846	55.8

Chapter 3 Analysis Techniques and Cluster Searching

3.1 Introduction

The use of graphical displays in the search for and examination of resonant particles has always been one of the basic techniques of bubble chamber film analysis. Amongst the many displays which have been devised, the most commonly used are those of the invariant masses of particle combinations, the Chew-Low plot of invariant mass against momentum transfer and, more specifically for 3-body final states, the Dalitz plot of the squared mass combinations. More recently, use has been made of the information contained in the Van-Hove plot of the centre of mass longitudinal momenta of the particles. Currently, interest is being shown in the classification of events using a multi-dimensional analysis, the Pless- or Prism Plot-technique, to separate the various resonant states from the overall final state. Analogous to the Pless analyses, although in basic concept completely different, are methods using statistical searching techniques in an n-dimensional space defined by the number of final state particles in an event. All of these techniques have as their aim the extraction of a background-free resonance signal from the data.

In this chapter a method of statistical searching will be described which has been developed in Durham. The conditions necessary for the technique to be successful will be discussed and the results of an analysis made on events generated by the Monte-Carlo simulation programme FAKE will be presented. In the next chapter the detailed results of this statistical search on real events in the channel $\pi^+d \rightarrow p_s p \pi^+ \pi^-$ will be discussed.

Firstly, however, a brief survey of the information contained in the graphical displays of the Mass, Dalitz and Chew-Low plots will be made. After this a detailed account will be given of the information contained in the Van-Hove plot, which forms the basis of the analysis technique to be presented, and the Prism plot analysis will be described as a prelude to the introduction of the cluster searching technique.

3.2 Mass, Dalitz and Chew-Low Plots

In any search for the production, and the determination of the properties, of a resonance, the parameters to be found are the mass, width, spin-parity and production mechanism of the particle. If this is to be done effectively it is necessary to remove as much background as possible from the signal.

In the sections which follow, reference will be made to the analysis of a 3-body final state such as arises in the reaction

$$\pi N \rightarrow N\pi_1\pi_2 \qquad 3.1$$

and where figures are shown for illustration of the various techniques the data used come from the reaction $\pi^+p \rightarrow p\pi^+\pi^0$ at 5 GeV/c (Ref. 3.1).

3.2.1 Mass Plots

The distributions of the invariant masses $N\pi_1$, $N\pi_2$, $\pi_1\pi_2$, are examined for structure or peaks which may indicate the presence of a resonance in that combination of the paired particles. Values of the mass and width of the resonance can be read directly from the graph at the peaks. However, as is well known, the presence of a resonance in the $\pi_1\pi_2$ combination may contribute structure to the plot of the $N\pi_1$ or $N\pi_2$ combinations and certainly contributes background to the $N\pi$ plots. Figs 3.1(a), (b) and (c) show the $(p\pi^+)$, $(\pi^+\pi^0)$ and $(p\,\pi^0)$ invariant mass distributions respectively, from the reaction $\pi^+p \rightarrow p\pi^+\pi^0$ at 5 GeV/c, showing the $\Delta^{++}(1236)$ in (a), the $\rho^+(765)$ in (b) and perhaps some $\Delta^0(1236)$ in (c).

3.2.2 Dalitz Plots

Here the effective masses squared of two of the three two-particle systems are plotted against one another. More information is stored in this display since now the resonances appear as bands on the plot and the distribution of the points in the bands is linear in $\cos\theta^*$, where θ^* is the decay angle in the rest system of the resonance (Helicity angle). Fig. 3.2 shows a Dalitz plot of $M^2(\pi^+\pi^0)$ against $M^2(p\pi^+)$ in which the bands of the ρ^+ and Δ^{++} resonances are clearly visible. Projection of the plot onto either axis gives the type of display described in section 3.2.1, but with mass squared instead of mass axes. The main value of the Dalitz plot is the information which it contains about $\cos\theta^*$, since an analysis of the spin of a particle may thus be made. Another important use of the plot lies in the ability to estimate from this plot the background present in a mass combination because of the effect of reflections from the other mass combinations.

3.2.3 Chew-Low Plots

The production angle ϕ of a resonance in the overall

Fig. 3.1

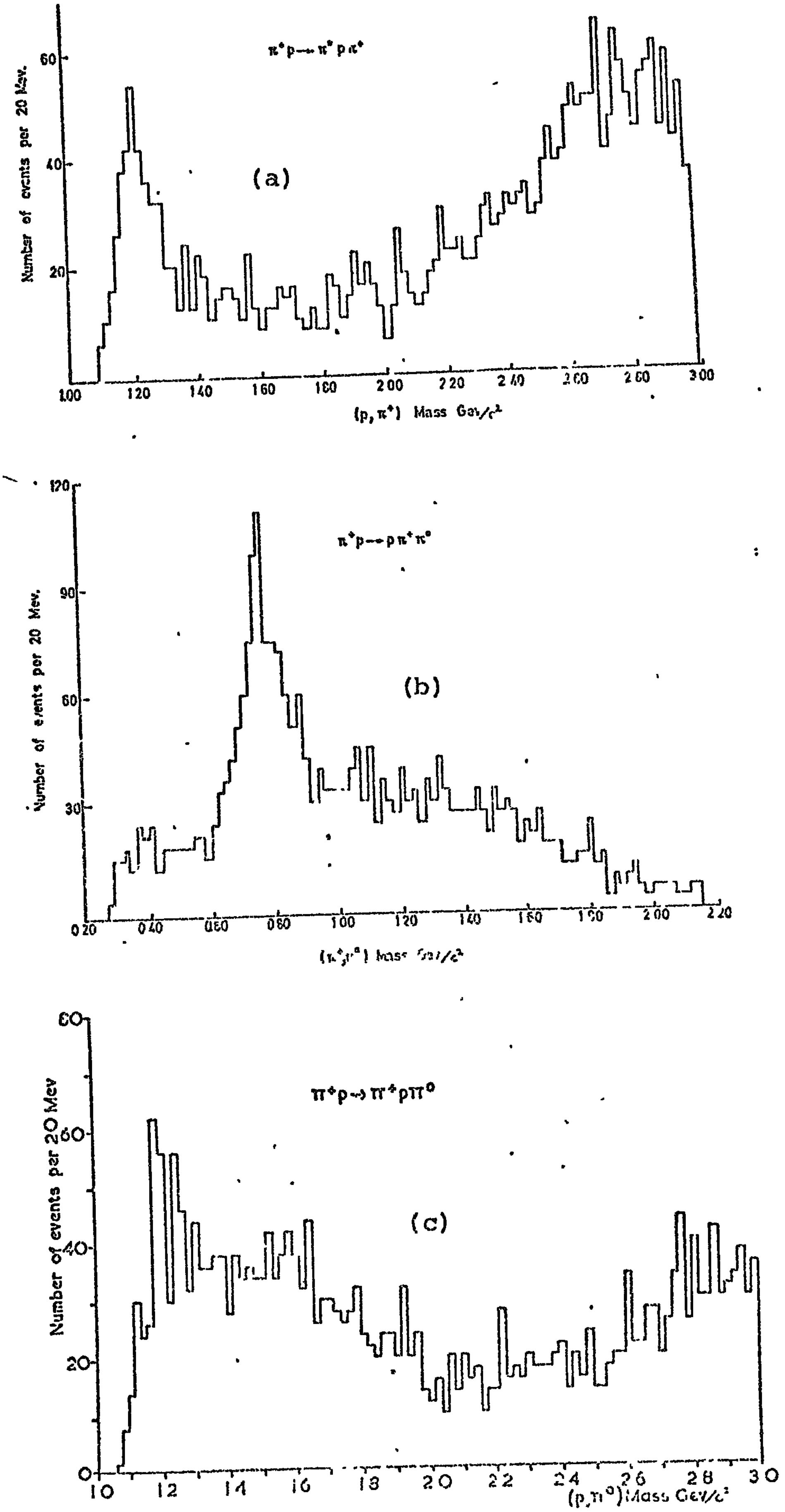

Invariant Mass distributions of 5 GeV/c $\pi^+p \to p\pi^+\pi^0$

Fig. 3.2

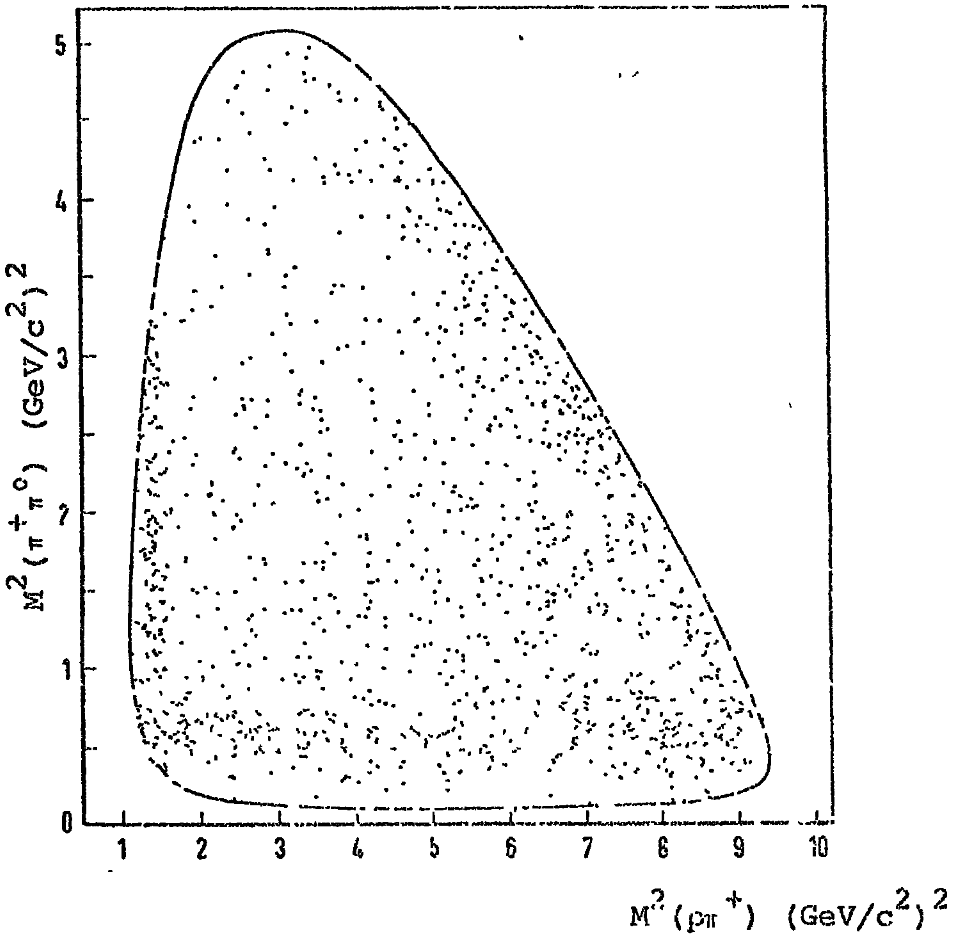

Dalitz Plot for the reaction $\pi^+p\to p\pi^+\pi^o$ at 5 GeV/c showing the contributions from the reactions $\pi^+p\to p\rho^+$, $\pi^+p\to\Delta^{++}\pi^o$, $\pi^+p\to\Delta^+\pi^+$. The solid outline represents the kinematic limit for this centre of mass energy.

centre of mass reference frame is the information which is carried in the Chew-Low plot, where the mass of a particle system is plotted against its 4-momentum transfer squared (t) from the beam for meson systems, or from the target for baryon systems. The t-distribution depends upon the production mechanism of the system being studied, and t is linear in cosϕ. Figs. 3.3 (a), (b) and (c) show Chew-Low plots of the $(\pi^+\pi^0)$, $(p\pi^+)$ and $(p\pi^0)$ systems, again in the reaction $\pi^+p \rightarrow p\pi^+\pi^0$ at 5 GeV/c.

3.2.4 Summary

All of the essential information of the produced resonances: their production and decay angular distributions, their mass, width and spin are displayed in the Mass, Dalitz and Chew-Low plots. However there is still background present in the data, and this may distort the various distributions.

Methods which are commonly used to overcome the basic difficulties which arise experimentally in handling the background, to meet the problem of obtaining pure resonant signals are:

(i) Mass cuts

By selecting only particle combination masses within a given mass interval where the resonance signal is at a maximum, the effect of the background is minimized at the expense of losing events from the tails of the resonance. For example the ρ-meson data are often chosen by selecting only those dipion masses between 0.68 and 0.88 GeV/c^2.

Fig. 3.3

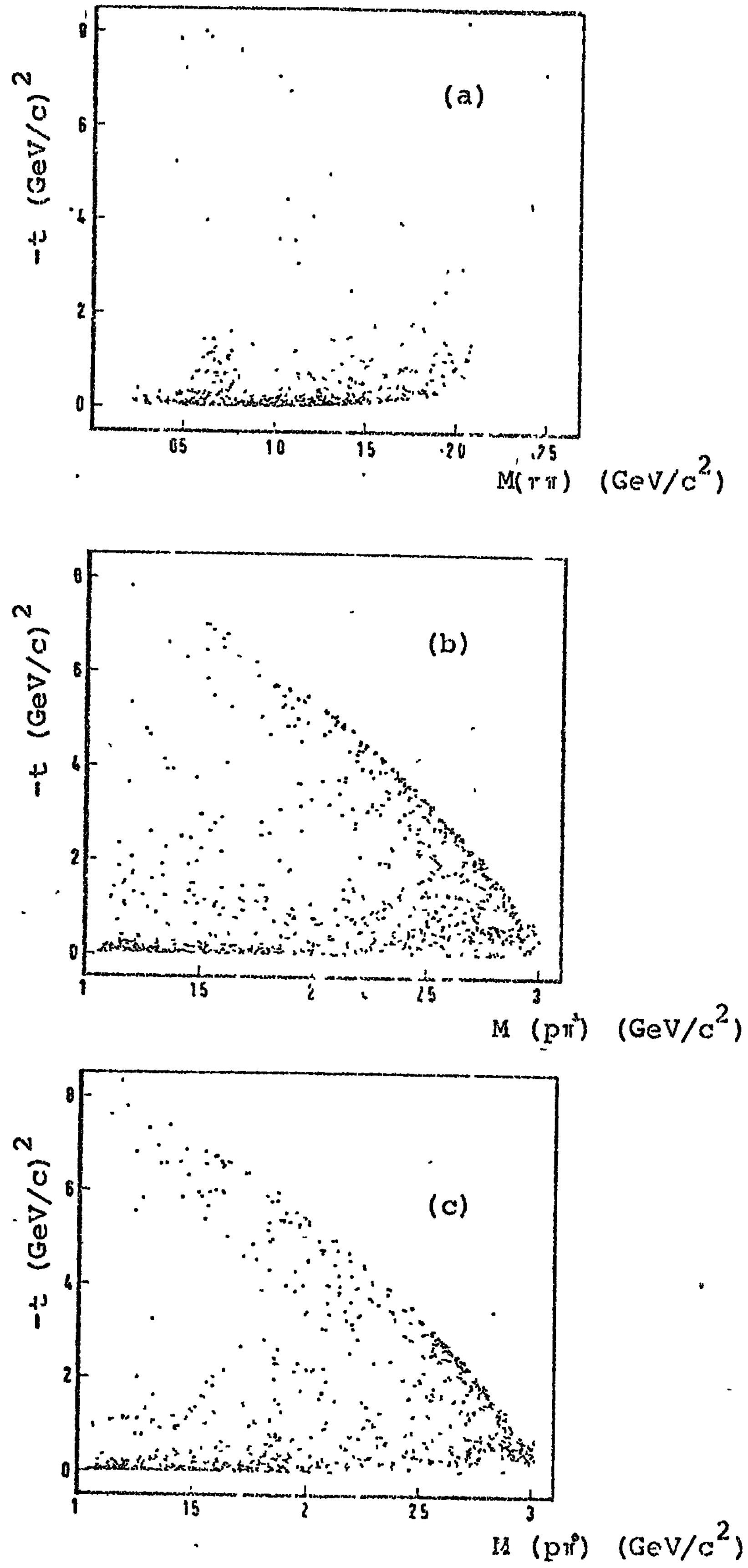

Chew-Low Plots from 5 GeV/c $\pi^+ p \to p \pi^+ \pi^0$

(ii) t-cuts

By selecting only those events for which the momentum transfer (t) is small, a particular production mechanism may be selected and hence a particular resonance may be selected preferentially to background.

3.3 The Van Hove Plot

This plot forms the basis of the cluster searching technique and combines in one plot most of the information available in the Mass, Dalitz and Chew-Low plots. The Van-Hove plot is described in this section in some detail.

The Van Hove plot, or Longitudinal Phase Space (LPS) analysis, is based upon the experimental observation that in strong interactions the variation of the transverse component of momentum in the centre of mass system is small compared with that of the longitudinal component. Typically, experiments show that whilst the longitudinal momentum varies over the whole of the kinematically allowed region, the transverse momentum distribution is concentrated below a value of 300 to 400 MeV/c. This led Van Hove (Ref. 3.2) to suggest that the transverse momentum may be discarded as an information carrying variable and that events may be parameterised by their longitudinal momenta alone. The Van Hove plot for the 3-particle final state of Eq. 3.1, the axes and definition of which are shown in Fig. 3.4, is summarized by the sum of the centre of mass longitudinal momenta,

$$q_N + q_{\pi_1} + q_{\pi_2} = 0 \qquad 3.2$$

An event is described by a single point in the plot,

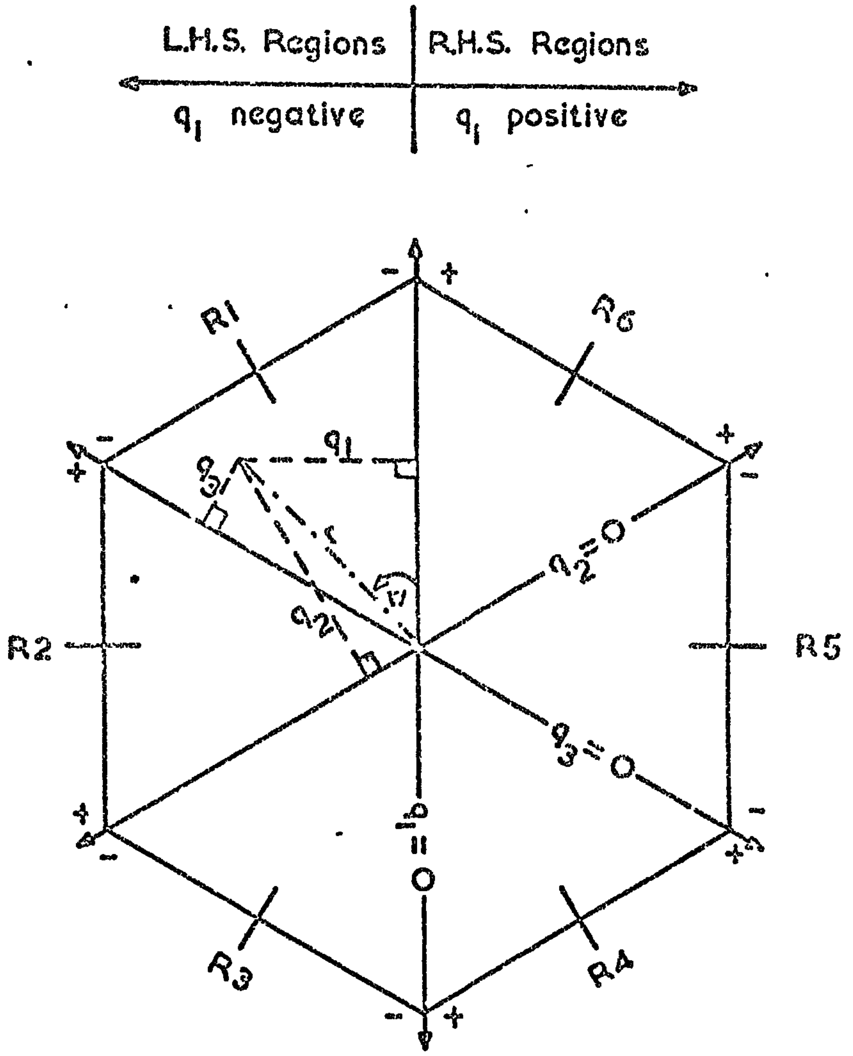

FIG. (3.4) Diagrammatic Representation of the VAN-HOVE Hexagon Plot.

and the information on q_N, q_{π_1} and q_{π_2} is contained in the radius vector (r) and the Van Hove angle (w) where (see Fig. 3.4)

$$r = \sqrt{\tfrac{2}{3}\left(q_N^2 + q_{\pi_1}^2 + q_{\pi_2}^2\right)} \qquad 3.3$$

and
$$\cot w = \frac{q_{\pi_1} - q_{\pi_2}}{\sqrt{3}\; q_N} \qquad 3.4$$

All of the data points are confined within the boundary which is approximately a hexagon of radius $^W/_2$ where W is the centre of mass energy.

3.3.1 Examination of Resonance Display on the Van Hove Plot

In the three body process of Eq. 3.1 a resonance is formed between two of the three particles. If the mass of the resonance is μ and the mass of the third particle is M_3 then the centre of mass momentum of the resonance and third particle is

$$p_3 = \left\{ \left[\frac{W^2+\mu^2-M_3^2}{2W}\right] - \mu^2 \right\}^{\frac{1}{2}} \qquad 3.5$$

The velocity $\beta\,(^V/C)$, and Lorentz factor γ of the resonance in the overall centre of mass are

$$\beta_R = \left\{ 1 - \mu^2 \Big/ \left[\frac{W^2+\mu^2-M_3^2}{2W}\right]^2 \right\}^{\frac{1}{2}} \qquad 3.6$$

and
$$\gamma_R = (W^2+M_3^2-\mu^2)/2WM_3 \qquad 3.7$$

When the resonance subsequently decays into its two secondaries of masses m_1 and m_2, their momenta in the overall centre of mass are

$$p_1 = \gamma_R \left[-p^*\cos\theta^* + \beta_R \sqrt{p^{*2}+m_1^2} \right] \qquad 3.8$$

and $$p_2 = \gamma_R \left[p^*\cos\theta^* + \beta_R \sqrt{p^{*2}+m_2^2} \right] \qquad 3.9$$

where p^* is the momentum of the two secondaries in the resonance rest system and θ^* is the angle of decay in the resonance helicity frame. Provided that the transverse momenta are small, then p_1, p_2 and p_3 are also the longitudinal momenta q_1, q_2 and q_3.

For a given mass μ, q_3 is fixed and q_1 and q_2 will vary between the limits determined by $\cos\theta^* = \pm 1$. When θ^* is 90^0 then for $m_1=m_2$ (2π-mesons in Eq. 3.1)

$$q_1 = q_2 = \gamma_R \beta_R \sqrt{p^{*2}+m_3^2} = q90 \qquad 3.10$$

For other values of θ^*

$$q_1 = q90 + \gamma_R p^* \cos\theta^* \qquad 3.11$$

$$q_2 = q90 - \gamma_R p^* \cos\theta^* \qquad 3.12$$

In Fig. 3.5 the variations of q_1 and q_2 are displayed at constant q_3 for a resonance of the equal mass particles 1 and 2. The point M represents $\theta^* = 90^0$, and at other values of θ^* the increase in q_1 by $\gamma_R q_3 \cos\theta^*$ is compensated by the decrease in q_2 by the same amount to a point P, again on the line of constant q_3. The change in position MP is $\frac{2\mu}{\sqrt{3}}\, q_3 \cos\theta^*$, that is the distribution along the line AB is linear in $\cos\theta^*$, A and B corresponding to $\cos\theta^* = \pm 1$. Hence at small momentum transfers the feature of the Dalitz plot, of linearity in $\cos\theta^*$, is retained in the Van Hove plot.

The variation of points, corresponding to the various

Fig. 3.5

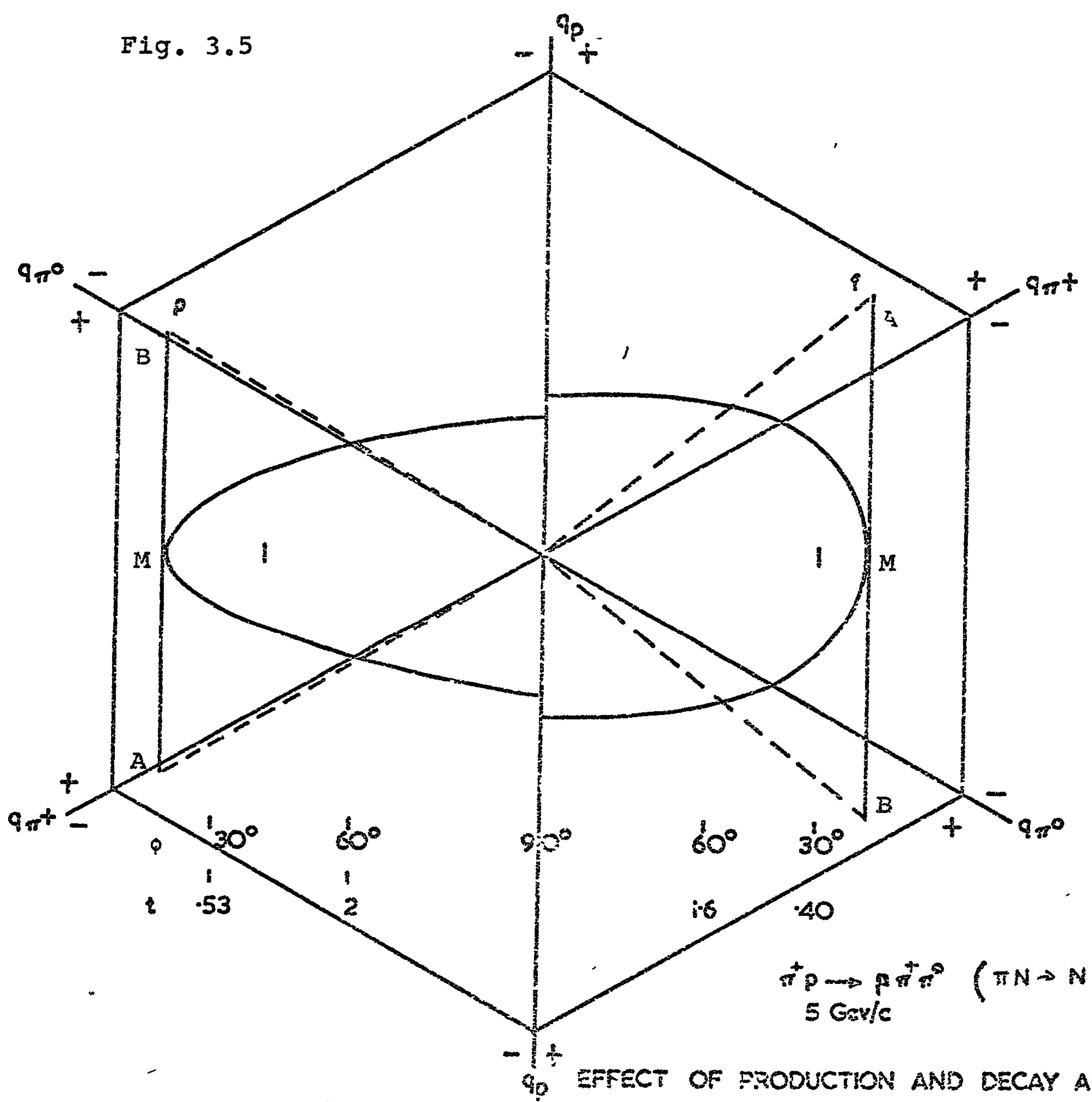

$\pi^+ p \longrightarrow p \pi^+ \pi^0$ $(\pi N \rightarrow N \pi, \pi_2)$
5 Gev/c

EFFECT OF PRODUCTION AND DECAY ANGLES

reaction configurations, through the effects of momentum transfer is more complex. Points A and B correspond to the collinear decay of the resonance ($\cos\theta^* = \pm 1$) and if a production angle ϕ is introduced then the longitudinal momenta change by $\cos\phi$, that is

$$q_i \rightarrow q_i \cos\phi \qquad i = 1,2,3 \qquad 3.13$$

Consequently, the points A and B will move along straight lines through the centre of the plot. For the point M the effect of the angle α (see Fig. 3.6), between p_1 (or p_2) and the momentum p_3 in the overall centre of mass, changes the longitudinal momenta to

$$q_3 = p_3 \cos\phi; \quad q_2 = p_2 \cos(\phi+\alpha); \quad q_1 = p_1 \cos(\phi-\alpha) \qquad 3.14$$

The variation of these co-ordinates with ϕ traces out the oval in Fig. 3.5.

The 4-momentum transfer squared (t) to the resonance is

$$t = -2Pp_3 \cos\phi - (M^2+\mu^2) + 2\sqrt{P^2+m^2}\sqrt{p_3^2+\mu^2} \qquad 3.15$$

where P, M refer to the primary particle. For a given resonance all of the quantities are constant apart from t and $\cos\phi$. From 3.15, for the point M

$$t = -Aq_3 + B$$

Consequently the distribution of points perpendicular to the $q_3=0$ axis is the distribution of t to the resonance of particles 1 and 2. Similar observations hold for the axes q_2 and q_1.

In summary, the Van Hove plot contains in a direct way the information of the Chew-Low plot (the t-distribution) and

Fig. 3.6

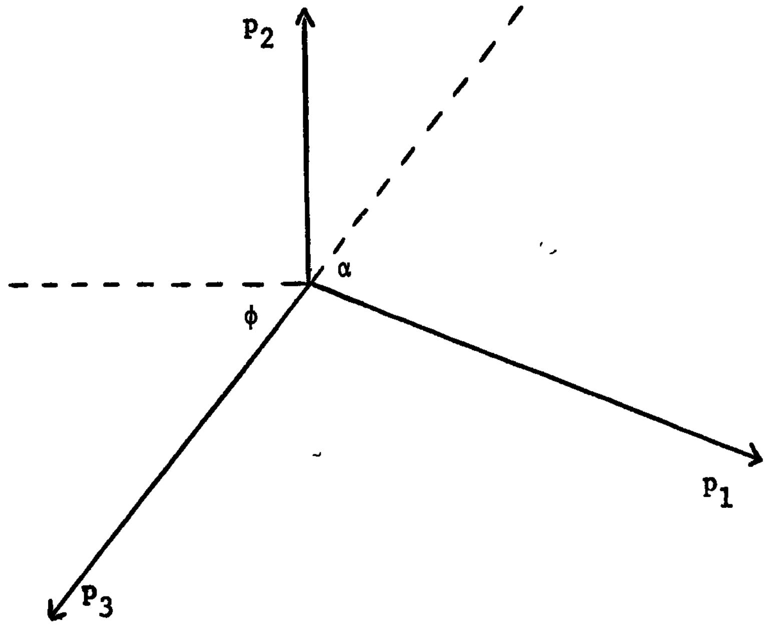

Illustration of angles α and ϕ .

at small t, where most of the experimental data lie, the Van Hove plot also contains the Dalitz plot information of $\cos\theta^*$ linearity.

3.3.2 Resonance Selection in the Van Hove Plot

Figs. 3.7(a) and (b) show a representation of the resonances in the $N\pi_1$, $N\pi_2$ and $\pi_1\pi_2$ systems at minimum t transfer for two π^+p experiments with incident pion momenta of 5 and 12 GeV/c respectively (Refs. 3.1 and 3.3). As can be seen from these figures, at 12 GeV/c the resonance bands are clearly separated whereas at 5 GeV/c there is some overlap at the extremities of the $\pi_1\pi_2$ band with the $N\pi_1$ and $N\pi_2$ bands. The effects of the t-distribution are such that, for example the ρ-meson data will be confined to one sector of the Van-Hove plot at 12 GeV/c and will be largely confined at 5 GeV/c. This suggests a selection method which is to plot only those dipion masses for events which fall in the $\pi\pi$ sector, and only $N\pi_1$ and $N\pi_2$ combinations for those events which fall in their respective sectors. No serious distortion should be found in either the mass or t-distribution of the resonance being considered although at lower incident momenta there may be some loss of the events in the decay angular distribution near $\cos\theta^* = \pm 1$. It must be noted however that a resonance with high Q value in its decay, such as the f^0 and g^0 mesons, would extend largely into the $N\pi_1$ and $N\pi_2$ sectors and thus give spurious structure to these mass plots.

To illustrate the above technique, Fig. 3.8 shows the three mass combinations $\pi^+\pi^0$, $p\pi^+$ and $p\pi^0$, for the reaction

Fig. 3.7

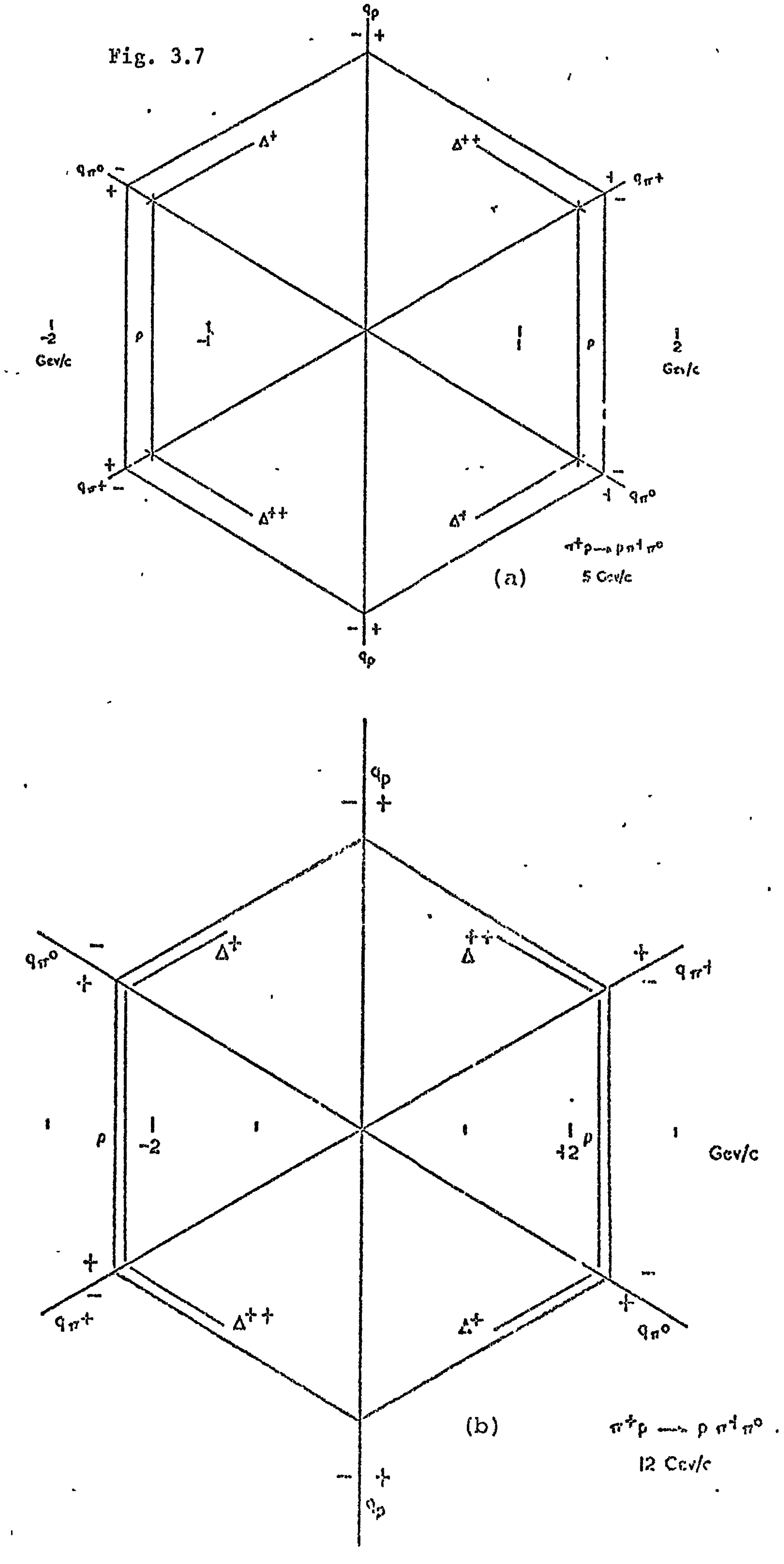

Representation of resonance position on Van-Hove Plot

$\pi^+p \rightarrow p\pi^+\pi^0$ at 5 GeV/c, in each of the three sectors of the Van-Hove plot R1, R2 and R3 of Fig. 3.4. These plots show the features described above:

(i) Δ^{++} is seen only in the $p\pi^+$ sector (R1)

(ii) ρ^+ is seen only in the $\pi^+\pi^0$ sector (R2)

(iii) Δ^+ is seen only in the $p\pi^0$ sector (R3), although there is considerable background present.

3.4 The Pless Analysis or Prism Plot Technique

The problem of separating the various sub-channels from a given reaction channel has been examined by Dao et al (Ref. 3.4) from the point of view of a complete parameterization of the events. In this way, by bringing together all of the information available on the individual events, it is hoped that better separation will be obtained than is possible by using the part-parameterization implicit in the plotting techniques previously described.

The information necessary to define an event completely is the 4-vector $(\vec{p},E)$ of each of the n final state particles. Not only are these 4n quantities too many to handle easily, but not all of them are independent. Since the masses of the outgoing particles are known then the n energies are known from $E_i = \sqrt{p_i^2+m_i^2}$. This imposes n constraints on the final state, and a further 4 constraints are supplied by the conservation of energy (1) and momentum (3). For experiments involving non-polarized beams and targets then production azimuthal isotropy leads to the independence of one further variable, the angle of rotation about the incident beam direction. This leaves, for an n-particle final state,

Fig. 3.8 Contents of Van-Hove sectors for 5 GeV/c $\pi^+p\to p\pi^+\pi^0$

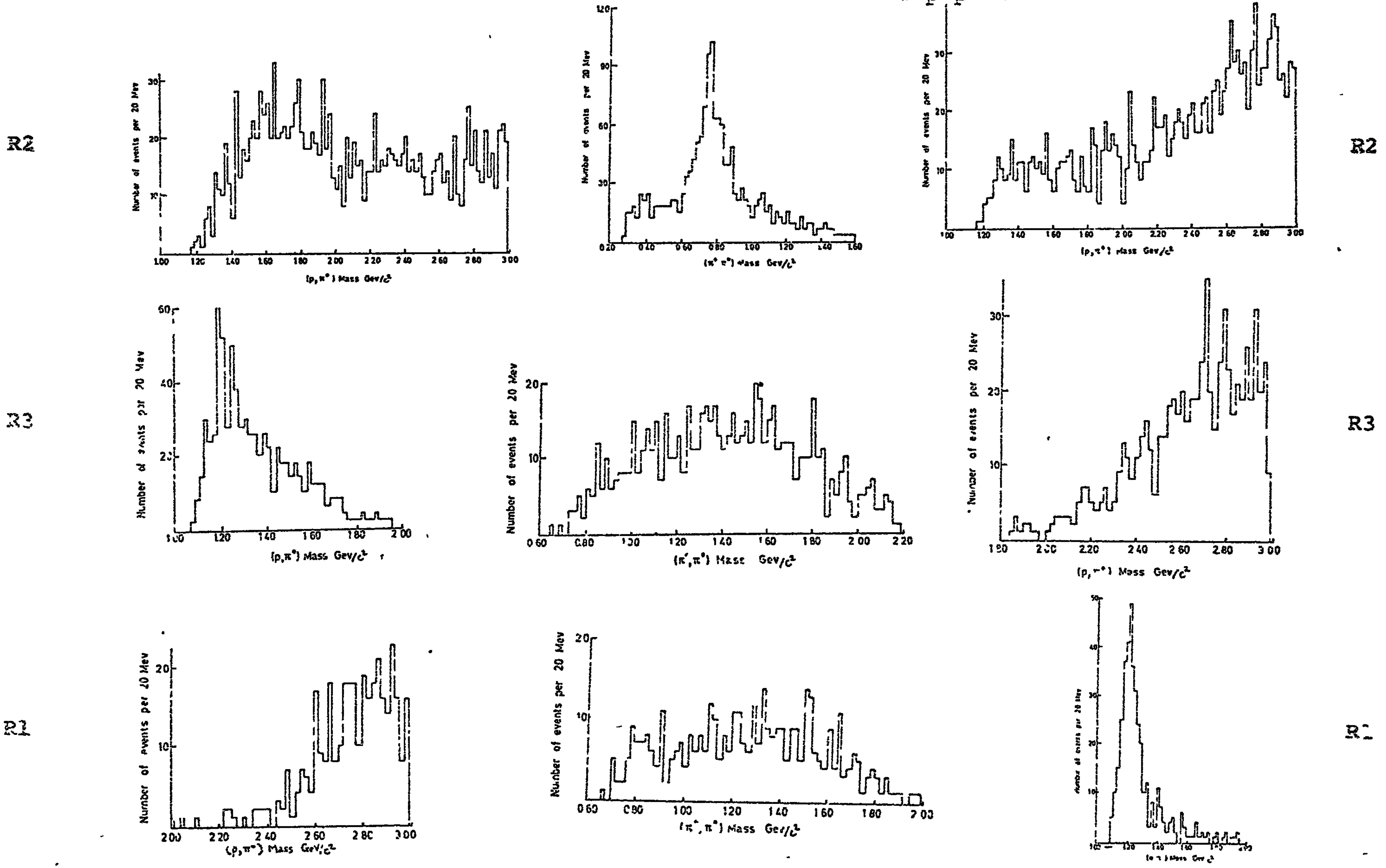

3n-5 independent variables which completely specify the event. These 3n-5 variables may be thought of as forming the axes of an N dimensional space in which the events are distributed. The basis of the Pless analysis is that the distribution of the events in this space is not uniform. Depending upon the production and decay mechanisms involved, groups or clusters of events may be found, that is some regions of the (3n-5)-dimensional space may be more heavily populated than others.

3.4.1 Example of the Prism Plot Technique

The reaction $\pi^+p \rightarrow p\pi^+\pi^0$ at 3.9 GeV/c has been examined by Pless et al (Ref. 3.5) from this point of view. For the case of unpolarized beam and target this reaction is characterised by 4 independent variables.

The Prism plot technique uses the 4-dimensional space defined by T_1 and T_2 (the kinetic energies of two of the three secondaries in the centre of mass system) and the two Van Hove plot variables w and r as described in the previous section. The Prism plot itself is a 3-dimensional plot with a Dalitz-Fabri triangle as base and with w as the height, as shown in Fig. 3.9. When the distribution of the events is examined in the 4-dimensional space of the variables T_1, T_2, w and r, and is compared with the distribution expected from Monte-Carlo generated events corresponding to the various reaction sub-channels, it becomes possible to tag an event that it originated in a particular one of the interaction schemes. For the reaction $\pi^+p \rightarrow p\pi^+\pi^0$ the interaction schemes considered by Pless were

Fig. 3.9

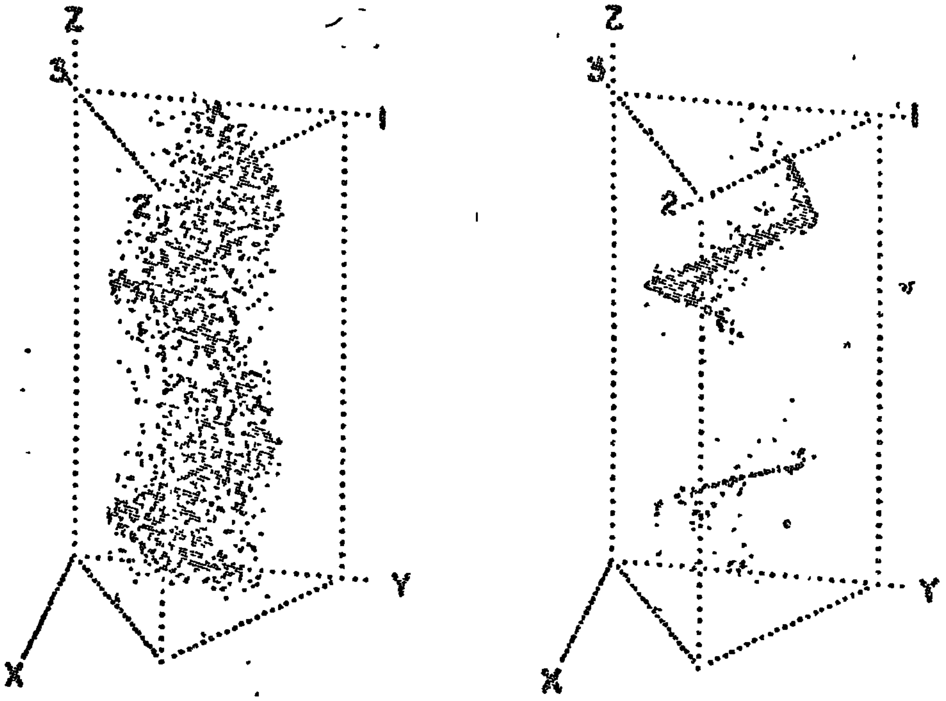

Prism plot of 3.9 GeV/c $\pi^+p\rightarrow p\pi^+\pi^0$. The Prism on the left shows the distribution expected for phase space events, the right hand Prism shows the experimental distribution. In the upper half of this plot are clearly visible the 3 tubes corresponding to Δ^+(lower), ρ^+(middle) and Δ^{++}(top). In the lower half of the plot some production of these same states is visible where the proton is forward in the centre of mass. The axes for the Prism plot are: the Van-Hove angle is plotted along the Z-axis, and the Dalitz triangle is in the X-Y plane.

$\pi^+p \rightarrow p\rho^+$
$\rightarrow \Delta^{++}\pi^0$
$\rightarrow \Delta^+\pi^+$
$\rightarrow (p\pi^0)\pi^+$ diffraction dissociation
$\rightarrow p\pi^+\pi^0$ phase space

When the $p\pi^+$, $p\pi^0$ and $\pi^+\pi^0$ invariant mass distributions were subsequently examined, it was found that Δ^{++} was seen only in tagged $\Delta^{++}\pi^0$ events, ρ^+ only in tagged $p\rho^+$ events, and Δ^+ only in tagged $\Delta^+\pi^+$ events. Although it is not visible in Fig. 3.9, it is claimed that the group corresponding to Δ^+ production (lower tube in the figure) is resolved into two tubes in the full 4-dimensions when the radial variable is included. This method, which by construction is model dependent, has apparently separated out the individual channels making up the $\pi^+p \rightarrow p\pi^+\pi^0$ reaction. In the events analysed by Pless the data were made up almost entirely of $\Delta^{++}\pi^0$, $\Delta^+\pi^+$, $p\rho^+$ and diffraction dissociation, the amount of phase space background required being approximately 2%. Shown in Table 3.1 below is a summary of the Pless results on the contributions from individual channels to the overall reaction.

Table 3.1 Cross-sections for 3.9 GeV/c $\pi^+p \rightarrow p\pi^+\pi^0$

Final State	σ(mb)	% of total
$p\rho^+$	0.85 ± 0.04	44
$\Delta^{++}\pi^0$	0.42 ± 0.03	22
$\Delta^+\pi^+$	0.23 ± 0.04	12
$(p\pi^0)\pi^+$	0.40 ± 0.05	20
Phase Space	0.04 ± 0.02	2

Shown in Fig. 3.10 are Prism plots of the channel $\pi^+p \to p\pi^+\pi^0$ at 5 GeV/c, the same final state as the Pless data, where the 3 tubes of the Δ^{++}(top), ρ^+(middle) and, Δ^0(bottom) are clearly visible from different angles of view of the prism. In none of these plots, despite the rotation, is the Δ^0 tube resolved into two separate tubes.

3.4.2 Discussion of the Pless Technique

Other experimental channels have been examined by the Prism plot technique.

Evans et al (Ref. 3.6) have examined the reaction $\pi^+p \to \pi^+p\pi^+\pi^-$ at 11.7 GeV/c where the full 3N-5 dimensional space is one of 7 variables. There the Prism plot selection method was tested by comparing the results with those from maximum likelihood fits and by applying it to a simulated experiment. The quasi two-body reactions were shown to be separated and their cross-sections correctly determined. The Prism plot method was shown to reproduce the differential distributions, at least of the more important sub-channels, without bias.

Ferrando et al (Ref. 3.7) have presented an analysis of 20,000 events corresponding to the 4-body reaction $\pi^-p \to p\pi^+\pi^+\pi^-$ at 3.93 GeV/c, again requiring 7 variables to specify the reaction. In this analysis also, the Prism plot technique was found to be quite powerful in separating the various sub-channels from the overall final state.

One criticism of the Pless method is that is is a model dependent technique. The basic forms of the sub-channels have to be known and such quantities as the numbers expected in

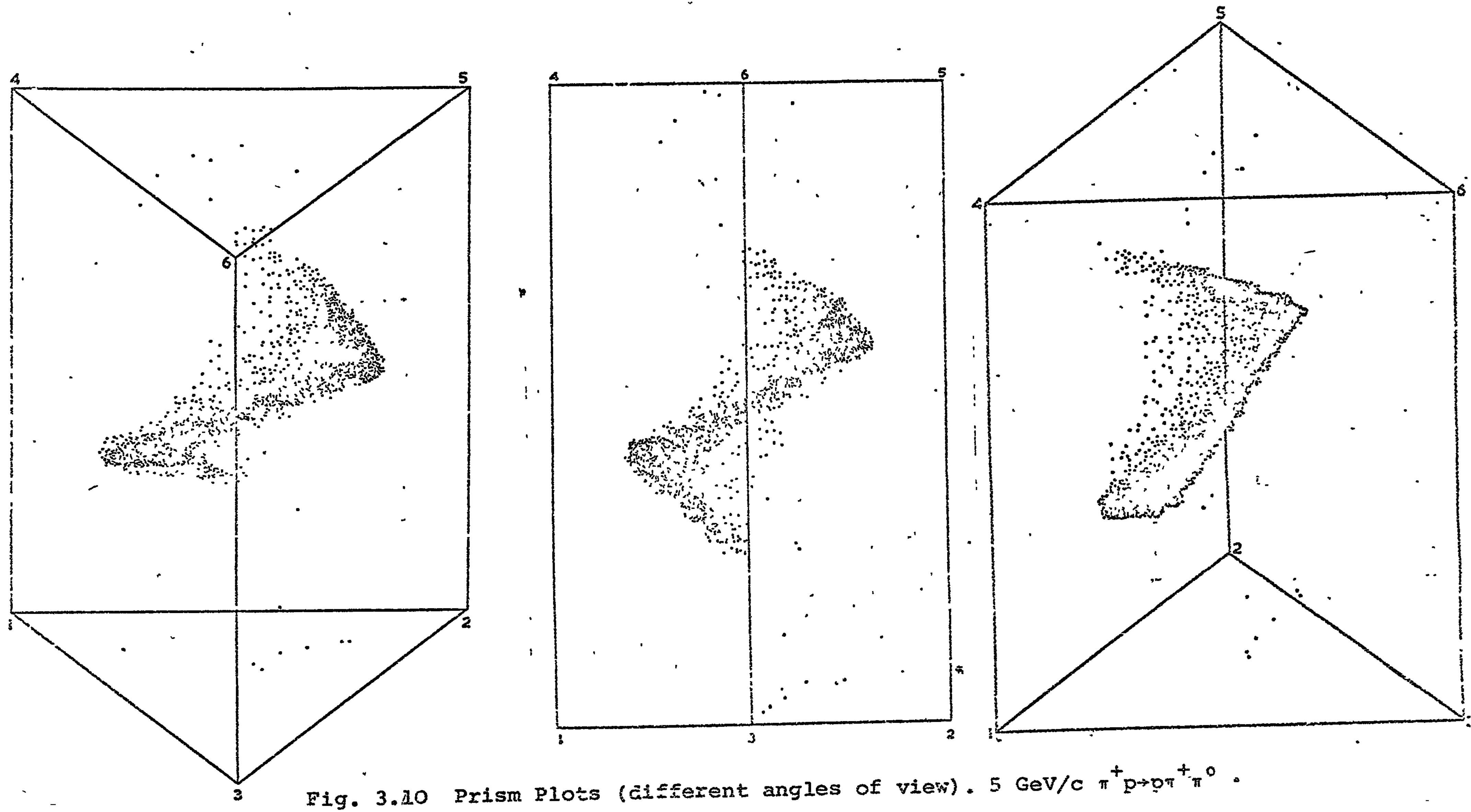

Fig. 3.10 Prism Plots (different angles of view). 5 GeV/c $\pi^+ p \rightarrow p \pi^+ \pi^0$.

each channel and the angular distributions of the decaying resonances have to be used as input. Thus there appears to be a great danger that the information extracted regarding the final state configurations will be little more than that inputed to the Monte-Carlo calculation used to assign the weights to the various volumes of the N-dimensional space being considered. Despite this criticism, what is well founded is that a more complete analysis of the data will be made by using all of the 3n-5 variables simultaneously, rather than by using sub-sets of them in the Dalitz, Chew-Low, and Van-Hove plots separately.

3.5 Cluster Analysis

Monte-Carlo simulations of an interaction, for example $\pi^+ p \rightarrow p\pi^+\pi^0$, indicate that events cluster together according to the particular kinematic configuration of the events. That is, $\Delta^{++}\pi^0$ events tend to group together in certain regions of the 4-dimensional prism and $p\rho^+$ events group, with perhaps some overlap into the $\Delta^{++}\pi^0$ region, in others. If the clusters are indeed well defined then it should be possible to locate them in a standard statistical manner without having to invoke any pre-determined physical models. This has been attempted by the use of a modified version of the CLUSTAN statistical analysis package written by D. Wishart of St. Andrews University.

Originally, the programme was capable of analysing only 1000 cases, with up to 200 variables in each case, but has been modified to be capable of handling a maximum of 10,000 cases with up to 20 variables in each case. By considering that 3n-5 variables are required to specify an event, this means that nuclear interactions up to a maximum of 8 final state particles are able to be examined.

3.5.1 Description of CLUSTAN

The method involved in clustering the data is iterative relocation with heirarchic fusion. The starting point of the programme is the classification of the population of N objects into K clusters. During one relocation scan, each object is considered in turn and its similarities with all K clusters are computed. If the similarity of an object X and its parent cluster P is S(X,P) and the similarity between X and any other cluster Q is S(X,Q), then if S(X,Q) exceeds S(X,P) the programme moves X from cluster P to cluster Q. The centroids of the clusters P and Q are re-computed to account for this change and the next case is then examined. The population is repeatedly scanned until no objects are relocated during one full scan, at which stage a local optimum for the K clusters in terms of the similarity criterion S has been obtained. Next, the similarities between all pairs of clusters are computed and, if desired by the user, those two clusters which are most similar are fused. The classification is thereby reduced to (K-1) clusters and the relocation phase is repeated until a local optimum for these (K-1) clusters is found. The fusion stage is then repeated to yield (K-2) clusters and so on until the specified minimum number of terminal clusters has been reached, whence the local optimum for that number of clusters is then found. In this way a local optimum is obtained for each step in the process if the number of initial clusters exceeds the number of final clusters required. For the case when the number of initial and final clusters required are equal, the relocation phase only is completed.

3.5.2 Methods of use of CLUSTAN

The programme may be used in a variety of modes, there are choices of relocation alone, relocation and fusion, and there is also a choice of many different similarity criteria. Basically, however, the programme is used as follows.

(a) The user must instruct the programme with the number of final clusters it must find. This is a difficult decision, but it does not matter if this number is too large since this will only result in some of the clusters dividing into smaller ones. One method of overcoming this difficulty is to instruct the programme to find firstly K clusters and then to combine the two most similar and re-cluster to give K-1, and continue the relocation and fusion processes until only a few clusters are left. The results at each step are available and an examination of these, to detect the stage just before resolution is lost, provides the lower limit of the number of final clusters that should be used.

(b) The events must be assigned to an initial classification array, that is each event must initially be associated with a cluster number. In practice this is done in a strict numerical order. For example, if 1000 events are to be processed in one run starting with 7 initial clusters then as the events are read from the data summary tape they are allocated in order to the clusters 1 to 7. Hence the initial composition of cluster 1 consists of events 1, 8, 15 etc. As the events occur in no particular order on the data summary tape then the initial allocation is completely random. This is obviously the worst starting point since the centroids of the 7 initial clusters must be very similar, however the programme is quite capable of recovering from this.

(c) In practice, the number of initial clusters is selected as being equal to the number of final clusters required. It has been checked that if, for example, the programme is instructed to start with 15 initial clusters and perform heirarchic fusion with relocation until 9 remain then precisely the same events are associated with those 9 clusters as are associated if only 9 clusters were chosen initially.

(d) After the initial classification array has been assigned, the programme takes in turn each event and constructs its similarity with each cluster. The choices of similarity criteria which have been found to be the most satisfactory are:

(i) The n-dimensional distance, or its square, between the event and the cluster centroids. If the event is nearer to one cluster centroid than that to which it is currently assigned, then it is transferred to the nearer cluster.

(ii) The current shape distribution of the clusters in the vicinity of the event point is used to assess the relative probabilities of which cluster the event should be assigned to.

(e). A facility exists for demanding the minimum size of a group of events which are to be classified as a cluster. This is useful since fluctuations may occur which throw up spurious clusters. In the event of an unacceptably small cluster occuring, the events in that cluster are reassigned amongst the remaining clusters according to the similarity co-efficient being used.

(f) Because some events may exist which have a very poor similarity with all of the clusters appearing in one relocation cycle, it is possible to invoke a minimum similarity co-efficient for acceptance of any event into a cluster. Events which then have a similarity smaller than this value are removed into a residue until the end of the current relocation cycle.

It must be emphasised that the clustering technique is independent of any physical model. In the use of the analysis programme the only features set externally are:-

(i) The number of final clusters required.
(ii) The initial (random) allocation of events into clusters.
(iii) The minimum acceptable cluster size, if required.
(iv) The threshold value for similarity coefficients, if required.

3.6 Cluster Analysis of FAKED Events

In order to examine objectively under what circumstances, and with what efficiency, events corresponding to various sub-channels of a given reaction may be separated, a control sample of Monte-Carlo generated events was set up. Knowing the exact designation of every event in a sample, the results of the cluster analysis can be checked for validity and an accurate examination of the background level and the extent of ad-mixture in each cluster can be made.

Events corresponding to the channel $\pi^+n \rightarrow p\pi^+\pi^-$ have been compiled using the Monte-Carlo generation routine FAKE, to simulate the signals and background by the sub-channels

$\pi^+n \rightarrow p\rho^0$
$\rightarrow pf^0$
$\rightarrow p\pi^+\pi^-$ phase space

For each event the four Pless variables T_1, T_2, w and r were calculated and the total sample of events was then clustered in the 4 dimensional space of these variables. The clusters were then examined as to what extent $p\rho^0$, pf^0 or phase space events only were clustered together, or whether there was a significant amount of mixing of the separate channels into the same cluster. Several groups of data were generated ranging from isotropy of production and decay distributions to realistic t-distributions and decay angular distributions of the ρ^0 and f^0 mesons.

3.7 Results of the FAKE Analysis

The groups of data used in the examination of the separation efficiency of the clustering technique comprised:

(i) $2000p\,^0$, $2000pf^0$, 2000 phase space (ϕ_s) events. Both production and decay angular distributions were generated isotropically.

(ii) 2000pρ^0, 2000pf, 2000ϕ_s. Momentum transfer distributions were generated of the form $\frac{dN}{dt} \alpha \exp(-a|t|)$ with a=10 for the pρ^0 channel and a=8 for the pf^0 channel to simulate typical experimental distributions. The decay angular distributions were generated isotropically.

(iii) Lowering the number of background ϕ_s events to 1000, but angular distributions as in (ii) above.

(iv) Removing background events completely and having 2000pρ^0, 2000pf^0 with realistic t-and decay angular-distributions.

(v) The final group contained 2000pρ^0, 1000pf^0 and 1000 ϕ_s, the pρ^0 and pf^0 channels incorporated realistic production and decay distributions.

Thus the effects of the t-distribution may be studied by comparing groups (i), (ii) and (v), the effect of background by comparing (ii) with (iii) and (iv); the fifth group shows the effect of realistic generation of all distributions with ratios of the numbers of events consistent with the 4 GeV/c experiment.

Table 3.2 below summarizes the groups in the analysis.

Table 3.2 Groups used in FAKE Analysis

Group Number	Number of Events of			t-distribution	decay distribution
	pρ^0	pf^0	ϕ_s		
1	2000	2000	2000	ISOTROPIC	ISOTROPIC
2	2000	2000	2000	REALISTIC	ISOTROPIC
3	2000	2000	1000	REALISTIC	ISOTROPIC
4	2000	2000	-	REALISTIC	REALISTIC
5	2000	1000	1000	REALISTIC	REALISTIC

3.7.1 Group 1 Isotropic production and decay distributions

There was only some little suggestion of the appropriate clustering when this control group was used. This is only to be expected, obviously, since the events generated only resemble true resonant signals in that the dipion mass distributions show ρ^0 and f^0 peaks. The complete isotropy of decay and production angles implies very little grouping of the distribution on the Van Hove Plot, and hence no grouping together of events in the variables r and w.

3.7.2 Group 2 Realistic t-distributions, Isotropic Decay Angles

Table 3.3 below shows the manner in which the events were distributed amongst the 6 clusters which were extracted, and the composition of each cluster. For example in table 3.3, cluster 1 consists of 3.5% ρ^0, 44.5% f^0 and 52.5% background, and this corresponds to 1.5% of the total ρ^0 signal, 19.5% of the total f^0 signal and 23.0% of the total background of the complete sample.

Table 3.3 Group 2 Cluster Statistics

Cluster Number	ρ^0		f^0		ϕ_s		Cluster Size
	% of Total	% of Cluster	% of Total	% of Cluster	% of Total	% of Cluster	% of Total
1	1.5	3.5	19.5	44.5	23.0	52.5	15.5
2	3.5	7.0	27.5	54.5	18.5	38.5	15.0
3	35.0	60.0	5.5	9.5	18.0	30.5	19.0
4	15.5	29.0	30.5	57.0	7.5	14.0	18.0
5	0.0	0.0	0.0	0.0	28.0	100.0	9.5
6	45.0	67.0	17.0	25.5	5.0	7.5	23.0

It is apparent from these data that the inclusion of t-distributions has resulted in a tendency towards correct classification of the events. Clusters number 3 and 6 comprise 60% and 70% respectively p^{0}, cluster 5 is made up completely of background events, and clusters 2 and 4 contain 55% and 57% pf^{0} respectively. However, there is still some wrong classification of events, and the extent of ad-mixture between clusters is high.

3.7.3 Group 3 Realistic t-, Isotropic Decay-distribution: 1000ϕ_s, 1000pf^0, 2000pρ^0

By simulating in more detail the numbers of events in the three sub-channels, that is constructing a situation were similar to that in the 4 GeV/c $\pi^+d \rightarrow p_s p\pi^+\pi^-$ experimental channel, a clearer separation of events was made. Table 3.4 below shows the distribution of events into the clusters for this case, where 8 final clusters were used.

Table 3.4 Group 3 Cluster Statistics

Cluster Number	ρ^0		f^0		ϕ_s		Cluster Size
	% of Total	% of Cluster	% of Total	% of Cluster	% of Total	% of Cluster	% Total
1	31.0	81.5	2.0	2.5	12.0	16.0	19.0
2	15.0	48.0	20.0	32.5	12.0	19.5	18.5
3	30.0	93.0	1.5	2.5	3.0	4.5	16.5
4	0.0	0.0	0.0	0.0	22.0	100.0	5.5
5	20.0	55.0	27.0	37.0	6.0	8.0	18.5
6	1.5	7.0	28.0	65.0	12.0	28.0	11.0
7	1.0	6.0	20.0	60.5	11.0	33.5	8.0
8	0.0	0.0	0	0.0	21.0	100.0	5.0

Clusters 4 and 8 consist solely of background events and together represent 43% of the total background events. Clusters 1 and 3 are dominated by the $p\rho^0$ sub-channel, corresponding to 60% of this process, and clusters 6 and 7 are dominated by the f^0 FAKE channel.

3.7.4 Group 4 $p\rho^0$ and pf^0 events alone

2000 events of the type $\pi^+ n \to p\rho^0$ and 2000 events of $\pi^+ n \to pf^0$ were analysed by the clustering technique, searching for 4 final clusters. No background was present and the ρ^0 and f^0 mesons were generated with exponential momentum transfer distributions of the form exp(-10t) and exp(-8t) respectively. The ρ^0 meson was given a decay angular distribution $0.9\cos^2\theta + 0.1$, and the f^0 meson a distribution of $0.8\cos^4\theta + 0.1\cos^2\theta + 0.1$ to simulate the 4 GeV/c experimental channel $\pi^+ d \to p_s p\pi^+\pi^-$. It was found that 97% of the events were correctly clustered, the remaining 3% being incorrectly assigned, indicating that the effects of background are still present in the analysis of Group 3 (Section 3.7.3).

3.7.5 Group 5 Full Generation

The events generated were as shown in Table 3.5 below, to simulate the experimental situation found in the 4 GeV/c $\pi^+ d$ experimental channel $\pi^+ d \to p_s p\pi^+\pi^-$.

Table 3.5 Description of Events Generated as Group 5

Channel Generated	Number Generated	t-distribution $\frac{dN}{d\lvert t\rvert}$ =	Decay distribution $\frac{dN}{d\cos\theta}$ =
$\pi^+ n \to p\rho^0$	2000	exp(-10t)	$0.9\cos^2\theta + 0.1$
$\pi^+ n \to pf^0$	1000	exp(-8t)	$0.8\cos^4\theta + 0.1\cos^2\theta + 0.1$
$\pi^+ n \to p\pi^+\pi^-$	1000	isotropic production angle	isotropic decay in Helicity frame

The cluster analysis was performed with 8 initial clusters and 8 final clusters. As a check 10 initial clusters were formed and reduced by fusion to 8 final clusters, and precisely the same events were found to occupy the 8 final clusters in each case. The separation of events into the three sub-channels was better than had been achieved before, and the results are summarized in Table 3.6 below.

Table 3.6 Group 5 Cluster Statistics

Cluster Number	ρ^0		f^0		ϕ_s		Cluster Size
	% of Total	% of Cluster	% of Total	% of Cluster	% of Total	% of Cluster	% of Total
1	0.4	3.8	2.0	9.5	18.2	86.7	5.3
2	0.0	0.0	0.0	0.0	17.2	100.0	4.3
3	3.1	10.3	44.4	74.2	9.3	15.5	15.0
4	0.0	0.0	0.0	0.0	21.4	100.0	5.4
5	45.6	94.3	2.6	2.7	2.9	3.0	24.2
6	3.9	13.7	44.6	77.5	5.1	8.8	14.4
7	0.5	5.4	4.7	24.7	13.2	70.0	4.7
8	46.5	86.6	1.6	1.5	12.7	11.8	26.8

Analysis of these data shows that 92% of all $p\rho^0$ events, 89% of all pf^0 and 70% of all phase space background events are correctly assigned to separate clusters, which would be tagged as corresponding to these processes.

3.8 Discussion of Clustan analysis of FAKE events

The separation into sub-channels of a given reaction channel is possible to a high degree of accuracy provided that certain conditions are fulfilled. The FAKE analysis using the clustering technique shows that these conditions are usually inherent in most physical processes. These conditions are:

i) Resonances must be produced with sharp t-distributions.

ii) The background present must not be so large as to conceal any signal present, that is the signal to background ratio in the reaction must be better than 1:1.

iii) To a lesser extent, separation becomes more acute if the decaying resonances have a non-isotropic angular distribution.

Examining these conditions with respect to the position that events would occupy on the Van-Hove plot it is apparent that the sharp t-distributions would force the resonances into well defined positions. This implies that the radial parameter r then becomes a sensitive variable when separation of two resonances in the same Van Hove sector is required, as was the case with the $p\rho^0$ and pf^0 events examined. Thus it is concluded that, so long as the number of background events is not too high, the most significant feature necessary for satisfactory separation to be possible is that the resonances should be peripherally produced, therefore ensuring that the t-distributions are sharp.

3.9 Conclusions

The analysis of an n-body final state, by using a cluster searching technique in the (3n-5)-variable space required to specify completely the events, has been shown to be highly efficient in separating the various sub-channels contributing to the overall final state of FAKED events $\pi^+n \to p\pi^+\pi^-$. The technique, useful mainly when sharp t-distributions are present in the data, brings together all of the necessary information into one analysis instead of making analyses using subsets of this information, such as is done in a Van Hove, Dalitz or Chew-Low plot analyses individually. Compared with the Prism plot analysis, the advantage of this technique is that it searches for clusters of data points in a way that is independent of any physical model.

Chapter 4 The Reaction $\pi^+d \rightarrow p_s p\pi^+\pi^-$

4.1 Introduction

The majority of the events corresponding to the inelastic charge exchange process $\pi^+d \rightarrow p_s p\pi^+\pi^-$ occur as either 3- or 4-pronged events in the bubble chamber. A small fraction of these events, estimated from FAKE calculations to be less than 3%, would appear as 2-pronged events where both protons have momenta too small to be seen in the chamber, and would therefore be rejected by the overall scanning criteria of the experiment. The events seen as 3- or 4-pronged interactions occur in the ratio of 2.2 to 1. This is expected from the Hulthen momentum distribution when a proton with momentum of 95 MeV/c is just seen in the bubble chamber. A plot of the spectator momentum distribution is shown as the histogram in Fig. 4.1 where the solid curve, which assumes the impulse approximation, represents the Hulthen momentum distribution normalised to the number of spectator protons with momentum of less than 300 MeV/c; it is seen to agree well with the experimental situation. For the Hulthen wave function (see Appendix B) it was assumed that the deuteron potential well has a hard core of radius 0.8 Fermi and an extended potential up to 4.5 Fermi. These values agree very well with the values observed by Christian and Gamel (Ref. 4.1) in an electron scattering experiment where the two effective ranges α and β ($\alpha, \beta \equiv {}^1/r_0$) were given as 1.268 and 0.232 Fermi^{-1} respectively. It is therefore assumed that the impulse approximation is a good

Fig. 4.1

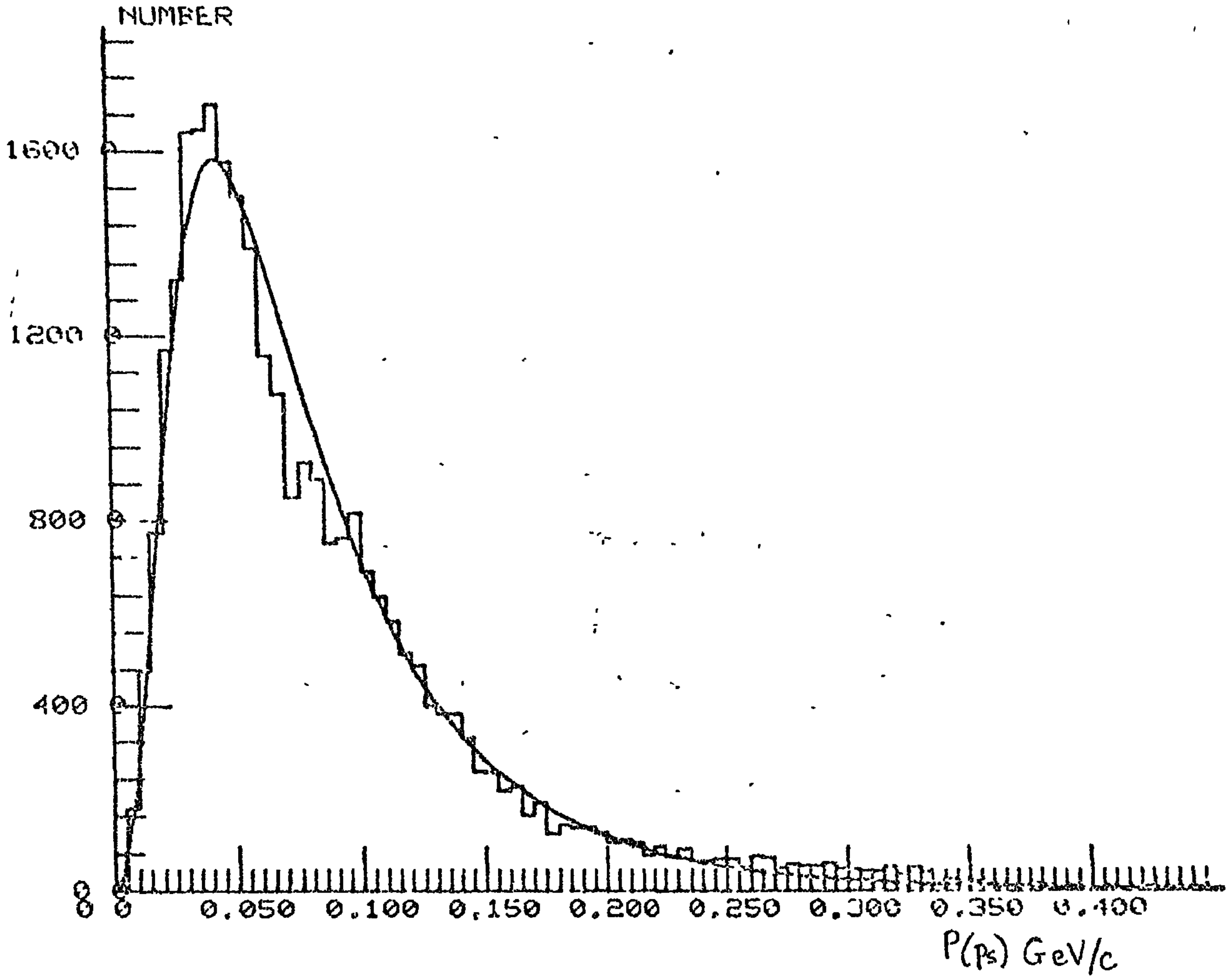

Spectator momentum spectrum for the reaction $\pi^+ d \to p_s p \pi^+ \pi^-$. Curve is the prediction of the Hulthen momentum distribution assuming the Impulse Approximation.

description of this channel and that the reaction may be written as

$$\underset{(p_s)}{\pi^+ n} \rightarrow \underset{(p_s)}{p} \quad \pi^+\pi^-$$

This channel may be described in terms of Feynman diagrams for meson exchange by the two processes shown in Figs. 4.2(a) and 4.2(b). In the first of these two diagrams the possible exchange particles are those with the quantum numbers of the π-meson and the A_2-meson. The second diagram corresponds to exchange of the quantum numbers of the vacuum (the pomeron) or the f^omeson, and is equivalent to the process of diffraction dissociation of the neutron into a proton and negative pion. For interactions which do not involve the exchange of a baryon these are the dominant processes which satisfy the conservation of quantum numbers, and thus this channel is expected to be dominated by production of dipion resonances and the diffractive process described above.

In this chapter the three particle combinations $\pi^+\pi^-$, π^+p and π^-p will be investigated with respect to resonance formation and these will then be examined from the point of view of cluster searching. The whole analysis is precceded by a general examination of the data and a description of the event selection criteria for this channel. The analysis presented is largely concerned with those processes where the mesonic systems are produced in the forward hemisphere of the centre of mass reference frame, but where backward produced meson systems occur in the data this will be pointed out .

Fig. 4.2

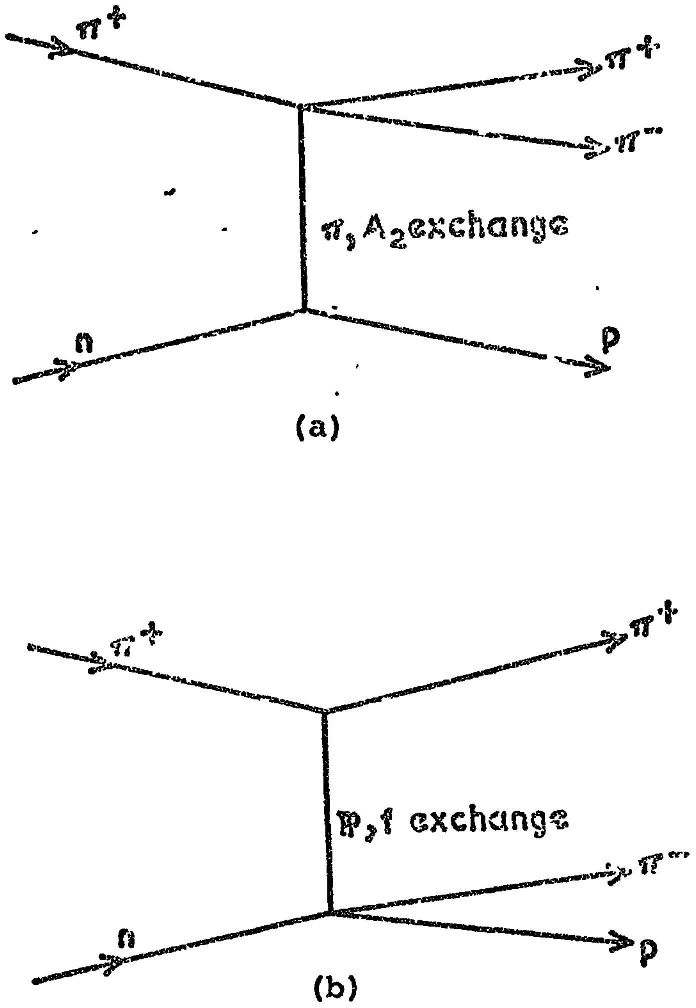

(a)

(b)

Feynman diagrams for the reaction $\pi^+ \underset{p_s}{n} \to \underset{p_s}{p}\pi^+\pi^-$.

In diagram (b) the exchanges shown lead to an $I=\frac{1}{2}$ (N^*) state for the π^-p system. ρ^0 exchange, which would lead to an $I=\frac{3}{2}$ (Δ) state, contributes to <3% of the channel.

4.2 Event Selection

The events presented were obtained in a sample of 400K pictures taken in an exposure of the CERN 2m bubble chamber filled with deuterium and exposed to a 4 GeV/c π^+ beam. A total of 18661 events giving a fit to the reaction

$$\pi^+ d \to p_s p \pi^+ \pi^-$$

was obtained. The number of fits were reduced to 15485 events after the selection criteria described below were applied.

(i) χ^2 probability

The χ^2 probability distribution for all, both 3- and 4-pronged, events fitting this 4-C channel is shown in Fig. 4.3(a) and the corresponding distribution of χ^2 in Fig. 4.3(b). The probability distribution of Fig. 4.3(a) is expected to be flat, that is it is equally probable that a true fit to the channel will give any χ^2 probability. However, experimentally it is found that there is a large peak for probabilities less than $\sim 0.5\%$. This effect is probably due to the contamination of the 4-C $\pi^+ d \to p_s p \pi^+ \pi^-$ channel by other reaction channels and hence events with χ^2 probability less than 0.5% were excluded from the analysis. In all 937 events failed this test.

(ii) Spectator momentum

Despite the fact that the Hulthen momentum distribution describes well the experimental spectator momentum distribution below 300 MeV/c, there is an excess of measured spectator protons with momenta above this value. These high values of momentum are assumed to be the result of secondary interactions of the spectator nucleon and since this type of interaction is

Fig. 4.3

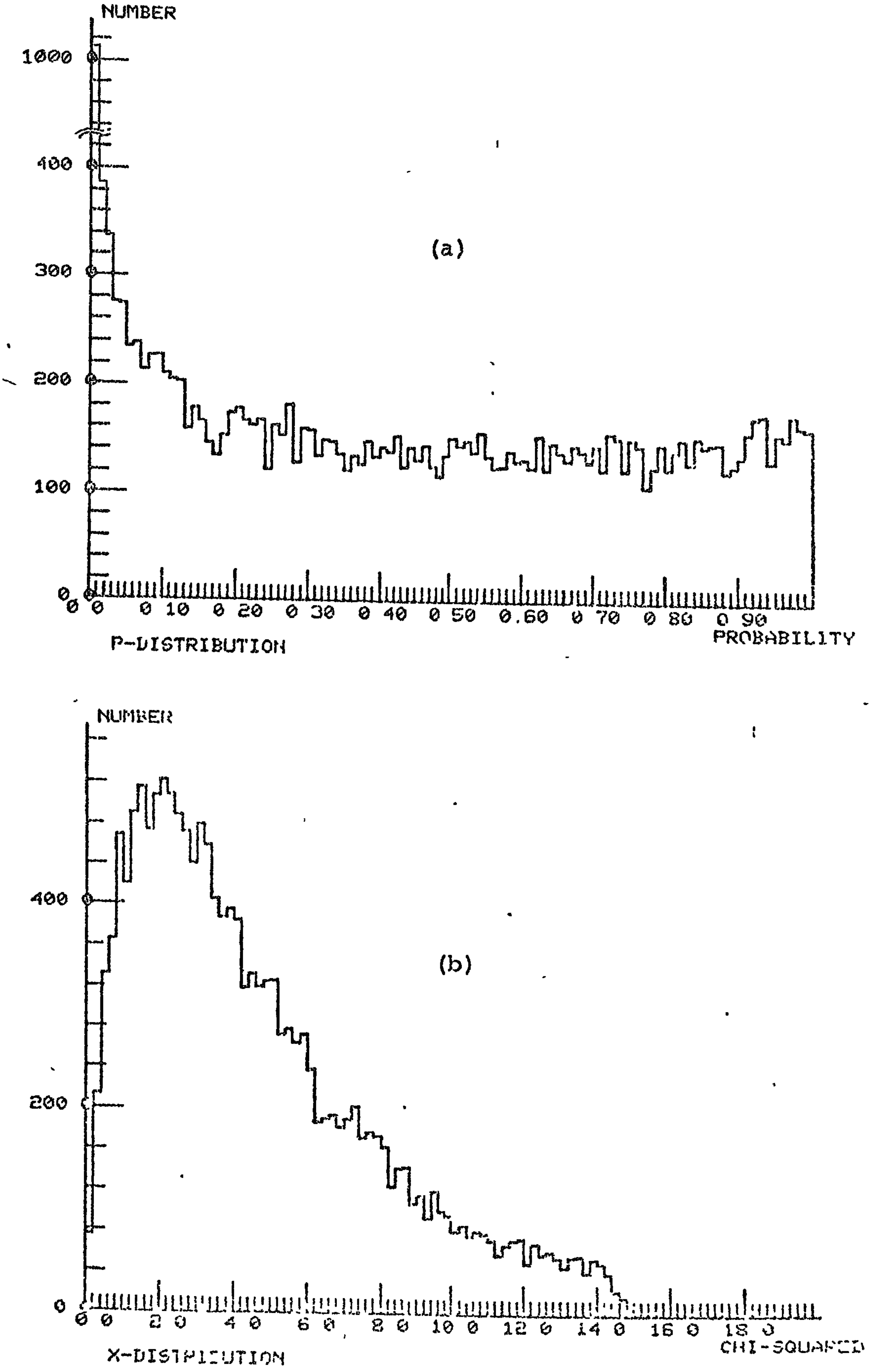

$P(\chi^2)$ and χ^2 distributions for 4 GeV/c $\pi^+ d \rightarrow p_s p \pi^+ \pi^-$.

in disagreement with the general formulation of the impulse approximation, all events with a spectator proton momentum greater than 300 MeV/c have been excluded. This leads to a loss of 1% of true spectator proton events which are indistinguishable from the spurious high momentum spectator events.

(iii) Missing Mass Squared

The missing mass squared (MM^2) was confined to the limits $-0.03 \leq MM^2 \leq 0.008$ $(GeV/c^2)^2$. Fig. 4.4 shows a frequency histogram of the missing mass squared after the full selection criteria were applied. The aim of this selection is to ensure that there is little chance of a neutral particle being present in the event, and hence that the fit is most probably a good 4-constraint fit. The distribution of Fig. 4.4 shows the expected asymmetry of the MM^2 to a 4-C channel.

(iv) Beam momentum

From the characteristics of the beam transport system at exposure time, the beam momentum should lie within a narrow band. Because of this the momentum of the incident pion has to lie between 3.96 and 4.04 GeV/c.

(v) Summary

In summary, the selection criteria devised in order to extract the good events from the initial sample of events fitting the channel $\pi^+ d \rightarrow p_s p \pi^+ \pi^-$ were:

(a) χ^2 probability $> 0.5\%$

(b) $P(p_s) \leq 300$ MeV/c

(c) $-0.03 \leq MM^2 \leq 0.008$ $(GeV/c^2)^2$

(d) $3.96 \leq P(beam) \leq 4.04$ GeV/c

Fig. 4.4

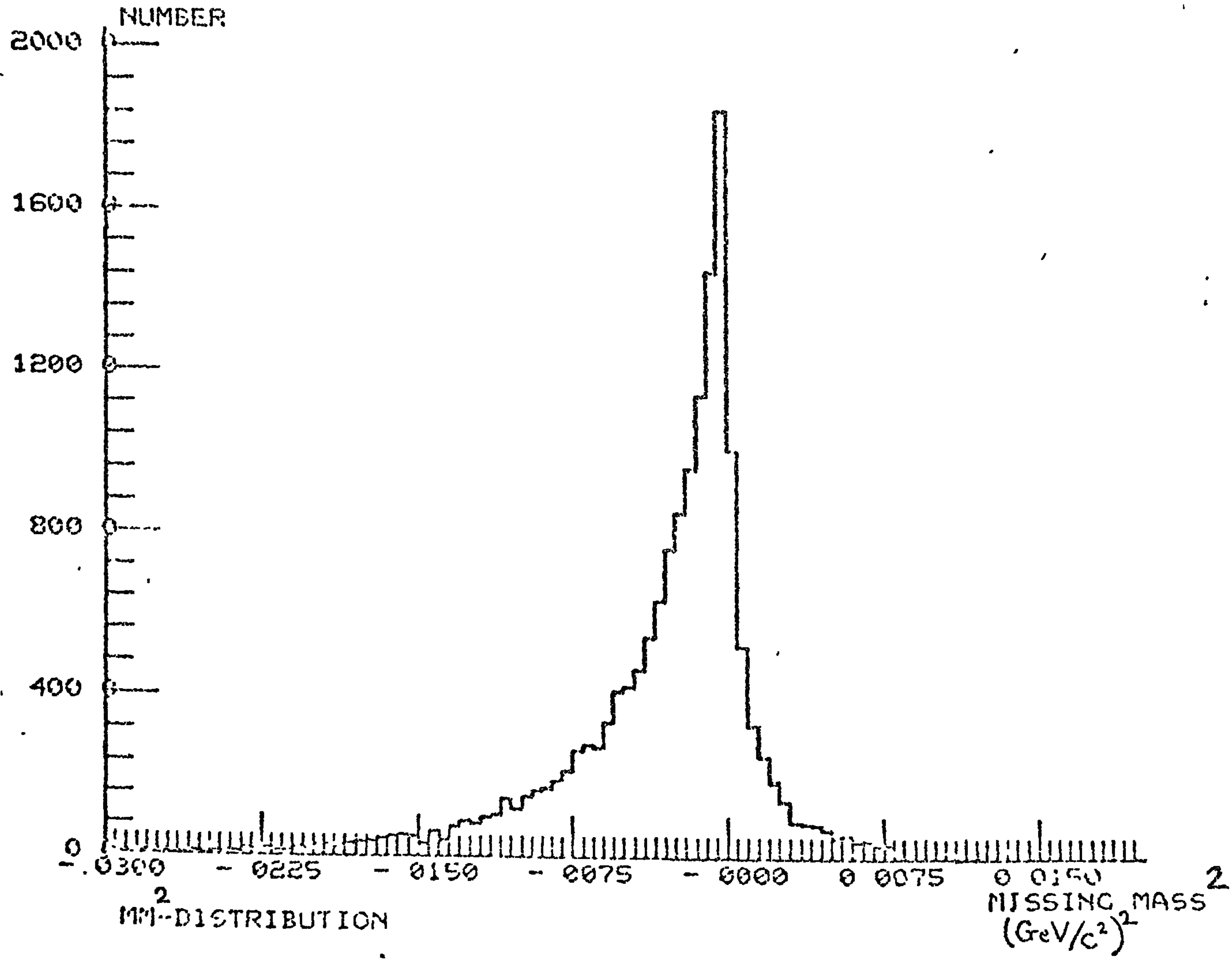

Distribution of Missing Mass Squared for 4 GeV/c $\pi^+ d \to p_s p \pi^+ \pi^-$.

4.3 Final Sample of Events

In imposing a set of selection criteria such as those described above, the aim is to obtain a collection of events which is considered to be an uncontaminated sample of the chosen events. If any meaningful analysis is to be performed then any biases in the data must be removed. Moreover, it is important that the selection criteria applied to the data do not themselves introduce biases or, if they do, that the biases introduced by the selections are well understood and account can be taken of them during analysis. It has been shown that the selection criteria described above did not introduce biases into the final sample of events used for analysis.

Table 4.1 shows the total number of events fitting the 4-C $\pi^+ d \rightarrow p_s p \pi^+ \pi^-$ channel together with the number ambiguous with each of a set of other hypotheses both before and after the selection criteria were applied. There are only two classes of ambiguity which are also 4-C fits:

(a) $\pi^+ d \rightarrow p p K^+ K^-$

and (b) $\pi^+ d \rightarrow d \pi^+ \pi^+ \pi^-$

and of these the ambiguity with the coherent channel (b) is a negligible number. Those $p p \pi^+ \pi^-$ events ambiguous with channel (a) have been examined and when the $(\pi^+ \pi^-)$ mass is plotted, strong ρ^0 and f^0 signals are seen to be present in the data implying that the events are really of the channel $\pi^+ d \rightarrow p_s p \pi^+ \pi^-$. Also, when the $K^+ K^-$ mass is examined in the fit to sub-set (a), there is no evidence for known resonance peaks in the data.

Table 4.1 Initial Events and Ambiguities of the Channel $\pi^+d\to p_s p\pi^+\pi^-$

Ambiguity Hypothesis Number	Reaction	4C/1C	Number Before Cuts	Number After Cuts	Comments
-	-	4C	6538	5641	Unambiguous
400011	$\pi^+d\to p_s p\pi^+\pi^-$	4C	1668	1367	Self-ambiguous
400021	$\pi^+d\to p_s p\pi^+\pi^-\pi^0$	1C	3699	2569	1Cπ^0 fit
400031	$\pi^+d\to p\pi^+\pi^+\pi^-n$	1C	1010	782	1C neutron fit
400041	$\pi^+d\to d\pi^+\pi^+\pi^-$	4C	120	100	coherent channel
400051	$\pi^+d\to d\pi^+\pi^+\pi^-\pi^0$	1C	2462	2149	1C coherent
400061	$\pi^+d\to p_s pK^+K^-$	4C	3386	2857	main 4-C ambiguity
400102	$\pi^+d\to p_s pK^+K^-\pi^0$	1C	1	0	
400112	$\pi^+d\to p_s pK^+\pi^-K^0$	1C	1	0	
400122	$\pi^+d\to p_s pK^-\pi^+K^0$	1C	1	0	
400192	$\pi^+d\to ppp\pi^-\bar{n}$	1C	1	0	
400222	$\pi^+d\to dp\pi^+\pi^-\bar{n}$	1C	33	26	
410421	$\pi^+d\to p_s p\pi^+K^0K^-$	1C	1	0	

Since it is far easier for a 4-C event to simulate a 1-C event than it is for the reverse to be true, the ambiguous fits to the 1-C reactions are thought to be largely spurious.

The only other class of ambiguities which present any problem in the analysis are those where the event is self-ambiguous, that is an event which gives two successful 4-C fits but with two of the particle identities interchanged. These events occur as

	Particle				
	1	2	3	4	5
Fit 1	$\pi^+d \rightarrow$	p_s	p	π^+	π^-
Fit 2	$\pi^+d \rightarrow$	p_s	π^+	p	π^-

where the fast outgoing positive track is π^+/p ambiguous after ionization testing has occurred. This class of events contributes 4% to the final sample and in the analysis each fit has been used, provided they pass the selection criteria, as if they were different events. This slightly, artificially, enhances the statistics in the channel but the effect only contributes background to the channel since if, say, FIT 1 were correct and the $(\pi^+\pi^-)$ combination were in the ρ^0 meson, then when the $(\pi^+\pi^-)$ invariant mass is plotted for the channel, FIT 2 would contribute a spurious $\pi^+\pi^-$ mass to the plot.

4.4 General Quality of the Data

The normalised stretch function for any of the three fitted variables, $^1/p$, $\tan\lambda$ and ϕ, of a track is defined as:

$$S(X) = \frac{X_u - X_f}{(\sigma_u^2 - \sigma_f^2)^{\frac{1}{2}}} \qquad 4.1$$

where f refers to the fitted value of the variable, u to the unfitted value and σ to the error on these quantities. This function has the property of being normally distributed with a mean of zero and unit variance, and any variation from this will be the result of systematic errors in the fitting chain. Therefore, the stretch functions are a test of the goodness of the data from the point of view of tuning of the analysis system. Shown in Fig. 4.5 (a) (b) and (c) are the distributions for $S(^1/p)$, $S(\tan\lambda)$ and $S(\phi)$ respectively, and as can be seen from these diagrams the data appear free from any systematic biases.

4.5 Channel Cross-section

The cross-section for the 4-C reaction $\pi^+d \rightarrow p_s p\pi^+\pi^-$ has been determined using the final number of fits obtained to this hypothesis as

$$\sigma(\pi^+d \rightarrow p_s p\pi^+\pi^-) = 2.10 \pm 0.17 \text{ mb}$$

In this an allowance of 5% contamination of the pion beam has been made, and only one of any self-ambiguous fits obtained has been counted.

4.6 Invariant Mass and Angular Distributions

The general features of the data for reaction A are shown in the Prism plot of Fig. 4.6 in which the mass combinations $M^2(\pi^+\pi^-)$ and $M^2(p\pi^-)$ are plotted parallel to the horizontal axes and the Van Hove angle ω is plotted parallel to the vertical axis. Events in which the $(\pi^+\pi^-)$ system is produced moving in the forward direction in the centre of

Fig. 4.5

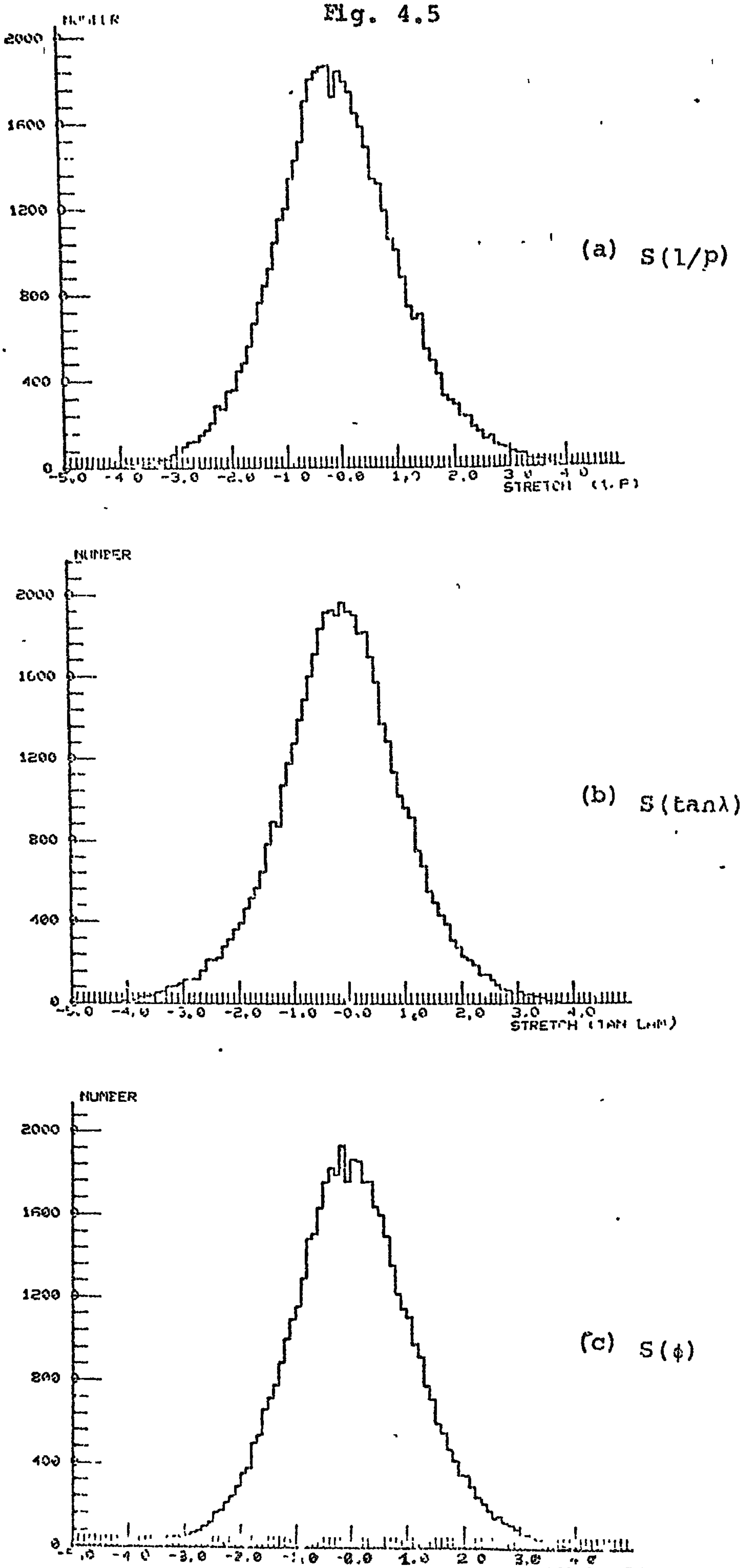

(a) S(1/p)

(b) S(tanλ)

(c) S(ϕ)

Stretch distributions for 4 GeV/c $\pi^+ d \to p_s p \pi^+ \pi^-$.

Fig. 4.6

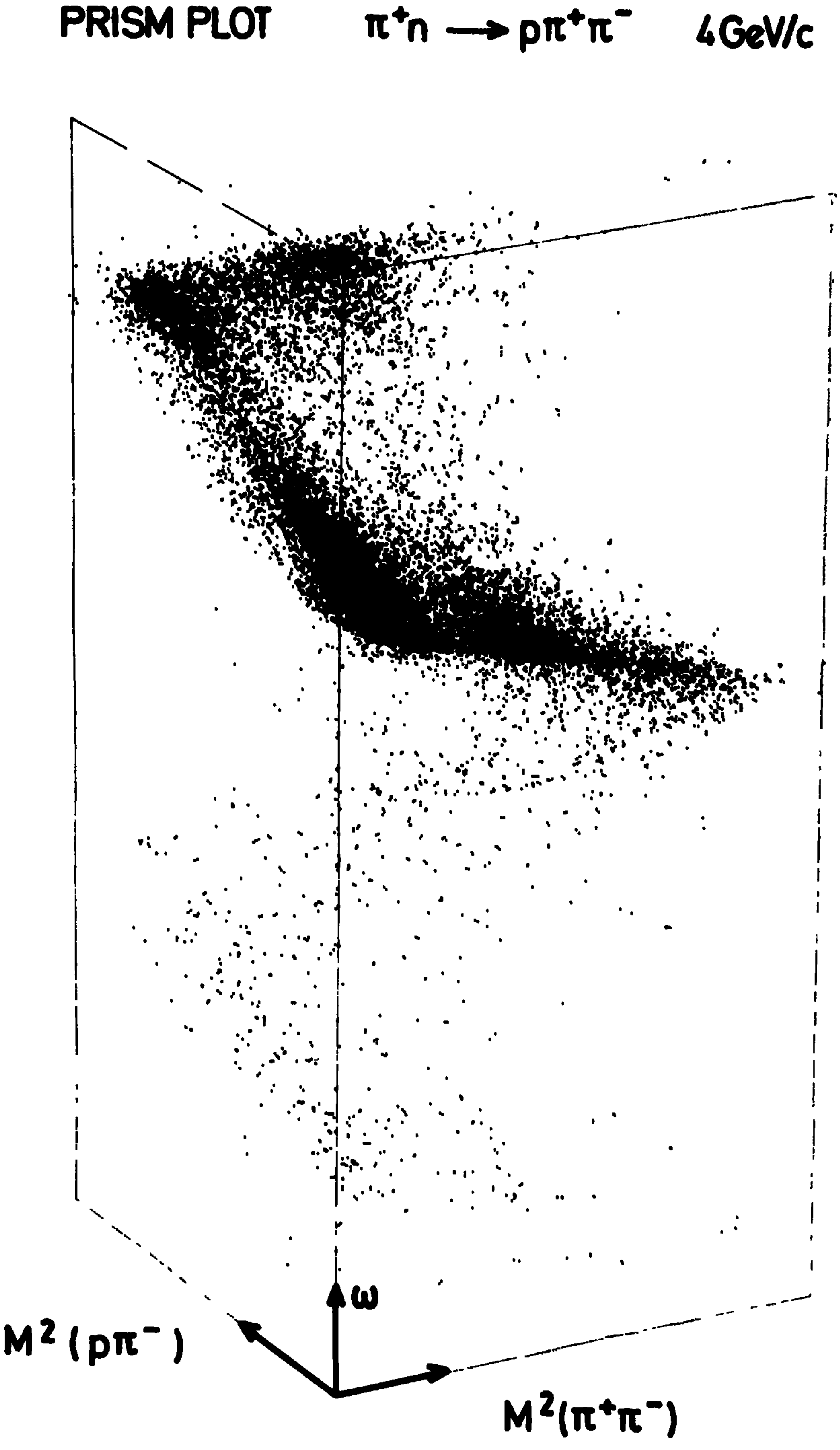

mass reference frame lie in the upper half of this plot. Those events where the recoiling proton is moving forwards, and hence the $(\pi^+\pi^-)$ system is moving backwards, in the centre of mass, appear in the lower half of the plot.

An examination of the distribution of data points in this plot reveals, in the upper half, strong bands due to forward production of the ρ^0 and f^0 mesons. The bands have the characteristic appearance of a decay angular distribution peaked strongly forwards and backwards in the resonance centre of mass system. In the lower half of the Prism plot there is evidence for some backward production of these same states. There is also, returning to the upper half of the plot, an accumulation of data at high $M^2(\pi^+\pi^-)$ but with low $M^2(p\pi^-)$ which could be interpreted either as the production of the $g^0(1686)$ meson or the production of a low mass N^* in the $(p\pi^-)$ system, an observation which will be returned to later.

Fig. 4.7 shows the Dalitz plot of $M^2(\pi^+\pi^-)$ against $M^2(p\pi^-)$ which is obtained by projecting the Prism plot of Fig. 4.6 onto its horizontal plane. Here the very strong bands corresponding to the ρ^0 and f^0 mesons are clearly visible. The solid outline in the plot of Fig. 4.7 corresponds to the kinematic limit of the Dalitz plot for a constant π^+n centre of mass energy of 2.9 GeV, which is equivalent to a stationary target neutron in the laboratory reference frame. Points falling outside this area are events in which the initial Fermi motion of the target neutron was towards the incident pion beam, thus increasing the centre of mass energy to a value above that of 2.9 GeV

Fig. 4.7

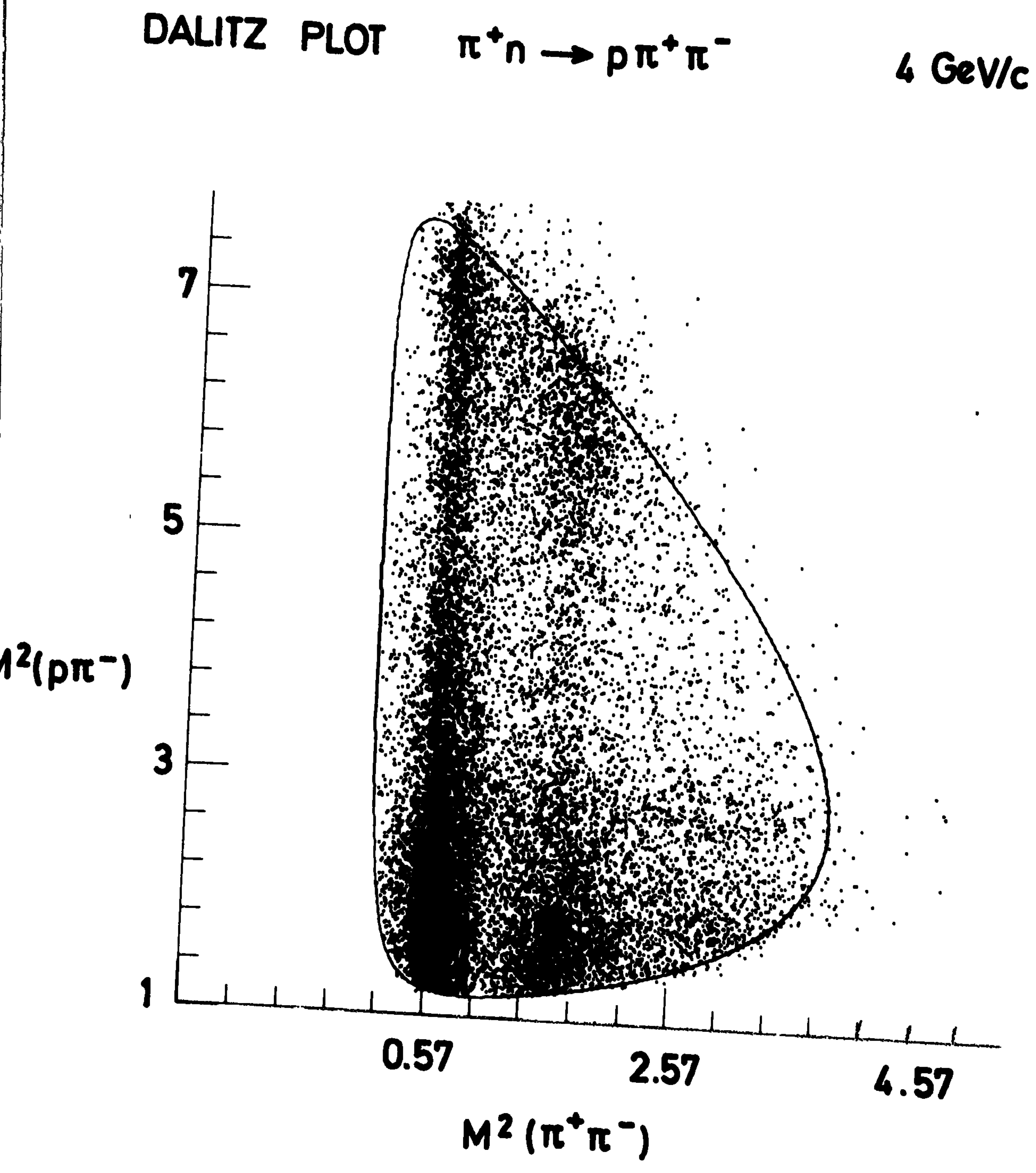
DALITZ PLOT $\pi^+ n \rightarrow p\pi^+\pi^-$ 4 GeV/c
7
5
3
1
$^2(p\pi^-)$
0.57
2.57
4.57
$M^2(\pi^+\pi^-)$

for the case of a static neutron target. The Dalitz plot is therefore a superposition of many static cases, the 10% centre of mass energy variation leading to the situation where no point in the Dalitz point is uniquely attributable to a particular centre of mass energy, that is a range of initial neutron momenta could account for any point on the Dalitz plot except those at the extreme edges.

4.6.1 Dipion System

A frequency histogram of the invariant mass of the dipion system is shown in Fig. 4.8. It is clear from this distribution that there is a large amount of ρ^0 and f^0 production, which is expected from the arguments based upon the possible exchange particles, as in the Feynman diagrams, contributing to this channel.

From this sample of events there are 5279 events corresponding to the reaction:

$$\pi^+ n \rightarrow p\rho^0$$

using the mass interval for the ρ^0 meson

$$0.68 \leq M(\pi^+\pi^-) \leq 0.88 \text{ GeV/c}^2$$

and 2385 events corresponding to the reaction:

$$\pi^+ n \rightarrow p f^0$$

using the mass interval for the f^0 meson

$$1.20 \leq M(\pi^+\pi^-) \leq 1.34 \text{ GeV/c}^2$$

and these regions are used in the plots which follow to define the samples of data corresponding to ρ^0 and f^0 production. The two samples together account for approximately 50% of the total data.

In Fig. 4.9(a) is shown the decay angular distribution, in the helicity frame*, of the outgoing π^+ meson from the dipion

---

* S-channel helicity frame, see page 88.

Fig. 4.8

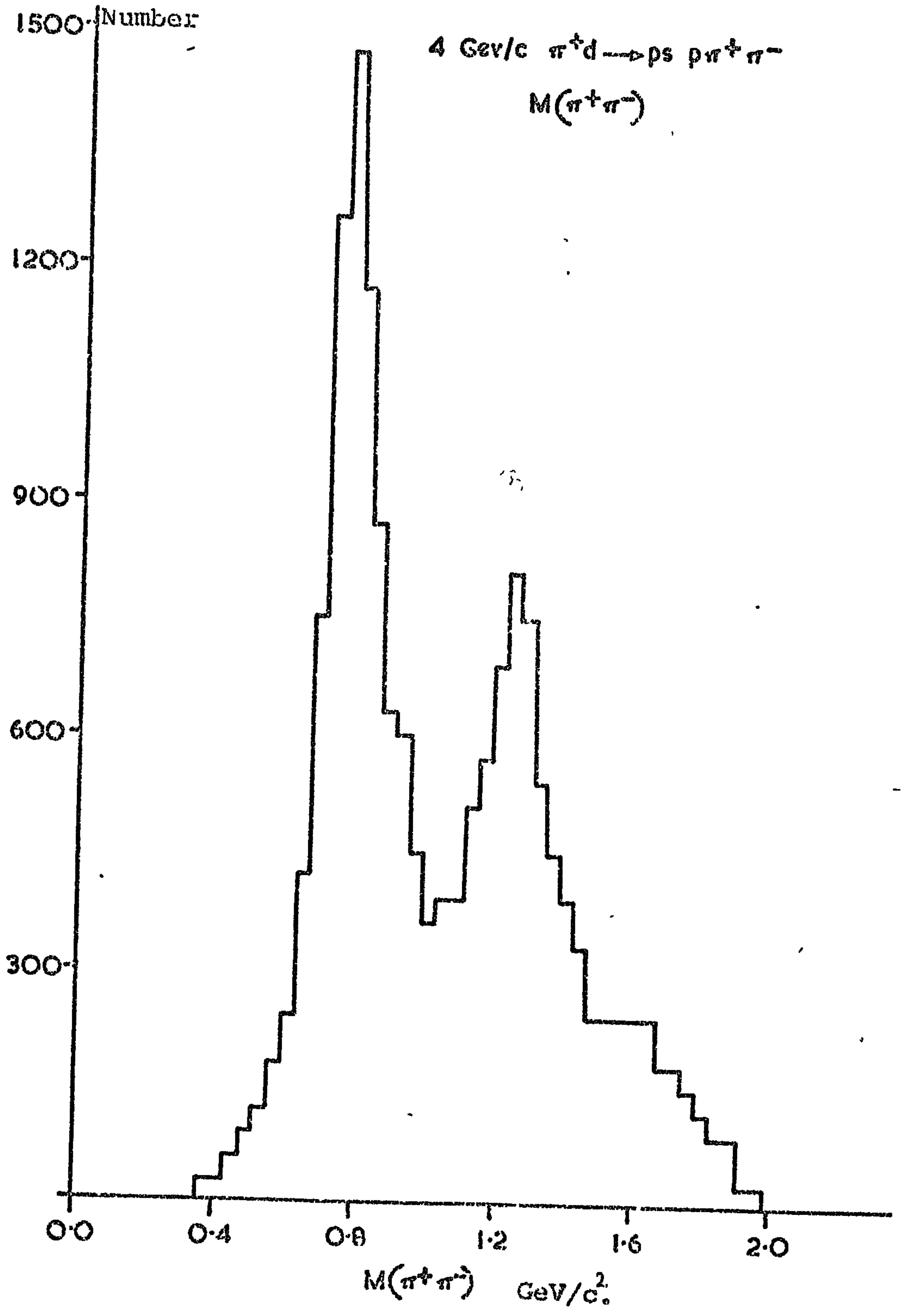
1500
Number
1200
900
600
300
4 Gev/c $\pi^+d \longrightarrow ps\ p\pi^+\pi^-$
$M(\pi^+\pi^-)$
0·0
0·4
0·8
1·2
1·6
2·0
$M(\pi^+\pi^-)$ GeV/c^2.

system in the ρ^0 mass region defined above. The distribution is consistent with a particle of spin-parity $J^P = 1^-$, being produced by pion exchange, with an interfering s-wave component causing the asymmetry in the distribution biased towards the forward direction of the π^+ meson in the decay $\rho^0 \rightarrow \pi^+\pi^-$. This effect will be dealt with in the next chapter.

The distribution of the relativistically invariant square of the 4-momentum transfer, t, from the beam particle to the $(\pi^+\pi^-)$ system is shown in Fig. 4.9(b). The slope of this distribution has been fitted with an exponential parameterisation of the form

$$\frac{dN}{d|t|} \propto \exp(-b|t|) \qquad 4.2$$

for values of $|t| < 0.3$ $(\mathrm{GeV}/c)^2$. The co-efficient b in the above exponential was found to be $b = 9.8 \pm 0.3$ $(\mathrm{GeV}/c)^{-2}$. This number is consistent with the value found in other experiments where the ρ^0 meson is formed by pion exchange. Also in Fig. 4.9(b) there appears a dip at the lowest value of $|t|$ which is an effect often attributed to the fact that there exists a minimum kinetically allowed value of t (t_{min}) for any given reaction configuration (see Appendix A). However, it is within this small range of t that the effects noted in Chapter 1, i.e. scanning losses and the Pauli exclusion principle, are expected to be manifest. Examining this point further, Fig. 4.9(c) shows a frequency histogram for the variable t', defined as

$$t' = t - t_{min}$$

and in this distribution there is still a clear dip at low values of $|t'|$. This dip is consistent with the loss of

Fig. 4.9

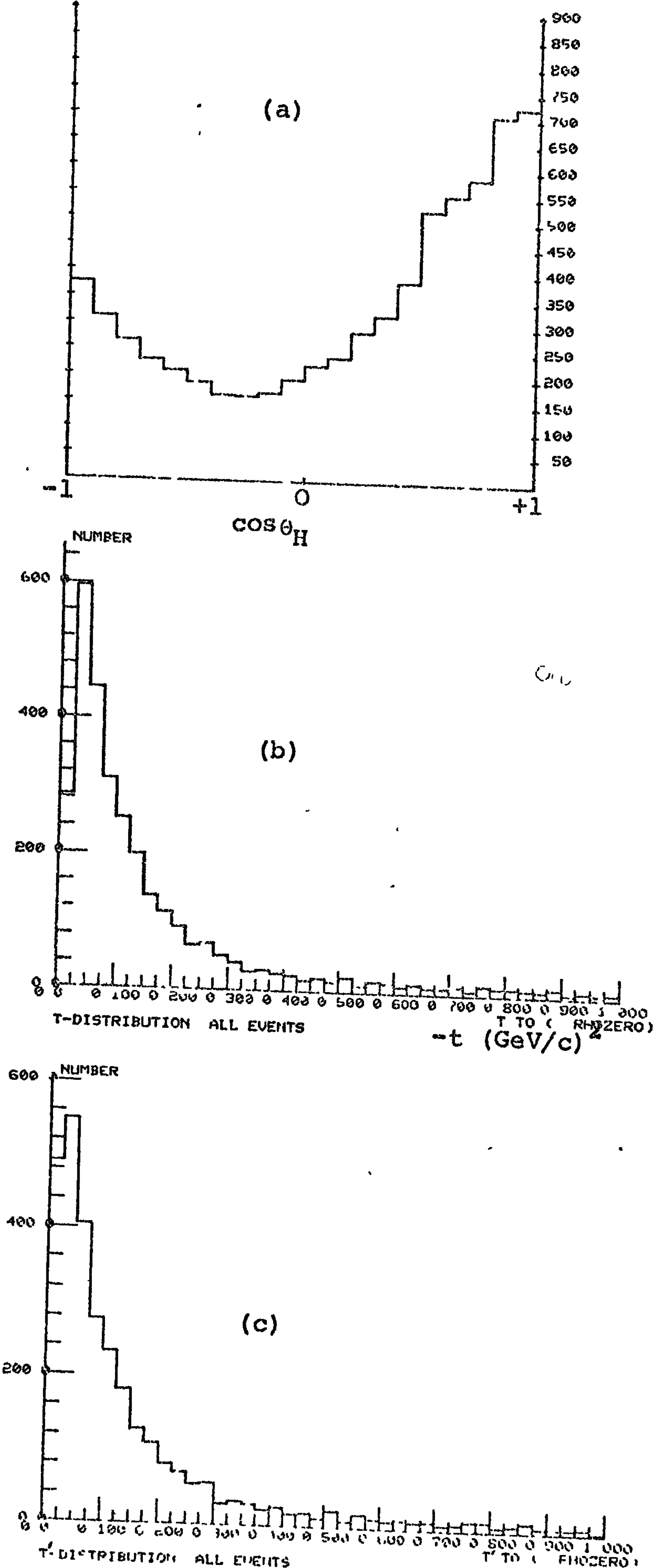

Distributions of $\cos\theta_H$, t, t' for the ρ^0 meson in 4 GeV/c $\pi^+ d \to p_s p \pi^+ \pi^-$. $0.68 < M(\pi\pi) < 0.88$ GeV/c^2

events predicted from the calculation of the 100% spin flip differential cross-section in Chapter 1, the spin flip cross-section being expected to dominate for the case of pion exchange.

Shown in Fig. 4.10(a) is the angular distribution of the outgoing π^+ in the helicity reference frame for those dipion mass combinations which fall in the f^0 region defined above as 1.20 to 1.34 GeV/c^2. An analysis of the f^0 decay distribution and its production mechanism in terms of the spin density matrix elements is presented in the next chapter of this thesis. It is sufficient for the moment to remark that a J=2 spin assignment of the $(\pi^+\pi^-)$ system in the f^0 region is only possible if there are interfering S- and P- wave components present in the region, since the decay angular distribution does not show the expected central peak and is asymmetrically biased towards the forward π^+ decay direction.

In Fig. 4.10(b) the distribution of t from the beam to the $\pi^+\pi^-$ system for the f^0 region is shown. This distribution has also been fitted with an exponential parameterisation of the form of Equation (4.2). In this case the value of the slope parameter b was found to be

$$b = (8.1 \pm 0.4)\ (\text{GeV}/c)^{-2}$$

for the $|t|$ interval

$$0.07 \leq |t| \leq 0.4\ (\text{GeV}/c)^2$$

The value of b is again consistent with the values found by other workers for the production of the f^0 meson by pion exchange. As in the case of the ρ^0 meson, the t distribution

Fig. 4.10

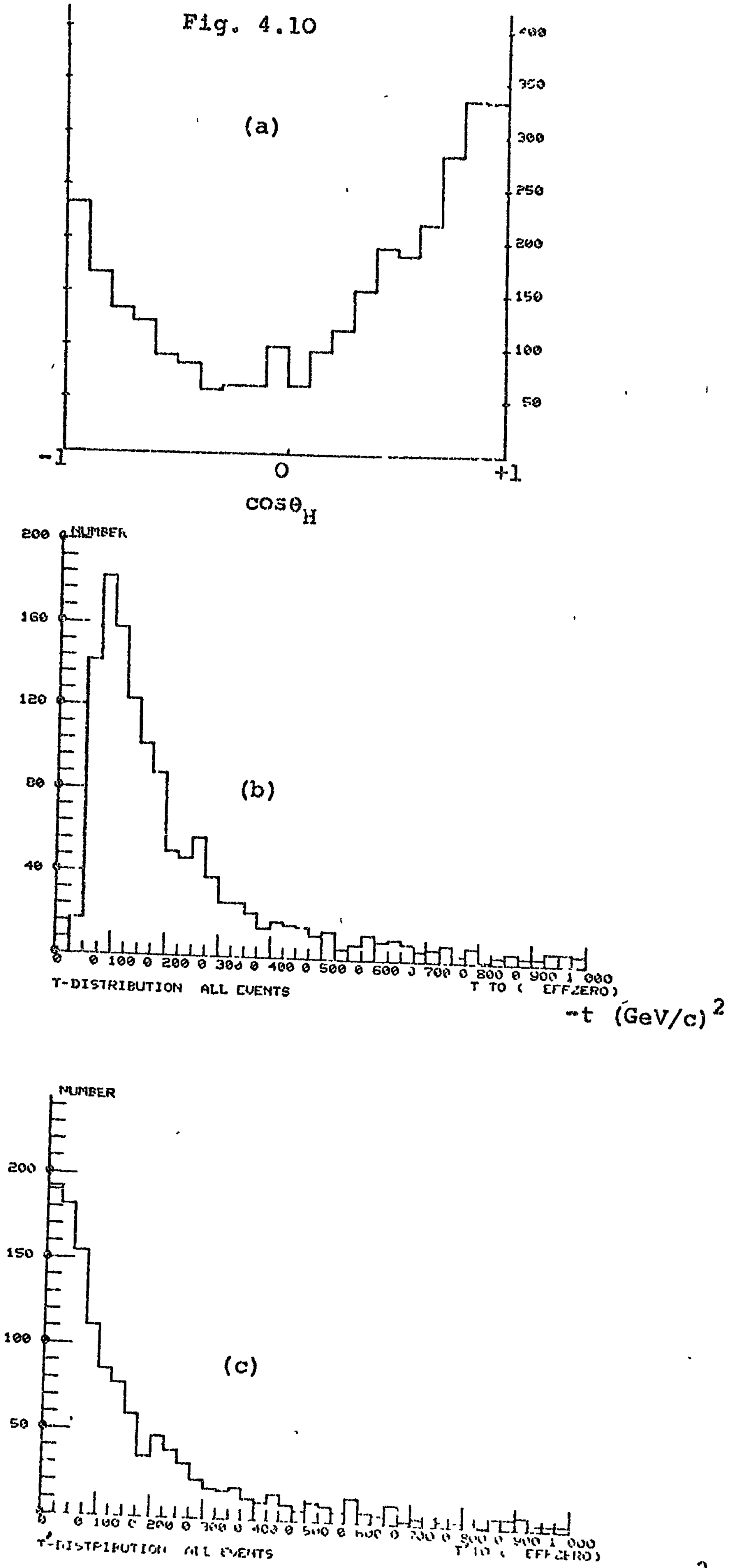

Distribution of $\cos\theta_H, t, t'$ for the f^0 meson in 4 GeV/c $\pi^+ d \rightarrow p_s p \pi^+ \pi^-$. $1.20 < M(\pi\pi) < 1.34$ GeV/c^2.

for those $(\pi^+\pi^-)$ combinations in the f^0 region shows a dip for values of $|t| < 0.07\ (\mathrm{GeV}/c)^2$. Fig. 4.10(c) shows the distribution of t', as defined above, from the beam to the $(\pi^+\pi^-)$ system. The loss of events at small values of $|t'|$ is again clearly visible and also explicable in terms of scanning losses and the Pauli exclusion principle as in the case of the ρ^0 meson.

In conclusion, therefore, the $(\pi^+\pi^-)$ system in the channel $\pi^+d \rightarrow p_s p\pi^+\pi^-$ has been shown to be consistent with ∿70% production of the ρ^0 and f^0 mesons, and approximately 50% of the channel is available for analysis with ρ^0 and f^0 mass region definitions of $0.68 \leqslant M(\pi^+\pi^-, \rho) \leqslant 0.88$ and $1.20 \leqslant M(\pi^+\pi^-, f) \leqslant 1.34\ \mathrm{GeV}/c^2$. Taking into account the full Breit-Wigner shapes for the ρ^0 and f^0 meson, the partial cross-sections for the production of these two resonances are

$$\pi^+d \rightarrow p_s p\rho^0 \quad : \quad 0.98 \pm 0.10 \ \text{mb}$$
$$\pi^+d \rightarrow p_s pf^0 \quad : \quad 0.48 \pm 0.05 \ \text{mb}$$

and both of these channels are, at small values of momentum transfer, consistent with resonance production by the exchange of a π meson.

4.6.2 Baryon Systems

For processes which do not involve the exchange of a baryon, the process of diffraction dissociation of the neutron target $n \rightarrow p + \pi^-$ of Fig. 4.2(b) is the only process which contributes to the production of a $(p\pi)$ system. That is to say, no production of Δ^{++} is expected, except by baryon exchange, since this would involve the exchange of an exotic doubly charged meson.

The invariant mass distribution of the $(p\pi^-)$ system is shown in Fig. 4.11(a) and that of the $(p\pi^+)$ system is shown in Fig. 4.11(b). There is no evidence in either of these distributions for any resonance peaks. Indeed, the broad enhancements at low and high $(p\pi^+)$ and $(p\pi^-)$ masses are due to reflections of the ρ^0 and f^0 signals from the $(\pi^+\pi^-)$ distribution into the $p\pi$ combinations. As evidence for this, Figs. 4.12(a), (b), (c) and (d) show the reflections of the ρ^0 and f^0 mesons respectively into the $p\pi^+$ and $p\pi^-$ mass distributions, from which it is clear that little true resonant signal is present in the baryon distributions. The lack of apparent resonant signal in the $p\pi$ systems tends to imply that the mass cuts used to define the ρ^0 and f^0 regions are too narrow since only 50% of the entire channel is used. However, widening the tolerances for acceptance of the $(\pi^+\pi^-)$ system into either ρ^0 or f^0 serves only to detract from the accuracy of the analysis performed because the signal to background ratio in the sample is decreased.

4.7 Cluster Analysis

In the previous chapter of this thesis (Analysis Techniques and Clustering) the cluster analysis technique was described and the use of the analysis programme CLUSTAN introduced. There the results were given to demonstrate the degree of success that the analysis technique had in isolating from the channel $\pi^+n\rightarrow p\pi^+\pi^-$ the FAKE subchannels: $p\rho^0$, pf^0 and $p\pi^+\pi^-$ phase space background. Provided that the t-distributions associated with the ρ^0 and f^0 mesons

Fig. 4.11

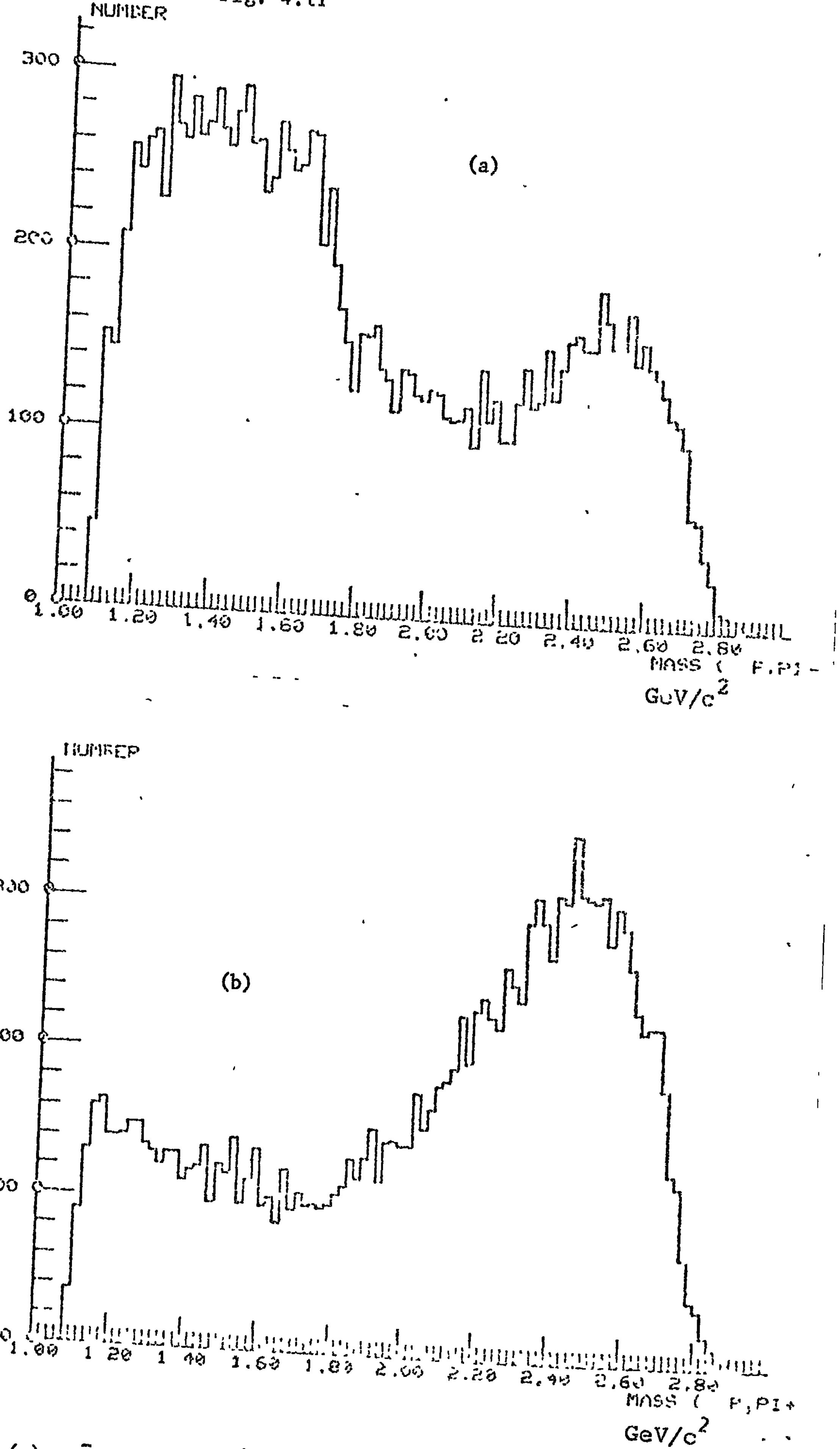

Mass of (a) $p\pi^-$, and (b) $p\pi^+$ systems for 4 GeV/c $\pi^+d \rightarrow p_s p\pi^+\pi^-$

Fig. 4.12

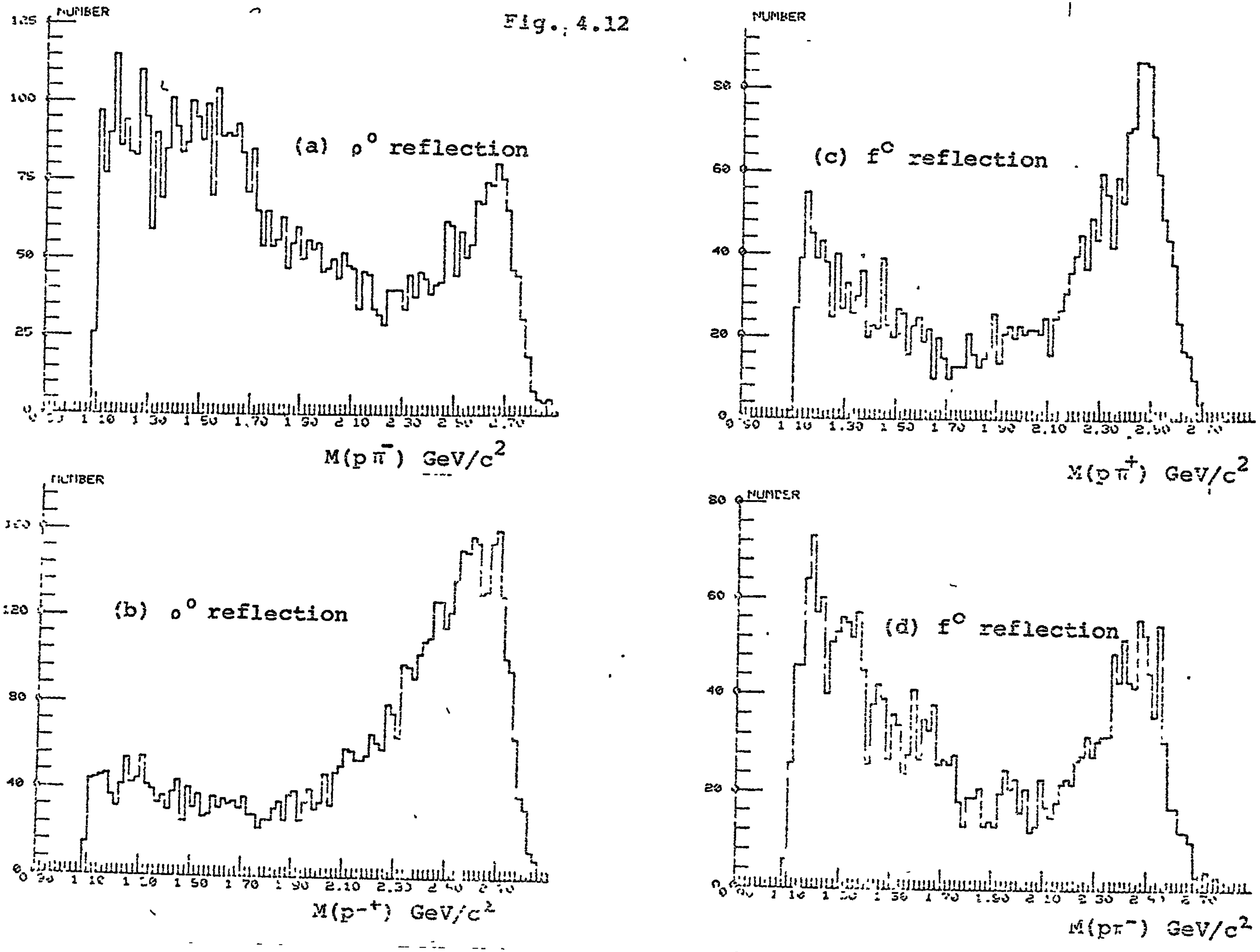
(a) ρ° reflection
NUMBER
125
100
75
50
25
0
M(pπ^-) GeV/c^2
(b) ρ° reflection
NUMBER
120
80
40
0
M(pπ^+) GeV/c^2
(c) f° reflection
NUMBER
80
60
40
20
0
M(pπ^+) GeV/c^2
(d) f° reflection
NUMBER
80
60
40
20
0
M(pπ^-) GeV/c^2
1.10
1.30
1.50
1.70
1.90
2.10
2.30
2.50
2.70

were sufficiently sharp then 90% of the $p\rho^0$, 90% of the pf^0 and 70% of the background events were correctly assigned.

In this section the same analysis is applied to the real data of about 16K events of the $\pi^+ n \to p\pi^+\pi^-$ channel at 4 GeV/c. An analysis of the dipion system of these events has been presented in the earlier sections of this chapter in which the ρ^0 and f^0 mesons have been selected by mass cuts. By the CLUSTAN method of selection it is shown that the number of ρ^0 and f^0 events available for analysis is approximately doubled.

Before describing the results of the CLUSTAN analysis it is worthwhile summarising the dipion results so far. The invariant mass distributions for the particle combinations $\pi^+\pi^-$, $p\pi^-$ and $p\pi^+$ have been shown already in Figs. 4.8, 4.11(a) and 4.11(b) respectively. In Fig. 4.8 it was seen that there is strong production of the ρ^0 and f^0 mesons with perhaps some g^0 production at $M(\pi^+\pi^-) \sim 1.6$ GeV/c^2. In Fig. 4.11(a) the mass plot of $M(\pi^-p)$ shows no evidence for a resonance in this combination. There is a similar lack of evidence for signal in the $M(\pi^+p)$ combination of Fig. 4.11(b).

4.7.1 The Variables Used in the Analysis

It was decided to use precisely the same variables as in the Pless analysis. These are the kinetic energies T_1 and T_2 of two of the three secondary particles in the centre of mass system of the 3 secondaries, the Van Hove angle ω and the Van Hove radius r. Strictly, because the channel arises in a π^+d reaction where the centre of mass energy varies in this case by approximately 10%, corrections of this order should have been made to the radial parameter and by normalising it to the maximum radius allowed for each of the possible centre of mass energies. This would make the separation of the data slightly more acute than it is.

The number of final clusters to be obtained was chosen to be 10. This was based upon initial runs in which it was seen that a resonance such as the ρ^0 meson was associated mainly with 3 clusters corresponding to the forward, backward and central directions of the π^+ meson from the ρ^0 decay, in the resonance rest frame. Even with 15 clusters the main sub-channels were seen to be ρ^0 and f^0 production with perhaps some structure in the $(p\pi^-)$ mass combination at ~ 1.4 GeV/c^2. Allowing for the possibility of three structures and background, 10 clusters were regarded as sufficient.

Earlier analyses with threshold parameters, such as the minimum number of events in a cluster that must be reached before the cluster is accepted, or the largest similarity co-efficient that a data point may have with a cluster before it is considered not to be a part of that cluster, showed that they did not improve the significance of the results. Threshold parameters are therefore not used in this present analysis.

The 16,000 events were analysed in 2 runs of approximately 10,000 and 6,000 events each, in the 4-dimensional space of the variables T_1, T_2, ω and r. Two runs were necessary since the clustering programme, even in its modified form, handles a maximum of 10,000 events. As the events were read from the data summary tape they were allocated in strict numerical order to the initial clusters numbered 1 to 10. Hence the initial composition of cluster 1 was that of events 1, 11, 21, 31 etc. As the events occur in no particular order on the data summary tape then the initial allocation of events to clusters was completely random. At the start of the first cycle therefore, the clusters must have been very similar in shape and centroid value.

As CLUSTAN ran, the similarity co-efficient of each data point to each of the 10 clusters was calculated from the distribution of the shapes of the clusters in the vicinity of each data point, and a data point was reallocated to the cluster to which it was most similar. In this way the initial similarity of the clusters and their centroids was changed. After 28 iterations it was found that there was no further reallocation of data points to clusters and hence that a stable solution had been found.

4.7.2 General Results

Table 4.2 below shows the breakdown of the data from the point of view as to which of the mass combinations, if any, of $M(\pi^+\pi^-)$, $M(\pi^+p)$, $M(\pi^-p)$ that cluster contributes structure.

Table 4.2 Cluster Contents

Cluster:Number	$M(\pi^+\pi^-)$	$M(N\pi)$	Background	Comments
1 : 1576	f^0	-	-	backward π^+ decay
2 : 1511	ρ^0	-	-	central π^+ decay
3 : 3068	ρ^0	-	-	very forward π^+ decay
4 : 2749	f^0	-	-	forward π^+ decay
5 : 612	ρ^0, f^0	-	Yes	)small amounts of ρ^0,)f^0 with large back-)ground
6 : 819	ρ^0, f^0	-	Yes	
7 : 1178	g^0?	N?	-	See Text
8 : 1907	ρ^0	-	-	backward π^+ decay
9 : 2620	ρ^0	-	-	forward π^+ decay
10 : 657	-		Yes	background only

Cluster 1 is dominated by f^0 production and examination of the decay configuration shows that this group corresponds to the f^0 decaying with a backward π^+ meson in the f^0 rest system. Similarly cluster 4 is dominated by f^0 production with forward decay of the associated π^+ meson. Production of the ρ^0 meson dominates clusters 2, 3, 8 and 9 which correspond to central, very forward, backward and forward decay of the π^+ meson in the ρ^0 rest frame respectively. Background dominates the small clusters 5, 6 and 10 with some small mixture of ρ^0 and f^0 in clusters 5 and 6.

Finally, cluster 7 appears to demonstrate the production of the g^0 meson. By reference to the ρ^0 and f^0 production it is apparent that these are seen in clusters which correspond to forward and backward decays. However, for cluster 7 which can correspond to the forward decay direction of the π^+ from the g^0 meson, there is no corresponding cluster for backward decay. A much more acceptable interpretation is seen from the Van Hove plot of Fig. 4.13(b) in which it is seen that this cluster could correspond to the diffraction dissociation of the neutron target into $p\pi^-$. In terms of this explanation the $M(p\pi^-)$ distribution of cluster 7 peaks at $\sim$1.4 GeV/c^2.

4.7.3 The ρ^0 and f^0 signals

A Van Hove plot of the total sample of events is shown in Fig. 4.13(a) for comparison both with the signal extracted as cluster 7 (Fig. 4.13(b)) and with the plots associated with the discussion which follows.

It has been seen above that the clusters 1 and 4 are dominated by f^0 production and that the clusters 2, 3, 8 and 9

Fig. 4.13

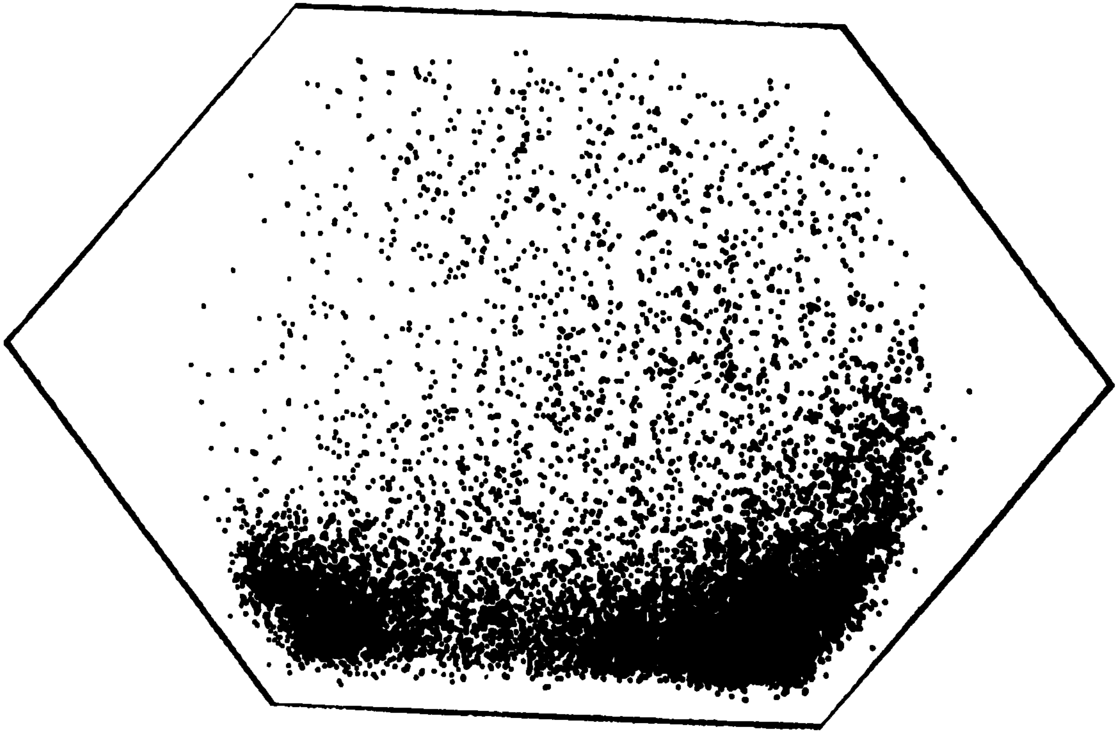

(a) Van-Hove Plot of total sample $\pi^+ d \rightarrow p_s p \pi^+ \pi^-$

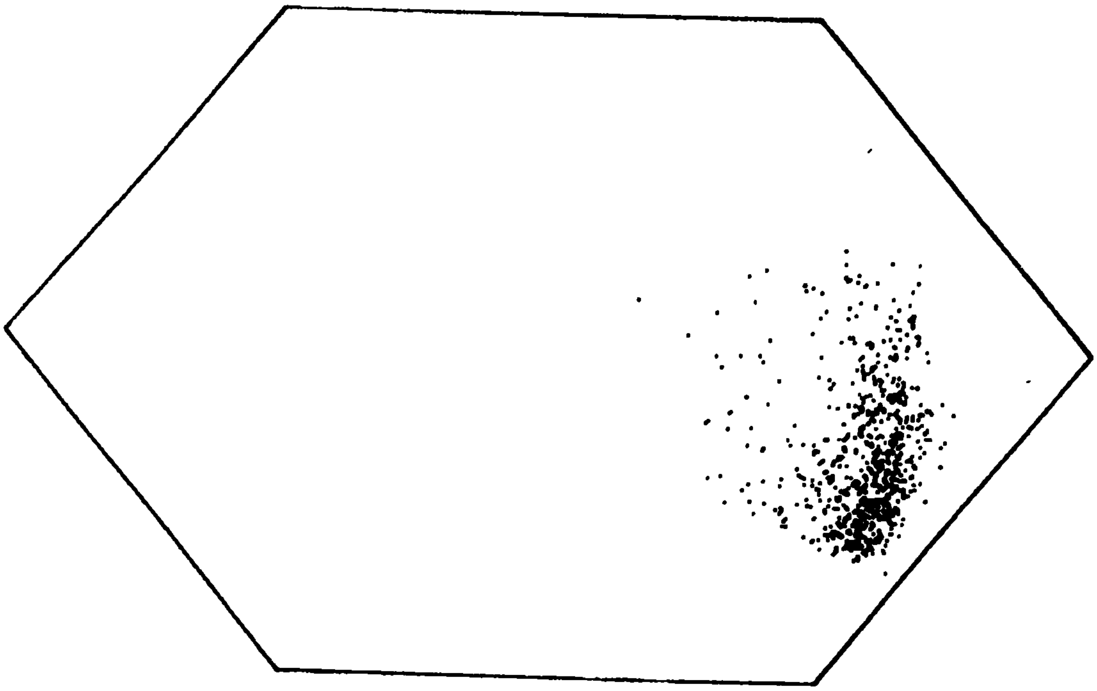

(b) Van-Hove Plot of signal extracted as Cluster 7.

are dominated by ρ^0 production. In these clusters there are 4325 f^0 events and 9106 ρ^0 events. In the mixed clusters 5 and 6 there are 612 and 819 events respectively, out of which about 100 events are estimated to be ρ^0 and f^0 by sketching in backgrounds to the $M(\pi\pi)$ distributions for these clusters. The loss of ρ^0 and f^0 events into clusters 5 and 6 is therefore less than 1% of the total signal. The fact that there is only a small amount of ρ^0 and f^0 signal in clusters 5 and 6 is supported by an examination of the decay angular distribution of these clusters which does not show the characteristic forward and backward peaks of ρ^0 or f^0 distributions.

In this analysis, therefore, only the dominant ρ^0 and f^0 clusters are used. Clusters 1 and 4 are combined and shown as a Van Hove plot of Fig. 4.14(a), and similarly the ρ^0 clusters 2, 3, 8 and 9 are combined in the Van Hove plot of Fig. 4.14(b). In both of these Figures, backwardly produced ρ^0 and f^0 mesons are to be seen but both are apparently decaying asymmetrically with the π^+ backwards in the ρ^0 and f^0 rest systems. The missing forward decays of these backwardly produced meson resonances are to be found in clusters 5 and 6 (which contain ρ^0, f^0 and background), but any analysis performed on the total sample would obviously be biased because of this loss and as a result, in the analysis of decay angular distributions, only dipion systems produced in the forward hemisphere of the overall centre of mass system have been included.

It is worthwhile to point out that simple cuts on the Van Hove sectors would not produce the same separation of data that is produced by the cluster analysis. For example, in the

Fig. 4.14

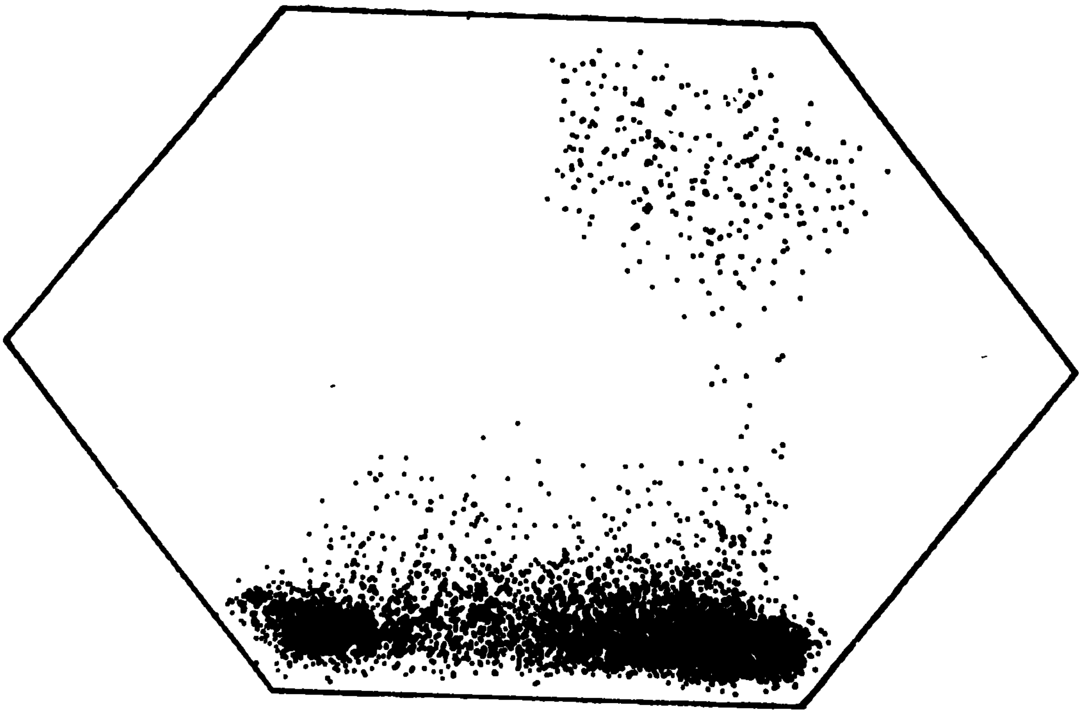

(a) Van-Hove Plot for signal extracted as ρ^0

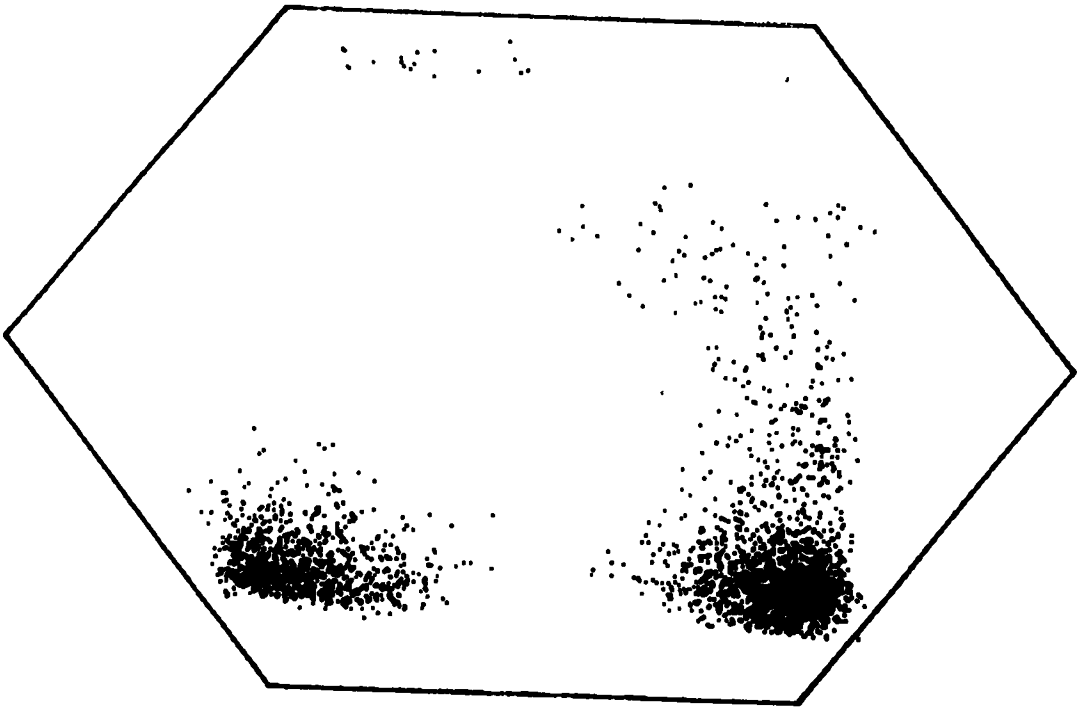

(b) Van-Hove Plot for signal extracted as f^0

reaction $\pi^+p \to p\pi^+\pi^0$ at 5 GeV/c, it was shown in the previous chapter that most of the ρ^0 signal could be extracted from the data by plotting only those dipion combinations falling in the π-π sector of the Van Hove plot. It is seen here in Fig. 4.14(a) at a lower energy, that a large part of the ρ^0 signal would be obtained in this way. However, refering to Fig. 4.14(b), it is evident that most of the f^0 signal would be lost.

Breit Wigner curves have been fitted to the dipion mass spectra shown in Figs. 4.15(a) and (b), that is for the ρ^0 and f^0 clustered samples respectively. The curves shown in these plots correspond to the Relativistic Jackson Breit Wigner function (Ref. 4.2)

$$BW(M) = \frac{\Gamma(m)}{(m^2-m_o^2)^2 + m_o^2\,\Gamma(m)^2} \cdot \frac{m}{q}$$

where $\Gamma(m) = \Gamma_o \left(\frac{q}{q_o}\right)^{2\ell+1}$ = the mass dependent width.

q = the momentum of a pion in the resonance rest frame, and the subscript 'o' corresponds to the parameter values at the central resonance mass.

These curves were fitted to the data together with a linear background. For the ρ^0 the fitted values of the central mass (M_o) and width Γ_o were:

$$M_o = 766 \pm 4 \quad \text{MeV/c}^2$$
$$\Gamma_o = 140 \pm 6 \quad \text{MeV/c}^2$$

For the fit to the f^0 meson sample the corresponding values are

$$M_o = 1265 \pm 5 \quad \text{MeV/c}^2$$
$$\Gamma_o = 120 \pm 5 \quad \text{MeV/c}^2$$

Fig. 4.15

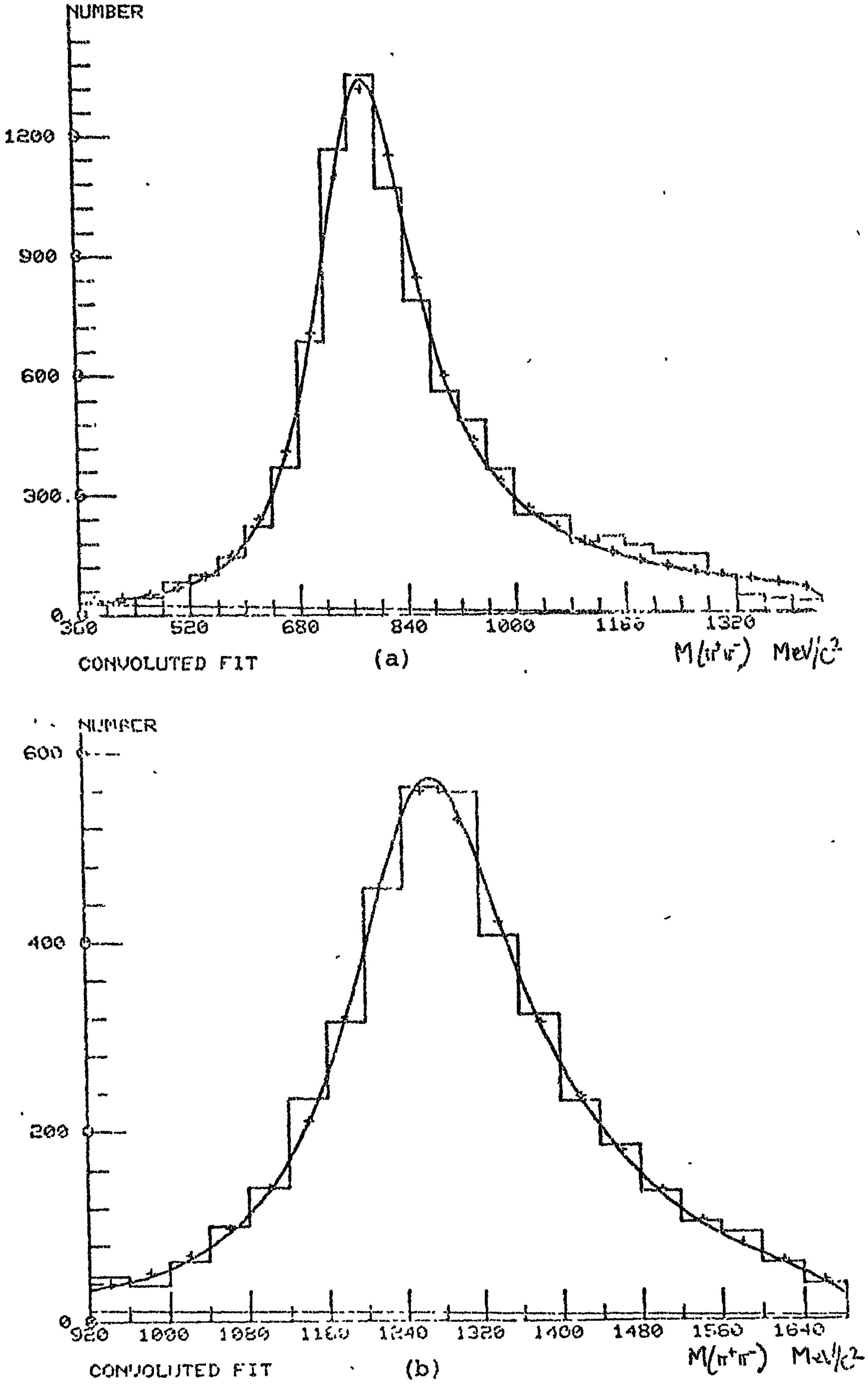

Relativistic Jackson Breit-Wigner fits, with linear background, to (a) the ρ^0 and (b) the f^0 signals extracted, by cluster analysis. Both fits are convoluted with Gaussian resolution functions.

In both the fitted background is very small.

Finally in Figs. 4.16(a) and (b) are shown the angular distributions of the π^+ meson in the Helicity reference frame of the clustered ρ^0 and f^0 mesons respectively. Both of these distributions are asymmetric, biased towards the forward decay direction of the π^+ meson, as was found previously in the analysis of the ρ^0 and f^0 mesons using mass cuts to define the regions of the signals. The distributions are very similar between the two methods of selection. If there is a difference then it is in the fact that the angular distributions extracted by the method of cluster searching are more sharp than those found by the earlier analysis. Indeed, this sharpness is a measure of the success of the cluster analysis since the decay angular distributions of the ρ^0 and f^0 mesons are sufficiently different that should there be much mixing of the ρ^0 and f^0 mesons in the clusters then the f^0 decay distribution should be considerably broadened and the ρ^0 distribution considerably sharpened.

4.7.4 Conclusions

It has been shown that in the channel $\pi^+n \rightarrow p\pi^+\pi^-$, very good separation of the ρ^0 and f^0 signals is possible by the method of cluster searching in the 4-dimensional space defined by the 3 particle final state of this interaction. The apparent g^0 signal is shown to be most likely due to diffraction dissociation of the neutron target, and from this point of view the $(p\pi^-)$ mass distribution shows structure at $M(p\pi^-) \sim 1.4$ GeV/c^2. The subchannels $\pi^+n \rightarrow p\rho^0$, and $\pi^+n \rightarrow pf^0$ account for 53% and 23% of the channel respectively and the

Fig. 4.16

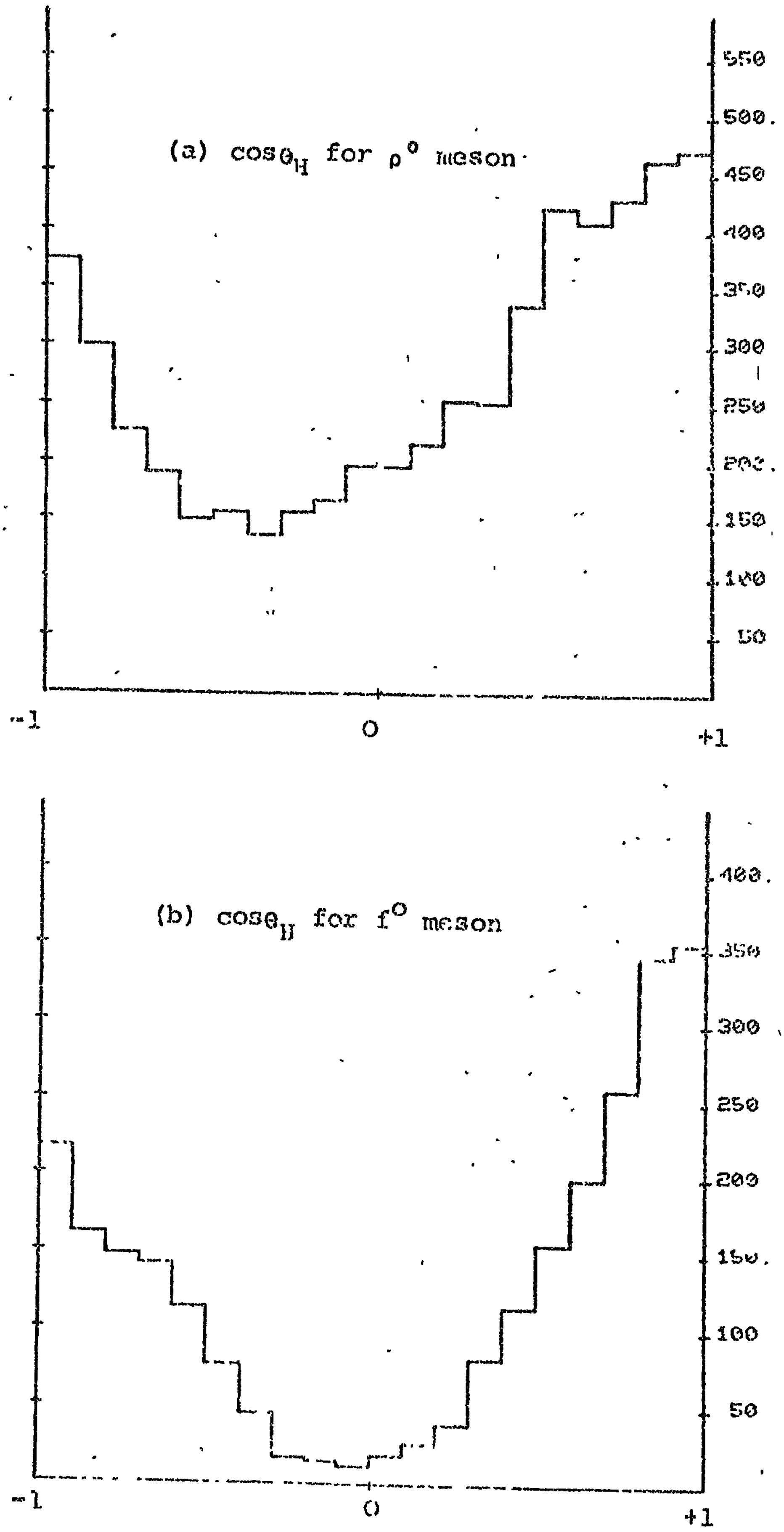

Decay angular distributions in the s-channel helicity frame for the ρ^0 and f^0 signals extracted by cluster analysis diffraction dissociation to 6%. In total 82% of the channel corresponds to precise physical processes.

Finally, it should be pointed out that the cluster analysis makes almost all of the ρ^o and f^o signal separately available for analysis whereas conventional mass cut techniques select only about one half of the available signal. This is seen in its correct context when it is realised that to obtain equivalent statistics to cluster analysis by using mass cut methods, as much film again would need to be exposed, scanned and measured.

Chapter 5 Density Matrix Element Analysis of the ρ^{0} and f^{0} Mesons

5.1 Introduction

A topic of particular interest in the study of neutral $\pi\pi$ systems is the spin structure in the region of the ρ^{0} and f^{0} mesons, and their production mechanisms in the π-N interaction. In recent years these spin structures have been examined very closely, and although the ρ^{0} and f^{0} mesons have been primarily thought of as having spin-parity $J^{P}=1^{-}$ and 2^{+} respectively, it has now become generally accepted that there is a substantial s-wave ($J^{P}=0^{+}$) component resonant near the ρ^{0} region, the ε^{0} meson. More recently, strong suggestions of a substantial s-wave state resonant close to the f^{0} mass have been made (Ref. 5.1).

A study of the production mechanisms of the ρ^{0} and f^{0} mesons involves the computation of their spin density matrix elements, $\rho_{mm'}$, and in this chapter these quantities are evaluated in both the s- and t-channel helicity frames. Throughout this analysis, the conventions used for the co-ordinate axes in the dipion rest frame are:

a) In the s-channel (Helicity frame), z is equal to the direction of the dipion system in the overall centre of mass transformed into the dipion rest frame.

b) In the t-channel (Gottfried-Jackson frame), z is the direction of the beam particle transformed into the dipion rest frame.

c) y is the direction $(\overrightarrow{\text{beam}}) \times (\overrightarrow{\text{outgoing dipion}})$ in both frames.

d) The decay angle θ is the angle between the outgoing positive pion and the z-axis, in the relevant reference frame.

The sample of data used in this analysis are the signals extracted from the channel $\pi^+ d \rightarrow p_s p \pi^+ \pi^-$ as the ρ^0 and f^0 mesons by the cluster searching technique described in Chapter 4 of this thesis. For the ρ^0 meson, the results obtained from the data are compared with the results from events generated, by the Monte-Carlo simulation programme FAKE, to simulate the experimental conditions found for one-pion exchange interactions. For both the ρ^0 and f^0 mesons the results obtained are compared with those found by using mass cut techniques to define the regions of these mesons.

5.2 The Density Matrix

For a pure spin state, the state vector of the system can be written as

$$\psi = \sum_m a_m \quad |j,m>$$

and the expectation value of any operator, Q, in this system is

$$<Q> = \sum_{m,k} a_m^* a_k \ <j,m\,|Q|\ j,k>$$

$$= \sum_{m,k} a_m^* \ a_k \ Q_{mk}$$

where $<j,m|Q|j,k> \equiv Q_{mk}$ is the matrix element of the operator Q.

For a statistical mixture of states ψ_i with probabilities p_i, the expectation value is

$$< Q > = \sum_i p_i <Q>_i = \sum_i p_i \quad \sum_{mk} a_m^{*(i)} \ a_k^{(i)} \ Q_{mk}$$

and the density matrix ρ is defined from this as

$$\rho_{mk} = \sum_i p^{(i)} \ a_m^{*(i)} \ a_k^{(i)}$$

such that $\langle Q \rangle$ can be written as

$$\langle Q \rangle = \sum_{m,k} \rho_{mk} Q^*_{km} = \sum_{m} (\rho Q^*) = T_r (\rho Q^*) \qquad (5.1)$$

The main properties of the density matrix $\rho_{mm'}$ are:

(i) It is Hermitian : $\rho_{mm'} = \rho^*_{m'm}$

(ii) It is an Unitary matrix : $T_r(\rho) = T_r(\rho^*) = 1$

(iii) Diagonal elements are real & positive: $\rho_{mm} \geq 0$

(iv) Parity conservation imposes : $\rho_{-m,-m'} = (-1)^{m-m'} \rho_{m,m'}$

For a spin 1 particle, the density matrix is

$$\rho(1) = \begin{bmatrix} \rho_{11} & \rho_{10} & \rho_{1-1} \\ \rho^*_{10} & \rho_{00} & -\rho^*_{10} \\ \rho_{1-1} & -\rho_{10} & \rho_{11} \end{bmatrix}$$

In order to express the decay angular distribution in terms of the density matrix elements, the decay matrix elements $A_{mm'}(\theta, \phi)$ must firstly be evaluated since, using Eq. 5.1, the decay angular distribution is

$$W(\theta,\phi) = \sum_{mm'} (\rho_{mm'} A_{mm'} (\theta, \phi)) = T_r(\rho A^*) \qquad (5.2)$$

It can be shown (Ref. 5.2) that for a particle of spin 1 decaying into two spin zero particles ($\rho^0 \rightarrow \pi^+ \pi^-$)

$$A_{mm'}(\theta, \phi) = \frac{3}{4\pi} D^{s*}_{m\lambda} D^{s}_{m'\lambda} \qquad (5.3)$$

where the D functions are rotation matrices.

From equations (5.2) and (5.3), the expression for the angular distribution in terms of the production density matrix elements $\rho_{mm'}$ may be derived. In order to evaluate the individual matrix elements, the method of moments has been used and this is explained in the next section.

5.2.1 The method of moments

One method of determining experimentally the values of the density matrix elements is the method of moments. The decay angular distribution of a resonance, from Eq. (5.2), may be written

$$W(\cos\theta, \phi) = \sum_{mm'} \rho_{mm'} f_{mm'} (\cos\theta, \phi) \qquad (5.4)$$

and the $f_{mm'}(\cos\theta, \phi)$ are known functions.

The average value $\bar{f}$ of a function $f(\cos\theta, \phi)$ of the decay angles θ and ϕ is given by

$$\bar{f} = \int_0^{2\pi} d\phi \int_{-1}^{+1} d\cos\theta \, f(\cos\theta, \phi) \; W(\cos\theta, \phi) \qquad (5.5)$$

since $W(\cos\theta, \phi)$ is normalised, i.e.

$$\int_0^{2\pi} d\phi \int_{-1}^{+1} d\cos\theta \, W(\cos\theta, \phi) = 1 \qquad (5.6)$$

The decay distribution for a particle of spin 1 decaying into 2 spin zero particles is given by

$$W(\cos\theta, \phi) = \frac{3}{4\pi} \{ \tfrac{1}{2}(1-\rho_{00}) + \tfrac{1}{2}(3\rho_{00}-1) \cos^2\theta - \rho_{1-1} \sin^2\theta$$

$$\cos 2\theta - \sqrt{2} \, \mathrm{Re} \, \rho_{10} \sin 2\theta \cos\phi \} \qquad (5.7)$$

Now, by inserting (5.7) into (5.5) for the functions f of $\cos^2\theta$, $\sin^2\theta \cos 2\phi$ and $\sin 2\theta \cos\phi$, the results are

$$\overline{\cos^2\theta} = \frac{1}{5} (1 + 2\rho_{00})$$

$$\overline{\sin^2\theta \cos 2\phi} = -\frac{4}{5} \rho_{1-1} \qquad (5.8)$$

$$\overline{\sin 2\theta \cos\phi} = -\frac{4\sqrt{2}}{5} \mathrm{Re} \, \rho_{10}$$

and hence from the experimental values for the averages on the L.H.S. of Eq. 5.8, the values of the density matrix elements ρ_{00}, ρ_{1-1} and Re ρ_{10} can be found. The error $\Delta\bar{f}$ on $\bar{f}$ is given by

$$\Delta\bar{f} = \sqrt{\frac{1}{n}\left(\overline{f^2} - \bar{f}^2\right)}$$

where n is the number of events.

5.3 The ρ^0 meson

The ρ^0 meson (Mass = 770 ± 10, Γ = 150 ± 10 MeV/c^2) is well known as having spin 1 and odd parity ($J^P = 1^-$). In the reaction $\pi^+n \to p\,\pi^+\pi^-$, the possible exchange trajectories for ρ^0 production are those of the π and the A_2 mesons. In terms of the production density matrix elements the decay distribution for the ρ^0 meson is given above in Eq. (5.7). The density matrix condition of trace unity imposes

$$\rho_{00} + 2\rho_{11} = 1 \qquad (5.9)$$

In Figs. 5.1(a) and 5.1(b) are shown the distributions of the decay angle cos θ for the s- and t-channel reference frames respectively. As can be seen from these distributions, the ρ^0 decay angular distribution is asymmetric. Defining the asymmetry parameter η as

$$\eta = \frac{F-B}{F+B} \qquad (5.10)$$

where F = no. of events with cos $\theta \geq 0$

B = no. of events with cos $\theta < 0$

η is found to be 0.31 ± 0.04. This asymmetry can be explained in terms of an interfering resonance in the ρ^0 region, the ε^0, with quantum numbers $I^G J^P = 0^+0^+$. In order that the ρ^0 production mechanism may be studied, taking into

Fig. 5.1

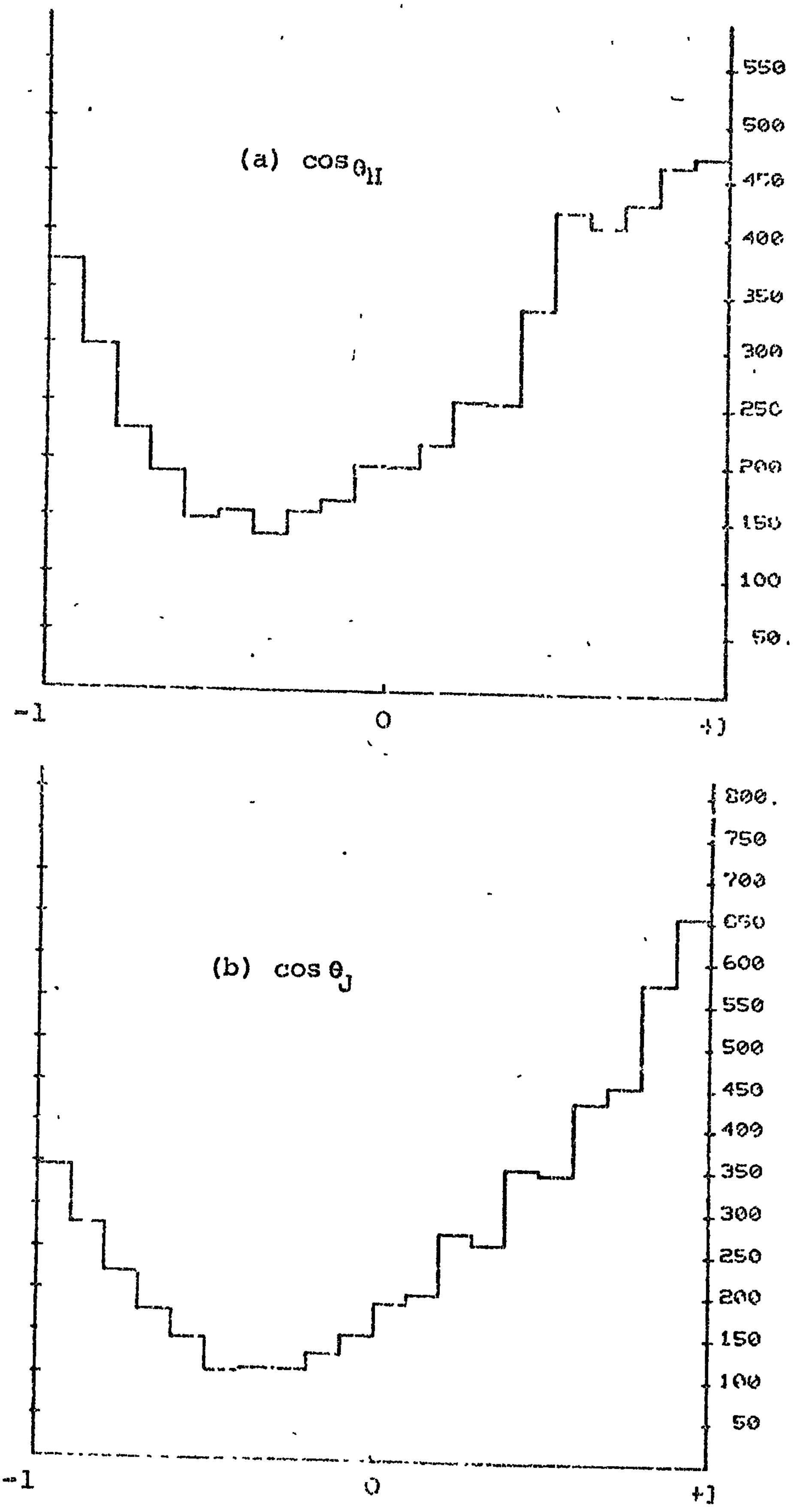

Decay angular distributions in (a) Helicity and (b) Jackson frames for the ρ^0 data extracted by cluster analysis for $\pi^+ d \to p_s p \pi^+ \pi^-$ at 4 GeV/c.

account the presence of this S-P interference, the decay angular distribution must be re-written as

$$W(\theta,\phi) = \Bigg\{ \frac{3}{4\pi} \Bigg[\rho^{11}_{00} \cos^2\theta + \rho^{11}_{11} \sin^2\theta - \sqrt{2}\,\mathrm{Re}\,\rho^{11}_{10} \sin 2\theta \cos\phi - \rho^{11}_{1-1} \sin^2\theta \cos 2\phi \Bigg] + \frac{\sqrt{3}}{4\pi} \Bigg[-2\sqrt{2}\,\mathrm{Re}\,\rho^{10}_{10} \sin\theta \cos\phi + 2\,\mathrm{Re}\,\rho^{10}_{00} \cos\theta \Bigg] + \frac{1}{4\pi} \rho^{00}_{00} \Bigg\} \qquad (5.11)$$

In this case the density matrix condition of trace unity, due to unitarity, imposes

$$\rho^{11}_{00} + 2\rho^{11}_{11} + \rho^{00}_{00} = 1 \qquad (5.12)$$

where, in Eqs. 5.11 and 5.12, the superscripts indicate the spin to which the density matrix element is associated, that is $\rho^{11}_{mm'} \equiv$ pure P wave, $\rho^{10}_{mm'} \equiv$ S-P interference and $\rho^{00}_{mm'}$ = pure S-wave.

Using Equation 5.11, the values of the ρ^0 density matrix elements have been calculated, together with their errors, by the method of moments as described in section 5.2.1. The average values of the density matrix elements for both the s- and t-channels are given in Tables 5.1 and 5.2 respectively, and also given in these tables is the variation of the density matrix elements with t, the four momentum transfer squared from the beam particle to the $\pi\pi$ system. The density matrix elements in these tables are shown in graphical form in Figs. 5.2 and 5.3, again for the s- and t-channel reference frames respectively. Also shown in these figures are the decay angular distributions of $\cos\theta$ and ϕ, and the predictions of these quantities from the evaluation of the density matrix elements by integrating Eq. 5.11 over $\cos\theta$ or ϕ.

Table 5.1 s-channel ρ^0 Density Matrix Elements

t-range $(\mathrm{GeV}/c)^2$	Number	DENSITY MATRIX ELEMENTS				
		$\rho^{11}_{00} - \rho^{11}_{11}$	ρ^{11}_{1-1}	ρ^{11}_{10}	ρ^{10}_{00}	ρ^{10}_{10}
ALL	4161	0.33 ± 0.03	−0.03 ± 0.01	0.12 ± 0.01	0.12 ± 0.01	0.06 ± 0.01
0.0 − 0.025	308	0.77 ± 0.08	0.01 ± 0.02	0.0 ± 0.03	0.28 ± 0.03	0.0 ± 0.02
0.025 − 0.05	698	0.65 ± 0.06	0.03 ± 0.02	0.05 ± 0.03	0.20 ± 0.02	0.01 ± 0.01
0.05 − 0.075	553	0.53 ± 0.07	−0.01 ± 0.02	0.11 ± 0.02	0.16 ± 0.02	0.06 ± 0.01
0.075 − 0.10	401	0.45 ± 0.08	0.02 ± 0.03	0.16 ± 0.02	0.17 ± 0.03	0.06 ± 0.02
0.10 − 0.125	348	0.48 ± 0.09	−0.04 ± 0.03	0.25 ± 0.02	0.17 ± 0.03	0.08 ± 0.02
0.125 − 0.15	264	0.27 ± 0.11	−0.04 ± 0.04	0.22 ± 0.03	0.19 ± 0.03	0.06 ± 0.02
0.15 − 0.20	335	0.20 ± 0.10	−0.05 ± 0.03	0.25 ± 0.02	0.12 ± 0.03	0.07 ± 0.02
0.20 − 0.30	380	0.14 ± 0.09	−0.12 ± 0.03	0.23 ± 0.02	0.13 ± 0.03	0.07 ± 0.02
0.30 − 0.45	225	−0.12 ± 0.13	−0.15 ± 0.04	0.15 ± 0.03	0.06 ± 0.03	0.07 ± 0.03
0.45 − 0.70	200	−0.19 ± 0.14	−0.08 ± 0.05	0.12 ± 0.03	0.07 ± 0.03	−0.02 ± 0.03
0.70 − 1.00	218	−0.23 ± 0.15	0.02 ± 0.05	0.05 ± 0.03	−0.07 ± 0.03	0.13 ± 0.02
>1.0	231	−0.08 ± 0.14	−0.08 ± 0.05	−0.14 ± 0.03	−0.37 ± 0.02	0.22 ± 0.02

Fig. 5.2 S-CHANNEL ρ^0 DENSITY MATRIX ELEMENTS AND DECAY ANGULAR DISTRIBUTIONS FOR REACTION $\pi^+ d \rightarrow pp\rho^0$

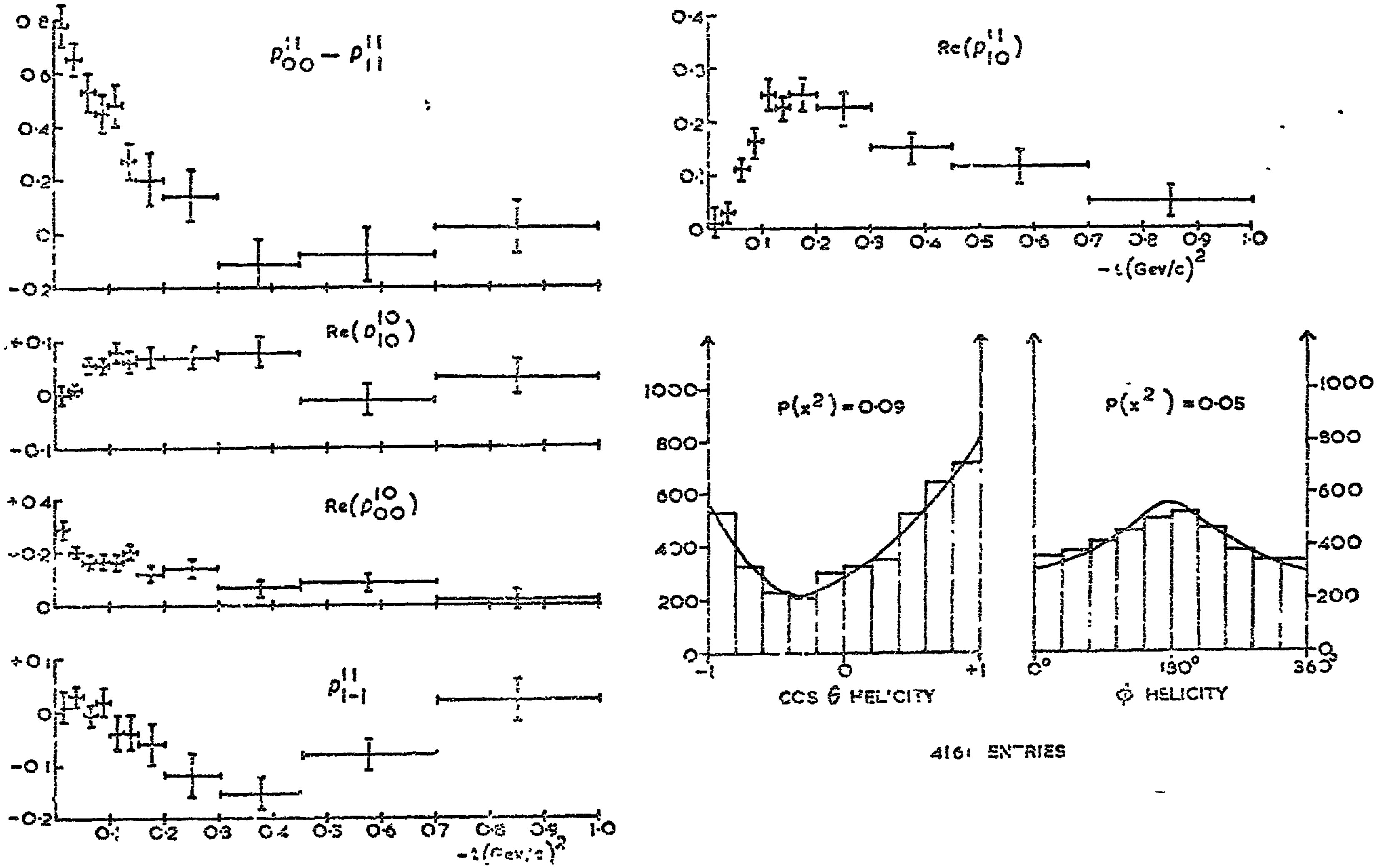

Table 5.2 t-channel ρ^{o} Density Matrix Elements

		DENSITY MATRIX ELEMENTS				
t-range $(GeV/c)^2$	Number	$\rho^{11}_{oo} - \rho^{11}_{11}$	ρ^{11}_{1-1}	ρ^{11}_{10}	ρ^{10}_{oo}	ρ^{10}_{10}
ALL	4161	0.46 ± 0.03	0.01 ± 0.01	−0.13 ± 0.01	0.18 ± 0.01	−0.05 ± 0.01
0.0 − 0.025	308	0.66 ± 0.08	−0.03 ± 0.03	−0.14 ± 0.03	0.25 ± 0.03	−0.06 ± 0.02
0.025 − 0.05	698	0.54 ± 0.06	−0.01 ± 0.02	−0.14 ± 0.02	0.17 ± 0.02	−0.06 ± 0.01
0.05 − 0.075	553	0.48 ± 0.07	−0.02 ± 0.02	−0.13 ± 0.02	0.17 ± 0.02	−0.03 ± 0.01
0.075 − 0.10	401	0.47 ± 0.08	0.03 ± 0.03	−0.15 ± 0.02	0.18 ± 0.03	−0.04 ± 0.02
0.10 − 0.125	348	0.64 ± 0.09	0.01 ± 0.03	−0.16 ± 0.02	0.19 ± 0.03	−0.04 ± 0.02
0.125 − 0.15	264	0.48 ± 0.10	0.04 ± 0.03	−0.10 ± 0.03	0.18 ± 0.03	−0.07 ± 0.02
0.15 − 0.20	335	0.52 ± 0.09	0.04 ± 0.03	−0.13 ± 0.03	0.14 ± 0.03	−0.05 ± 0.02
0.20 − 0.30	380	0.46 ± 0.08	−0.02 ± 0.03	−0.14 ± 0.02	0.14 ± 0.03	−0.05 ± 0.02
0.30 − 0.45	225	0.42 ± 0.11	0.03 ± 0.04	−0.07 ± 0.03	0.11 ± 0.04	−0.03 ± 0.02
0.45 − 0.70	200	0.17 ± 0.13	0.05 ± 0.04	−0.07 ± 0.03	−0.04 ± 0.04	−0.05 ± 0.02
0.70 − 1.00	218	−0.02 ± 0.14	0.10 ± 0.05	−0.07 ± 0.03	0.20 ± 0.03	0.01 ± 0.02
>1.0	231	0.26 ± 0.12	0.03 ± 0.04	−0.13 ± 0.03	0.48 ± 0.02	−0.11 ± 0.02

Fig. 5.3 t-CHANNEL ρ^0 DENSITY MATRIX ELEMENTS AND DECAY ANGULAR DISTRIBUTIONS FOR REACTION $\pi^+ d \rightarrow p p \rho^0$

4161 ENTRIES

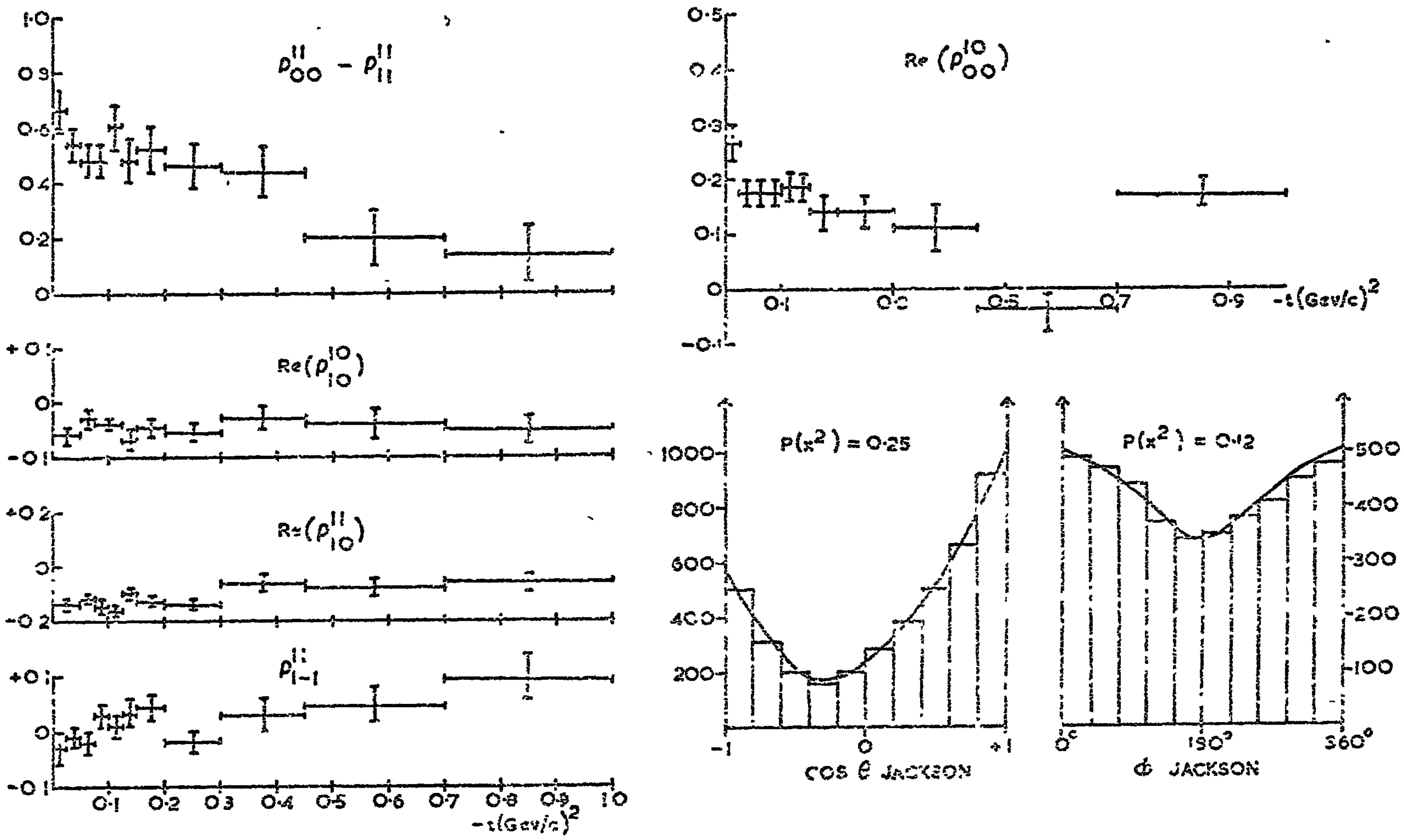

These distributions are those for all t, such that the superimposed curves are those obtained from the average values of the density matrix elements. As can be seen from these figures the agreement between the data and the calculation is quite satisfactory, implying that the extracted values of the density matrix elements are reliable.

One difficulty which is encountered in this type of analysis is that the number of observables (the co-efficients of the spherical harmonic expansion of the $\pi\pi$ decay angular distribution) are not sufficient to determine independently all the real parts of the mixed spin density matrix i.e. all the diagonal elements. As can be seen from the Tables 5.1 and 5.2, ρ^{11}_{00} and ρ^{11}_{11} are determined only in linear combination, and not independently. This difficulty can also be readily appreciated on examination of Eq. 5.4 from which, after extracting terms in ρ^{11}_{00} and ρ^{11}_{11} the result is

$$W(\theta,\ \rho_{00},\ \rho_{11}) = \frac{3}{4\pi}\left[\cos^2\theta\,(\rho^{11}_{00}-\rho^{11}_{11}) + \rho^{11}_{11}\right] - \frac{1}{4\pi}\left[\rho^{11}_{00} + 2\,\rho^{11}_{11}\right] \qquad (5.13)$$

and from which by the method of moments $\overline{\cos^2\theta}$ yields only the linear combination of density matrix elements $\rho^{11}_{00} - \rho^{11}_{11}$.

Recently, attempts have been made to form an analysis in which the real elements of the density matrix can be extracted separately. For example, Estabrooks and Martin (Ref. 5.3) have assumed that exchanges with quantum numbers of the A1 meson are negligible. These assumptions reduce the equations to a soluble set: however these analyses are only valid at very small momentum transfers, $t<0.1\ (\mathrm{GeV}/c)^2$. The distribution of momentum transfer from the beam to the dipion system is shown in Fig. 5.4 and, as can be seen, this distribution extends well above the value of $t = 0.1\ (\mathrm{GeV}/c)^2$. As a result of this, no attempt has been made here to carry out an Estabrooks and Martin analysis throughout the t range. However an analysis is presented, which is based upon the considerations of helicity amplitudes to estimate the contributions of ρ^{11}_{00} and ρ^{11}_{11} at small values of t.

In the discussion which follows the fact is used that in the asymptotic limit of s/t (s is the centre of mass energy squared), the natural and unnatural parity exchange components in the production of a final state of spin J helicity λ, $|J, \lambda\rangle$, can be written as

$$\left(\begin{smallmatrix}N\\U\end{smallmatrix}\right)^{J}_{\lambda} = \rho^{JJ}_{\lambda\lambda} \mp (-1)^{\lambda}\, \rho^{JJ}_{\lambda-\lambda} \tag{5.14}$$

5.4 Discussion of the ρ^0 density matrix elements

Information relating to the exchange particles in the s-channel reaction $\pi^+ n\to p\rho^0$ may be extracted by an analysis of the t-channel density matrix elements. In the corresponding t-channel reaction $n\bar{p}\to X\to\rho^0\pi^-$, X is the exchange particle in the s-channel reaction. For the s-channel itself, $\pi^+ n\to Y\to p\rho^0$, the information on the isobaric states Y can be extracted from the s-channel density matrix elements. The relationship between the s-channel physical interaction and the t-channel reaction occurs through the analyticity of the reaction amplitude and crossing symmetry (see Appendix A).

Fig. 5.4

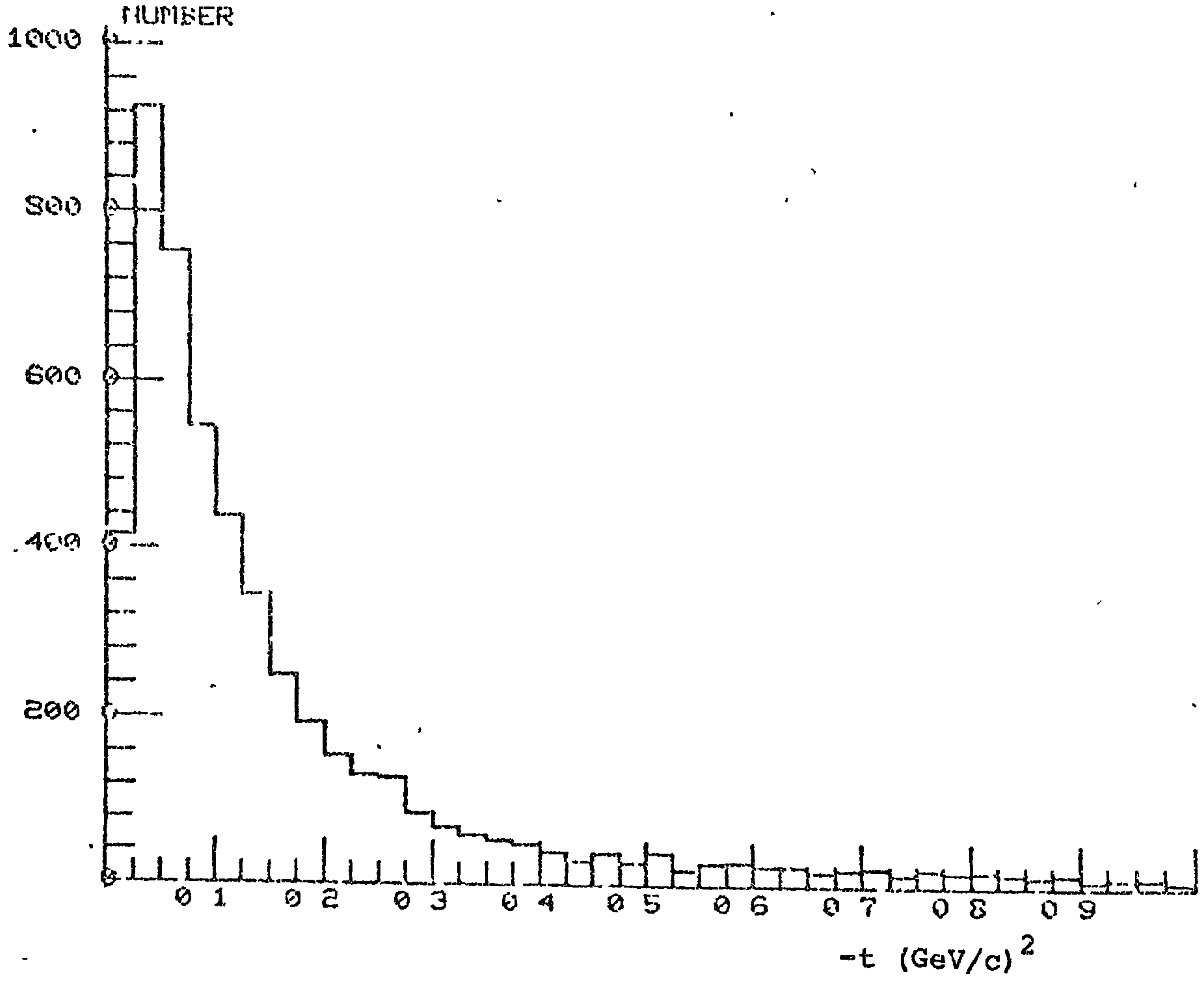

Momentum transfer distribution for the ρ^0 mesons extracted by cluster analysis for 4 GeV/c $\pi^+d \to p_s p \pi^+ \pi^-$.

The most relevant information on the reaction $\pi^+n\rightarrow p\rho^0$, apart from the analysis of the properties of the ρ^0 meson itself, is the information on the exchanges involved. Thus the broad part of this discussion is related to the t-channel density matrix elements, and unless stated otherwise these are the elements being considered.

For comparison with the experimental data, shown in Figs. 5.5 and 5.6 are the density matrix elements in the s- and t-channel helicity frames respectively for 2000 events generated using the Monte-Carlo simulation programme FAKE. The events generated were of the type $\pi^+n\rightarrow p\rho^0$, where the ρ^0 meson was generated with a t'-distribution from the beam of the form:

$$\frac{dN}{dt'} \propto e^{-10t'} \quad \text{where } t' = t-t_{min}$$

and a decay distribution in the helicity frame of

$$\frac{dN}{d(\cos\theta)} = 0.9\cos^2\theta + 0.1$$

The events were generated with the above parameters so as to simulate the distributions expected from a one pion exchange mechanism.

The immediate conclusion drawn from a comparison of Figs. 5.3 and 5.6 is that, except at the small values of momentum transfer $t<0.075$ $(GeV/c)^2$, the experimental distributions are not compatible with those expected from a simple one-pion exchange model.

In the experimental data the density matrix element ρ^{11}_{1-1}, which is determined uniquely from the method of moments, is negative over the $|t|$ range 0.0 to 0.75$(GeV/c)^2$ and is

Fig. 5.5 S-CHANNEL ρ^0 DENSITY MATRIX ELEMENTS FOR FAKED EVENTS $\pi^+ N \longrightarrow P\rho^0$

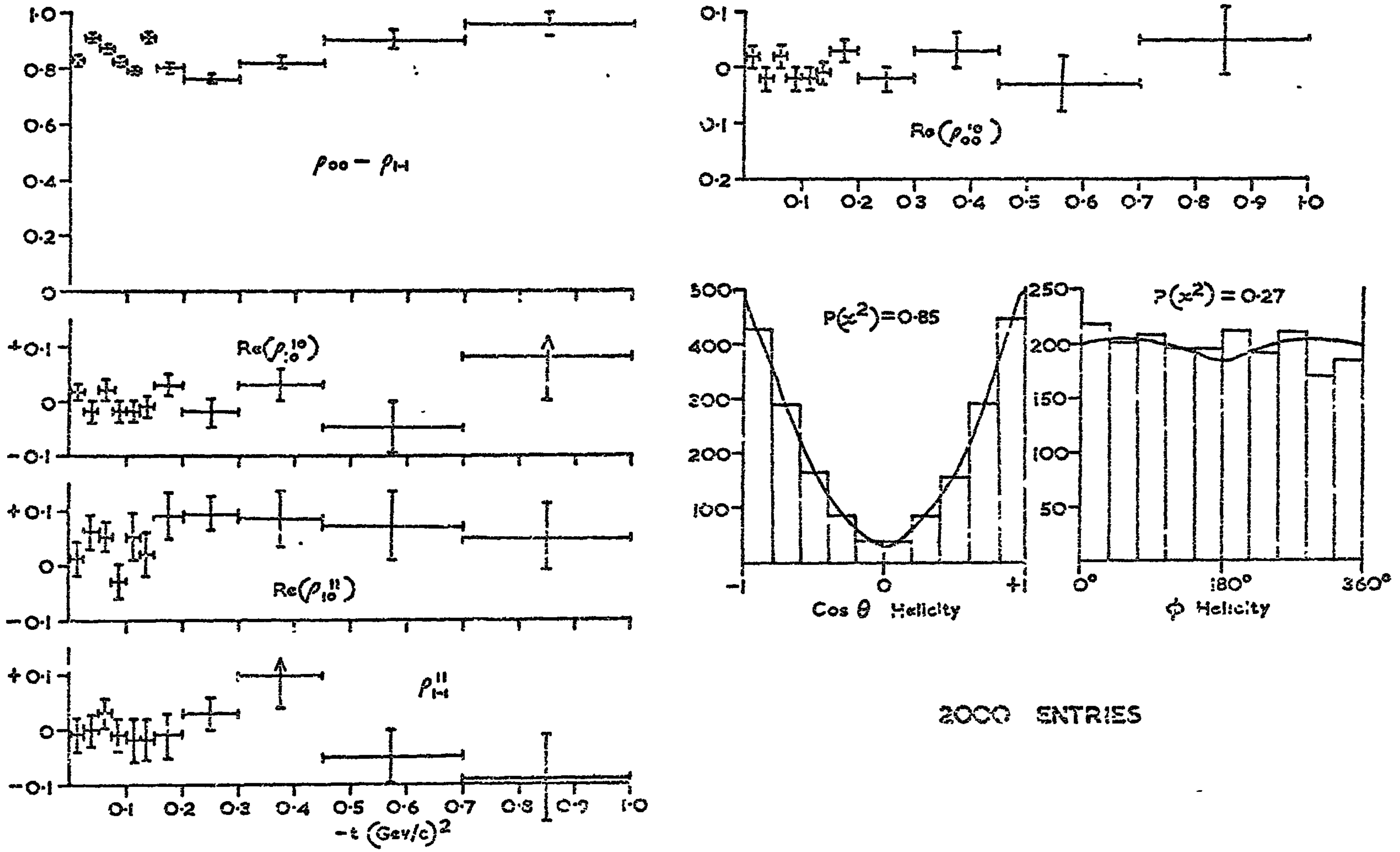

Fig. 5.6 t-CHANNEL ρ^0 DENSITY MATRIX ELEMENTS FOR FAKED EVENTS $\pi^+N \longrightarrow P\rho^0$—2000 EVENTS.

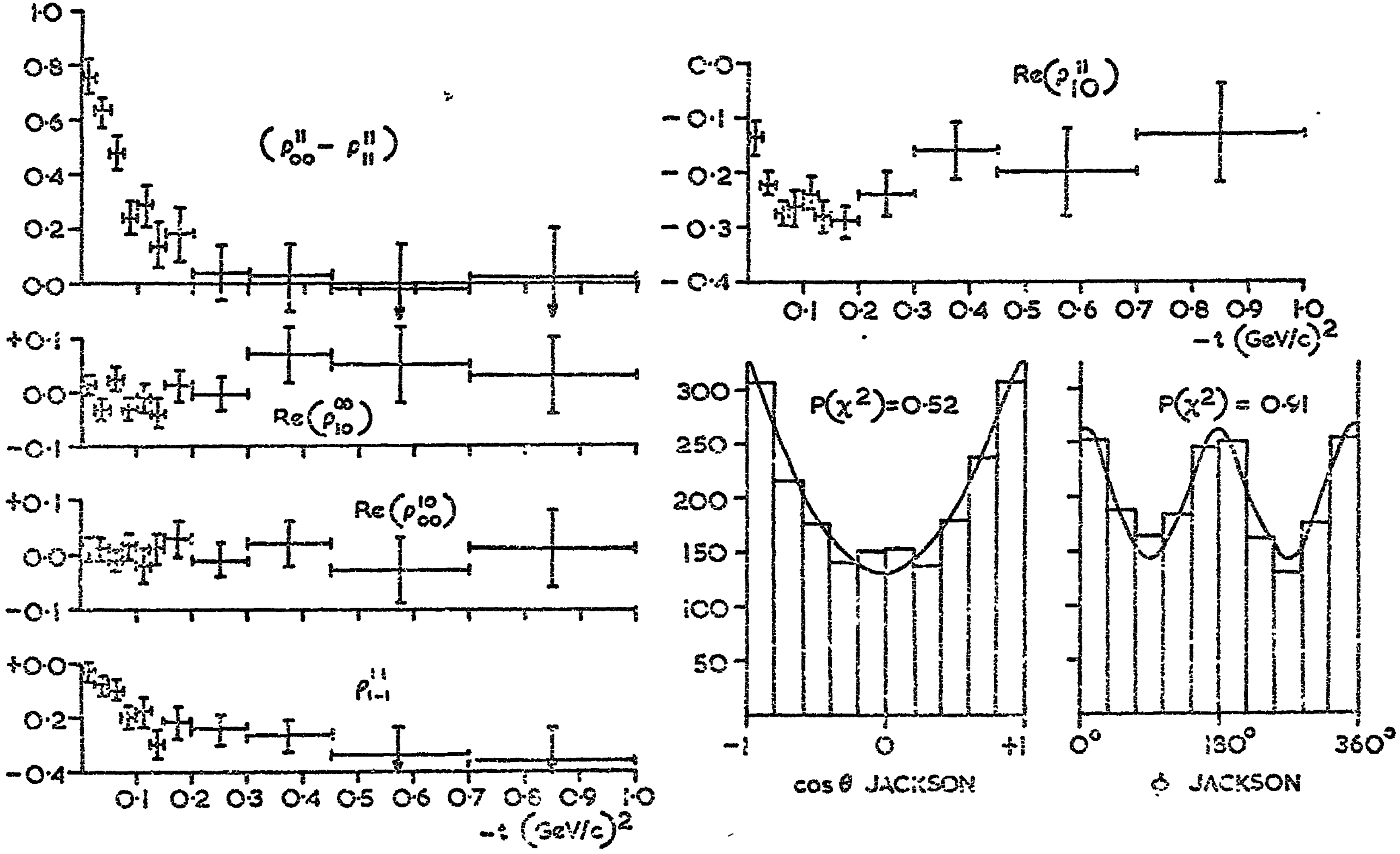

either negative or zero over the $|t|$ range 0.0 to 0.6 $(\mathrm{GeV}/c)^2$. These facts alone are sufficient to conclude that, from Eq. 5.14

$$U_1^1 > N_1^1 \quad \text{for} \quad 0.0 \leqslant |t| \leqslant 0.075\ (\mathrm{GeV}/c)^2$$

$$U_1^1 \sim N_1^1 \quad \text{for} \quad 0.075 < |t| \leqslant 0.6\ (\mathrm{GeV}/c)^2$$

$$U_1^1 < N_1^1 \quad \text{for} \quad |t| > 0.6\ (\mathrm{GeV}/c)^2$$

That is, the unnatural parity exchange component, pion exchange can be said to dominate only at very small values of $|t|$. The effect of the A_2 pole (natural parity exchange) can only be said to dominate for values of $|t|$ greater than 0.6 $(\mathrm{GeV}/c)^2$.

In order to investigate further the amount of pion exchange present in the experimental data, it is necessary to expand the density matrix elements in terms of their associated helicity amplitudes. If there were no ε^0 interference in the region of the ρ^0 meson then the element ρ_{00}^{11} is predicted to take the value unity for interactions proceeding by one pion exchange. However, with the effects of ε^0 interference the equivalent value for ρ_{00}^{11} for one pion exchange is the maximum allowed from the trace condition of Eq. 5.12, that is

$$\rho_{00}^{11}\ (\max) = 1 - \rho_{00}^{00} \qquad (5.15)$$

In the momentum transfer interval $t_{\min} \leqslant |t| \leqslant 0.025$, the values obtained for the density matrix elements $(\rho_{00}^{11} - \rho_{11}^{11})$, $\mathrm{Re}(\rho_{10}^{11})$ and ρ_{1-1} are 0.657, -0.137 and -0.030 respectively. If the assumption is made that in this small region of t either the spin flip or the spin non-flip amplitudes are negligible, the spin non-flip amplitudes being zero for pion exchange, then it is possible to extract from these elements the values of ρ^{11}_{00} and ρ^{11}_{11} separately. This leads to an assessment both of the pion exchange component in this region and the amount of interfering s-wave that is present.

Expanding the state in helicity amplitudes for the p-wave gives

$$\left.\begin{aligned} |\rho, p=+\tfrac{1}{2}\rangle &= A_0|0\rangle + A_1 e^{i\phi_+}|1\rangle + A_1 e^{i\phi_-}|-1\rangle \\ |\rho, p=-\tfrac{1}{2}\rangle &= A_0|0\rangle - A_1 e^{i\phi_-}|1\rangle - A_1 e^{i\phi_+}|-1\rangle \end{aligned}\right. \qquad (5.16)$$

where A_0, A_1 are the amplitudes; ϕ_+ and ϕ_- are phase angles with respect to the helicity zero amplitude and the $p=\pm\frac{1}{2}$ refers to the helicity state of the recoil proton. The negative signs of the $p=-\frac{1}{2}$ state are due to parity conservation, and the relationships between the amplitudes and the density matrix elements are

$$\left.\begin{aligned} \rho^{11}_{00} &= |A_0|^2 \\ \rho^{11}_{11} &= |A_1|^2 \\ \mathrm{Re}(\rho^{11}_{10}) &= \tfrac{1}{2} A_0 A_1 (\cos\phi_+ - \cos\phi_-) \\ \rho^{11}_{1-1} &= A_1^2 \cos(\phi_+ - \phi_-) \end{aligned}\right\} \qquad (5.17)$$

The equations 5.17 together with the trace condition of Eq. 5.12 are sufficient to solve for ρ^{11}_{00} and ρ^{11}_{11} independently. In fact, there are two solutions but for one of them the value of the density matrix element ρ^{00}_{00} is zero which is obviously not the case since the decay angular distribution of the ρ^0 meson is asymmetric. The values obtained for the elements ρ_{00}^{11}, ρ_{11}^{11} and ρ_{00}^{00} are

$$\rho_{00}^{11} = 0.69$$

$$\rho_{11}^{11} = 0.03$$

$$\rho_{00}^{00} = 0.25$$

Thus from eq. 5.15 the value of the density matrix element ρ_{00}^{11} is very close (92%) to that expected for simple one pion exchange. The value of ρ_{00}^{00} of 0.25 for this t region implies that $\frac{3}{4}$ of the produced state is P-wave and $\frac{1}{4}$ of the state is s-wave.

Using this method of evaluation of the density matrix elements enables solutions to be obtained for the values of ρ_{00}^{11} and ρ_{11}^{11} in the first 3 t bins of Table 5.2, that is the equations are soluble in the momentum transfer interval $0.0 \leq |t| \leq 0.075$, which contains 40% of the ρ^0 meson data. Above this region of t the assumption that the amplitudes corresponding to spin non-flip are negligible is not consistent with the extracted values of the pure pion exchange component, and the equations are also no longer unambiguously soluble. Throughout the first 3 t-bins the phase angles ϕ_+ and ϕ_-, between the helicity zero and the helicity states +1 and -1 respectively, retain the constant relationship of $\phi_+ - \phi_- = 180^\circ$. Shown in Table 5.3 below are the values of the extracted density matrix elements, the proportion of P- and s-wave in the produced $\pi\pi$ state, and the estimation of the pion exchange component in the t range $0.0 \leq |t| \leq 0.075$.

Table 5.3 Extracted Values of the Density Matrix Elements ρ^{11}_{oo} and ρ^{11}_{11}

$t(GeV/c)^2$	ρ^{11}_{oo}	ρ^{11}_{11}	ρ^{oo}_{oo}	P-wave	S-wave	π-exchange
0.0-0.025	0.69	0.03	0.25	75%	25%	92%
0.025-0.050	0.56	0.02	0.40	60%	40%	93%
0.050-0.075	0.51	0.02	0.45	55%	55%	92%

An interesting feature of the ρ^0 density matrix elements, appearing in the distribution of $Re(\rho^{10}_{oo})$, is the pronounced dip at a t value of about 0.6 $(GeV/c)^2$. This effect is attributed to the presence of the Nonsense Wrong Signature Zero (NWSZ) point of the A_2 pole. The value of this NWSZ point is obtained by extrapolating back from the A_2 pole in the Regge trajectory diagram of $Re(\alpha(t))$ against mass squared. The value of t corresponding to $Re\ (\alpha(t)) = 1$ is $t = 0.69\ (GeV/c)^2$ for an extrapolation gradient of 0.5. The dip in the distribution of $Re(\rho^{10}_{oo})$ agrees adequately with the predicted value of the NWSZ which is calculated neglecting the natural width of the A_2-meson which is 100 ± 10 MeV/c^2.

In the s-channel helicity frame the element ρ^{11}_{1-1} is negative for $0.0 < |t| \leqslant 0.45$ implying that $U^1_1(s) > N^1_1(s)$ and supporting the conclusion that the exchange is predominantly of an unnatural parity state. The S-channel density matrix element $Re(\rho^{10}_{oo})$, which occurs as the co-efficient of $\cos\theta$ in the decay angular distribution of Eq. 5.11, shows a slow fall-off with t. This implies that the ρ^0 decay angular distribution becomes less asymmetric as t increases, a fact that is echoed in the t-channel distribution up to a value of $|t|$ of 0.7 $(\mathrm{GeV/c})^2$. Again, in the s-channel distributions, the experimental distributions are not compatible with those events generated by the programme FAKE except at very small values of momentum transfer, implying that a simple one pion exchange mechanism is inadequate in explaining the data above $|t| \sim 0.1\ (\mathrm{GeV/c})^2$.

5.5 The f^o meson

The f^o meson (Mass = 1270 ± 10, Γ = 170 ± 30 $\mathrm{MeV/c^2}$), is a well established resonant particle having spin 2 and even parity ($J^P = 2^+$). Shown in Figs. 5.7(a) and 5.7(b) are the distributions of the decay angle $\cos\theta$ in the s- and t-channel reference frames respectively for those events selected as f^o events by the cluster searching technique, the sample amounting to 4325 events.

Two remarks may be made immediately, concerning the spin structure of the f^o meson, upon inspection of the decay angular distributions of Figs. 5.7(a) and 5.7(b).

(i) There is an asymmetry in the angular distribution biased towards the forward π^+ decay configuration. For the t-channel distribution the asymmetry parameter η, as previously defined, is found to be $\eta = 0.24 \pm 0.04$. Although this is not such a marked effect as in the ρ^o decay angular distribution, the implication is that some interfering P-wave component must be present in the data.

(ii) The central peak expected in the decay of a 2^+ particle into two 0^- particles, when the 2^+ object has been produced by pion exchange, is absent. This effect

Fig. 5.7

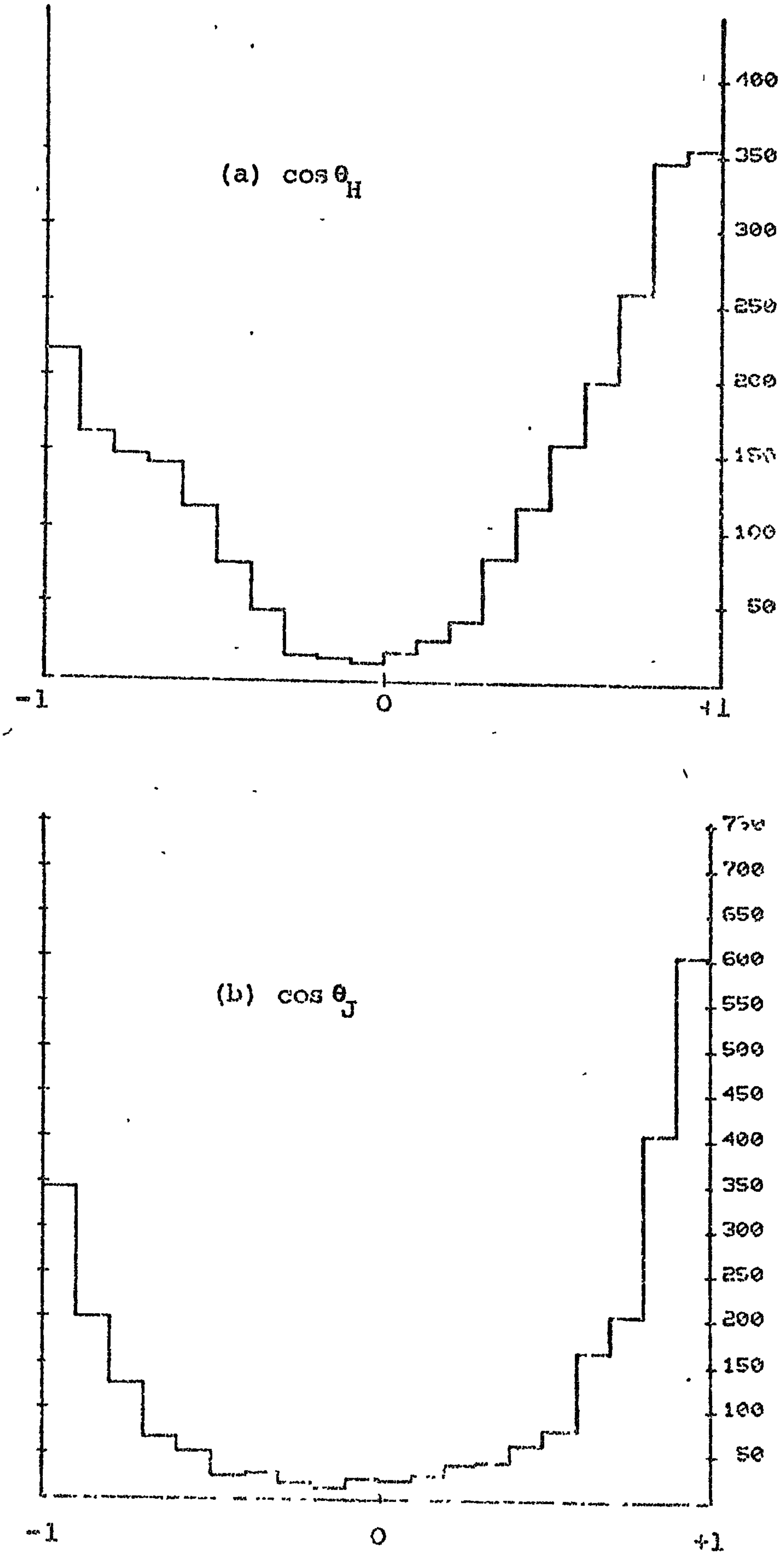

Decay angular distributions in (a) Helicity and (b) Jackson frames for the f^0 cluster extracted data for $\pi^+ d \to p_s p \pi^+ \pi^-$, 4 GeV/c.

is attributed to the presence of an interfering s-wave component in the same mass region as the f^o meson. The lack of a central peak has been reported in many previous experiments, and although the general explanation is in terms of an interfering s-wave resonance it has recently been pointed out that the effect could also be explained by the presence of a p-wave component, either interfering or non-interfering.

The decay angular distribution $W(\theta,\phi)$ for the process $2^+ \to 0^- 0^-$ may be written in terms of the production density matrix elements as:

$$W(\theta,\phi) = \frac{15}{16\pi} \Big\{ \sin^4\theta \; (\rho_{22} + \rho_{2-2} \cos 4\phi) + \sin^2 2\theta \; (\rho_{11} - \rho_{1-1} \cos 2\phi)$$
$$+ 3\,\rho_{oo} (\cos^2\theta - \tfrac{1}{3})^2 - 4 \sin^3\theta \cos\theta \; (\mathrm{Re}(\rho_{21}) \cos\phi - \mathrm{Re}(\rho_{2-1}) \cos 3\phi)$$
$$+ \sqrt{\tfrac{2}{3}}\; \mathrm{Re}(\rho_{20}) \sin^2\theta (\cos^2\theta - \tfrac{1}{3}) \cos 2\phi + 2\sqrt{6}\; \mathrm{Re}(\rho_{10}) \sin 2\theta$$
$$(\cos^2\theta - \tfrac{1}{3}) \cos\phi \Big\} \qquad (5.18)$$

and the density matrix element condition of trace unity imposes

$$2\,\rho_{22} + 2\,\rho_{11} + \rho_{oo} = 1 \qquad (5.19)$$

Using the method of moments, the values of the pure spin 2 density matrix elements have been extracted from equation (5.18). In Tables 5.4 and 5.5 are shown the values of these density matrix elements averaged over all values of momentum transfer, and their variation with t for the s- and t-channel helicity reference frames respectively. Figure 5.8 shows the distributions of the density matrix elements ρ_{oo} and ρ_{11} with t, and the angular distributions of $\cos\theta$ and ϕ in the Gottfied-

Table 5.4 s-channel Density matrix elements (pure spin 2) for the f^o signal

t-range (GeV/c/^{2}	Number	Density Matrix Elements					
		ρ_{00}	ρ_{11}	ρ_{1-1}	Re(ρ_{22})	Re(ρ_{20})	Re(ρ_{10})
All	2153	0.41±0.02	0.39±0.01	−0.21±0.01	0.24±0.01	−0.11±0.04	−0.19±0.01
0.0 −0.05	63	0.71±0.13	0.40±0.05	0.09±0.09	0.01±0.04	−0.16±0.15	−0.06±0.08
0.05 −0.075	179	0.72±0.08	0.38±0.03	0.01±0.05	0.05±0.03	−0.06±0.09	−0.05±0.05
0.075−0.10	225	0.74±0.07	0.36±0.03	−0.04±0.05	0.11±0.02	0.05±0.09	−0.19±0.04
0.10 −0.125	222	0.57±0.07	0.43±0.02	−0.12±0.05	0.18±0.02	0.08±0.08	−0.29±0.04
0.125−0.15	176	0.56±0.08	0.42±0.03	−0.18±0.05	0.18±0.03	0.25±0.10	−0.25±0.05
0.15 −0.20	288	0.50±0.06	0.44±0.02	−0.28±0.04	0.24±0.02	0.25±0.08	−0.35±0.03
0.20 −0.30	304	0.26±0.05	0.47±0.02	−0.33±0.04	0.35±0.02	0.22±0.08	−0.28±0.03
0.30 −0.45	206	0.21±0.06	0.39±0.03	−0.38±0.04	0.41±0.02	−0.19±0.13	−0.19±0.04
0.45 −0.70	154	0.15±0.07	0.40±0.03	−0.27±0.05	0.38±0.03	−0.33±0.14	−0.14±0.04

Not shown in the table is the element ρ_{22}, which can be evaluated from the trace condition, or the elements ρ_{2-2} and ρ_{2-1}, both of which are zero throughout the t-range

Table 5.5 t-channel Density Matrix Elements (pure spin 2) for the f^o signal

t-range (GeV/c)2	Number	Density Matrix Elements					
		ρ_{oo}	ρ_{11}	ρ_{1-1}	$Re(\rho_{21})$	$Re(\rho_{20})$	$Re(\rho_{10})$
All	2153	0.86±0.02	0.27±0.01	0.01±0.01	-0.12±0.01	-0.22±0.03	0.08±0.01
0.0 -0.05	63	0.71±0.13	0.39±0.05	0.06±0.09	-0.09±0.04	-0.07±0.14	0.05±0.08
0.05 -0.075	179	0.74±0.08	0.37±0.03	0.0 ±0.05	-0.09±0.02	-0.03±0.09	0.05±0.05
0.075-0.10	225	0.91±0.07	0.29±0.03	0.03±0.04	-0.07±0.02	-0.06±0.10	0.03±0.04
0.10 -0.125	222	0.94±0.07	0.29±0.03	0.05±0.04	-0.06±0.02	-0.20±0.10	-0.05±0.04
0.125-0.15	176	0.94±0.09	0.26±0.03	0.04±0.04	-0.09±0.02	0.20±0.11	0.01±0.04
0.15 -0.20	288	1.16±0.07	0.18±0.03	0.04±0.03	-0.07±0.02	-0.23±0.09	0.05±0.04
0.20 -0.30	304	1.10±0.06	0.22±0.03	1.00±0.03	-0.06±0.02	-0.27±0.08	0.10±0.03
0.30 -0.45	206	0.98±0.07	0.27±0.03	-0.04±0.05	-0.11±0.02	-0.02±0.10	0.17±0.05
0.45 -0.70	154	0.73±0.08	0.27±0.08	-0.02±0.05	-0.18±0.03	-0.28±0.13	0.26±0.04

Not shown in the table is the element ρ_{22} which can be evaluated from the trace condition, or the elements ρ_{2-2} and ρ_{2-1} both of which are zero throughout the t range

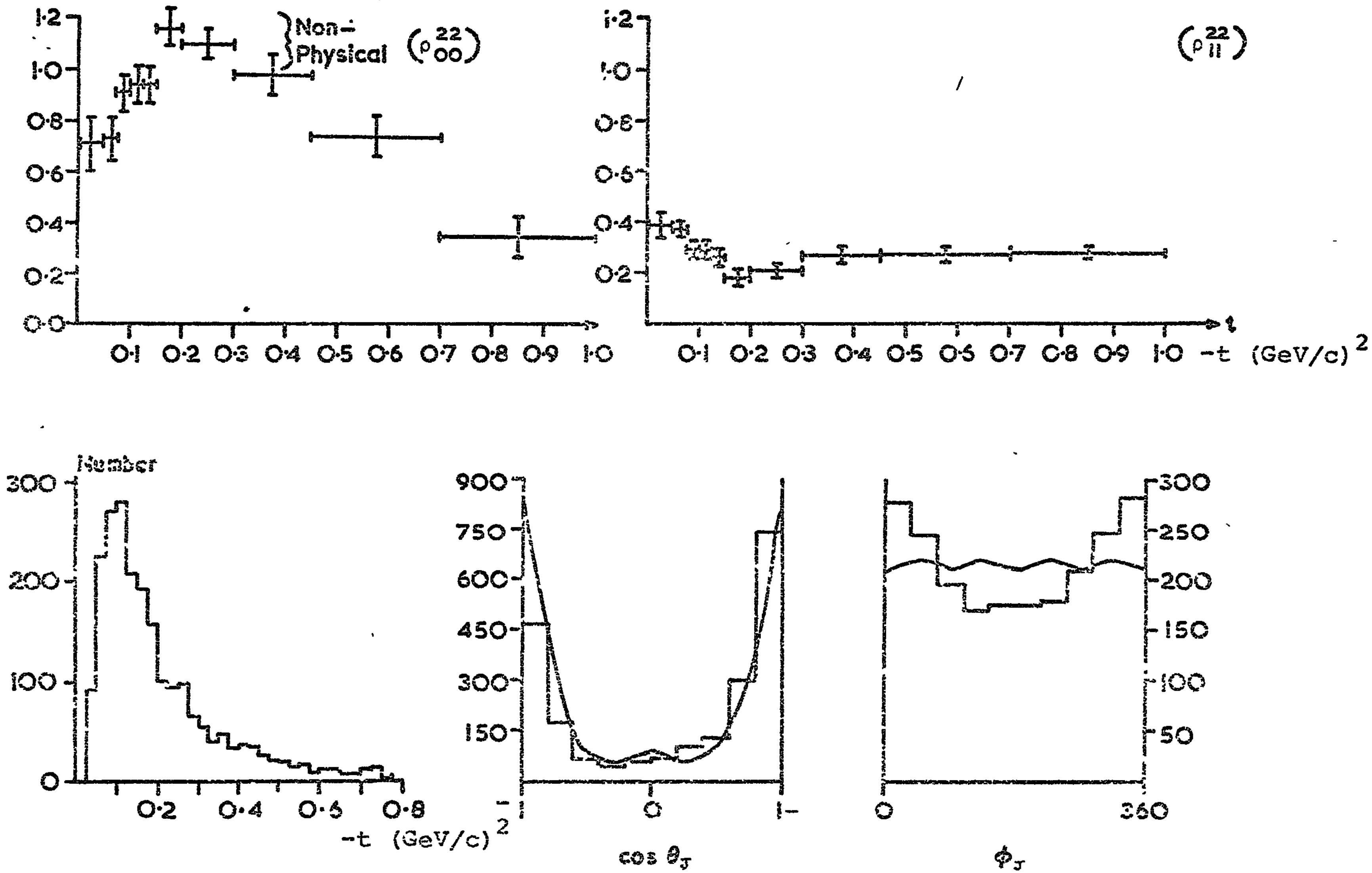

Fig. 5.8 f^o-meson density matrix elements, t-distribution and decay angular distributions.

Jackson reference frame. Also shown in this figure, as the solid curves in the decay angular distributions, are the fits to these distributions as predicted from the average values of the density matrix elements of Equation (5.18).

The consequences of treating the f^{o} signal as a pure D-wave spin system are clear:

(i) The density matrix elements exhibit non-physical values over some of their range and the element ρ_{22}, which is the square of the amplitude of the helicity 2 state, takes on non-physical values throughout the whole of the range of momentum transfer being considered.

(ii) The predicted form of the decay angular distributions of $\cos\theta$ and ϕ, which are calculated from the overall values of the pure spin 2 density matrix elements, are in very poor agreement with the experimental values. This implies that the calculated values of the elements of the density matrix are not good estimates of the experimental situation.

It is therefore necessary to consider the f^{o} region as containing not only pure D-wave, but a mixture of S-, P- and D-wave components. The evaluation of the density matrix elements is most conveniently performed in this case by an expansion of the spherical harmonic co-efficients $a_{\ell m}$ in terms of the elements of the mixed J = 0, 1 and 2 density matrix. This gives rise to a set of 15 equations containing the real parts of 25 density matrix elements (Ref. 5.4). The density matrix condition of trace unity imposes, in this case

$$2\,\rho^{22}_{22} + 2\,\rho^{22}_{11} + \rho^{22}_{00} + 2\,\rho^{11}_{11} + \rho^{11}_{00} + \rho^{00}_{00} = 1 \qquad (5.20)$$

It is obviously impossible to solve uniquely the values of the density matrix elements, but an analysis has been performed by the collaborating laboratories (Ref. 5.5) by applying the positivity conditions of the Schwartz inequalities

$$|\rho^{JJ'}_{\lambda\lambda'}| \leq \sqrt{\rho^{JJ}_{\lambda\lambda} \quad \rho^{J'J'}_{\lambda'\lambda'}} \qquad (5.21)$$

to the expansion of the spherical hramonic moments in terms of the density matrix elements in order to determine regions in which these elements must lie.

In this thesis a method has been used for the f^0 density matrix elements similar to that previously described in the sections discussing the ρ^0 meson, in which limitations have been put on the possible populations of the various helicity states in order to solve at low t for the density matrix elements. In the lowest part of the t distribution for the f^0 meson, $0.04 \leq |t| \leq 0.07$ $(\mathrm{GeV}/c)^2$, which contains 12% of the f^0 meson data, all of the experimentally determined moments with $M \neq 0$ are close to zero. Under the hypothesis, therefore, that only the helicity zero states of the $(\pi\pi)$ system are occupied then the spherical harmonic expansion of Ref. 5.4 contracts to a set of 5 equations containing 6 density matrix elements:

$$a_{10} = \frac{1}{\sqrt{4\pi}} \left\{ 4\sqrt{\frac{1}{5}}\ \rho^{21}_{00} + 2\rho^{10}_{00} \right\} \qquad (5.22)$$

$$a_{20} = \frac{1}{\sqrt{4\pi}} \left\{ \frac{2}{7}\sqrt{5}\ \rho^{22}_{00} + 2\,\rho^{20}_{00} + 2\sqrt{\frac{1}{5}\,\rho^{11}_{00}} \right\} \qquad (5.23)$$

$$a_{30} = \frac{1}{\sqrt{4\pi}}\ 6\sqrt{\frac{3}{7}}\ \rho^{21}_{00} \qquad (5.24)$$

$$a_{40} = \frac{1}{\sqrt{4\pi}}\ \frac{6}{7}\ \rho^{22}_{00} \qquad (5.25)$$

and with the trace condition

$$\rho_{00}^{22} + \rho_{00}^{11} + \rho_{00}^{00} = 1$$

these equations can be solved for the combinations ρ_{00}^{22}, $\rho_{00}^{11} + \rho_{00}^{00}$, $\rho_{00}^{11} + \sqrt{5}\,\rho_{00}^{20}$, ρ_{00}^{21} and ρ_{00}^{10}. The elements of most interest are ρ_{00}^{22} and $(\rho_{00}^{11} + \rho_{00}^{00})$ which give the proportion of the observed $\pi\pi$ state due to D-wave and S + P- wave respectively. It is unfortunate that in this analysis it is impossible to further separate the S- and P- wave components, but from the evaluation of the spherical harmonic co-efficients the values of the density matrix elements are:

$$\begin{aligned} \rho_{00}^{22} &= 0.45 \pm 0.09 \\ \rho_{00}^{11} + \rho_{00}^{00} &= 0.55 \pm 0.11 \end{aligned} \tag{5.26}$$

These two results state that, in the t region being considered of $0.04 \leqslant |t| \leqslant 0.07$, (45 ± 9)% of the observed state is due to production of a d-wave $\pi\pi$ system whilst (55±11)% comprises a mixture of S- and p-waves. Above the first t bin the values of the spherical harmonic co-efficients corresponding to $M \neq 0$ are non-zero and therefore no similar assumptions concerning the population of helicity states can be made.

5.6 Conclusions

The main parts of the previous discussion concerning the spin structure and production properties of the $(\pi^+\pi^-)$ system in the regions of the ρ^0 and f^0 mesons are summarized in the sections which follow.

(a) The ρ^0 region

The expansion of the decay angular distribution $W(\theta,\phi)$ in terms of the mixed spin density matrix elements for J=1 and J=0, as given in Eq. 5.11, leads to a good description of the experimental data. Using an helicity amplitude analysis at small values of momentum transfer, assuming that the $\pi\pi$ state is produced by a spin-flip mechanism, the relative amount of P- to S-wave component in the $\pi^+\pi^-$ system is 2:1. The S-P wave decay phase difference is either 0° or 180°. Up to a $|t|$ value of 0.075 $(GeV/c)^2$ the data are compatible with ~90% pion exchange, and as $|t|$ increases so the natural parity exchange component, A_2 exchange, becomes significant. The data show a dip in the density matrix element Re (ρ^{10}_{00}) at a value of $|t|$ consistent with that expected from the presence of a nonsense wrong-signature zero point of the A_2 pole, and there is evidence of a decrease with increasing $|t|$ of the relative amount of s-wave component in the $\pi^+\pi^-$ system.

(b) The f^0 region

An expansion of the decay angular distribution in terms of the pure spin 2 density matrix for the process $2^+\rightarrow0^-0^-$ is inadequate in explaining the experimental data. The decay angular distribution of cosθ is itself sufficient to infer that there is a substantial S- and P-wave component in this region. An analysis of the low $|t|$ region considering the mixed J=0, 1 and 2 density matrix, and assuming that only the helicity zero states of the produced $\pi\pi$ system are populated, leads to an estimate of the relative amount of D-wave to S- and P-wave combined as approximately 1:1.

5.7 Comparison with mass cut techniques

An examination of the spin structures of the ρ^0 and f^0 mesons has been made by the 3 collaborating laboratories (Ref. 5.5) in which the signals used as ρ^0 and f^0 were defined by mass cut techniques. The regions of $M(\pi^+\pi^-)$ selected were

for the ρ^0 meson $0.68 \leqslant M(\pi^+\pi^-) \leqslant 0.88$ GeV/c^2

for the f^0 meson $1.20 \leqslant M(\pi^+\pi^-) \leqslant 1.34$ GeV/c^2

The results of this analysis are now briefly reviewed and compared with the results of the analysis performed here on the signals extracted as ρ^0 and f^0 by the cluster searching technique.

(i) The ρ^0 region

The analysis showed that the natural parity exchange component, A_2 exchange, is less important at 4 GeV/c than at higher energies; and further that at low $|t|$ values the pion pole dominates through the helicity zero amplitude. This is in agreement with the results presented here on the CLUSTAN extracted signal for the ρ^0 meson.

(ii) The f^0 region

Components corresponding to S-, P- and D- wave production of the $\pi^+\pi^-$ system were found to be present in the f^0 region. In the sample extracted by mass cut technique the proportion of pure D-wave in the $\pi^+\pi^-$ system at low values of momentum transfer was found to be $(34\pm10)\%$ compared with $(45\pm9)\%$ by the CLUSTAN technique.

Extending the mass cut analysis throughout the $|t|$ range available, it was found that there was always a domination of unnatural parity exchange in the interaction and that even at high values of $|t|$ the amount of pure d-wave present in the data did not rise above 80%.

Chapter 6 Coherent Deuteron Interactions

6.1 Introduction

The reactions considered in the earlier parts of this thesis have been concerned with interactions of pions on the neutron target provided by the deuteron. These have been selected from a total number of events the remainder of which correspond largely to pion interactions upon the proton of the deuteron. A small fraction of the total number of events however, is due to the interactions of the pion with the whole of the deuteron in which the deuteron emerges as one of the final state particles.

At the present stage of the experiment the events available for analysis are those where the number of pions is three, and comprises $\pi^+\pi^+\pi^-$. That is, events where the final state particles are given by:

$\pi^+ d \rightarrow d\pi^+\pi^+\pi^-$ Reaction C

In terms of Feynman exchange diagrams, the two basic processes which are involved are shown in Figs. 6.1(a) and 6.1(b).

The sample of events is not made up entirely of those described by Fig. 6.1(a) and (b). The formation of final state deuterons by "pick-up" processes is well known and it is expected that, for example, there may be contributions to this channel from reactions such as that described by the Feynman diagram of Fig. 6.1(c). In this diagram the formation of an intermediate $\Delta(1236)$, by a pi-meson with one of the nucleons within the deuteron, is represented. On the

Fig. 6.1

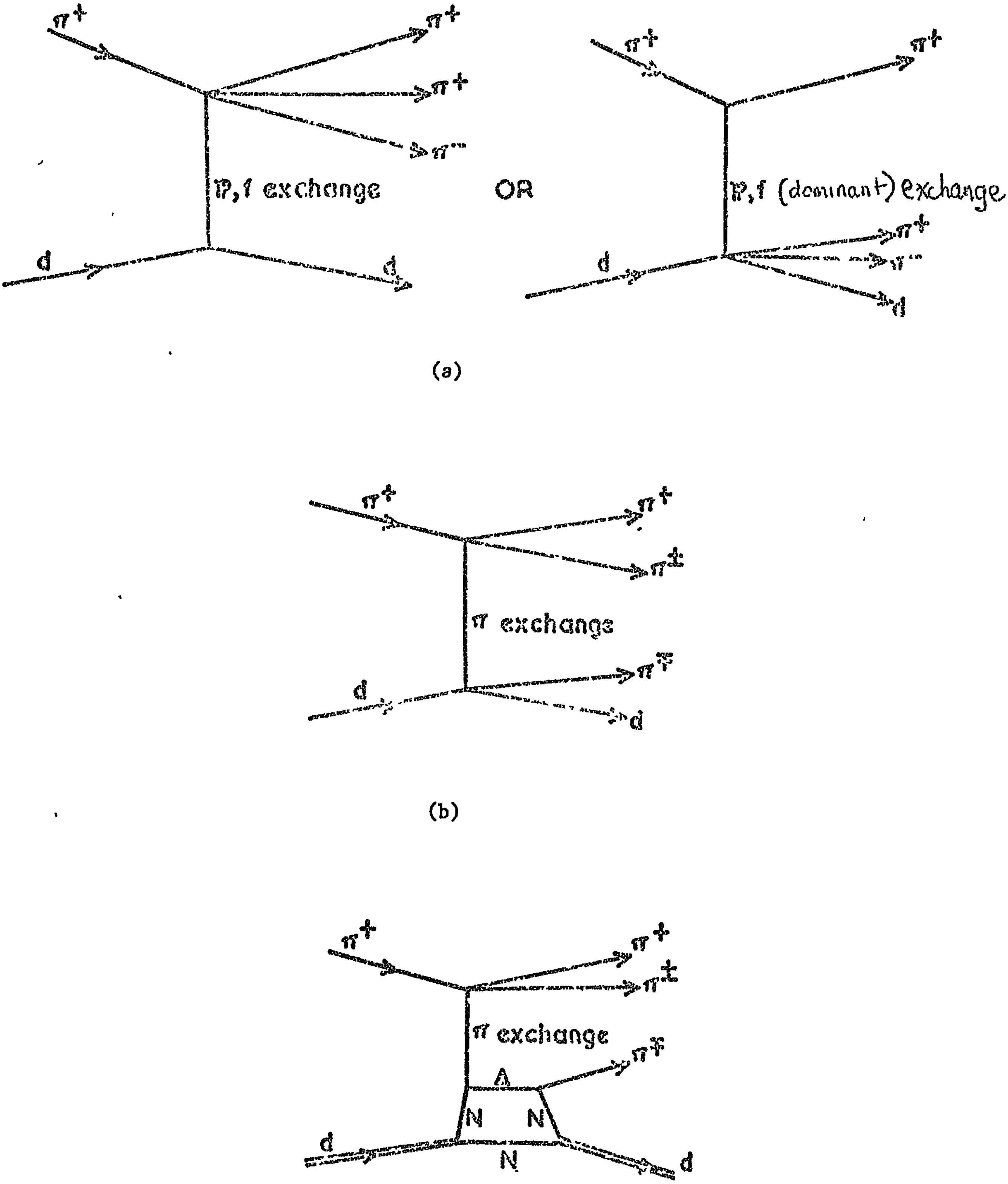

Feynman diagrams for : $\pi^+ d \to d\pi^+\pi^+\pi^-$

subsequent decay of the Δ, the released nucleon is picked up by the remaining nucleon, again forming a deuteron.

The process of Fig. 6.1(a) proceeds by pomeron-type exchange (i.e. no quantum numbers are exchanged) and is known as inelastic diffraction scattering in which the 3 pion secondaries are produced by the diffractive break up of the primary pion.

The second process (Fig. 6.1(b)) proceeds by pion-type exchange and these two processes together represent the truly coherent processes, that is the interaction is on the deuteron as a whole.

In diagram (a) of Fig. 6.1, the interaction is

$\pi^+ \longrightarrow \pi^+ \pi^+ \pi^-$ pion vertex

$d \longrightarrow d$ deuteron vertex

In this diagram the possible exchange particles are the pomeron (P) and the f^0-meson, and the three pions are expected to be produced moving forwards in the centre of mass frame with the deuteron continuing backwards. Conservation of quantum numbers imposes that the three pions must be in the same state as the initial pion, apart from orbital angular momentum and parity related by $P_{\pi\pi\pi} = -(-1)^{\ell}$. In this case, since the spin of the pion is zero, the orbital angular momentum (ℓ) is equal to the overall angular momentum (J) of the tripion system. Isospin conservation imposes that the tripion system must have $I^G = 1^-$. The possible final states for the tripion system are given below

$\pi = 1^-(0^-) \rightarrow \pi\pi\pi$ $1^G(J^P)$

$1^-(0^-)$: $\ell = 0$

$1^-(1^+)$: $\ell = 1$

$1^-(2^-)$: $\ell = 2$ etc.

Thus the final states are those of $I^G=1^-$, and in the unnatural parity series; hence it is possible that the tripion system is produced as the A1 meson but not as the A2 meson.

In diagram (b) of Fig. 6.1, where the first two possible exchange particles are the π-meson and the A_2 meson, the parity of the meson vertex dipon system is given by $P_{\pi\pi} = (-1)^\ell$. Shown below are the possible final states for the dipion system, enforcing the fact that for any 2-pion system if I is even both C and P are even, and if I is odd both C and P are odd. Again the orbital angular momentum (ℓ) equals the overall angular momentum (J).

$\pi = 1^-(0)^- \to \pi\pi$	$\ell=0$	$\ell=1$	$\ell=2$	etc
I=0	$0^+(0^+)$	-	$0^+(2^+)$	
I=1	-	$1^+(1^-)$	-	
I=2	$2^+(0^+)$	-	$2^+(2^+)$	

Examination of the various predicted states shown above for diagram 6.1(b) leads to the expectation of production of such mesons as the $\varepsilon(0^+(0^+))$, $\rho(1^+(1^-))$, and if the centre of mass energy were high enough the f^0-meson $(0^+(2^+))$. The ρ^0 meson may, of course, be produced from diagram 6.1(a) after the decay A1 $\to \rho\pi$.

In the collaboration of this experiment, this channel has been analysed by Birmingham and Durham simultaneously, Birmingham concentrating on an Ascoli Spin-Parity analysis of the tripion system, and Durham on resonance production. In this chapter, firstly the characteristics of the whole of the channel will be examined from this (resonance production) point of view and secondly, methods involving Van Hove plots and Cluster Analysis will be used to divide the events into those corresponding to diffractive production and those corresponding to other effects. Where necessary, reference will be made to the work carried out at Birmingham. The whole analysis is preceeded by a discussion of the ambiguities of the events and quality of the data; and the cross-section of the coherent channel is calculated.

6.2 Selection of Events

Since the deuteron in flight corresponds to a proton and neutron moving with the same momentum and with zero degrees between their trajectories it is expected that errors of measurement will lead to a contamination of the deuteron channel from events of the kind

$$\pi^+ d \rightarrow pn\pi^+\pi^+\pi^- \quad \text{(1-C, p-n fit) Ambiguity C1}$$

where either the final state proton or neutron is a spectator nucleon and where the proton and neutron are of similar low momentum and moving in the same direction. This ambiguity is resolvable in the case of 4-prong events where the fit to reaction C is a true 4-C fit, but in the case of a 3-prong (unseen deuteron) event the ambiguity is very difficult to resolve (Ref. 6.7) and thus only 4-pronged events have been used in the analysis.

Generally, experiments have found up to 15% contamination of the coherent channel with the 1-C p-n fit. However, at the energy of this experiment and with HPD measuring accuracy the contamination expected from this source is small, being <5%. For example, Vegni et al (Ref. 6.1), at an incident pion momentum of 6 GeV/c, found that only 2% of their original sample of coherent events were excluded after tests (described below) to remove the ambiguity C1. For these reasons the 1-C p-n fit was not considered a serious contamination, and any event which gave the 4-C coherent fit was assumed to be truly coherent in preference to the 1-C ambiguity C1.

This assumption, that the 1-C p-n fit is not a significant contaminate of the sample of events giving the 4-C coherent fit, has been confirmed by an examination of the mass of the p-n system, the opening angle θ_{pn} between the outgoing proton and neutron, and the ratio of the momenta of the proton and neutron, in the ambiguous fit to reaction C1. The tests which are normally used to distinguish between the coherent and 1-C p-n fits are:

a) Mass of the p-n system

For a true event in reaction C, the mass of the p-n system in ambiguity C1 should lie in the deuteron mass.

b) Opening angle θ_{pn}

For the channel $\pi^+ d \rightarrow pn\pi^+\pi^+\pi^-$, $\cos\theta_{pn}$ should be an isotropic distribution. What is seen experimentally is that $\cos\theta_{pn}$ has a strong peak at very small angles ($\cos\theta_{pn} \sim 1$) and it is only events in this peak which also give the 4-C coherent fit $\pi^+ d \rightarrow d\pi^+\pi^+\pi^-$.

c) $R = P_{(p)}/P_{(n)}$

From range momentum considerations R, the ratio of proton to neutron momenta, is determined to be 1.54 for the real deuteron misinterpreted as a proton. The distribution of R for ambiguous events shows a strong peak at this value, indicating those events which are coherent candidates.

At Birmingham, the selection criteria

$M(p,n) < 1.882$ GeV/c^2

$\cos\theta_{pn} > 0.9$

$R(=P_p/P_n) = 1.54 \pm 0.3$

have been applied to the ambiguous fits to the coherent channel, and it was found that <4% of the original fits were then rejected. Figs. 6.2a, b and c show the distributions of M(p,n), $\cos\theta_{pn}$ and R respectively for all events fitting the ambiguity $\pi^+d\to pn\,\pi^+\pi^+\pi^-$, and the shaded distributions in these figures indicate those events which give the coherent fit, showing clearly the features described above, justifying the use of the total 4C sample.

The reaction C also has a small ambiguity with the 4C channel $\pi^+d\to pp\,\pi^+\pi^-$ and, since this is a more likely 4-C fit, these events have been excluded. Finally, a probability cut has been made at the 1% level leaving a sample of events used in the analysis amounting to 1082 events.

6.2.1 Channel Cross-Section

The cross-section for the coherent reaction $\pi^+d\to d\,\pi^+\pi^+\pi^-$ has been estimated, allowing for a beam contamination of 5% and taking into account the reactions that would give an unseen deuteron in the final state (~20%, see ref. 6.2) as

Fig. 6.2

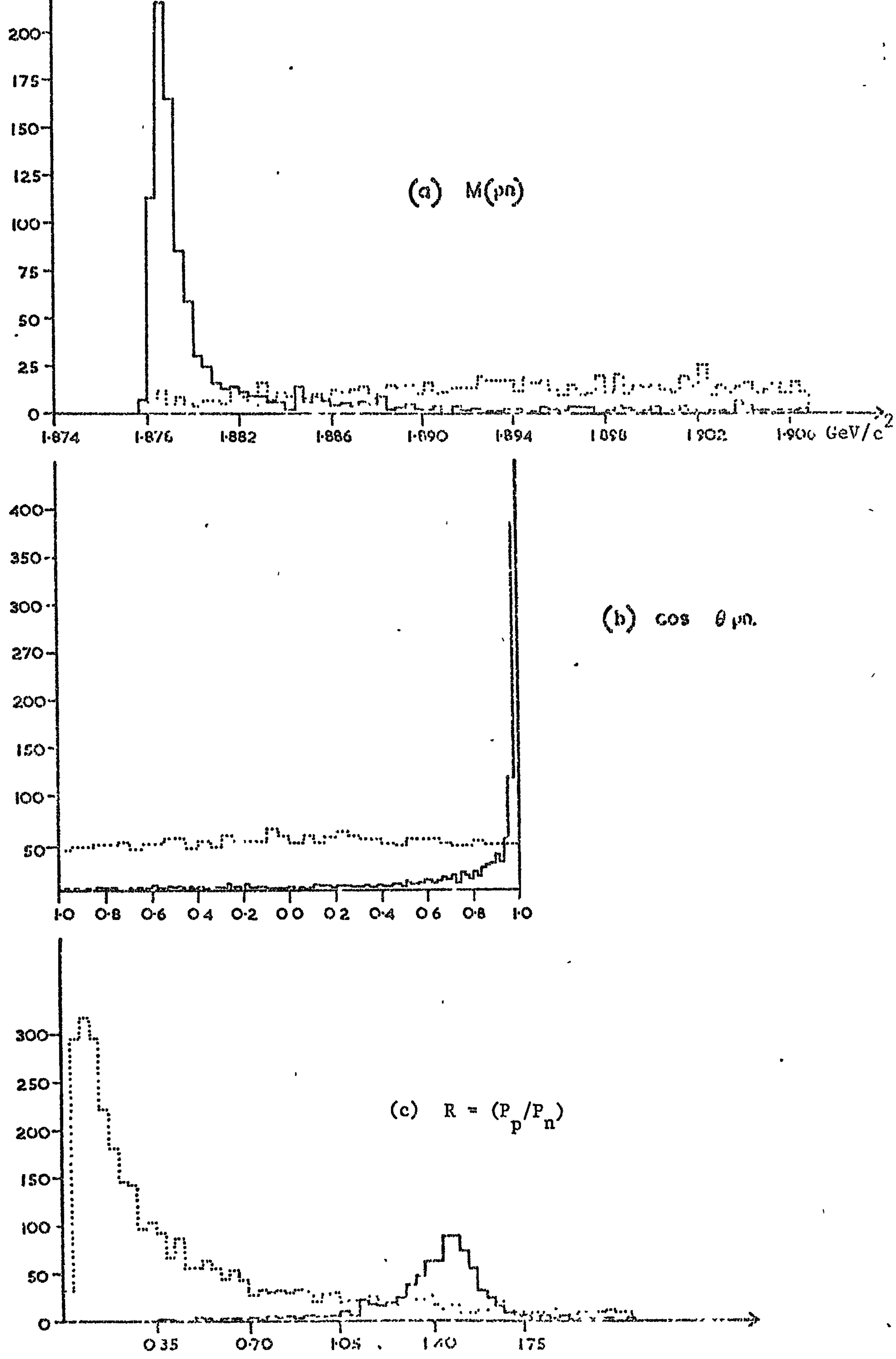

Distributions for unambiguous (dotted) 1-C n fits, and 3-C neutron fits ambiguous (solid) with coherent channel

$$\sigma(\pi^+ d \to d\,\pi^+\pi^+\pi^-) = 316 \pm 26\ \mu b$$

and hence one event corresponds to a cross section of $0.292\ \mu b$.

6.2.2 Momentum Transfer and Coherence

Since, in a definition of a coherent interaction, the interaction is demanded to be on the deuteron as a whole such that the deuteron remains intact throughout the event and emerges as one of the final state particles, it is possible to calculate the magnitude of a typical momentum transfer for such an event.

Using the definition of momentum transfer t (see Appendix A)

$$t = 2M_D^2 - 2E_D M_D \qquad M_D = \text{deuteron mass}$$

$$= 2M_D(M_D - E_D) \qquad E_D = \text{deuteron energy}$$

$$= -\,2M_D T_D$$

where T_D is the kinetic energy of the deuteron. Since the final state deuteron is non-relativistic, then

$$t \simeq -\,p^2$$

that is, the modulus of the momentum transfer is equal to the magnitude of the three momentum squared of the final state deuteron. The size of p for a coherent reaction can be estimated by demanding that the incident particle does not resolve the structure of the deuteron. Taking the deuteron diameter $\Delta x \sim 2$ Fermi, then from the uncertainty principle, $\Delta p \sim 200$ MeV/c. This leads to a typical momentum transfer, in order that the deuteron does not break up, of $t = 0.04\ (\text{GeV}/c)^2$. Below this value of t there is a negligible probability of splitting the deuteron, whereas above this value the probability increases rapidly.

6.3 Invariant Mass, and Angular Distributions: Meson Systems

In order to facilitate the separation of the various kinematic configurations described by the Feynman diagrams in Fig. 6.1, it was found to be necessary to devise some mechanism to distinguish between the two positive pions present in each event. To this end a definition of π_f^+ (fast π^+) was made as being that positive pion with the largest longitudinal centre of mass momentum. The other positively charged pion is then π^+_s(slowπ^+). Thus in diagram 6.1(b) the π^+ produced at the meson vertex is expected to be π^+_f, whilst the π^+ produced at the baryon vertex is expected to be π^+_s.

6.3.1 (π^+_f, π^-), (π^+_s, π^-) spectra: the ρ^0 meson

Fig. 6.3 (a) shows the invariant mass distribution for the dipion combination π^+_f, π^-. The dominant feature of this distribution is the ρ^0 meson. Shown in Fig. 6.3 (b) is the mass distribution of the $(\pi^+_s \pi^-)$ system, and as can be seen from this figure, there is some small amount of ρ^0 signal still present after the distinction between π^+_f π^+_s has been made. The decay angular distribution, in the Gottfried-Jackson Frame, for all π^+_f π^- combinations whose mass falls in the region $0.66 \leq M_{\pi^+_f \pi^-} \leq 0.86$ GeV/c^2 is plotted as the shaded histogram in Fig. 6.4. It will be noted that there is a large asymmetry in this distribution, biassed towards the forward decay of the π^+ meson in the ρ^0 rest frame. Most of this asymmetry is due solely to the method of selecting the π^+ associated with the ρ^0 meson, for when this distribution is compared with the unshaded histogram in Fig. 6.4, in which the distribution shown is

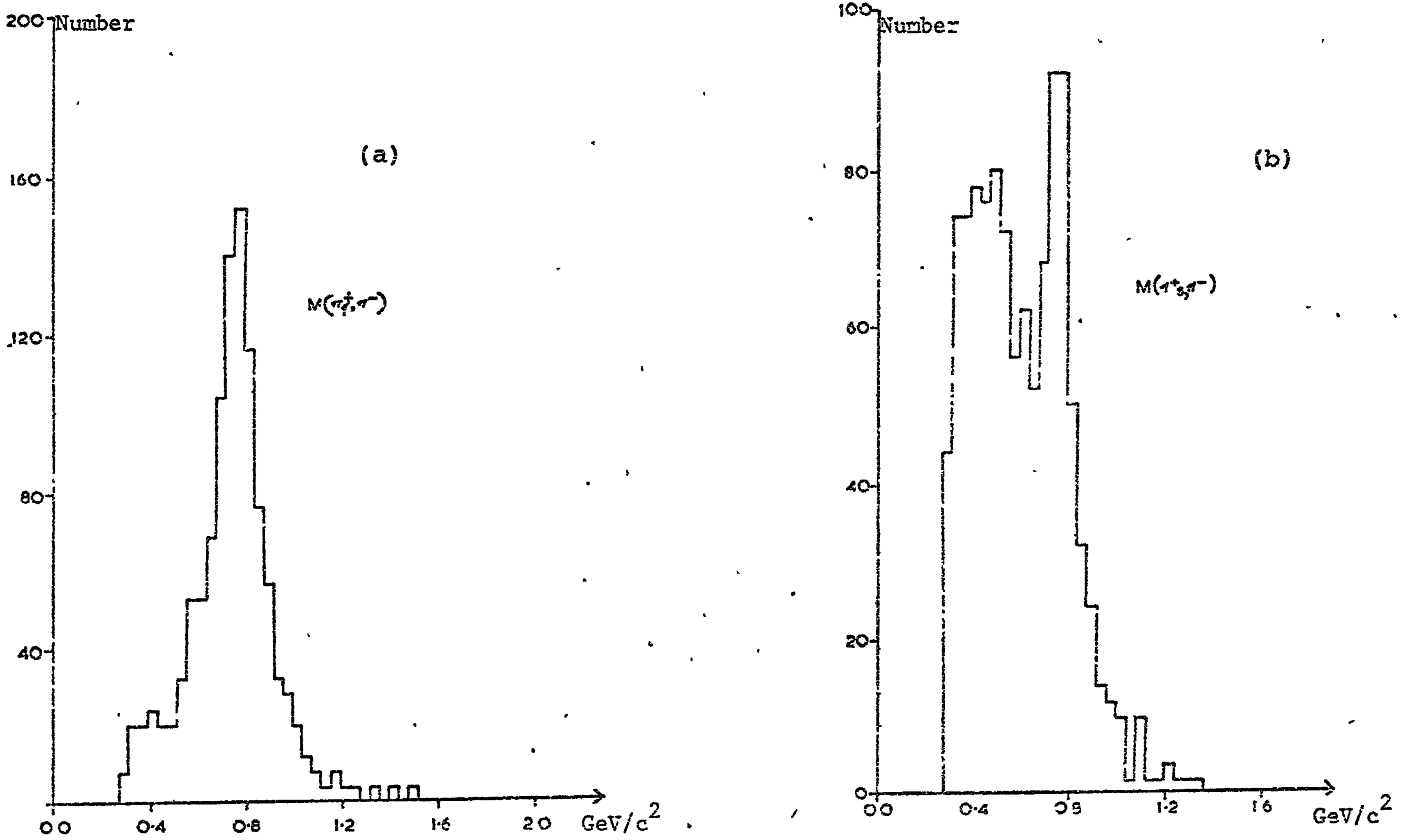

Fig. 6.3 Invariant Mass distributions for 4 GeV/c $\pi^+d\to d\pi^+\pi^+\pi^-$.

Fig. 6.4

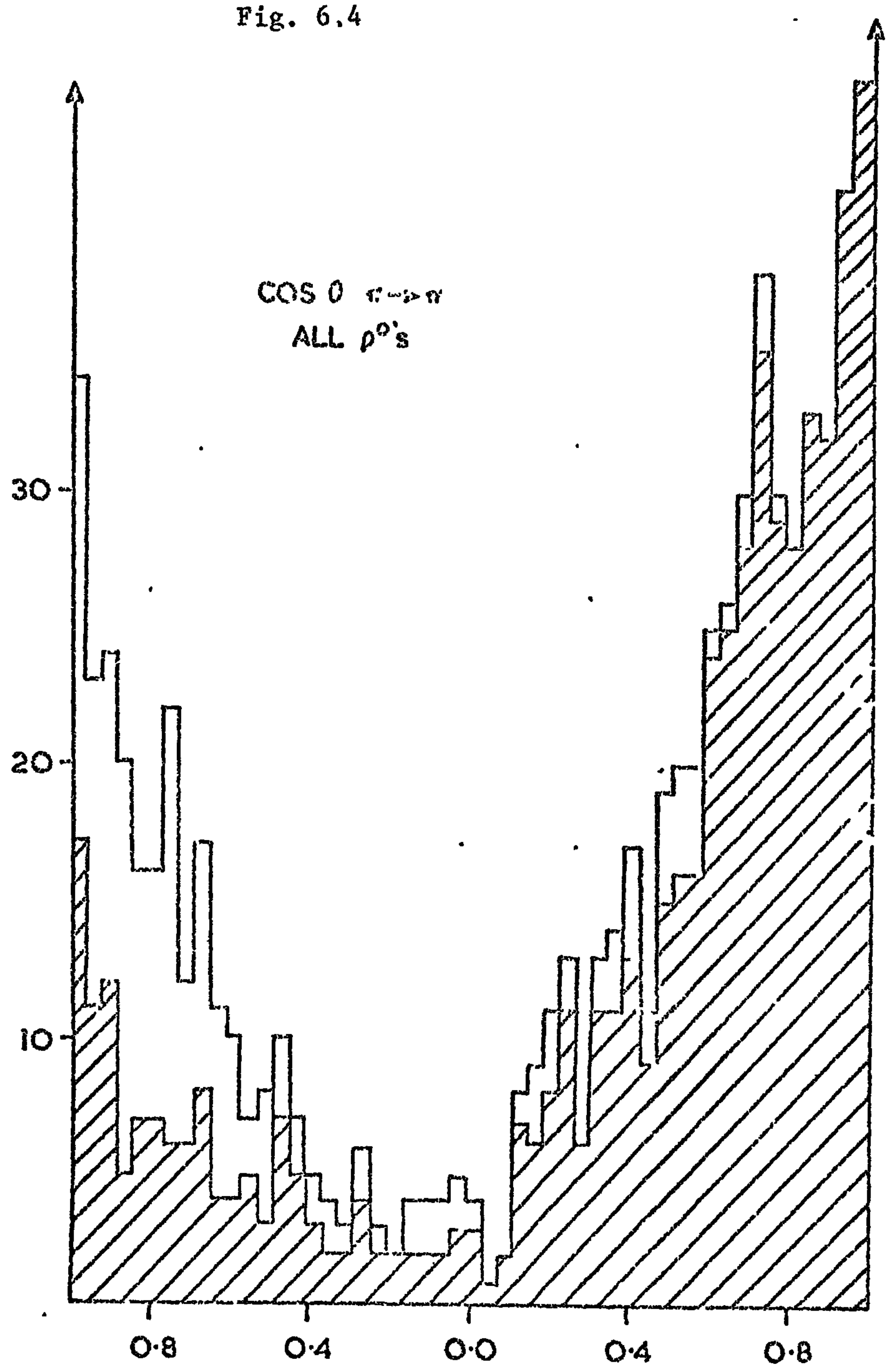

Angular distributions for all ρ^0 mesons and (shaded) $\pi_f^+\pi^-$ pairs in the ρ^0 mass region for all $\pi^+\pi^-$ pairs (whether π^+_f or π^+_s) whose mass falls in the ρ^0 mass region defined above, the asymmetry is reduced. In the unshaded histogram of Fig. 6.4, any event for which both $\pi^+\pi^-$ mass combinations fall in the ρ^0 region is given weight $^1/2$. It is apparent from this figure that only ~10% of all "real" ρ^0 mesons are lost because of the selection π^+_f, π^+_s. The kinematic reason for losing ρ^0 mesons is that if they are produced moving with low longitudinal centre of mass momentum (P_L) then when, on decay, the π^+ meson is produced moving backwards in the ρ^0 frame, it is possible for the π^+ associated with the ρ^0 decay to be moving with a smaller P_L than the other π^+, in the overall centre of mass frame. This explains also the fact that the ρ^0 mesons are lost from the backward going π^+ decay configuration.

Another method widely used for tagging the π^+ mesons is to define π^+_1 (say) as the member of that $\pi^+\pi^-$ combination which is produced with the smaller momentum transfer to the beam. This method (Ref. 6.2) appears to be no more successful than the simpler method used here since the percentage of lost ρ^0 events compares well at ~10%.

The forward-backward asymmetry parameter η, as defined in Chapter 5, for all ρ^0 mesons is evaluated as

$$\eta = 0.29 \pm 0.05$$

As described in Chapter 5, this asymmetry is attributable to the presence of an interfering s-wave $\pi\pi$ system resonant near the ρ^0 mass, the ε meson. Unfortunately, it is not possible to invoke any restraint on the amount of possible A1 production from the presence of the ε meson, since the A1 can decay into $\varepsilon\pi$ ($\varepsilon\pi$ in L=1 state) just as it can into $\rho^0\pi$ ($\rho\pi$ in L=0 state).

6.3.2 The Tripion System

The Invariant mass spectrum for the tripion system is shown in Fig. 6.5(a). Although one would have expected to see a peak at the A1 mass region (M(A1)=1070 MeV/c^2, Γ = 200-400 MeV/c^2) there is no evidence for such a resonance. There appears only a broad enhancement throughout the whole tripion mass range. Since the A1 decays: A1$\to\rho\pi$, it may be thought that selecting a ($\pi^+\pi^-$) combination in the ρ^0 mass would enhance any possible structure around the A1 meson. However, since the A1 signal is obviously weak if it is present and since ρ^0 mesons are produced in ~65% of the events, then selecting the ρ virtually selects every event and does not specifically enhance the A1 meson. Indeed, kinematically, any tripion system with mass as in Fig. 6.4(a) is bound to give one combination of the dipion masses in the ρ region; conversely, any dipion system with mass in the ρ meson will give a tripion mass near the A1 mass.

The effective mass distribution for the $\pi^+\pi^+$ system is shown in Fig. 6.5(b). As is expected, since no Ispin 2 (exotic) mesons are known, there are no enhancements in the spectrum of this system.

6.4 Invariant Mass and Angular Distributions: Baryonic Systems

In searching for enhancements in (dπ) systems, the mechanism being considered is basically that of one-pion exchange as indicated in Fig. 6.1(b). That is, no contribution from pomeron-type exchange is expected in this context.

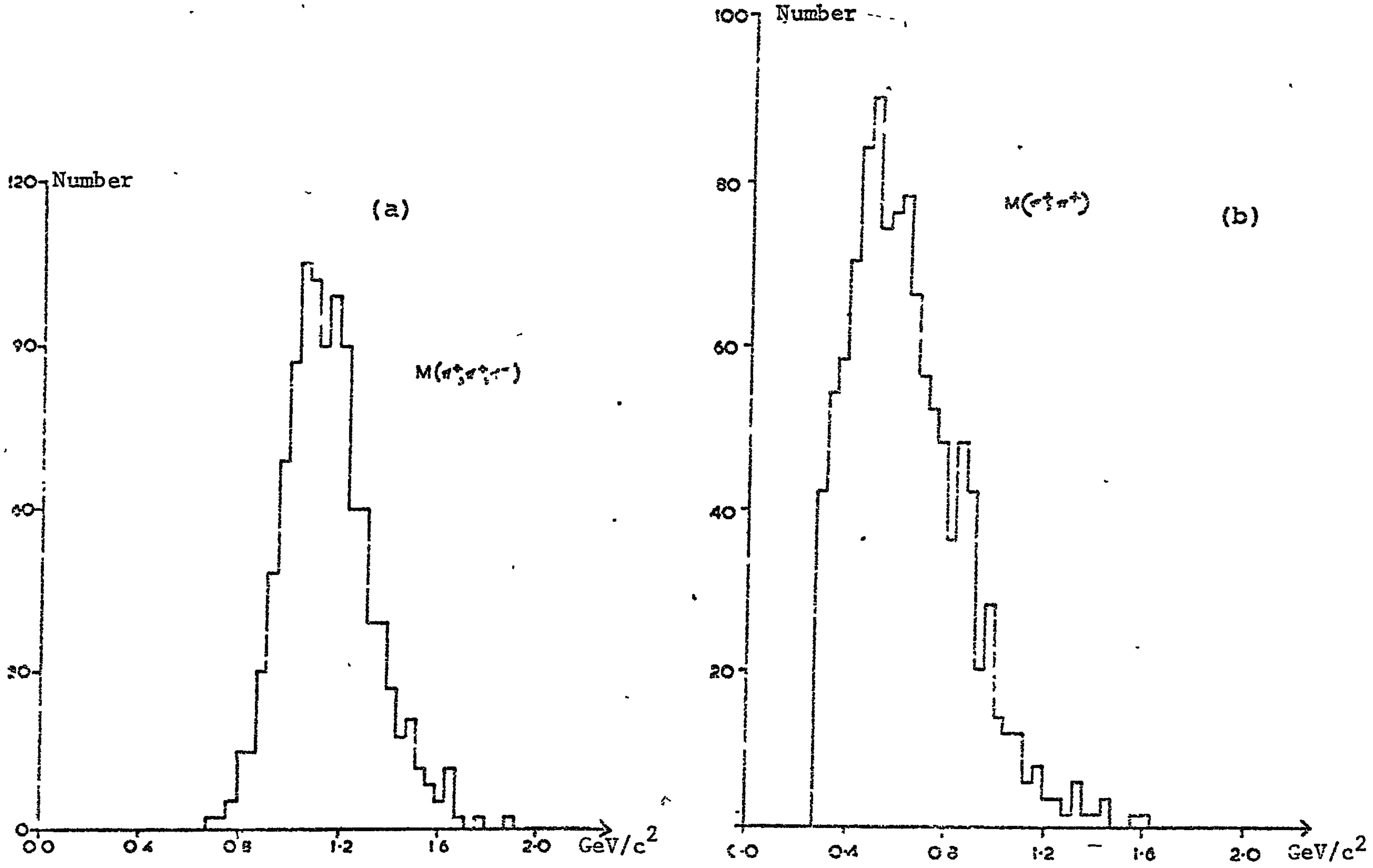

Fig. 6.5 Invariant Mass distributions for 4 GeV/c $\pi^+ d \to d \pi^+ \pi^+ \pi^-$.

There are, of course, more complicated exchange mechanisms such as the pick-up process shown in Fig. 6.1(c), and these will be dealt with as evidence for them occurs.

6.4.1 The (π^+_sd) system

The effective mass of this system is shown in Fig. 6.6(a). The very clear enhancement at M(πd) ~ 2200 MeV/c^2 has been noted in several experiments (see table 6.1 below). This peak is the d* effect and here it is seen in the d^{*++} mode, the mass region defined as the d* being: $2.0 \leq M(\pi d) \leq 2.4$ GeV/c^2.

Table 6.1 %D* For Various Incident Momenta

Beam Momentum GeV/c	%D*	Ref
3.7	35	6.8
4.0	45	This expt.
4.2	40	6.2
5.04	36	6.4
5.4	15	6.5
6.0	10	6.1
8.0	10	6.6
11.7	12	6.7

In order to determine whether or not the d* is a resonance, it is necessary to examine the decay angular distribution. Fig. 6.7 shows a plot of the cosine of the angle ($d_{in} \to d_{out}$) in the d* rest system (Gottfried-Jackson frame). As can be seen the distribution is very forward peaked, and either very high terms of ℓ in Legendre Polynomials ($\Sigma a_\ell P_\ell (\cos\theta)$) or very large interference terms will be required to fit the distribution. This asymmetry

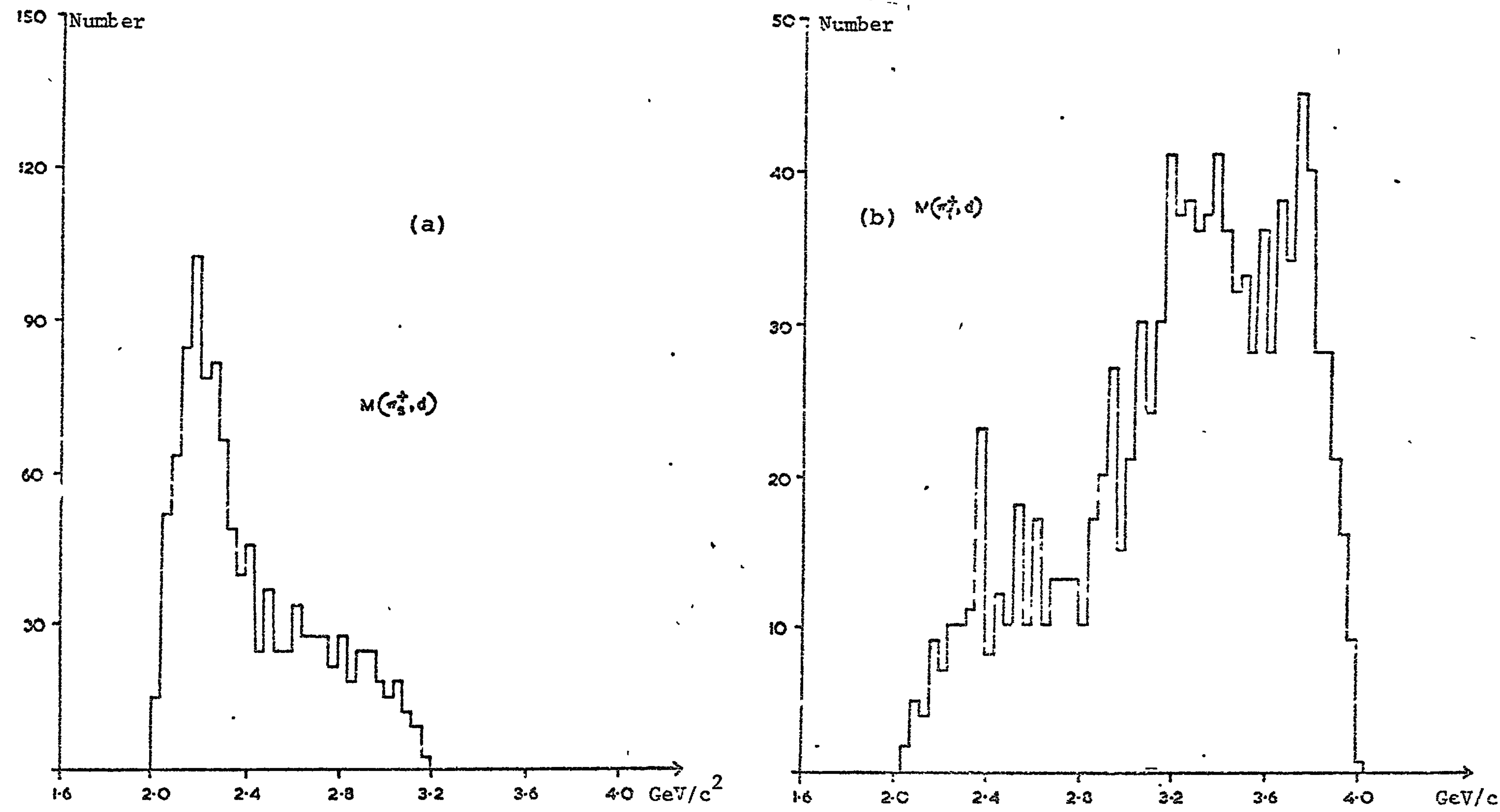

Fig. 6.6 Invariant Mass distributions for 4 GeV/c $\pi^+d\to d\pi^+\pi^+\pi^-$.

Fig. 6.7

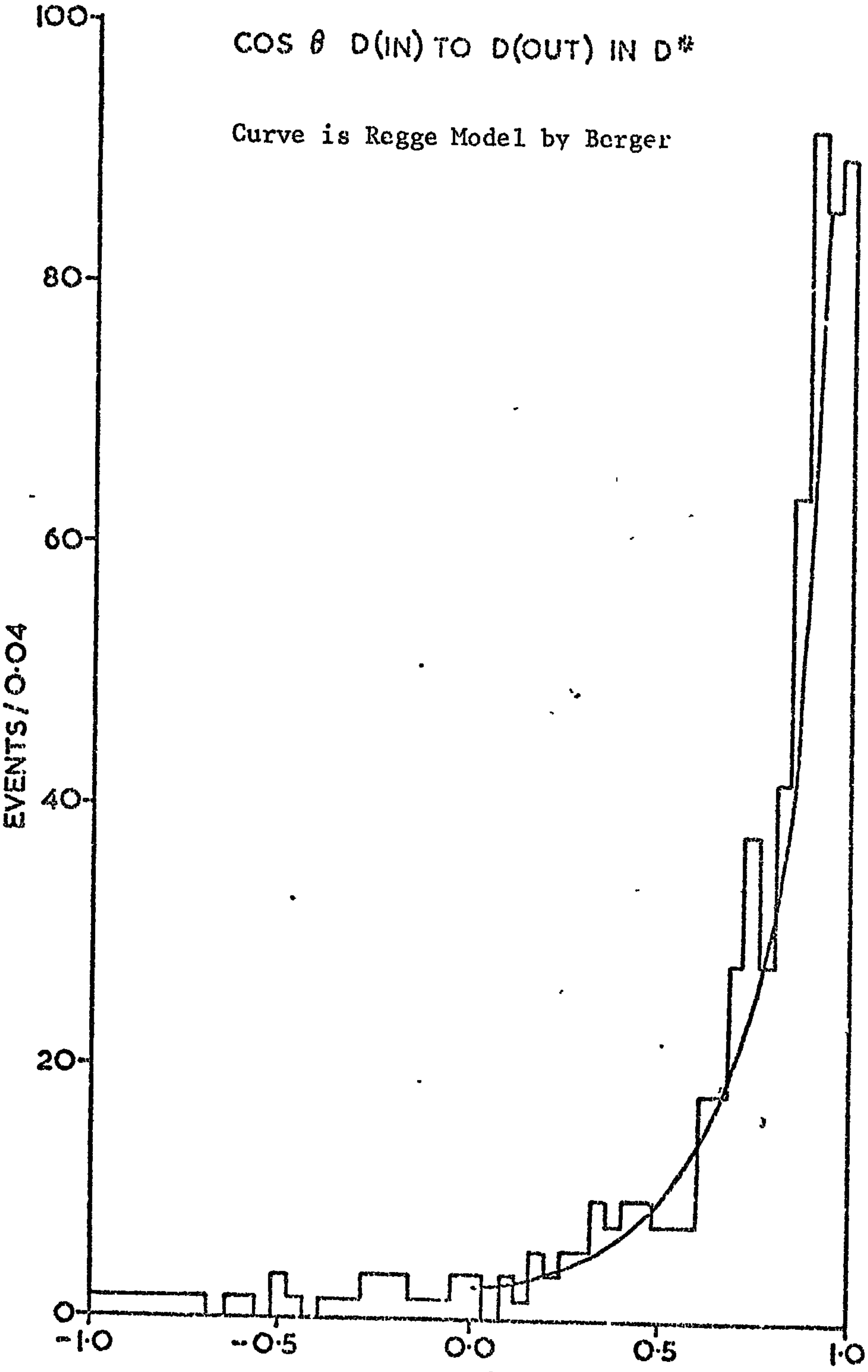
COS θ D(IN) TO D(OUT) IN D*
Curve is Regge Model by Berger
EVENTS / 0·04
100
80
60
40
20
0
-1·0
-0·5
0·0
0·5
1·0
COS θ

is inconsistent with a particle of definite spin and parity and it is therefore concluded that the d^* is not a resonance. An explanation of the d^* effect has been suggested by Eisenstein and Gordon (Ref. 6.2) using a one-pion exchange-type model of the form of the Feynman diagram of Fig. 6.1(c). The d^* is assumed to be an enhancement in πd scattering, which results from the formation of a $\Delta(1236)$ by the pion with one of the nucleons within the deuteron. As evidence for this it is noted that experimentally

$$M(d^*) = M(\Delta) + M(N)$$

When the Δ subsequently decays into $N\pi$, it does so in such a way as to leave an intact deuteron in the final state.

It is possible, on a very simple picture, to give a plausibility argument for this type of effect, without requiring the deuteron to be broken up into its two nucleonic constituents.

The lifetime of a $\Delta(1236)$, $\sim 10^{-23}$ secs, is comparable with its time to cross the deuteron thus there is sufficient time for the Δ to decay within the deuteron diameter. Also, in the decay of a Δ at rest ($\Delta \to \pi N$), the momentum of the nucleon is $p_N \sim 200$ MeV/c. According to the Hulthen distribution (see Appendix B) of nucleon momenta within the deuteron, ~10% of nucleons have a momentum $\gtrsim 200$ MeV/c. Thus one may conclude that a nucleon given an impulse equivalent to a kinetic energy of ~20 MeV, could be captured within the deuteron potential well, to form a final state deuteron.

6.4.2 Momentum Transfer to the d*

The t distribution from d to d* is shown in Fig. 6.8. The solid curve superimposed on the histogram is that calculated from a simple one pion exchange (OPE) peripheral model, with a pion propagator of the form:

$$Pr = \frac{1}{(t_{d^*} - m_\pi^2)^2} \qquad \text{(See Appendix C)}$$

and normalised to the data for $0.1 \leq |t_{d^*}| \leq 0.6$ $\text{GeV}/c)^2$. As can be seen from the figure, the fit is satisfactory. The reason for the lower limit of $|t| = 0.1$ $(\text{GeV}/c)^2$ in the normalisation is that for some events t_{min} may be large. ($t_{min} \sim 0.08$ $(\text{GeV}/c)^2$.

6.4.3 Decay Angular Distribution of the d*

The distribution of cos θ from incoming to outgoing deuteron in the d* rest system was shown above in Fig. 6.7. In this case the superimposed curve is from a calculation given by Berger (ref. 6.3), using a Regge-pole exchange model with a trajectory for the pion given by

$$\alpha(t_{d^*}) = t_{d^*} - m_\pi^2$$

where $\frac{d\sigma}{dt} \propto s^{2\alpha(t)-2}$ $\qquad s = (\text{c. of m energy})^2$

Here, also, the fit is adequate although the agreement between model and experiment is not so close as in the fit to the t distribution by the simple OPE model described above.

6.4.4 Angular distribution NOT in the d*

Figure 6.9 shows the distribution of cos θ (d_{in}-d_{out}) in the (dπ) system, for a mass of (dπ)>2.4 GeV/c^2. This distribution is even more forward peaked than that of cosθ_{d^*}

Fig. 6.8

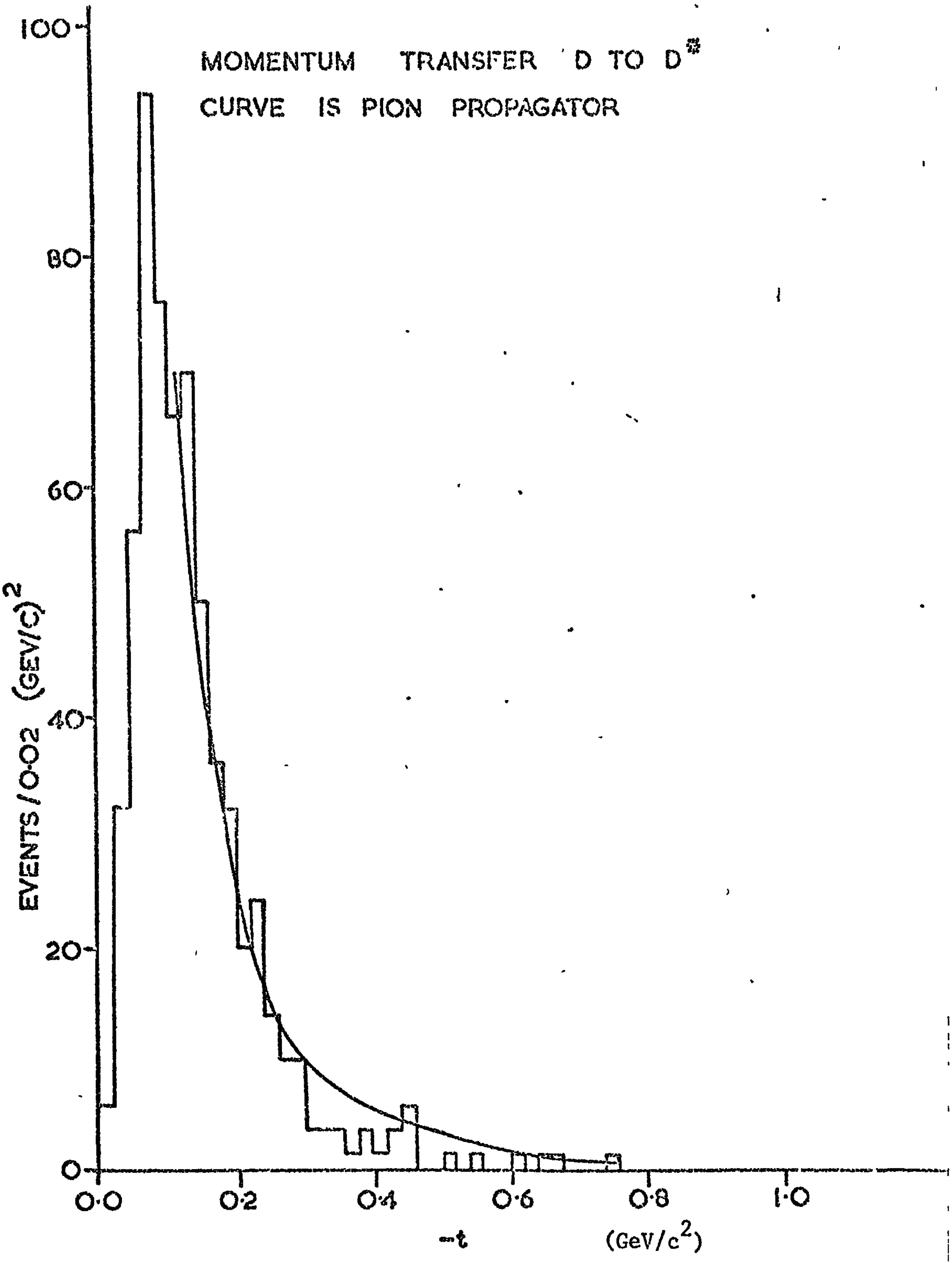
MOMENTUM TRANSFER D TO D*
CURVE IS PION PROPAGATOR
EVENTS / 0·02 (GEV/C)^2
100
80
60
40
20
0
0·0
0·2
0·4
0·6
0·8
1·0
−t
(GeV/c^2)

Fig. 6.9

Cos θ d(in) $\longrightarrow$ d(out) in $d\pi^+_s$ system.
not d^*

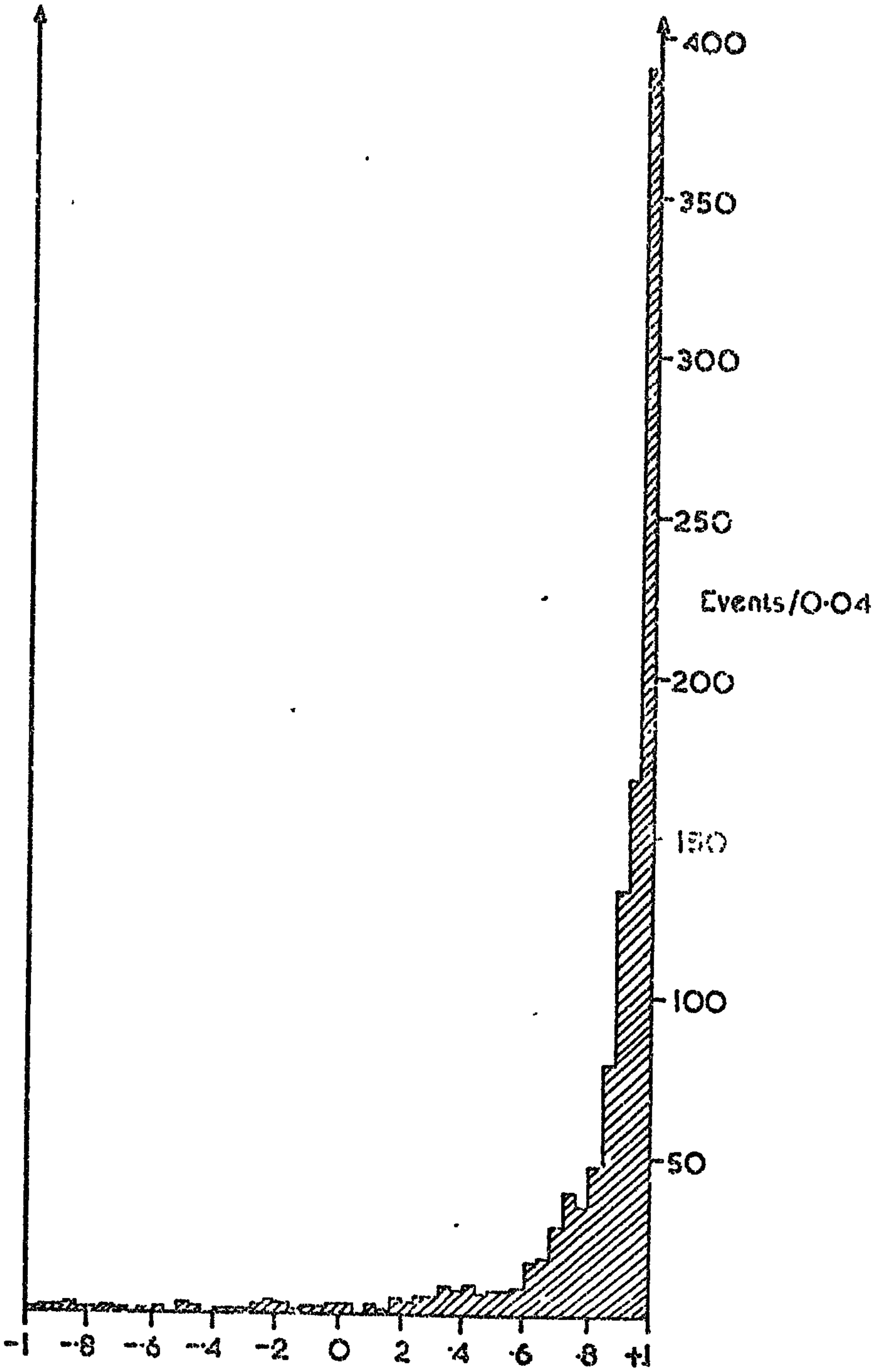

Fig. 6.10

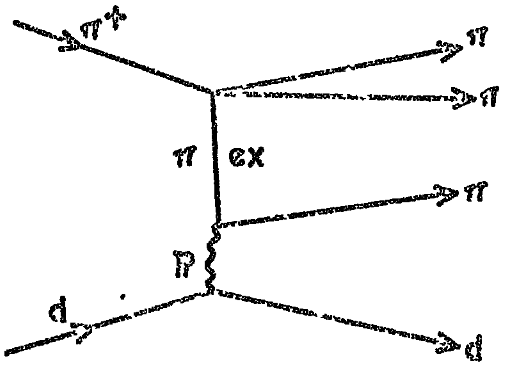

Feynman diagram of Deck effect.

in the d^* mass region. This type of angular distribution can only be attributed to a highly peripheral type of interaction. The Feynman Diagram shown in Fig. 6.10, illustrating the Deck Effect, is employed in the explanation of this process where it is thought that the exchange pion is elastically scattered from the deuteron. This elastic scattering is equivalent to pomeron exchange, the deuteron experiencing only a very small momentum transfer, and thus its momentum vector is changed only slightly in angle.

6.4.5 Mass of (π_f^+, d) system

The invariant mass spectrum of the (π_f^+, d) system is shown in Fig. 6.6(b), where there is a complete absence of d^* signal, as is expected if the π_f^+ is associated with the meson vertex. The rather broad enhancement in the distribution at $M(\pi_f^+, d) \sim 3.3$ GeV/c^2 is the result of the reflection of the ρ^0 meson formed in the (π_f^+, π^-) pair.

6.4.6 Mass of $(\pi^- d)$ system

The mass spectrum shown in Fig. 6.11(a) is the effective mass distribution of the $(\pi^- d)$ system. The definite peak at $M(\pi^- d) \sim 2.15$ GeV/c^2 is the non-charged mode of the d^*. Employing the Feynman diagram of Fig. 6.1(b) it may be seen that the background under any signal can be reduced by eliminating any events having a (π_f^+, π^-) combination in the ρ^0 region. Fig. 6.11(b) shows the distribution of $M(\pi^- d)$ where events with a ρ^0 meson in $M(\pi_f^+, \pi^-)$ have been removed. The d^{*0} peak, although reduced in intensity, is still clearly visible; furthermore, removal of pairs of $(\pi^+_s \pi^-)$ in the ρ^0 mass region does not affect the d^{*0} peak, merely reducing

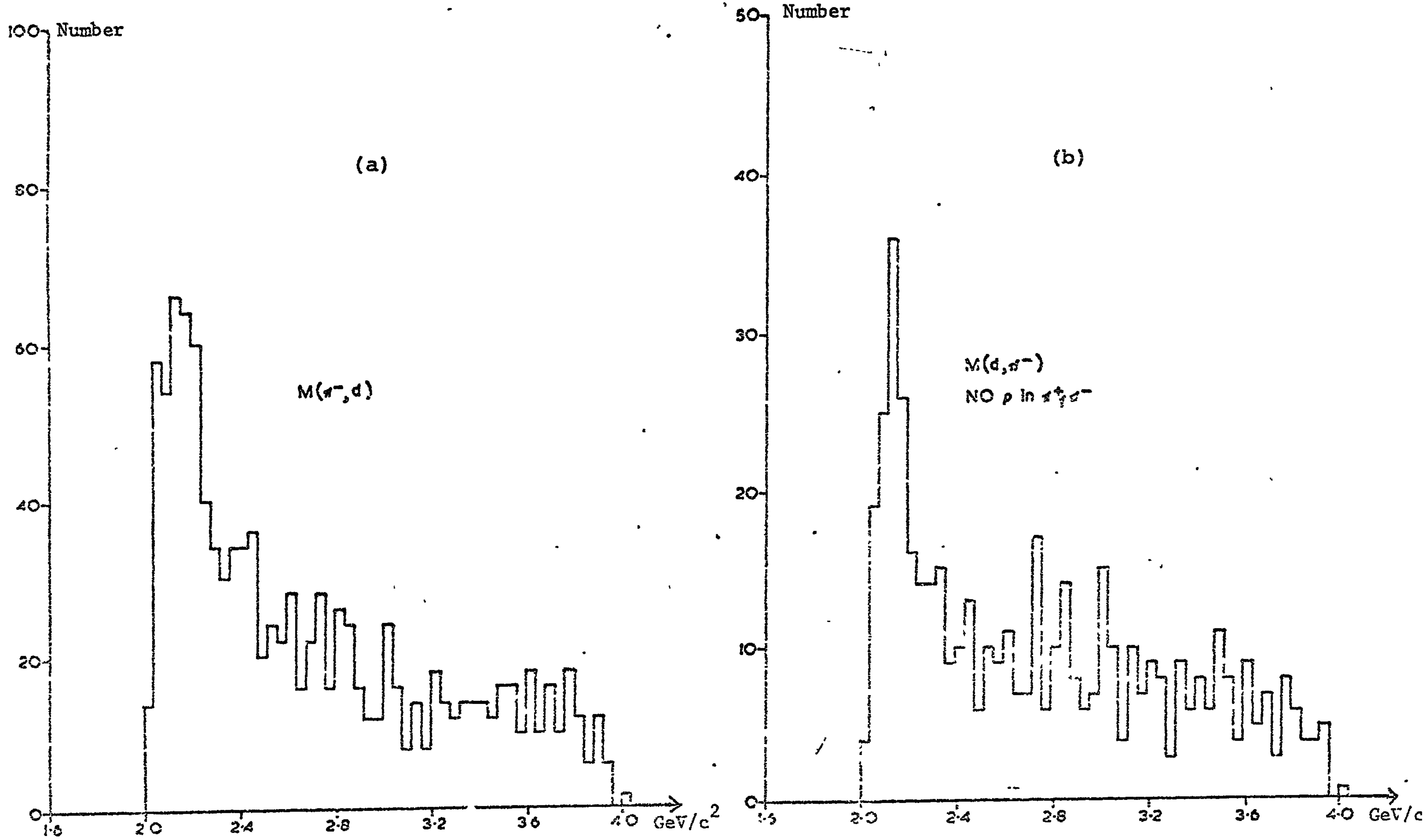

Fig. 6.11 Invariant Mass distributions for 4 GeV/c $\pi^+d \to d\pi^+\pi^+\pi^-$.

the signal above 2.8 GeV/c^2.

6.5 Summary of Results

The channel $\pi^+ d \rightarrow d \pi^+ \pi^+ \pi^-$ is dominated by production of the ρ^0 meson, accounting for ~65% of the $\pi^+\pi^-$ spectrum, and the d^* effect. The rho meson is produced mainly in the $\pi^+ \pi^-$ combination, where π_f^+ is the π^+ with the largest longitudinal centre of mass momentum, and the d^* is produced as

a) The d^{*++} in the $d\pi^+_s$ system

b) The d^{*o} in the $d\pi^-$ system

where $\frac{d^{*++}}{d^{*o}} \sim \frac{5}{1}$

The d^* enhancement is explained in terms of the box diagram shown in Fig. 6.1(c), one pion exchange and Regge pole calculations fitting the data quite well, especially the peripheral model calculation fit to the t distribution of t $(d \rightarrow d^*)$. The selection criteria based upon π_f^+, π^+_s are as effective as considerations based upon the momentum transfer to the $\pi^+\pi^-$ system: about 10% of all real ρ mesons being excluded. Although it is difficult to exclude any production of the A1 meson, the invariant mass distribution of the tripion system lends no weight to an argument for its presence. The Ascoli spin analysis carried out at Birmingham, however, has indicated a substantial $J^P = 1^+$ component in the $\pi^+ \pi^+ \pi^-$ system consistent with A1 production (Ref. 6.9).

The high mass $(d\pi^+_s)$ system $(M(d\pi) > 2.4$ GeV/$c^2)$ may be thought of as either elastic scattering on the deuteron by the Deck mechanism of Fig. 6.10 or the inelastic process of Fig. 6.1(b); the nature of the decay angular distribution, however, implies the former of these two processes.

6.6 Discussion of Results

A comparison of cross sections, for the coherent channel $\pi^+ d \rightarrow d \pi^+ \pi^+ \pi^-$, for various incident momenta is shown below in Table 6.2.

Table 6.2 Variation of X-Section with Beam Momentum

Beam Momentum (GeV/c)	X-section (μb)	Reference
3.7	420±	6.8
4.0	316±25	This expt.
4.2	304±70	6.2
5.04	324±25	6.4
5.4	528±37	6.5
6.0	300±50	6.1
8.0	344±35	6.6
11.7	353±30	6.7

Apart from the very large cross-section quoted in entry number 5 of Table 6.2, the cross section for this channel appears independent of energy. This is consistent with a diffractive process, the pomeron trajectory dominating, which leads to a prediction of constant cross section as the centre of mass energy squared, $s, \rightarrow \infty$. However, since the d^* effect (Table 6.1) is present, and the cross section for this process, which is a definite indication of a pion exchange component in the data, falls as $\sim p^{-2}$ (p = incident momentum) then there is an immediate contradiction of the assumption of a diffractive process drawn from the channel cross-section data. Subtraction of this pion exchange component leads to a cross-section for the non pion-exchange component which rises approximately as p^2 up to a centre of mass energy of $\sqrt{6.33}$ GeV/c^2 (entry 6 in table 6.2), and then remains constant.

In order to attempt to resolve this ambiguity, the distribution of the events in the 4-body longitudinal phase space plot has been examined. This plot is shown in Fig. 6.12 where the 2 Van hove angles are plotted. The numbered areas correspond to the reaction configurations shown in Fig. 6.13. The solid lines are those of zero longitudinal centre of mass momentum for the various particles and the broken lines correspond to a transverse momentum of ∿200 MeV/c. The region marked 5 is that in which events of the type shown in Fig. 6.1(a), that is diffraction dissociation events, would be expected to fall. Inspection of this plot leads to the conclusion that there is not a significant amount of real diffraction dissociation present in the data. This would account for the fact, inferred from the lack of events in region 5, that there is no substantial production of the A1 meson.

6.7 Cluster Analysis

6.7.1 Choice of Variables

In order to search for n dimensional clustering in this channel where there are 4 particles in the final state : $d\pi^+\pi^+\pi^-$, 7 variables are required to describe the system. The variables chosen were, again, those recommended by Dao et al (ref. 6.10). When considering the definitions of the Van-Hove variables for a three body final state (Chapter 3), it was found that the c of m longitudinal momentum distribution

Fig. 6.12

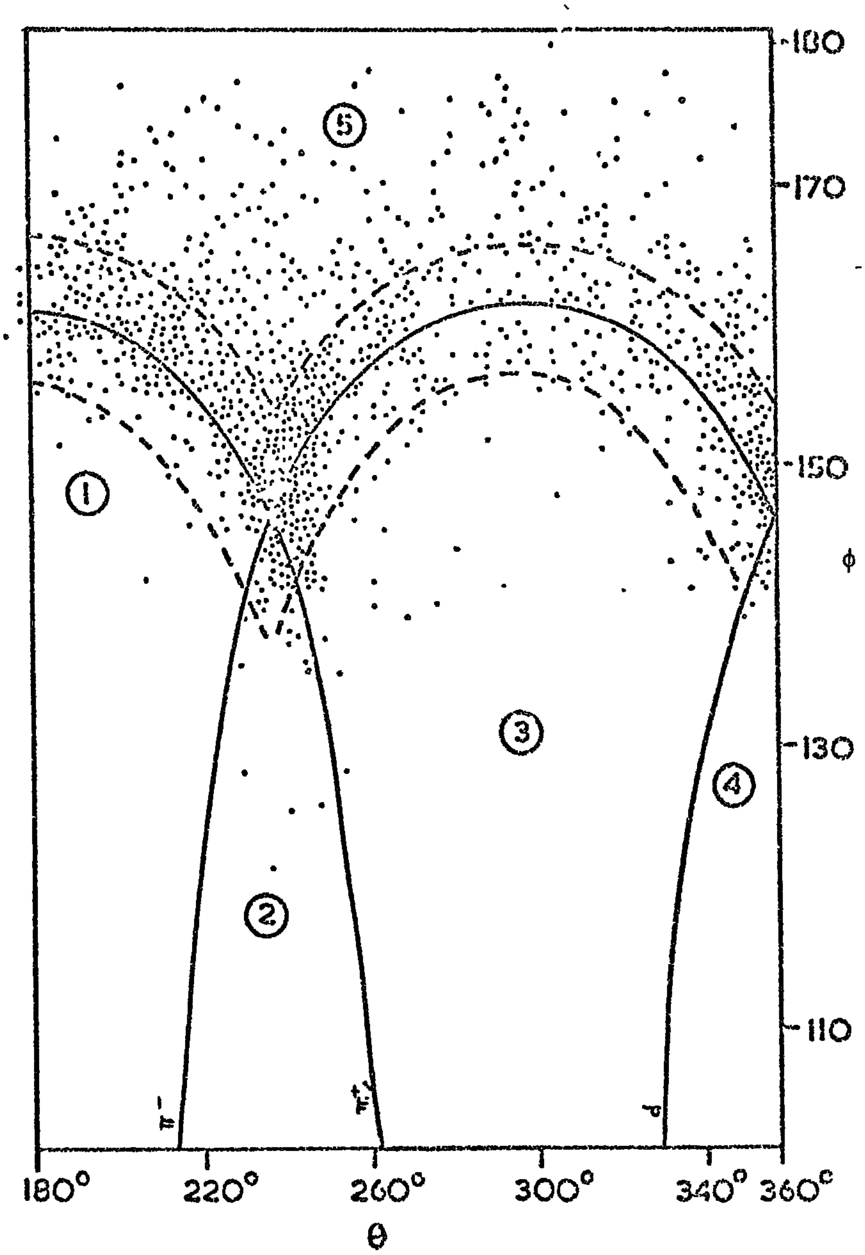

Distributions of events in 4-body LPS plot

For key to regions see Fig. 6.13

Fig. 6.13

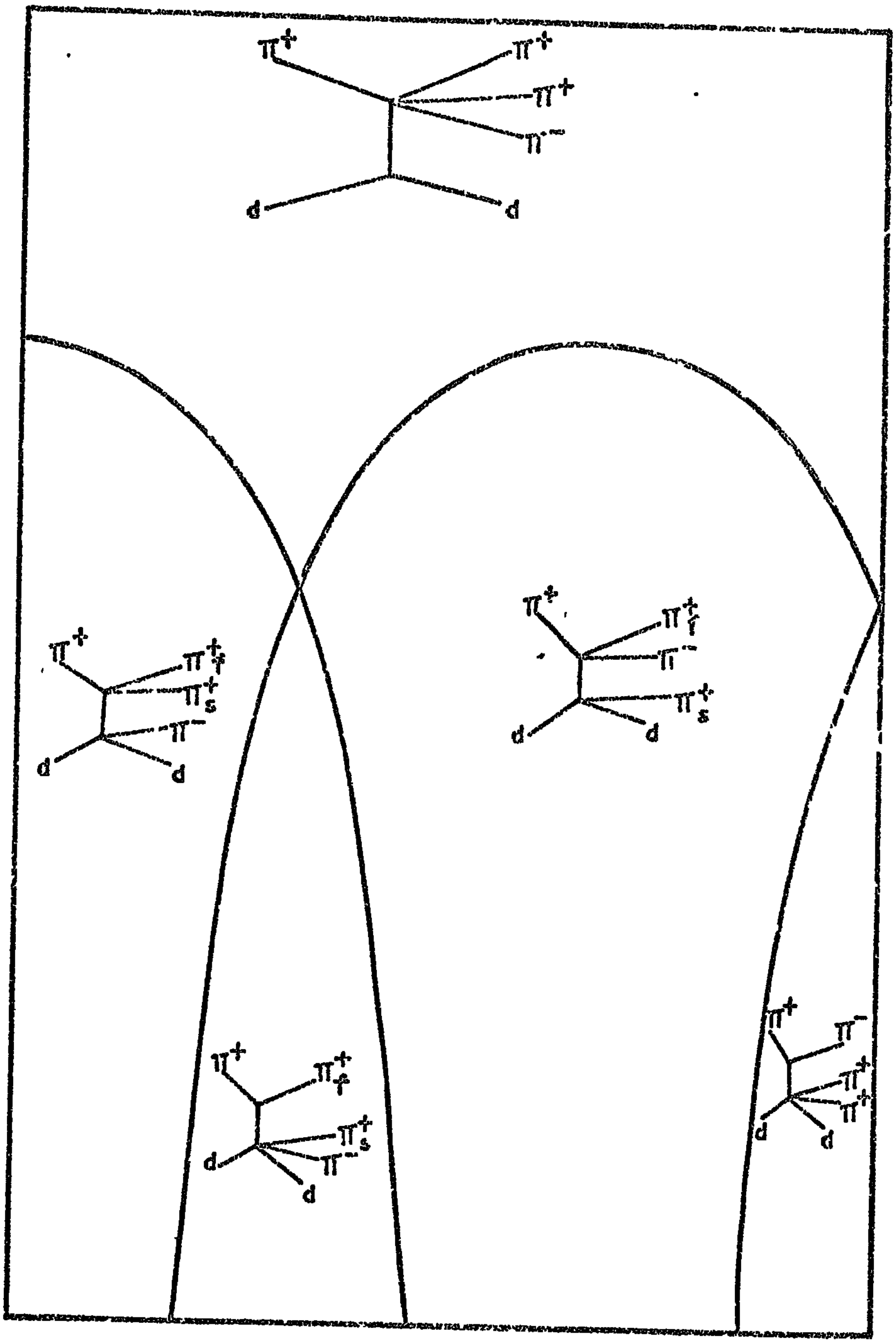

Kinematic configurations corresponding to numbered regions of Fig. 6.12

was defined within a hexagon. In this case the longitudinal momentum distribution is defined within a cuboctahedron as shown in Fig. 6.14. The three Van-Hove variables defined within this figure are the two Van-Hove angles θ_1 and θ_2 and the length of the radius vector $\vec{R}$. These variables are defined as:

$$R = \sqrt{3/4 \sum_{i=1}^{4} q^2_j}$$

$$\theta_1 = \cos^{-1} \left(\frac{qd}{r}\right)$$

$$\theta_2 = \tan^{-1} \frac{\sqrt{3}(q_{\pi^+_2} - q_{\pi^-})}{3q_{\pi^+_1} + q_d}$$

where 'q_a' represents the c of m longitudinal momentum for particle 'a'. Three other variables used are the kinetic energies of three of the four particles: π^+_f, π^- and the deuteron. The seventh variable recommended is the invariant mass of a combination of the final state particles. It is essential that great care is taken in the choice of which particles to group together for this seventh variable. The introduction of biases into the analysis was avoided by choosing two particles whose invariant mass distribution showed no resonant shapes. This restriction leads to the choice of the mass of the two positive pions as the best combination since, as can be seen from Fig. 6.5(b), their mass distribution contains no structure. Thus the seven variables chosen for the analyses were: θ_1, θ_2, R, T_{π^+f}, T_{π^-}, T_d and $M(\pi^+,\pi^+)$.

Fig. 6.14

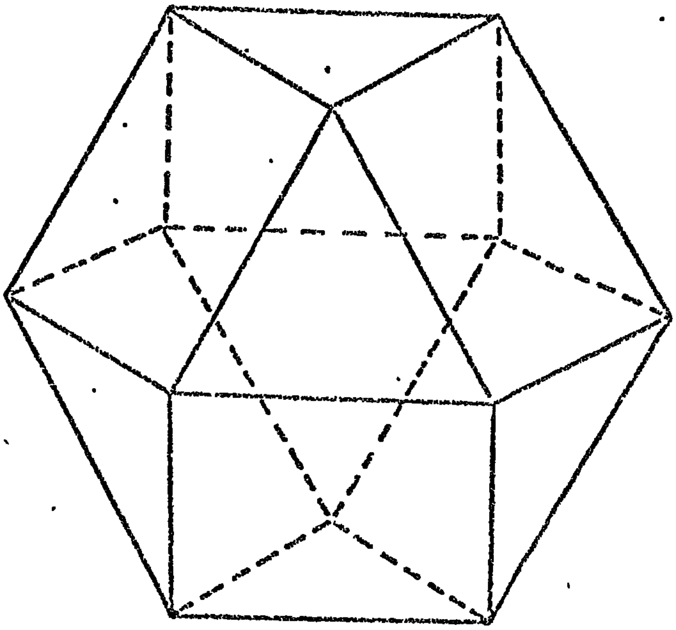

LPS CUBOCTAHEDRON

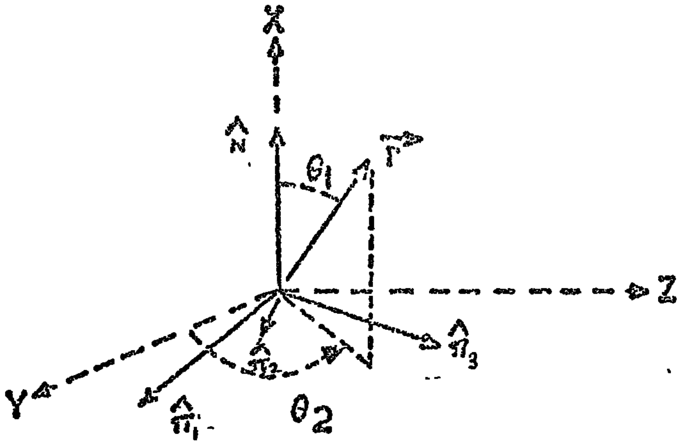

$\hat{N} = (1,0,0)$	$q_N = \hat{N}\cdot\vec{r}$	$r = \sqrt{\frac{3}{4}\left(q_N^2 + q_{\pi_1}^2 + q_{\pi_2}^2 + q_{\pi_3}^2\right)}$
$\hat{\pi}_1 = \left(-\frac{1}{3}, \frac{2\sqrt{2}}{3}, 0\right)$	$q_{\pi_1} = \hat{\pi}_1\cdot\vec{r}$	$\theta_1 = \cos^{-1}\left(\frac{q_N}{r}\right)$
$\hat{\pi}_2 = \left(-\frac{1}{3}, -\frac{\sqrt{2}}{3}, -\frac{\sqrt{6}}{3}\right)$	$q_{\pi_2} = \hat{\pi}_2\cdot\vec{r}$	
$\hat{\pi}_3 = \left(-\frac{1}{3}, -\frac{\sqrt{2}}{3}, \frac{\sqrt{6}}{3}\right)$	$q_{\pi_3} = \hat{\pi}_3\cdot\vec{r}$	$\theta_2 = \tan^{-1}\left(\frac{\sqrt{3}\,(q_{\pi_3} - q_{\pi_2})}{3q_{\pi_1} + q_N}\right)$

Definitions and conventions of 4-body L.P.S. cuboctahedron.

6.7.2 The Analysis

The statistical analysis programme CLUSTAN was supplied with the above seven variables for each of 1000 cases in the total sample of 1082 events for reaction C. Six independent clusters were obtained with sizes as shown in table 6.3 below.

Table 6.3 Size of final clusters

Cluster No.	Size
1	161
2	216
3	150
4	222
5	201
6	50

Increasing the number of final clusters required was found not to have any effect on the salient features of the clustered data. This is probably an effect of the low statistics, since increasing the number of clusters decreases the population size for some of the clusters, thereby making an analysis of a single cluster more difficult, because of the smaller statistics in that cluster. In table 6.4 below, is shown a general survey of the clusters and their contents.

Table 6.4 Survey of Cluster Contents

Cluster No.	$D^{++}_{d\pi^+_s}$	$D^{0}_{d\pi^-}$	$\overset{\rho}{\pi^+_f\pi^-}$	$\overset{\rho}{\pi^+_s\pi^-}$	A1
1	✓	X	✓	X	X
2	X	X	✓	X	X
3	✓	X	X	✓	X
4	X	X	✓	X	X
5	X	✓	X	X	X
6	X	X	X	X	X

The two clusters, 5 and 6 are general background clusters, except in the fact that cluster 5 contains some d^{*0}. This cluster alone was reclustered and was found to split into two segments the smaller cluster contained 53 cases and was centred on the d^* mass ($\sim$2150 MeV/c^2). In none of the clusters was any sign of the A1 meson found. This confirms the indication found in section 6.3.2 that any A1 present is negligible. It is interesting to note that one of the clusters separated, namely cluster 1, is an example of the quasi two-body reaction:

$$\begin{array}{lll} \pi^+ d \rightarrow d^{*++} & \rho^0 & \\ \qquad\quad \hookrightarrow d\pi^+_s & \quad\hookrightarrow & \pi^+_f \pi^- \end{array}$$

this amounting to some 16% of the total sample. This is consistent with the figures of 45% d^* and 65% ρ, which implies at least 10% of this quasi two-body process.

Cluster 1 is quasi two-body with the ρ meson in the $\pi^+_f\pi^-$ combination. Cluster 3, which contains d^* in the $(d\pi^+_s)$ combination, also contains some admixture of the ρ meson in the $\pi^+_s\pi^-$ combination although this is a small amount. Cluster 2 contains only ρ^0, formed in the $\pi^+_f\pi^-$ combination, and cluster 4 again contains ρ^0 $(\pi^+_f\pi^-)$, but with a small admixture of ρ in $(\pi^+_s\pi^-)$.

6.7.3 Clustan Plots

a) States of Rho in $\pi^+_f\pi^-$, $\pi^+_s\pi^-$

The invariant mass of the $\pi^+_f\pi^-$ combination is shown in Fig. 6.15(b) for cluster 2. This is also shown in Fig. 6.15(a) for the combination of clusters 1, 2 and 4. The mass of $(\pi^+_s\pi^-)$ for cluster 3 (admixture cluster) is shown in Fig. 6.16(a).

Fig. 6.15

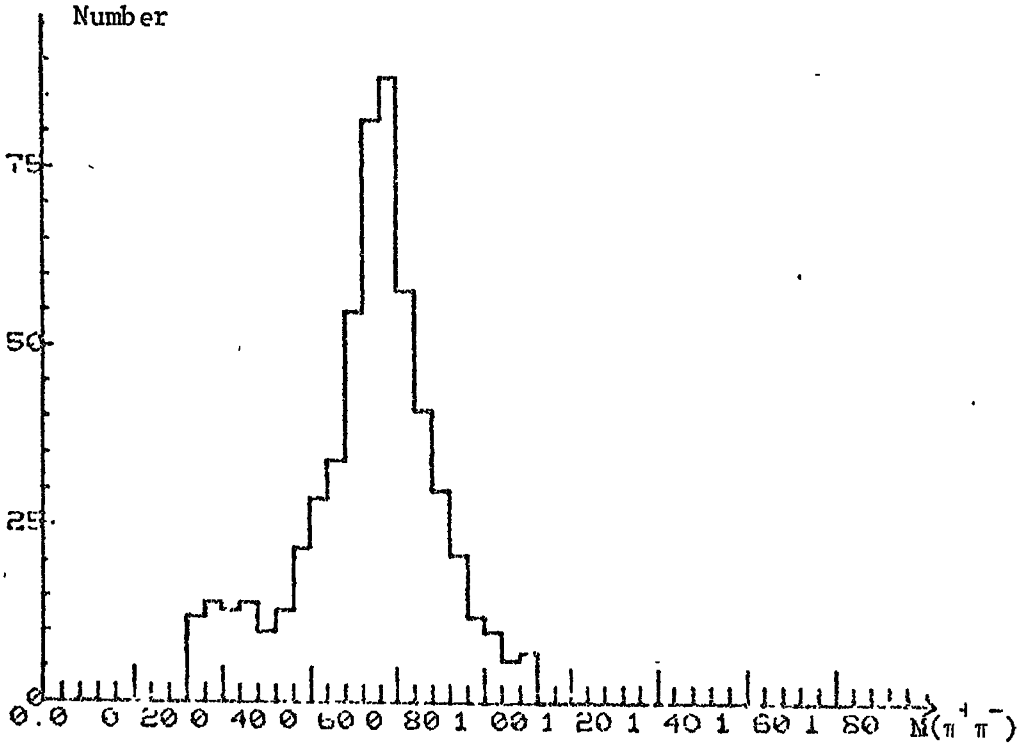

(a) $M(\pi^+_f\pi^-)$ for combined ρ^0 clusters

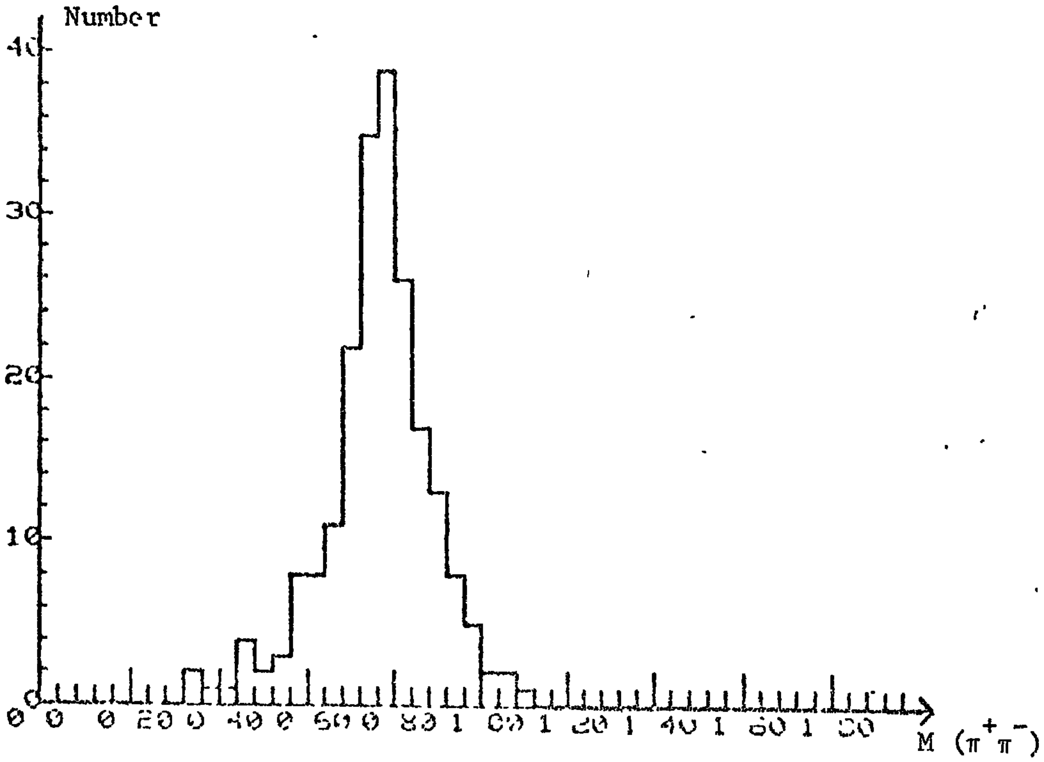

(b) $M(\pi^+_f\pi^-)$ for cluster 2

Despite the poor statistics the rho peak is clearly visible. Cluster 4 ($\pi^+_s\pi^-$) is shown in Fig. 6.16(b) and here there is some doubt about the authenticity of the signal.

b) States of $d\pi^+_s$

The invariant mass distribution of $d\pi^+_s$ for clusters 1 and 3 is shown in fig. 6.16(c). The corresponding t distribution from deuteron to d^* is shown in fig. 6.17. The solid curve in this figure represents the pion propagator given in Section 6.4.2, and renormalised to the data between t values of -0.1 and -0.6. It is apparent, from a comparison with Fig. 6.8, that the clustered data gives a better fit to this model than does the non-clustered data.

The Berger model, using a Regge-ised pion trajectory as described in section 6.4.3, has also been fitted to the clustered data. The angular distribution $\cos\theta$ $(d_{in}\to d_{out})$ in clusters 1 and 3 is shown in Fig. 6.18, the curves being the theoretical values given by the model. This is to be compared with the same fit to the non-clustered data shown previously in Fig. 6.7.

6.7.4 Summary of the Clustan Results

In the main, the fact that only ∿1000 events were available for this analysis, the statistics are a little too low for any obscure effects to be separated into clusters. In fact, the two clusters which show some admixture of states detract a little from the power of the analysis in this case. However, as was explained, any further clustering is useless because of the sizes of the samples being considered. Despite this, the method is not without its benefits.

Fig. 6.16

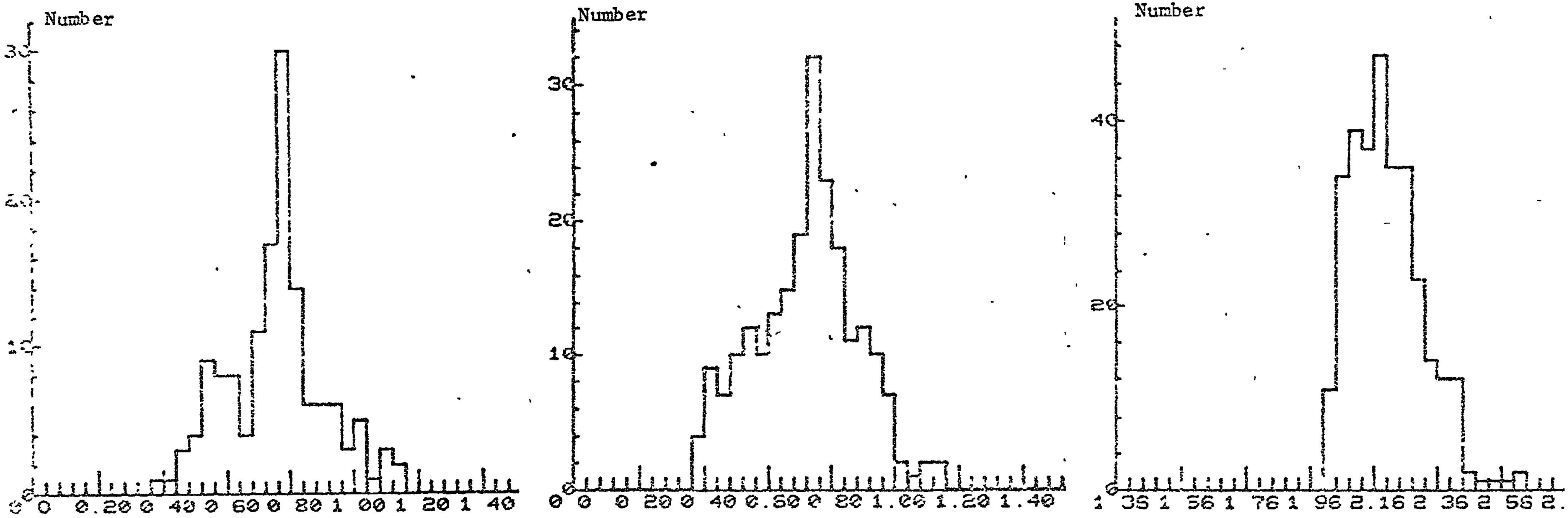

(a)

$M(\pi^+_s\pi^-)$ GeV/c^2 cluster 3

(b)

$M(\pi^+_s\pi^-)$ GeV/c^2 cluster 4

(c)

$M(d\pi^+_s)$ GeV/c^2 clusters 1 and 3

Fig. 6.17

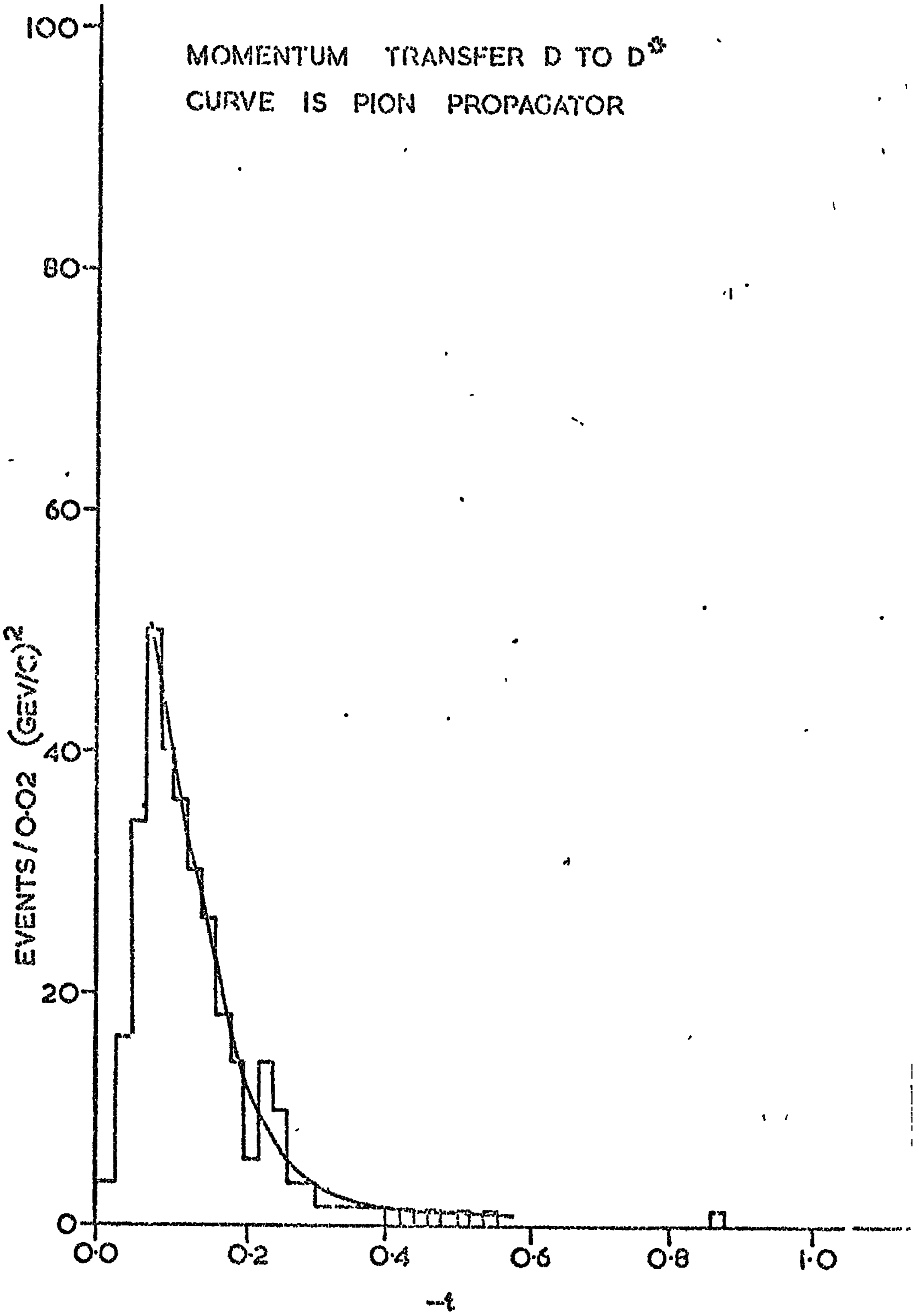
MOMENTUM TRANSFER D TO D*
CURVE IS PION PROPAGATOR
EVENTS / 0·02 (GEV/C)^2
100
80
60
40
20
0
0·0
0·2
0·4
0·6
0·8
1·0
−t

Fig. 6.18

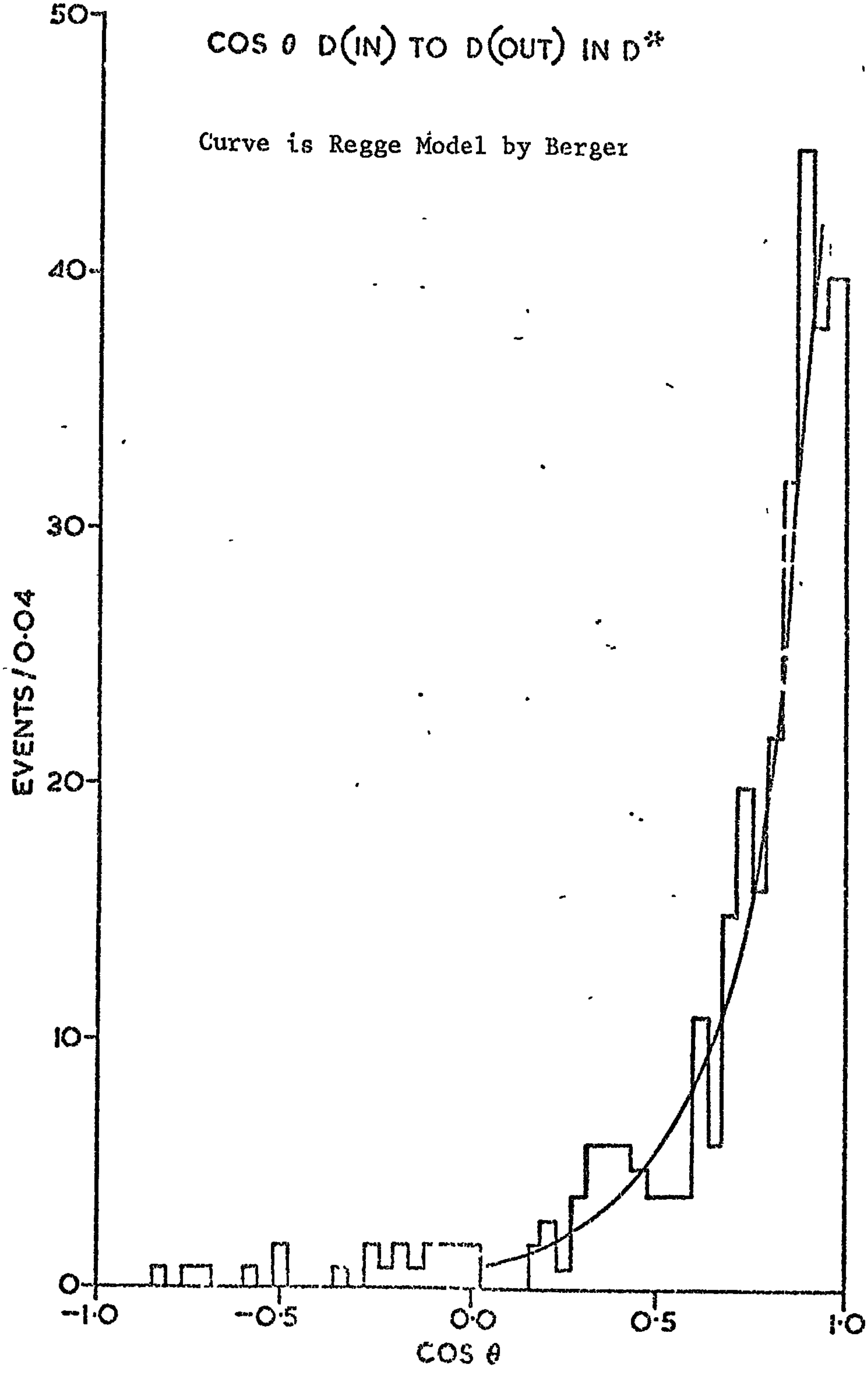

COS θ D(IN) TO D(OUT) IN D*
Curve is Regge Model by Berger
EVENTS/0·04
0
10
20
30
40
50
−1·0
−0·5
0·0
0·5
1·0
COS θ

The analysis clearly shows the quasi two-body d^* production which is not easily appreciated from the conventional approach, it also gives a very pure (no background) sample of these events. Just as it was possible to separate the admixture of d^{*o} from cluster 5, it may (with more statistics) be possible to separate cluster 3 if indeed this is not some real effect where the slow pion is 'shared' by the deuteron and the π^-.

After comparing the fits to the peripheral one pion exchange model with propagator $Pr = \frac{1}{(t_{d^*} - m_\pi{}^2)^2}$ for the momentum transfer distributions for clustered and non-clustered data, it is apparent that the more satisfactory fit is obtained to the clustered data. The predictions of the angular decay distributions of the d* give adequate fits for both sets of data, using the reggeised pion trajectory $\alpha(t) = t_{d^*} - m_\pi^2$, and in this case too the fit to the clustered data is better. The ρ^{o} signal is easily extracted in the clustered data, this amounting to 60% of the $(\pi^+ f \pi^-)$ system.

In conclusion, then, it must be said that the use of a technique for searching in a 7 dimensional space can be profitable even when the number of cases to be examined is not high.

Chapter 7 Conclusions

This thesis has presented the results of an analysis on the two channels

$$\pi^+ d \to p_s p \pi^+ \pi^- \qquad 1$$

and $$\pi^+ d \to d \pi^+ \pi^+ \pi^- \qquad 2$$

from a 4 GeV/c $\pi^+ d$ experiment. The method of analysis involves a multidimensional statistical searching (clustering) technique in an n-dimensional space defined by the number of final state particles in an event. By using the cluster analysis it has been shown that resonant signals containing a minimum of background can be extracted from the data.

The clustering technique has been shown to be highly efficient in separating three sub-channels from a Monte Carlo simulated experiment of $\pi^+ n \to p \pi^+ \pi^-$, a similar reaction to the 4 GeV/c experimental channel $\pi^+ d \to p_s p \pi^+ \pi^-$. The three sub-channels are:-

$\pi^+ n \to p \rho^0$

$\pi^+ n \to p f^0$

$\pi^+ n \to p \pi^+ \pi^-$ phase space background.

A variety of conditions for the production and decay distributions were generated ranging from complete isotropy to the conditions found in the 4 GeV/c experimental channel of reaction 1 above. It was found that the most significant single property which must be present in the data for a correct assignment of events to occur is the sharp t distribution usually found in experiment. Table 7.1 gives a summary of the amount of each of the three sub-channels found in clusters which would be tagged as being predomi-

Table 7.1 Separation of 3 FAKE Sub-Channels

Sub-channel	No. of Events Generated	Generated Distributions		Events in Identified Clusters		Total size of Identified Cluster	% of cluster which is true signal
		Production	Decay	No.	% of Original		
po^{o}	2000	$\frac{dN}{dt'}\alpha\ \exp(-10t')$	$a\cos^2\theta+b$	1841	92%	2034	90.5%
pf^{o}	1000	$\frac{dN}{dt'}\alpha\ \exp(-8t')$	$d\cos^4\theta+$ $e\cos^2\theta+f$	890	89%	1175	76%
$p\pi^+\pi^-$	1000	Isotropic Production Angle	Isotropic Decay	700	70%	786	89%

nantly that process, together with the amount of each cluster which corresponds to the reaction scheme to which that cluster was assigned. The clustering was performed on 2000 $p\rho^o$, 1000 pf^o and 1000 phase space background events generated with production and decay distributions consistent with those found in the experimental channel $\pi^+d \rightarrow p_s p \pi^+ \pi^-$.

7.1 The Channel $\pi^+d \rightarrow p_s p \pi^+ \pi^-$

The general properties of the experimental channel of reaction 1 above have been examined by mass cut techniques and a density matrix element analysis of the ρ^o and f^o signals extracted from this channel by the cluster analysis has been presented. The channel cross-section was found to be $\sigma(\pi^+d \rightarrow p_s p \pi^+ \pi^-) = 2.10 \pm 0.17$ mb.

(a) General Properties of Reaction 1: Mass Cut Methods

Parameterisation of the differential cross sections for the ρ^o and f^o mesons of the form

$$\frac{dN}{dt} = A \exp(-bt)$$

yielded values of the slope parameter b as shown in Table 7.2 below. Also shown in this table are the individual cross-sections for ρ^o and f^o production, which have been estimated by allowing for the Breit Wigner tails of the resonances.

Table 2.2 ρ^o and f^o cross-sections

Sub-channel	Cross-section	% of total $\pi^+d \rightarrow p_s p \pi^+ \pi^-$	Slope of differential Cross-section $(GeV/c)^{-2}$
$\pi^+d \rightarrow p_s p \rho^o$	0.98 ± 0.10	47%	9.8 ± 0.4
$\pi^+d \rightarrow p_s p f^o$	0.48 ± 0.07	23%	8.1 ± 0.4

Both of the cross-sections agree well with those found by other experiments (Ref. 7.1), and in the case of the t-distributions the slopes agree with other experiments where the ρ^0 and f^0 mesons were produced by similar production mechanisms. A depletion of events at low values of momentum transfer has been shown to be consistent with that expected from the effects of the Pauli Exclusion Principle on a 100% spin-flip interaction, spin flip at the nucleon vertex being expected for the case of pion exchange.

(b) Clustering Technique

Using the clustering technique to extract the signals of the ρ^0 and f^0 mesons it has been shown that the amount of data available for analysis is approximately double that from mass cuts, and that the total channel $\pi^+d \rightarrow p_s p\pi^+\pi^-$ is consistent with 82% precise physical processes. This 82% corresponds to 53% ρ^0 production, 23% f^0 production and 6% diffraction dissociation of the neutron target. These partial cross-sections, calculated by assuming that the relative separations given in Table 7.1 for the FAKE simulation are valid for the clustering of the experimental channel, are in agreement with those found by mass cut methods shown above in Table 7.2.

7.2 Density Matrix Analysis

A mixed spin S and P wave density matrix element analysis on the ρ^0 data extracted by the cluster searching technique has been performed throughout the available t range. A more specific analysis at low values of $|t|$ was used to separate the density matrix elements ρ^{11}_{00} and ρ^{11}_{11} which are only available in linear combination after the application of the method of moments. The analysis shows that up to a $-t$ value of 0.075 $(GeV/c)^2$, which corresponds to ~20% of the available data, the ρ^0 meson data are compatible with >90% pure pion exchange. There was also shown to be a substantial amount of pure S-wave component in the ρ^0 region which falls off slowly with $|t|$ from a $|t|$ value of 0.1 $(GeV/c)^2$. The presence of an interfering S-wave component is also apparent upon examination of the ρ^0 decay angular distribution which exhibits an asymmetry parameter η of 0.31 ± 0.04.

For the f^0 meson, again extracted by the cluster analysis from the channel $\pi^+d \rightarrow p_s p\pi^+\pi^-$, an analysis in terms of the pure D-wave spin density matrix elements has been shown to be inadequate in explaining the experimental data. This can be appreciated from an examination of the f^0 decay angular distribution where the expected central peak is not present and the asymmetry parameter η has a value 0.24 ± 0.04. An analysis involving the computation of the density matrix elements from the spherical harmonic moments for $m=0$ in the low t region $0.04 \leq |t| \leq 0.07$ has been performed. This analysis, valid only in this t region since above $|t| = 0.07$ the spherical harmonic moments for $m\neq0$ are non-zero, has shown that there is a substantial S+P wave component in the f^0 region and that the ratio of D-wave to S+P wave constituents is 1:1. The momentum transfer region $0.04 \leq |t| \leq 0.07$ contains only ~10% of the available f^0 meson data, but it is within this t interval that the S+P wave interference is a maximum.

These results, for both the ρ^0 and f^0 meson data, are consistent with an analysis performed by the collaborating laboratories in which mass cuts were used to define the respective signals. Compared with the signals extracted by the clustering technique, that is the signals identified as the ρ^0 and f^0 mesons, the angular distributions for the signals defined by mass cuts are broader. Indeed, the sharpness of the Clustan signals is a measure of the success of the technique since if there were any significant mixing between the clusters then the f^0 decay angular distribution would be considerably broadened and the ρ^0 distribution considerably sharpened.

7.3 The Coherent Channel

For the second reaction considered, namely the coherent channel $\pi^+d \rightarrow d\pi^+\pi^+\pi^-$, there was found to be no evidence for the presence of the A1 meson in the tripion mass spectrum. This channel, with a cross-section of 316±26 μb, was found to be dominated by ρ^0 production and the d^* effect. These two processes account for 65% and 45% of the channel respectively which implies >10% quasi two-body $\rho^0 d$ production. The d^* peak was shown to be non-resonant and is most probably due to the formation of an intermediate Δ state, the subsequent decay of which leaves an intact deuteron as one of the final state particles. The momentum transfer distribution from d to d^* was shown to be in good agreement with that predicted from a simple one-pion exchange peripheral model, and a model by Berger was shown to predict quite well the decay angular distribution of the d^*.

Application of the cluster searching technique in the full 7-dimensional space defined by the 4 final state particles in this channel also showed no evidence for A1 production, and 15% of the channel was shown to be quasi two-body $\rho^o d^*$. Applying the same models to the t-distribution and decay angular distribution of the d* signal extracted by clustering, it was found that both the peripheral one-pion exchange model and the Regge model of Berger gave better fits than they did to the signals defined by mass cut techniques.

Appendix A

A1 Mandelstam Variables and Crossing Symmetry

Consider the general collision process $a+b \rightarrow c+d$ where a, b, c and d are hadronic states. These particles have four-momenta denoted by p_a, p_b, p_c and p_d respectively. The four momentum, p_a, $= (\vec{p}_a, E_a)$, where $\vec{p}$ is the three momentum and E the total energy of the particle.

There are two independent Lorentz invariant quantities one can form from these four-vectors apart from the particle rest mass $p_i^2 = - m_i^2$. These are denoted by the so-called Mandelstam variables

$$s = -(p_a+p_b)^2 = -(p_c+p_d)^2 = E^2 \qquad \text{(a1)}$$

$$t = -(p_a-p_c)^2 = -(p_b-p_d)^2 = -\Delta^2 \qquad \text{(a2)}$$

In the centre of momentum system of the collision, a and b have equal and opposite three-momentum, so that $s=E^2$ the square of the total CMS energy. t is the square of the four-momentum transfer between a and c, or b and d. For an elastic collision with centre of mass momenta for a and c of $\vec{k}$ and $\vec{k}'$ $(|\vec{k}|=|\vec{k}'|)$ then $t = -2k^2(1-\cos\theta)$ where θ is the CMS scattering angle. That is, t is negative for a scattering process.

It is also possible to consider the crossed momentum transfer, u, where

$$u = -(p_a-p_d)^2 = -(p_c-p_b)^2 \qquad \text{(a3)}$$

and by combining s, t and u we have

$$s + t + u = m_a{}^2 + m_b{}^2 + m_c{}^2 + m_a{}^2 \qquad \text{(a4)}$$

such that u is not an independent quantity.

In order to examine the properties of an intermediate state formed from a and b it is natural to describe the partial wave scattering amplitude in terms of the s-channel quantities, i.e. $f(\ell,E)$ where ℓ and E are the angular momentum and energy of the combination of a and b. At low energies (<1 GeV) this description is well founded but for energies greater than a few GeV the cross section for the pion nucleon interaction varies smoothly with energy and another description is required. This is that the s-channel scattering is dominated by the exchange of poles in the momentum transfer or t-channel. Since t is negative, these exchange particles are outside the physical region for the reaction $a + b \rightarrow c + d$. However, by replacing b and c by their anti-particles $\bar{b}$ and $\bar{c}$ and reversing their momenta (see Fig. A1) then in Eqs. a1 and a2 s and t change sign. t is now the energy variable for the t-channel reaction $a + \bar{c} \rightarrow \bar{b} + d$. s is negative and is now the momentum transfer variable for the t-channel reaction, that is $t \rightarrow \bar{s}$ and $s \rightarrow \bar{t}$. The reaction $a + \bar{c} \rightarrow \bar{b} + d$ is called the crossed reaction to $a + b \rightarrow c + d$. The point is that the t-channel exchange poles of the original reaction now become the s-channel resonances, in the physical region of the crossed channel.

The principle of crossing symmetry states that both reactions are described by one amplitude:

$$\bar{F}(\bar{s},\bar{t}) = F(t\rightarrow\bar{s},\ s\rightarrow\bar{t})$$

and the principle also requires that the function F can be continued into the unphysical regions of the s,t plane. For example $\bar{s}>0$ for the t-channel corresponds to the unphysical

FIG. A1

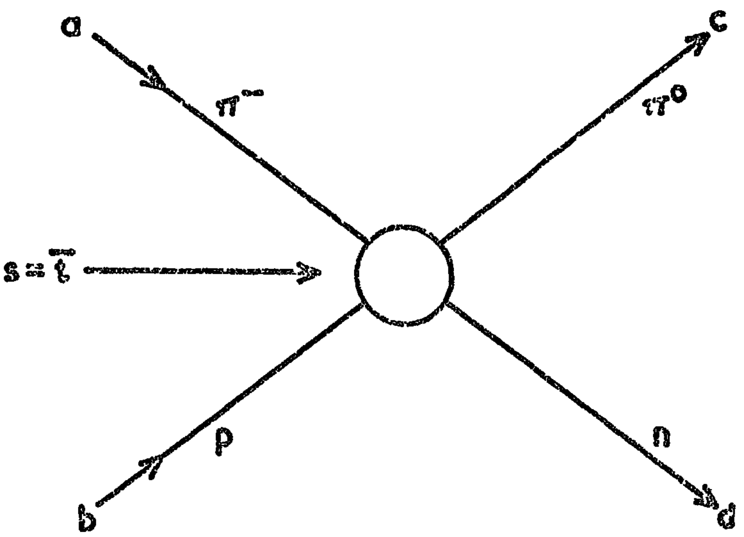

s-channel reaction
$a + b \rightarrow c + d$
e.g. $\pi^- + p \rightarrow \pi^0 + n$

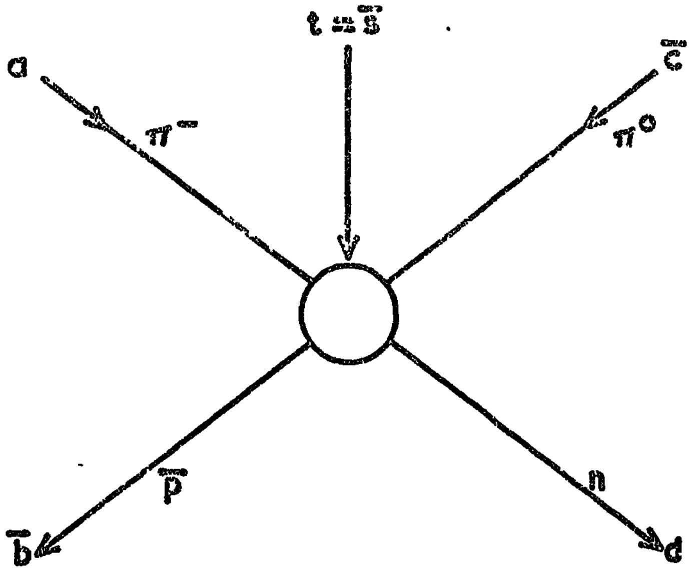

t-channel reaction
$a + \bar{c} \rightarrow \bar{b} + d$
e.g. $\pi^- + \pi^0 \rightarrow p + n$

ILLUSTRATION OF CROSS-CHANNEL REACTIONS

values $t>0$ (or cos >1) in the s-channel. Crossing symmetry is of vital importance in seeking to describe high energy processes in the Regge picture.

A2 Momentum transfer: t and t'

From section A1, t is defined as

$$\begin{aligned} t &= -(p_c-p_a)^2 - (p_d-p_b)^2 \\ &= (\vec{p}_c-\vec{p}_a)^2 - (E_c-E_a)^2 \\ &= -(m^2{}_c+m^2{}_a) + 2E_cE_a - 2p_cp_a \cos\theta \end{aligned}$$

It is apparent that for fixed values of m_a and m_c for given momenta p_a and p_c then there exists a minimum value of $|t|$, t_{min} and this leads to the definition of t' as

$$t' = t - t_{min}$$

$$t' = -2p_ap_c\ (1-\cos\theta)$$

Appendix B

B1 Hulthen Momentum Distribution

The Hulthen wave function for the deuteron, in terms of the two effective ranges α and β, is the double Yukawa function

$$U(r) = \left[\frac{2\alpha\beta(\alpha+\beta)}{(\alpha-\beta)^2}\right]^{\frac{1}{2}} \left[\frac{e^{-\alpha r} - e^{-\beta r}}{r}\right] \qquad \text{Ref. B.1.}$$

where $\alpha = 0.23$ Fermi^{-1} and $\beta = 1.27$ Fermi^{-1}. The two ranges have been evaluated accurately from electron scattering experiments. This wave function can be expressed in momentum space as $\psi(p)$ by applying the Fourier transformation

$$\psi(p) = \int_0^\infty U(\vec{r}) \; e^{i\vec{p}\vec{r}} \; d^3\vec{r}$$

$$= \int_0^\infty U(r) \; \frac{\sin pr}{pr} \; 4\pi r^2 \, dr$$

$$\psi(p) = A \left[\frac{2\alpha\beta(\alpha+\beta)}{(\alpha-\beta)^2}\right]^{\frac{1}{2}} \int \frac{e^{-\alpha r} - e^{-\beta r}}{r} \; \frac{\sin pr}{pr} \, r^2 \, dr$$

$$\psi(p) = A \left[\frac{2\alpha\beta(\alpha+\beta)}{(\alpha-\beta)^2}\right]^{\frac{1}{2}} \left[\frac{1}{\alpha^2+p^2} - \frac{1}{\beta^2+p^2}\right]$$

By the impulse approximation, which basically states that the production amplitude from the deuteron is a linear combination of the individual nucleon production amplitudes, this momentum wave function will remain unaltered for one of the nucleons i.e. the spectator nucleon. Thus the momentum distribution for the spectator may be written, from $P(p)dp = 4\pi p^2 \psi^2(p)\, dp$, as

$$P(p)\, dp = B \; \frac{\alpha\beta(\alpha+\beta)}{(\alpha-\beta)^2} \left[\frac{1}{\alpha^2+p^2} - \frac{1}{\beta^2+p^2}\right]^2 p^2 \, dp$$

where B is a normalication constant.

B2 Deuteron Form Factor

The form factor is the Fourier transform of the deuteron density distribution, and the form factor squared reflects the probability distribution of momentum transfer that the deuteron can withstand without breaking up. (Ref. B.2).

The density distribution $\rho(r)$ is the square of the deuteron space distribution U(r) and hence the form factor H(q), where q is the three momentum transfer $\sim\sqrt{t}$, can be written as (Ref. B.3)

$$H(q) = \int U^2(r) \; \frac{\sin qr}{qr} \; 4\pi r^2 \, dr$$

which becomes

$$H(q) = \frac{2\alpha\beta(\alpha+\beta)}{(\alpha-\beta)^2 q} \left[\tan^{-1}\frac{q}{2\alpha} + \tan^{-1}\frac{q}{2\beta} - 2\tan^{-1}\frac{q}{\alpha+\beta} \right]$$

which satisfies the condition that at $q=0$ the form factor $H(0)=1$. The evaluation of H(q) is particularly useful in predicting the effects of the Pauli Exclusion Principle on the final state p-p system after charge exchange scattering upon the neutron has occurred.

Acknowledgements

I would like to thank Professors G. D. Rochester and A. W. Wolfendale who, as sequential heads of the department, made available the facilities of the Physics Department at Durham during my work for this thesis. My particular thanks go to my supervisor Dr. J. V. Major without whose guidance, patience, and help during all phases of the work, this thesis would not have been possible.

I would also like to thank all the other members of the High Energy Nuclear Physics Group at Durham for their many discussions during the course of the work, particularly Dr. D. Evans, Mr. M. Dale and Mr. A. P. Lotts. I am grateful to the staff of the collaborating laboratories, both academic and technical, for the provision of their data.

My thanks are due to all the scanning and measuring staff at Durham University for their work on this experiment, and particularly to Mrs. J. Gibson and Mrs. D. Pickles the former for taking charge of the measuring and the latter since she was responsible for making a good fraction of the diagrams. I wish also to thank Mrs. D. Philpot for taking on the task of typing the manuscript and doing so in such a professional way.

Lastly, but by no means least, I would like to thank my wife, Margaret, for her constant encouragement and interest in the work.

To these, and many others who have helped and encouraged me throughout, I am much indebted.

This work was financed by the Science Research Council.

References

Chapter 1

1.1 See for example K. A. Kamakhy Ph.D Thesis University of Durham 1973

1.2 Fischer, C.M. R.H.E.L. HEP/MISC/8

Chapter 2

2.1 Lazeyras CERN/D.PLII/BEAM/68-9

2.2 CERN 2-m Handbook

2.3 Gordon Ph.D Thesis University of Illinois 1970

2.4 Fabian, B.N. Rev. Sc. Inst. 34 (1963) 484

2.5 Bubble and Spark Chambers Edit. Shutt Ac. Press (1967)

2.6 R.H.E.L. Geometry Programme Manual

2.7 McEwan and Daniell R.H.E.L. report RL/73/093 .

2.8 Compilation of Cross Sections: Particle Data Group LBL/53/1973

Compilation of π^+ induced cross-sections CERN/HERA 70/5

Chapter 3

3.1 Bonn-Durham-Nijmegan-Paris-Turin Collaboration 5 GeV/c π^+p

3.2 Van-Hove P.L. 28B 429 (196), N.P. B9 (1969) 331

3.3 Durham-Hamburg-Genoa-Milan-Saclay Collaboration 11.5 GeV/c π^+p

3.4 Dao et al PEPR Programming Note Number 101 Jan 15 1971

3.5 Brau, Pless et al PRL 27 No. 21 (1971) 1481

3.6 Evans et al IInd Aix en Provence International Conference on Elementary Particles Paper 361

3.7 Ferrando et al IInd Aix en Provence International Conference on Elementary Particles Paper 219

Chapter 4

4.1 Christien and Gamel P.R. 91 (1953) 100

4.2 Jackson N.C. 34 (1964) 1645

Chapter 5

5.1 Bartsh et al N.P. B22 (1970) 109
Carroll et al PRL 28 (1972) 318
Whitehead et al NP B48 (1972) 365

5.2 Pilkuhn 'Interaction of Hadrons' North Holland 1967

5.3 Estabrooks and Martin P.L. 40B (1972) 655

5.4 Sekulin N.P. B56 (1973) 227

5.5 Charlesworth et al NP B65 (1973) 253

Chapter 6

6.1 Vegni et al P.L. 19 (1965) 526

6.2 Eisenstein and Gordon P.R. D1 (1970) 841

6.3 Berger E.L. P.R. 166 (1968) 1525/Month M. P.R. 155 (1967) 1689

6.4 Vanderhagen et al N.P. B13 (1969) 329

6.5 Deery et al P.L. 31B (1970) 82

6.6 Cnops et al PRL 21 (1968) 1609
P.L. 29B (1969) 45

6.7 D. Kemp Ph.D. Thesis Univ. of Durham 1974

6.8 Abolins et al P.R.L. 15 (1965) 125

6.9 B. J. Stacey Ph.D. Thesis Univ. of Birmingham 1975

Chapter 7

7.1 Compilation of π^+d interactions LBL-53 (Parts 1 & 2) 1973

Appendices

B1 Hulthen & Sugaware Handbuch der Physik Vol. 39

B2 Bingham CERN/D.Ph II/70-60

B3 Perkins 'Introduction to H.E. Physics';
Addition Wesley 1972